DYNAMICAL AND RADIATIVE PROCESSES IN THE TROPICAL TROPOPAUSE LAYER

By

Kai-Wei Chang

A dissertation submitted in partial fulfillment of

the requirements for the degree of

Doctor of Philosophy

(Department of Atmospheric & Oceanic Sciences)

at the

UNIVERSITY OF WISCONSIN-MADISON

2019

Date of final oral examination: 11/25/2019

The dissertation is approved by the following members of the Final Oral Committee:

Tristan S. L'Ecuyer, Associate Professor, Atmospheric and Oceanic Sciences
Steven A. Ackerman, Professor, Atmospheric and Oceanic Sciences
Matthew H. Hitchman, Professor, Nelson Institute for Environmental Studies
Andrew K. Heidinger, Physical Scientist, National Oceanic and Atmospheric Administration
Grant W. Petty, Professor, Atmospheric and Oceanic Sciences

Acknowledgments

I would like to thank my advisor, Tristan L'Ecuyer, for his guidance and support the course of my degree. It was fortunate that he and Brian Kahn were willing to bring me onboard to work on their project as a graduate student without having previously met me in person. My first two years in Madison working on that project had been rewarding and my collaboration with Brian was very pleasant. I appreciate Tristan's willingness to let me eventually pursue my own research paths, which proved to be risky at several junctures but ultimately worked out well.

My PhD dissertation committee provided valuable feedback on my research ever since our first meeting. Through to their input I was able to improve the quality of my research and gain different perspectives on the problems I worked on.

During my first three years here I am fortunate to have shared office with Alex Matus, with whom I had many discussions that shaped my knowledge and perception of atmospheric science. I would like to thank Mark Smalley, who helped me many times during my first year. Often I would seek the advice of Elin Mcilhattan and Ethan Nelson, who have helped me throughout my degree. I was also fortunate to have had the assistance of Norm Wood and Dave Henderson when I needed their expertise in CloudSat data. Collaborating with Aronne Merrelli on a side research project was engaging and I learned many coding techniques from looking at his code. My research has some overlap with that of Andrew Dzambo's and I enjoyed our discussions. My thanks also go to all past and current members of the L'Ecuyer research group who have made our group a friendly and productive work environment. I would also like to acknowledge the AOS department staff, Sue Foldy, Sonja Johnson, Chelsea Dahmen, and Dee Van Ruyven, for their assistance.

I'd like to thank Zach Hansen for inviting me to the Colloquium Committee. Working on the committee was a daunting idea at first, as the thought of having to organize visitors' schedules and converse with them was intimidating. Thanks to Claire Petterson, Melissa Breeden, and many others on the committee, I was able to manage, and their help made things much easier. I want to thank Juliet Pilewskie, Julia Shates, and all members for continuing the work of the committee.

At several stages of my research I consulted Kai-Yuan Cheng who had helped me with things inside and outside of academics. It is nice to spend time with a fellow countrymen who works in the same field, and I am grateful for his support and input which were integral parts of my dissertation and defense.

Finally I'd like to thank my family. My time in the USA was a lot easier thanks to the support of my uncle who helped me in various ways. The support from my parents and my sister is what makes my work possible.

Abstract

As a gateway of troposphere-to-stratosphere transport, the tropical tropopause layer (TTL) plays a key role in determining the concentration and distribution of water vapor in the upper troposphere and lower stratosphere (UTLS). This dissertation presents three studies on the dynamical and radiative processes that influence the TTL and also the Brewer-Dobson circulation (BDC) in the global UTLS.

Water vapor in the tropical lower stratosphere is strongly correlated with TTL temperatures, which are closely associated with latent heating (LH) in tropical convection. The first study examines the role of latent heating (LH) vertical distribution in TTL cooling and upper-tropospheric warming associated with equatorial wave responses. Using cross-spectral analysis on time series of LH and UTLS temperature, we show that heating above 6 km was found to have the highest coherence with the equatorial wave cooling and warming pattern in the mean temperature profile. We distinguish the effects of convective and stratiform LH, whose heating altitudes differ. Stratiform LH exhibits higher coherence with temperature throughout the UTLS, especially in the equatorial Rossby wave response as seen in the cross-spectral analysis. Highest coherences occur mostly at time scales of the Madden-Julian Oscillation (MJO), suggesting the importance of MJO convection in TTL cooling and subsequent dehydration processes.

The second study explores the relationship of TTL cirrus clouds to gravity and Kelvin waves. Motivated by the recent interest in understanding how the vertical gradient of temperature anomalies (dT'/dz) from waves influence clouds, we collocate lidar observations of TTL clouds and wave temperature anomalies from radio occultation to understand how cloud occurrence relates to wave anomalies. Throughout the TTL, 57% of clouds were found in the wave phases where both the temperature anomaly (T') and dT'/dz were negative. In contrast, 24% of clouds

were in the phase of negative T' but positive dT'/dz, suggesting that regions of negative dT'/dz significantly promote the formation and/or maintenance of clouds. We show that larger (smaller) values T' are associated with a lower (higher) probability of cloud occurrence, demonstrating connection of wave amplitude to TTL cloud formation.

The BDC is a balance between wave–mean-flow interaction and radiative heating rates in the middle atmosphere. Since clouds modulate the amount of upwelling radiation, they can also influence the radiative heating in the UTLS. Using the CloudSat/CALIPSO 2B-FLXHR-LIDAR data set and the MERRA-2 reanalysis, the final study evaluates cloud effects on the BDC by comparing the mass circulation diagnosed from clear-sky and all-sky radiative heating rates. Cloud effects are strongest during boreal winter when the vertical and meridional components of the BDC below 80 hPa exhibit differences on the order of 0.1 mm/s and 10 cm/s, respectively. These magnitudes are comparable to the BDC itself, illustrating that cloud effects on radiative heating rates can have a significant influence on the strength of tropical upwelling and meridional mixing. TTL cirrus, which tends to impose weak heating in the TTL, were found to enhance the tropical upwelling and also the poleward transport, while the aggregate effect of all other cloud types was to weaken them instead.

Table of contents

Abstract…… i

Table of contents……... iii

List of figures...……...…….……....……. vi

List of tables…..…….…… xv

Chapter 1 Background……. 1

1.1 Stratospheric water vapor and the Brewer-Dobson circulation……..... 1

1.2 Tropical tropopause layer…….……..… 8

1.3 Cirrus clouds in the tropical tropopause layer……...…….. 12

1.4 Radio occultation……...……. 16

1.5 Outline of these and relevance of research…….…… 18

Chapter 2 Role of latent heating vertical distribution in the formation of the boreal winter tropical cold trap…….. 20

2.1 Introduction……..…….. 20

2.2 Data sets……...……..…… 24

2.2.1 The wetPrf radio occultation data set……...……... 24

2.2.2 TRMM spectral latent heating……...……. 25

2.2.3 Radiative heating from CERES and its consistency with TRMM Estimates……...……. 27

2.3 Time series processing and cross-spectral analysis……..…….. 29

2.2.1 Construction and preprocessing of time series……..……...……... 29

2.3.2 Cross-spectral analysis……..……..... 31

2.4 Coherence and time-lag between latent heating and UTLS temperature…….…….. 32

2.5 Empirical orthogonal functions of latent heating and cross-spectral analysis of principal component time series……...……. 42

2.6 Chapter summary…….……..…….…….. 48

Chapter 3 Influence of gravity wave temperature anomalies on cirrus clouds in the tropical tropopause layer…….. 51

3.1 Introduction…… 51

3.2 Data sets……. 53

3.3 Methodology…….. 54

3.3.1 Extraction of gravity wave temperature anomalies…… 54

3.3.2 Collocation of CALIPSO observations to RO profiles……... 56

3.4 Population of clouds in wave phases…….. 57

3.5 Composite time evolution of wave anomalies and cirrus occurrence……. 62

3.6 Comparing satellite-observed features to theoretical predictions…...…… 70

3.7 Chapter summary……...……...……. 73

Chapter 4 Influence of clouds on the radiative heating and residual circulation of the upper troposphere and lower stratosphere..…. 77

4.1 Introduction……..…….. 77

4.2 Data sets……. 78

4.2.1 2B-CLDCLASS-LIDAR and 2B-FLXHR-LIDAR…… 78

4.2.2 Radio occultation temperature profiles…….…….. 80

4.2.3 MERRA-2 reanalysis…….....…… 80

4.3 Effect of clouds on TTL radiative heating rates……. 81

4.4 Global UTLS radiative heating rates under clear-sky and all-sky conditions……...…… 84

4.5 Residual velocities diagnosed from satellite data sets and MERRA-2….. 93

4.6 Radiative influence of cirrus on the residual circulation……... 104

4.7 Chapter summary……. 108

Chapter 5 Summary…….....… 112

Appendix Information Content of Visible and Mid-Infrared Radiances for Retrieving Tropical Ice Cloud Properties…… 116

A.1 Introduction…….. 116

A.2 Ice cloud database construction…… 121

A.3 Channel selection using information content…… 125

A.3.1 Radiative transfer model……... 125

A.3.2 Information content……..…… 126

A.3.3 Uncertainty sources…….…….. 130

A.4 Optimal channels for ice cloud retrievals…….…… 137

A.4.1 Stand-alone AIRS retrieval……... 137

A.4.2 Stand-alone MODIS retrievals…….…… 143

A.4.3 Surface and viewing angle dependence……..……..… 145

A.4.4 Combined AIRS+MODIS retrievals……. 148

A.4.5 Combined active+passive retrievals…….. 150

A.5 Conclusion……... 152

References……...…….....… 158

List of Figures

1.1 (Left column) Climatology of upper-tropospheric and stratospheric water vapor (Aura MLS) for January (top) and July (bottom). Black contours are zonal-mean zonal wind from the ERA-Interim reanalysis. Red dashed lines are the zonal-mean lapse-rate tropopause (FORMOSAT-3/COSMIC). (Right column) Climatology of temperature (ERA-Interim). Contours are identical to the left column. All values were calculated using data in 2007–2013……... 2

1.2 Schematic of the Brewer-Dobson circulation by Dunkerton (1978) (left) and by Brewer (1949) (right)…….3

1.3 Time-height section of mean water vapor mixing ratio between between 12°N/S from the (a) Microwave Limb Sounder and (b) the Halogen Occultation Experiment (HALOE). (Mote et al., 1996)…… 4

1.4 (a) Mean age of air during year 2000 (contours) and the difference of mean age between 2080 and 2000 (colors). (b) Residual vertical velocity (similar to vertical velocity of BDC) during 2000–2019 (contours) and difference between 2080–2099 and 2000–2019. (c) Same as (b) except for residual meridional velocity. (Li et al., 2012)…… 5

1.5 Schematic of the BDC and pathways of stratosphere-troposphere exchange. Wave breaking in the midlatitude stratosphere causes poleward flow, resulting in descent in the poles and ascent in the tropics. In the subtropical and midlatitude upper troposphere, exchange can occur on short timescales through tropopause folding and wave breaking of the subtropical jet. (Holton et al., 1995)…….. 6

1.6 Water vapor measured from balloons (black) at Boulder, Colorado (40°N, 105.25°W), and from satellite measurements centered on 82 hPa averaged over 35°-45° N (Aura MLS, light blue; HALOE, blue; SAGE-II, red). (Solomon et al., 2010)……... 7

1.7 (Left column) January average of temperature from the ERA-Interim reanalysis at 70 hPa (top), 100 hPa (middle), and 150 hPa (bottom). Arrows represent the mean horizontal winds from ERA-Interim. White contours represent outgoing longwave radiation; highest contoured value is 220 W/m^2 and contour intervals are 20 W/m^2. (Right column) January average of water vapor from the Aura MLS at approximately the same pressure levels. Green contours denote the temperature departure from the mean at intervals of 3 K. Negative contours are dashed…… 10

1.8 Same as Figure 1.7 except for July…… 10

1.9 Radiative heating rates based on soundings at Galapagos Islands, estimated using various radiative transfer models. (Gettelman et al., 2004)…… 12

1.10 (Top) annual mean of cirrus occurrence based on one year of data from CALIPSO. (Bottom) Zonal mean cloud occurrence from the same data and time period. (Sassen et al., 2008)……. 13

1.11 Cirrus with large horizontal scale observed by the Lidar In-space Technology Experiment (LITE). (Winker and Trepte, 1998)…… 15

1.12 (a) Temperature anomalies observed at 8.0°S, 80.5°E. Purple dots indicate the location of the cold-point tropopause. (b) <7-day filtered temperature anomalies (colored) and wind velocities (contours and shading at intervals of 1.5 m/s). (c) Temperature anomalies (colored) overlaid by 1064 nm lidar attenuated backscatter coefficient (green dots for all cirrus and black dots for subvisual cirrus). Red circles indicate regions where observed cirrus clouds coincided with cold wave anomalies. (Suzuki et al., 2013)…….. 15

1.13 Diagram of the radio occultation technique. GPS/GNSS satellites send radio signals that penetrate the atmosphere and then are received by the LEO satellite. The amount of radio signal bending caused by the atmosphere can then be retrieved and used to infer the atmospheric state. As the LEO satellite moves from position A to C, the radio signal passes through the atmosphere at different altitudes, enabling the profiling of atmospheric thermodynamic conditions……..... 17

1.14 Distribution of RO profiles obtained by COSMIC in one day (green dots). Red dots denote stations deploying radiosondes…….. 17

2.1 December-January-February (DJF) climatology of 82 hPa temperature (top row), water vapor mixing ratio retrieved by the Aura MLS (middle row), and frequency of cirrus clouds with cloud base above 15 km (bottom row) based on the CALIPSO 5-km cloud layer product. The left column shows composites on DJF periods with the Oceanic Niño Index < −0.5 (2008, 2009, 2011, and 2012), and those on the right correspond to DJF periods with Oceanic Niño Index > 0.5 (2007 and 2010)…….. 21

2.2 Wind and pressure response of a resting atmosphere to latent heating centered at (0,0). The units of the x and y-axis are non-dimensional and roughly correspond to 10° per unit. (Gill 1980)……. 23

2.3 Schematic of circulation and temperature anomaly induced by tropospheric heating at the location indicated by the bold gray arrow in a resting atmosphere. High- and low-pressure anomalies are indicated by H and L, respectively, while cold and warm anomalies are indicated by blue C and orange W letters. The lower tropospheric response would be

identical to Figure 2.2, while the upper tropospheric response would have the same pattern but opposing signs. Adapted from Highwood and Hoskins (1998)…… 23

2.4 Mean convective (red), stratiform (blue), and total (black) latent heating profiles within a box over the Maritime Continent (10°N/S and 110–150°E), calculated using the TRMM SLH product over years 2006–2014……. 24

2.5 Daily count of wetPrf profiles within 25°N/S from each RO mission. Dashed lines indicate the beginning and end of the period used in this study. COSMIC = Constellation Observation System for Meteorology, Ionosphere, and Climate; Metop = Meteorological Operational Polar Satellite; CHAMP = Challenging Minisatellite Payload……. 25

2.6 Scatterplot of vertically integrated $\boldsymbol{Q_r}$ inside the Indian Ocean Center box (Figure 2.8) estimated from the CERES SYN1deg and TRMM HERB product. Each dot represents daily mean values inside the box. Top row shows values in physical units (W/m2), with the mean value of each data set denoted in the legend. The bottom row is in standardized space, with the correlation coefficient *r* denoted……... 28

2.7 Same as Figure 2.6 except for the Maritime Continent Center box…….. 29

2.8 Boxes in which temperature and LH time series were constructed. LH time series are constructed inside the IO/MC Center boxes labeled in red, while temperature time series were constructed in the IO/MC North, South, East, and Center boxes. Contours at intervals of 15 W/m^2 are mean outgoing longwave radiation through 2006 –2014 derived from the National Oceanic and Atmospheric Administration Interpolated Outgoing Longwave Radiation daily data set. IO = Indian Ocean; MC = Maritime Continent…….. 30

2.9 Coherence spectra between 100-hPa mean temperature inside Indian Ocean South box (see Figure 2.8) and stratiform (left column), convective (middle column), or total (right column) heating inside Indian Ocean Center in the five vertical layers defined in section 2.3.1. Dashed lines indicate 99% significance level. Phases for coherences above this level are plotted as stars. The max coherence in each case and the corresponding period and phase are summarized in the legends……..… 33

2.10 Maximum coherence between total heating at each of the five layers (y-axis) and temperature at 250 hPa (top) or 100 hPa (bottom). The maximum coherence represents the highest value of the coherence spectrum (see Figure 2.9) out of all frequencies. IO = Indian Ocean; MC = Maritime Continent……. 35

2.11 (Left) Phases corresponding to statistically significant coherences between 9–12 km total latent heating (LH) and temperature at the altitude indicated by the y-axis. Stars indicate that the time scale of the phase falls within 20–90 days, while the X marks phases outside

this time scale. Positive phases indicate that the temperature lags LH. (Right) The lag in days, calculated from the phases in the left column. Positive lag indicates that temperature lags LH. Above 150 hPa, the 180° phase is assumed to be day 0 to estimate the lag of the cooling response (see text for explanation)…….. 37

2.12 Highest coherence at each pressure level (ordinate) and frequency (absicca) for convective (first row), stratiform (second row), total heating (third row), and radiative heating (fourth row) for the IO North, South, East, and Center boxes. The ordinate axis denotes the altitude of the temperature time series. White spaces indicate pressures and frequencies at which no coherences passed the significance testing. IO = Indian Ocean…… 39

2.13 Same as Figure 2.12 except for the MC boxes. MC = Maritime Continent..... 40

2.14 Profile of maximum coherence between temperature and latent heating for the North (left), South (middle), and East (right) boxes. The temperature time series from each pressure level (indicated by the ordinate axis) is paired with the latent heating time series from each of the five layers, and the coherence value plotted at each pressure represents the maximum coherence of the five possible pairings. Solid and dashed lines represent the Maritime Continent and Indian Ocean regions, respectively, while the colors distinguish the type of heating……...…… 41

2.15 The first three EOFs of latent heating the IO and MC box (left), and the variance explained by the first five EOFs (right)…….. 43

2.16 Same as Figure 2.11 except for the first EOF…… 44

2.17 Same as Figure 2.11 except for the second EOF…… 45

2.18 (Top row) Coherence between the first EOF and time series of temperature at each pressure level. (Bottom row) Same as top row except for the second EOF……. 46

2.19 Same as Figure 2.18 except for the MC boxes……..…… 46

3.1 (Left) Temperature profile (solid line) from COSMIC at 155° 43' W, 18° 16' N on 1 Jan 2007 and its corresponding mean-state (dashed). (Right) T' of the given profile and its four phases based on the sign of T' and dT'/dz……..… 55

3.2 Schematic of collocation between RO profile and CALIPSO footprints. The perigee points of the RO profile throughout all altitudes are shown in the red dashed line, while the position of the perigee point in the middle of the TTL (17.25 km) is denoted by the red X. The CALIPSO 5-km product provides estimates of cloud properties at 5-km footprints, and all footprints within 100 km of the red X are collocated to the RO profile, as indicated by the black dots. Gray dots are CALIPSO footprints considered too far from the RO profile

and not collocated. The shown RO profile was taken at approximately 0120UTC 2 Jan 2009……... 56

3.3 Population of CALIPSO Cloud Profile cloud bins inside each wave phase from 1 November 2006 to 30 April 2014. Plot (a) shows the cloud fraction for all of TTL (14.5 to 20 km), while (b)–(e) show the population in four different 1-km layers. The percentage in parenthesis denote the portion of clouds found in that vertical layer relative to all TTL clouds…… 58

3.4 Same as Figure 3.3(a) except for different longitudinal belts. Top six plots are for December-January-February and bottom six plots are for June-July-August……..…... 60

3.5 Distribution of vertical cloud fraction in each gravity wave phase. Note that the ordinate is in log-scale. Blue and red colored lines indicate the cold and warm phase, respectively, while the solid and dashed lines represent dT'/dz>0 and dT'/dz<0…….…….. 61

3.6 Composite of T' (top left), dT'/dz (top right), and buoyancy frequency (N^2) anomaly (bottom right) in height coordinate relative to cloud top. Colored contours in these three plots are at or above the 95% significance level according to the Student's t-test. Solid (dashed) contours represent positive (negative) anomalies and are at the same intervals as the colored contours. The abscissa denotes the time offset between the CALIPSO observation and RO sounding. The bottom left plot shows the number of unique RO profiles in each 2-hour time bin used to calculate the composites……..... 63

3.7 Same as Figure 3.6, except the composites are evaluated with respect to height above mean sea level instead of cloud top. Colored contours are at or above the 95% significance level according to the Student's t-test. Contour levels are identical to Figure 3.6……. 64

3.8 Schematic for creating the composite temporal evolution of cloud frequency with respect to T' minima. In this example, as shown in (a), during day *i* there is a collocated pair of CALIPSO and RO observations. The RO observation occurs $\Delta \boldsymbol{t_i}$ hours after that of CALIPSO, and the vertical distance between the height of local T' minimum (dashed horizontal line) and the cloud top (base) is depicted by the dashed (solid) magenta lines with length $\boldsymbol{h_i^{(t)}}$ ($\boldsymbol{h_i^{(b)}}$). For the temporal compositing (b), inside the time bin corresponding to $\Delta \boldsymbol{t_i}$ hours before observing T', the cloud fraction is calculated according to how much each vertical bin overlaps with the interval $[\boldsymbol{h_i^{(b)}}, \boldsymbol{h_i^{(t)}}]$. The same procedure is carried out for the collocated pair at day *j*. Also see text for explanation…… 66

3.9 Composite of cloud frequency with respect to local minima (first row) or maxima (second row) of T'. The columns correspond to composites made from subsets of T' extrema with magnitudes greater or equal to 0.5 K (left column), 1.0 K(middle), and 1.5 K (right). Dashed horizontal indicates the position of the local T' extrema. The third row shows the

background frequency (see text for explanation). The fourth and fifth rows are the cloud frequencies anomalies associated with cold or warm anomalies, calculated as the difference between the cloud frequency composites and the background cloud frequency. Contours in the bottom two rows are at intervals of 1% (dashed negative), matching the filled color contours which show values at or above the 95% significance level…… 67

3.10 Normalized density function of r_e in each gravity wave phase for all of TTL (top left) and 1-km vertical layers (top right and bottom row). The mean and standard deviation (SD) are given in the legend……. 71

3.11 Fraction of TTL clouds inside each wave phase categorized by background relative humidity with respect to ice (RH_{ic})……..... 73

4.1 (Top row) Mean radiative heating rates at 70 hPa (left) and 100 hPa (right) in 2007–2010 calculated using 2B-FLXHR-LIDAR**.** (Bottom row) Vertical velocity of the Brewer Dobson circulation diagnosed using ERA-Interim data in 1989-2009 (Seviour et al., 2012); contours are in mm/s, dashed negative…….. 78

4.2 Height-latitude sections of 2B-CLDCLASS-LIDAR cloud classification (top), 2C-ICE ice cloud optical depth (middle), and 2B-FLXHR-LIDAR radiative heating rates……. 79

4.3 (Left column) Mean radiative heating rates calculated from 2B-FLXHR-LIDAR footprints containing the labeled cloud type. Horizontal dotted lines indicate the level of mean clear-sky LZRH, solid lines denote the mean cloudy-sky LZRH, and the dashed line is where the y-axis height is equal to the cloud top height. Calculated from data with 20° of the equator. (Right column) Difference between cloudy-sky and clear-sky radiative heating rates. Positive values mean that the presence of clouds increase the radiative heating rate….. 83

4.4 Same as Figure 4.3 except for cirrus, altostratus, and altocumulus clouds. In the left plot for cirrus, the green line indicates the mean LZH when cirrus clouds are inside the TTL……... 84

4.5 2B-FLXHR-LIDAR monthly zonal averages of radiative heating rate at 70 hPa (top row) and 100 hPa (bottom row) through 2007–2010. Q refers to all-sky radiative heating rates, while Q_{clear} and Q_{cloud} are the clear-sky and cloudy-sky heating rates. Contours intervals are 0.1 K/day……... 86

4.6 Same as Figure 4.5 except for MERRA-2…… 87

4.7 Difference between the all-sky (Q) and clear-sky radiative heating rate (Q_{clear}) for FLXHR (left column) and MERRA-2 (right column) at 70 (top row) and 100 hPa (bottom row). Contour intervals are 0.02 K/Day…… 88

4.8 Height-latitude cross-section of monthly mean all-sky (Q, top row), clear-sky (Q_{clear}, middle row), and cloudy-sky (Q_{clear}, bottom row) radiative heating rates from 2B-FLXHR-LIDAR. Left column is for January and right column is for July. Contour intervals are 0.1 K/day……. 90

4.9 Same as Figure 4.8 except for MERRA-2……. 91

4.10 Difference between the all-sky (Q) and clear-sky radiative heating rate (Q_{clear}) from FLXHR (top row) and MERRA-2 (bottom row). Left column is for January and right column is for July. Contour intervals are 0.025 K/Day……. 92

4.11 (Left column) MERRA-2 dynamic residual vertical and meridional velocities ($\overline{\boldsymbol{w}}^*$ and $\overline{\boldsymbol{v}}^*$), (middle column) radiative $\overline{\boldsymbol{w}}^*$ and $\overline{\boldsymbol{v}}^*$ solved using all-sky radiative heating Q, and (right column) radiative $\overline{\boldsymbol{w}}^*$ and $\overline{\boldsymbol{v}}^*$ solved using clear-sky radiative heating Q_{clear}. Colored contours are for $\overline{\boldsymbol{w}}^*$ at intervals of 0.1 mm/s. Black contours are for $\overline{\boldsymbol{v}}^*$ at intervals of 20 cm/s; dashed negative…… 96

4.12 2B-FLXHR-LIDAR radiative $\overline{\boldsymbol{w}}^*$ and $\overline{\boldsymbol{v}}^*$ calculated using Q (left column) and Q_{clear} (right column) at 70 (top) and 100 hPa (bottom). Colored contours are for $\overline{\boldsymbol{w}}^*$ at intervals of 0.1 mm/s. Black contours are for $\overline{\boldsymbol{v}}^*$ at intervals of 10 cm/s; dashed negative…… 98

4.13 The difference between $\overline{\boldsymbol{w}}^*/\overline{\boldsymbol{v}}^*$ solved using Q and Q_{clear} at 70 (top row) and 100 hPa (bottom). Left column is for FLXHR and right column is for MERRA-2. Colored contours are for $\overline{\boldsymbol{w}}^*$; note that the top and bottom rows have the same contour intervals (0.05 mm/s) but different color scales. Black contours are for $\overline{\boldsymbol{v}}^*$ at intervals of 2 cm/s for the top row and 10 cm/s for the bottom row; dashed negative……. 99

4.14 MERRA-2 January (left column) and July (right column) mean residual circulation calculated from dynamical fields (top), Q (middle), and Q_{clear} (bottom). Colored contours are for $\overline{\boldsymbol{w}}^*$ at intervals of 0.1 mm/s. Black contours in units of cm/s are for $\overline{\boldsymbol{v}}^*$ at intervals of 20 cm/s; dashed negative……. 101

4.15 FLXHR January (left column) and July (right column) mean residual circulation calculated from Q (top row) and Q_{clear} (bottom). Colored contours are for $\overline{\boldsymbol{w}}^*$ at intervals of 0.1 mm/s. Black contours in units of cm/s are for $\overline{\boldsymbol{v}}^*$ at intervals of 10 cm/s; dashed negative..… 102

4.16 Differences between $\overline{\boldsymbol{w}}^*/\overline{\boldsymbol{v}}^*$ solved using Q and Q_{clear} for January (top row), April (second row), July (third row), and October (bottom row). Left column is for FLXHR and right column is for MERRA-2. Colored contours are for $\overline{\boldsymbol{w}}^*$ at intervals of 0.05 mm/s. Black contours are for $\overline{\boldsymbol{v}}^*$ at intervals of 10 cm/s for the top two rows and 5 cm/s for the bottom two rows; dashed negative……... 103

4.17 Cloud fraction at 100 hPa from 2B-CLDCLASS-LIDAR (left) and MERRA-2 (right) in 2007–2010……...… 104

4.18 (Left column) Difference in mean radiative heating rates calculated from cloudy CloudSat footprints without cirrus (Q_{noci}) and from only clear-sky footprints (Q_{clear}). Contour intervals are 0.02 K/Day. (Right column) Difference between solutions of $\overline{\boldsymbol{w}}^*/\overline{\boldsymbol{v}}^*$ using Q_{noci} and Q_{clear}. Contour intervals are 0.05 mm/s……. 106

4.19 (Left column) Vertical cross sections of the difference in mean radiative heating rates calculated from cloudy CloudSat footprints without cirrus (Q_{noci}) and from only clear-sky footprints (Q_{clear}). (Right column) Difference between solutions of $\overline{\boldsymbol{w}}^*/\overline{\boldsymbol{v}}^*$ using Q_{noci} and Q_{clear}. Contour intervals are 0.05 mm/s……... 107

4.20 Same as Figure 4.14 except for 100 to 0.1 hPa. Colored contours are for $\overline{\boldsymbol{w}}^*$ at intervals of 1 mm/s. Black contours in units of cm/s are for $\overline{\boldsymbol{v}}^*$ at intervals of 40 cm/s; dashed negative……... 110

4.21 Difference between $\overline{\boldsymbol{w}}^*/\overline{\boldsymbol{v}}^*$ solved from Q and Q_{clear}, calculated from MERRA-2. Colored contours are for $\overline{\boldsymbol{w}}^*$ at intervals of 0.05 mm/s, and black contours are for $\overline{\boldsymbol{v}}^*$ at intervals of 2 cm/s……...……... 111

A.1 Distribution of cluster center COTs from k = 50, 100, 200, 400 and 700 clusters. Error bars represent the intra-cluster standard deviation. Gray dots indicate clusters deemed unusable, due to its standard deviation being greater than the center value…… 123

A.2 Top row: Density plots of all data before clustering, for geometric thickness versus mean D_e (top left), and T_c versus mean IWC (top right). Bottom row: Scatter plot of cluster centers; gray stars indicate clusters not used in the simulations due to particle size being outside the valid range of the ice crystal scattering properties. Cluster used in the IC analysis are represented as stars colored by COT…… 124

A.3 Spectral emissivities of ocean, vegetation (grass), and bare soil (loamy sand)……... 126

A.4 Demonstration of channel selection using IC: AIRS Information spectrum before channel selection (magenta), after adding the 936.78 cm^{-1} channel to the a priori error covariance matrix (teal), and after adding both 936.78 cm^{-1} and 2616.38 cm^{-1} channels (maroon). Stars indicate the channel with highest IC during each step……. 129

A.5 Uncertainty due to the specified source for AIRS (left column) and MODIS (right column) channels. Percentages indicate the magnitude of the error standard deviation relative to the mean radiance of the simulations used to generate each uncertainty…… 131

A.6 Visualization of (top row) AIRS and (bottom row) MODIS error covariance matrices for temperature, humidity, and assumptions in the ice crystal habit and particle size distribution, calculated using equation (11). In the top row, the white gaps are regions where AIRS does not have channels……..……. 134

A.7 (Top) Number of AIRS channel selections within each 5 cm^{-1} bin for ocean surface simulations, over all clusters and all viewing angles, categorized by COT. (Bottom) Total number of AIRS channel selections within each 5 cm^{-1} bin…… 138

A.8 (Left column) Singular vectors and (right column) their corresponding basis in measurement space for a cloud with a COT of 1.36. The singular vectors indicate which retrieved variables the measurement bases help constrain. In the top row, for instance, since the singular vector value for T_c is near zero, the measurement basis on the right does not help retrieve Tc but rather contribute most to COT and then, to a lesser magnitude, to D_e. The values shown on the top part are the singular value from $\mathbf{\Lambda}$ of equation (A14)…… 141

A.9 (Left column) Transformed singular vectors and (right column) their corresponding measurement basis after applying the transformation of equation (A17) onto the same cloud as used in Figure A.8. After the transformation, the singular vectors point only to one retrieval variable, and the measurement basis can be interpreted to be contributing to one variable only……..……. 142

A.10 Weighted average of (left column) AIRS and (right column) MODIS measurement bases corresponding to (top row) COT, (middle row) D_e, and (bottom row) T_c, for thin clouds (cyan), thick clouds (magenta), and all clouds (black)…… 143

A.11 (Top) Number of MODIS band selections for ocean surface simulations, over all clusters and all viewing angles, categorized by COT. (Bottom) Total number of MODIS band selections. Note that MODIS has two channels, channels 21 and 22, with center wavelengths at 3.96 μm…….... 144

A12. Same as Figure A.7, except over grass……. 146

A.13 Same as Figure A.11, except over grass……..……. 147

A.14 Same as Figure A.7, except over bare soil…… 147

A.15 Same as Figure A.11, except over bare soil……. 148

A.16 Number of channel selections when simultaneously selecting from AIRS and MODIS for ocean surface simulations. (top plot) The number of AIRS selections in 5 cm^{-1} bins and (bottom plot) the number of selections for each MODIS channel. Note that the wave

number axis of the top plot has been reversed to facilitate comparison between AIRS and MODIS……...……. 149

A.17 AIRS channel selection over ocean assuming a temperature a priori standard deviation of 2K…… 151

A.18 MODIS channel selection over ocean assuming a temperature a priori standard deviation of 2K…… 151

A.19 Relative weight of AIRS channels for (a) all clouds, (b) clouds with optical thickness less than 1, and (c) clouds with optical thickness larger than 3…….. 155

List of Tables

A.1 List of Habit and PSD Combinations for Obtaining the Habit/PSD Uncertainties……. 135

A.2 Channel sets obtained from IC channel selection, weighted by cloud cluster populations. Leftmost column denotes channel selection and weights for stand-alone AIRS retrievals; middle column denotes selection and weights for combined AIRS-MODIS retrievals; rightmost column is for retrievals combining active sensors and AIRS. The weights are relative to the highest weighted channel in each category, so that the channel with highest weight has a relative weight of unity. Only the first 15 highest weighted channels are shown. Channels colored green indicate weights favoring thin clouds (COT < 1), blue indicates those favoring clouds with 1 < COT < 3, and orange indicates those favoring thick clouds (COT >3)…….. 156

Chapter 1

Background

This dissertation presents research on dynamical and radiative processes that modulate the tropical tropopause layer (TTL). As the TTL is the main gateway of troposphere-to-stratosphere transport, conditions of the TTL, such as tropopause temperature, radiative heating rates, formation of cirrus clouds, and wave perturbations, among others, influence the composition and rate of air entering the stratosphere. This chapter begins with an overview of the Brewer-Dobson circulation (BDC), stratospheric water vapor, and the role of BDC in troposphere-stratosphere transport. Characteristics of the TTL and its role in the BDC are then described, followed by a discussion of cirrus clouds in the TTL. A short overview of radio occultation is then presented. This chapter concludes with the motivation for studying each of the topics in this dissertation and how they contribute to our understanding of troposphere-stratosphere transport and stratospheric water vapor.

1.1 Stratospheric water vapor and the Brewer-Dobson circulation

Compared to the troposphere, the stratosphere is much drier, containing water vapor concentrations on the order of a few parts per million by volume. Figure 1.1 shows climatologies of zonal mean water vapor from the Aura Microwave Limb sounder, temperature zonal winds from the ERA-Interim reanalysis, and lapse-rate tropopause height from radio occultation for January and July. During boreal winter, a minimum of water vapor concentration is observed in the deep tropics near the tropopause, and above 20 km water vapor tends to increase with height

due to methane oxidation. The boreal summer climatology shows a similar contour pattern although water vapor concentrations near the tropical tropopause are higher. It is generally accepted that this pattern is correlated to the Brewer-Dobson circulation (BDC), a large-scale circulation that extends from the upper troposphere to the mesosphere, as shown in the schematic

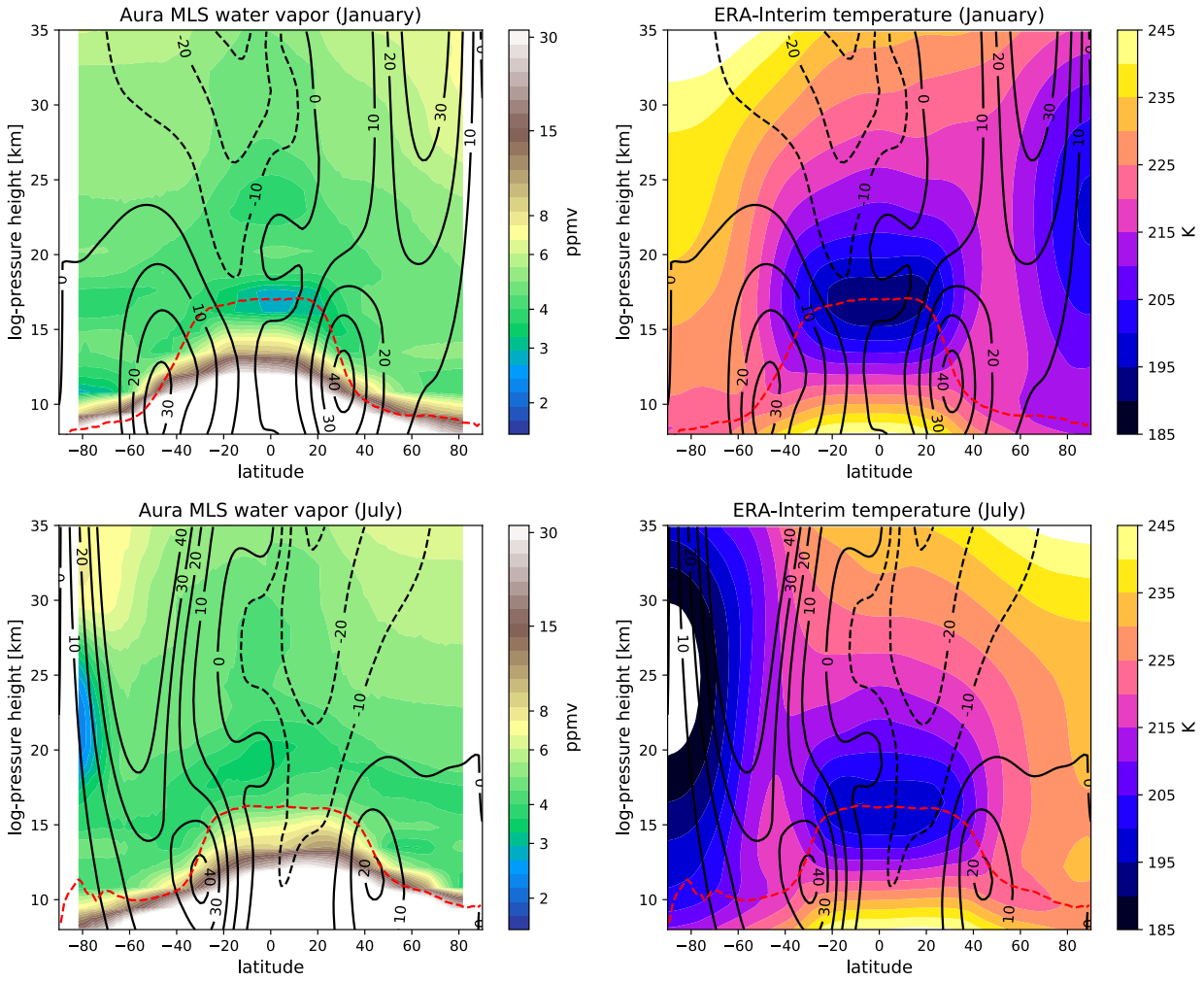

Figure 1.1 (Left column) Climatology of upper-tropospheric and stratospheric water vapor (Aura MLS) for January (top) and July (bottom). Black contours are zonal-mean zonal wind from the ERA-Interim reanalysis. Red dashed lines are the zonal-mean lapse-rate tropopause (FORMOSAT-3/COSMIC). (Right column) Climatology of temperature (ERA-Interim). Contours are identical to the left column. All values were calculated using data in 2007–2013.

by Dunkerton (1978) (Figure 1.2). The existence of this circulation was put forth by Dobson (1929) as a possible explanation of high ozone concentration at the poles and low concentration in the tropics. To explain the dryness of the stratosphere, Brewer (1949) hypothesized a circulation (Figure 1.2) with upwelling through the tropical tropopause, poleward motion in the midlatitudes, and descent at high latitudes. He posited that the low temperatures at the tropical tropopause cause ice formation and retain water in the troposphere.

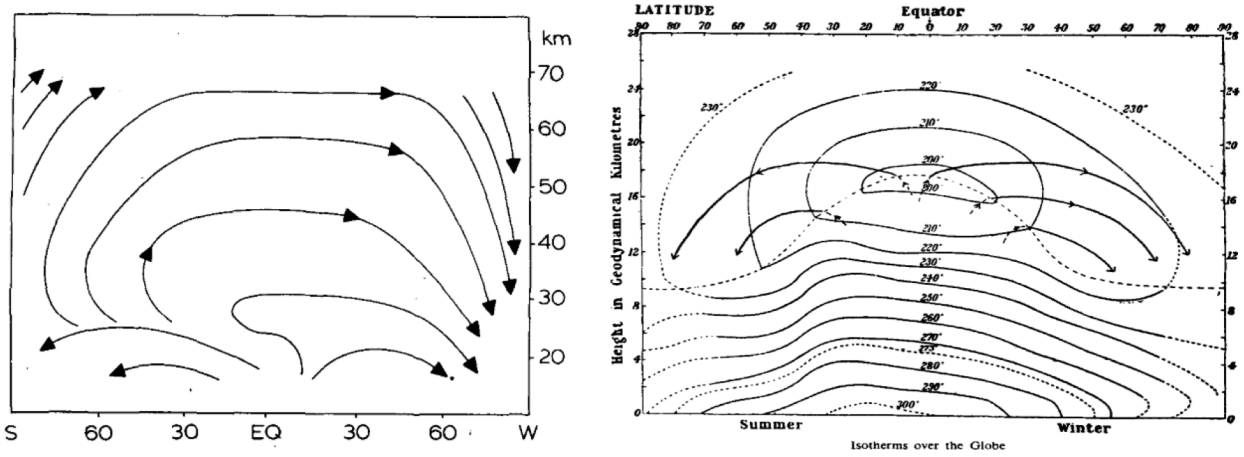

Figure 1.2 Schematic of the Brewer-Dobson circulation by Dunkerton (1978) (left) and by Brewer (1949) (right).

Mote et al. (1996) presented observational evidence of tropical upwelling using satellite retrievals of water vapor concentration from the Halogen Occultation Experiment (HALOE) and the Microwave Limb Sounder (MLS). As shown in Figure 1.3, the mean equatorial water vapor concentration is typically low near the beginning of each year, and the dry signature is observed to migrate upward into the lower stratosphere over the course of several months. A similar upward trend is observed for the wet signature occurring in boreal summer. The pattern in Figure 1.3, showing the imprinting of tropopause-level signals onto the higher altitudes, is referred to as

the “tape recorder” effect. The signal decreases with height due to a number of factors such as horizontal and vertical diffusion/mixing and the production of water vapor through methane oxidation. This finding simultaneously presented evidence of tropical upwelling as well as an estimate of the upwelling velocity.

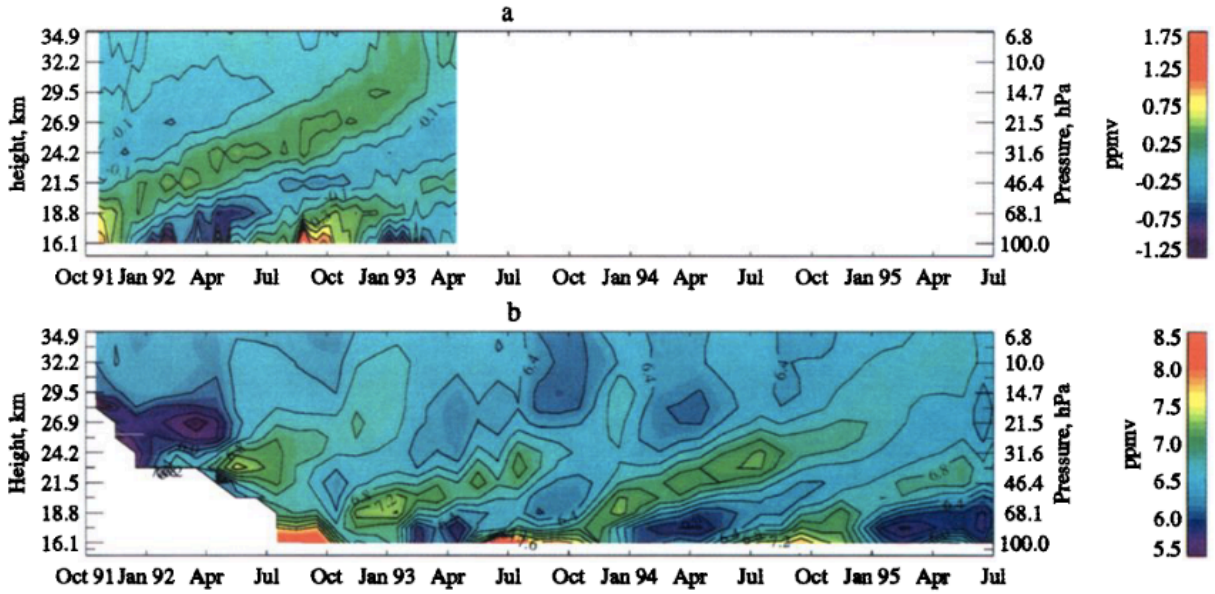

Figure 1.3 Time-height section of mean water vapor mixing ratio between between 12°N/S from the (a) Microwave Limb Sounder and (b) the Halogen Occultation Experiment (HALOE). (Mote et al., 1996)

General circulation models are also able to produce circulations qualitatively consistent with Dunkerton’s schematic. Figure 1.4 shows the mean age of air and residual vertical/meridional velocities from the Goddard Earth Observing System Chemistry-Climate Model (GEOSCCM). The age-of-air contours show that the youngest air originate from the tropics. Contour shapes here resemble those of water vapor in Figure 1.1, suggesting that the distribution of stratospheric water vapor is dependent on the BDC. The vertical and meridional velocities are similar to the proposed circulation by Dunkerton (1978) based on theoretical

considerations, with a deep vertical extension of equatorial upwelling throughout and significant meridional velocities in the upper stratosphere and mesosphere. More relevant to the research presented herein is the "shallow branch" of the BDC, which comprises upwelling near the tropical tropopause (~100 hPa) and an associated meridional circulation at similar altitudes around the subtropics.

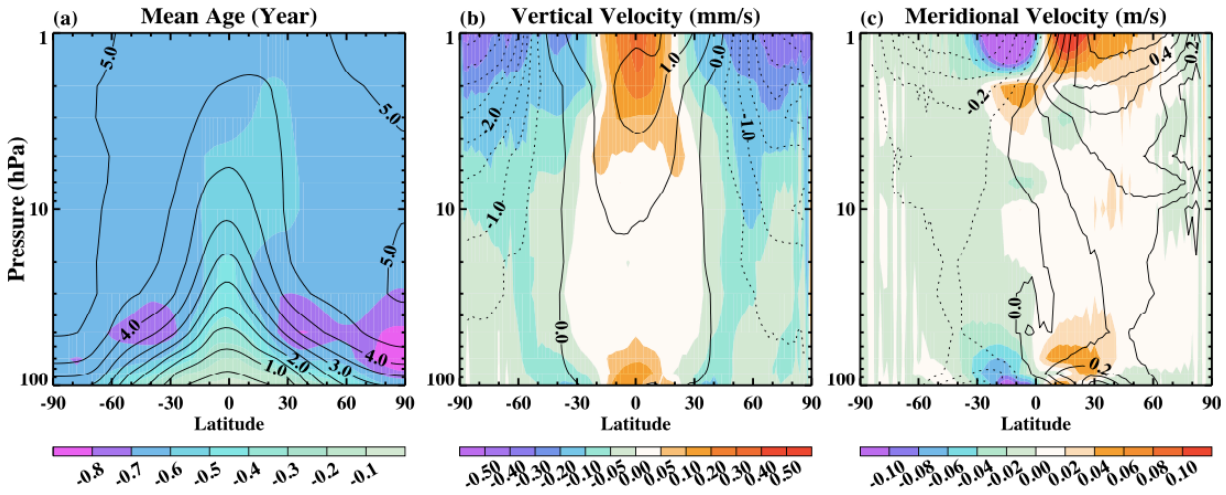

Figure 1.4 (a) Mean age of air during year 2000 (contours) and the difference of mean age between 2080 and 2000 (colors). (b) Residual vertical velocity (similar to vertical velocity of BDC) during 2000–2019 (contours) and difference between 2080–2099 and 2000–2019. (c) Same as (b) except for residual meridional velocity. (Li et al., 2012)

Figure 1.5 illustrates the key mechanism responsible for the BDC. Breaking of planetary and gravity waves in the extratropical stratosphere and mesosphere induces a westward force on the flow and tends to drive air poleward (Holton et al., 1995). This results in a "suction pump" mechanism, which causes ascent near the equator and descent at the poles. In the winter hemisphere, the polar night creates a strong meridional temperature gradient and therefore strong zonal winds. This tends to favor a stronger BDC since westerly winds are required for the upward propagation of planetary waves (Charney and Drazin, 1961). Because of topography, the

northern hemisphere has more waves than the southern hemisphere, and as a result the BDC is strongest during boreal winter. The tropical ascent causes cooling, so the seasonal variation of BDC strength is reflected in equatorial tropopause temperatures. As Figure 1.1 shows, tropical tropopause temperatures are significantly colder in boreal winter than in austral winter.

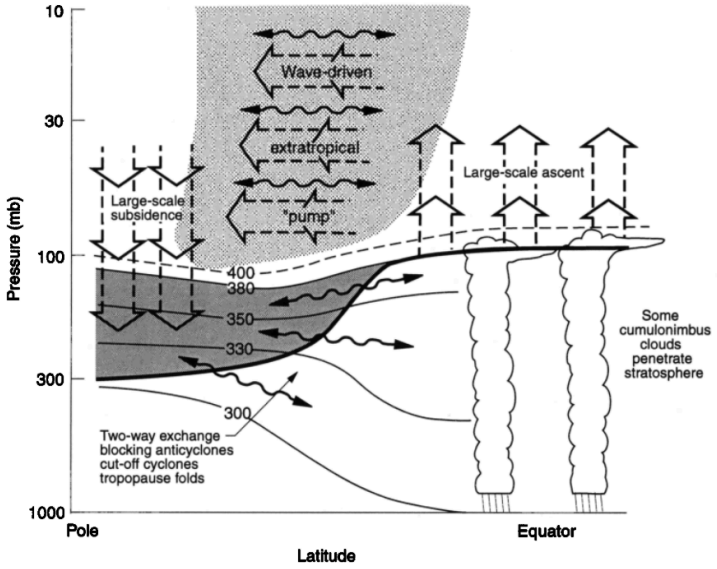

Figure 1.5 Schematic of the BDC and pathways of stratosphere-troposphere exchange. Wave breaking in the midlatitude stratosphere causes poleward flow, resulting in descent in the poles and ascent in the tropics. In the subtropical and midlatitude upper troposphere, exchange can occur on short timescales through tropopause folding and wave breaking of the subtropical jet. (Holton et al., 1995)

Stratospheric water vapor is an important factor in the radiative cooling of the stratosphere in response to climate change. Its increase is found to warm global surface temperatures (Rind and Lonergan, 1995) and plays a role in the removal of ozone by polar stratospheric clouds (Solomon et al., 1986). Figure 1.6 shows lower stratospheric water vapor measured by balloon soundings and satellite retrievals. Relative to levels between 1980 and 2000, there was a considerably sharp drop of water vapor concentration during 2000. Solomon et

al. (2010) showed that this imposed a 25% reduction in the rate of global surface temperature increase due to greenhouse gases. There is also a possible climate feedback associated with stratospheric water vapor, as Dessler et al. (2013) found a feedback of + 0.3 W/m^2 K. On the contrary, Huang et al. (2016) finds only a minor feedback of 0.02 W/m^2 K, so the existence of any feedback remains debatable. Despite these uncertainties, the role of stratospheric water vapor in influencing the climate through various pathways is demonstrated in the literature.

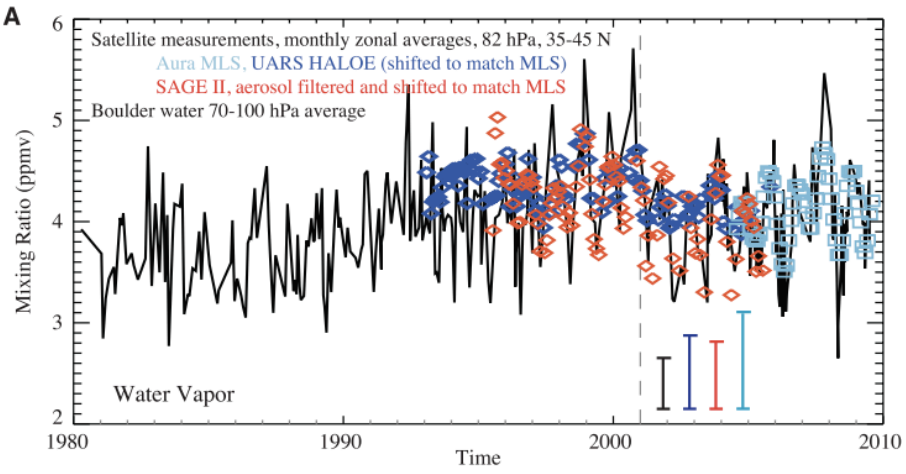

Figure 1.6 Water vapor measured from balloons (black) at Boulder, Colorado (40°N, 105.25°W), and from satellite measurements centered on 82 hPa averaged over 35°-45° N (Aura MLS, light blue; HALOE, blue; SAGE-II, red). (Solomon et al., 2010)

Determining the long-term trend of stratospheric water vapor is an active subject of research. While tropospheric water vapor has an identifiable increasing trend over the past several decades (Chen and Liu, 2016), stratospheric water vapor on the other hand has a trend, if any, that is very subtle and hard to detect. Rosenlof et al. (2001) suggests there is a 1% increase in stratospheric water vapor from 1954 and 2000 based on in-situ aircraft and balloon data as well as satellite estimates. However, after 2000 there are alternating periods of increasing or decreasing trends in lower and middle stratospheric water vapor (Hurst et al., 2011). Climate

models simulate a 0.5–1 ppmv per century trend in lower stratospheric water vapor in response to a ~1 K increase in the cold-point tropopause (Gettelman et al., 2010). It is therefore important to understand processes near the tropopause that modulate temperature and in turn water vapor concentration.

Lower stratospheric water vapor is closely connected to TTL temperatures (Randel et al. 2019), and the influence of QBO and ENSO on it can partially be explained based on these oscillations' effects on tropopause temperatures. For instance, when the easterly zonal wind of the QBO descends down to tropopause levels, the negative wind shear causes a cold anomaly, and this is found to be responsible for decreased lower stratospheric water vapor (Kawatani et al., 2014). Since TTL conditions are strongly correlated with lower stratospheric water vapor, it is necessary to understand TTL processes in order accurately assess how stratospheric water vapor will change in the future.

1.2 Tropical tropopause layer

The TTL is a transition layer from tropospheric to stratospheric conditions and acts as a gateway of troposphere-to-stratosphere transport (Fueglistaler et al., 2009). It is necessary to separate the TTL from the rest of the troposphere because the influence of convection lessens as altitude increases. At these higher altitudes the vertical mixing is eddy-driven and more similar to the stratosphere. TTL air possesses characteristics of stratospheric air such as elevated concentrations of ozone (relative to tropospheric air), while its composition, thermodynamics, and circulation is still influenced by convection. Since the transition from tropospheric to stratospheric conditions is gradual, there is no clearly defined upper and lower boundary for the TTL. Fueglistaler et al. (2009) propose synthetic bounds of 150 hPa and 70 hPa, which roughly

corresponds to 14 km to 18.5 km above mean sea level. Likewise, there are no clear horizontal bounds but as shown in Figure 1.1 the tropical tropopause varies very little with latitude within the region encompassed by the subtropical jets. The meridional positions of these jets can be seen as the north and south boundaries, since at these latitudes and beyond the stratosphere-troposphere exchange is no longer determined mostly by the BDC but through mixing via wave breaking and tropopause folding.

Climatological temperature, water vapor, and winds at 70, 100, and 150 hPa are shown in Figure 1.7 and 1.8, for January and July, respectively. Outgoing longwave radiation (OLR) at and below 220 W/m^2 are contoured to demonstrate the connection between convection and TTL conditions. In January, temperatures at 150 hPa are quite uniform zonally. There are small spots of cold over equatorial Africa and Indonesia both of which have frequent intense convection. The influence of the Southern Pacific Convergence Zone (SPCZ) is also arguably visible since the temperature contours over the central Pacific also has a southeastward tilt. At this altitude, high concentrations of water vapor are found over areas of low OLR, showing that the air composition is strongly modulated by detrainment from convection. Qualitatively similar features are found in July, when high water vapor concentrations and low temperatures are found over convection associated with the South Asian Monsoon and North American Monsoon. Water vapor concentrations at this altitude are similar between January and July.

At 100 hPa, which is close to the tropical tropopause, the relationship between convection and water vapor is reversed. Low water vapor concentrations are observed near areas of low OLR and this is most evident over the west and central Pacific. Temperatures at this level exhibit two cold regions, one over South American and another over the Western Pacific. The cold region over the latter area possesses a distinct shape similar to a horseshoe. This is

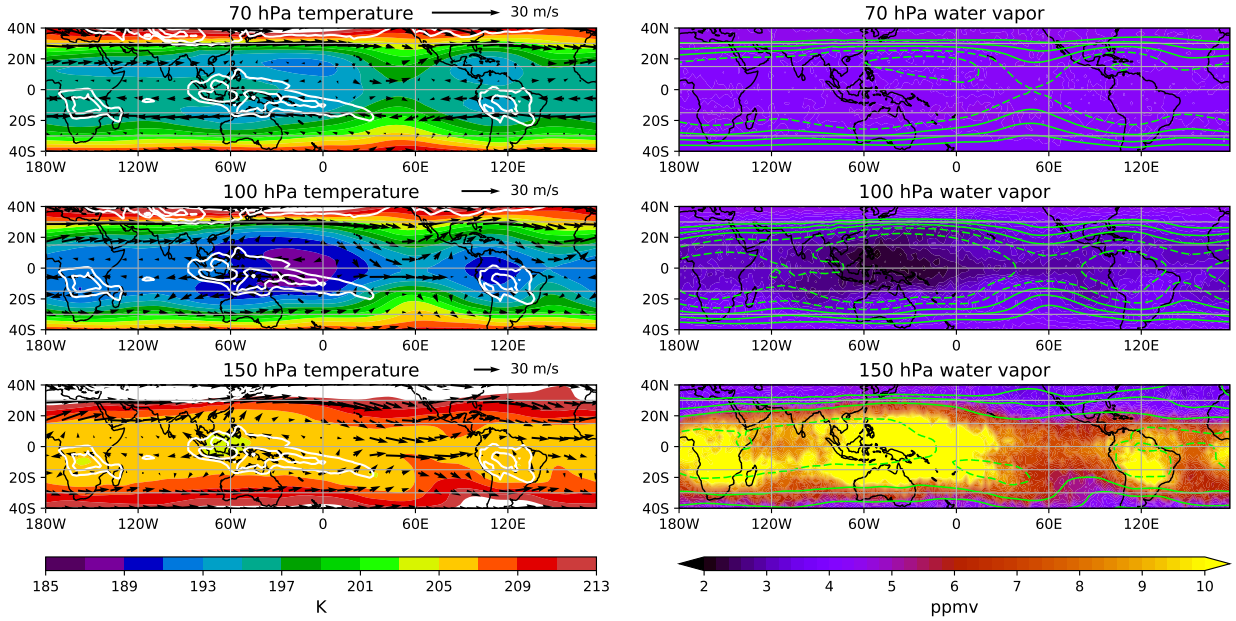

Figure 1.7 (Left column) January average of temperature from the ERA-Interim reanalysis at 70 hPa (top), 100 hPa (middle), and 150 hPa (bottom). Arrows represent the mean horizontal winds from ERA-Interim. White contours represent outgoing longwave radiation; highest contoured value is 220 W/m^2 and contour intervals are 20 W/m^2. (Right column) January average of water vapor from the Aura MLS at approximately the same pressure levels. Green contours denote the temperature departure from the mean at intervals of 3 K. Negative contours are dashed.

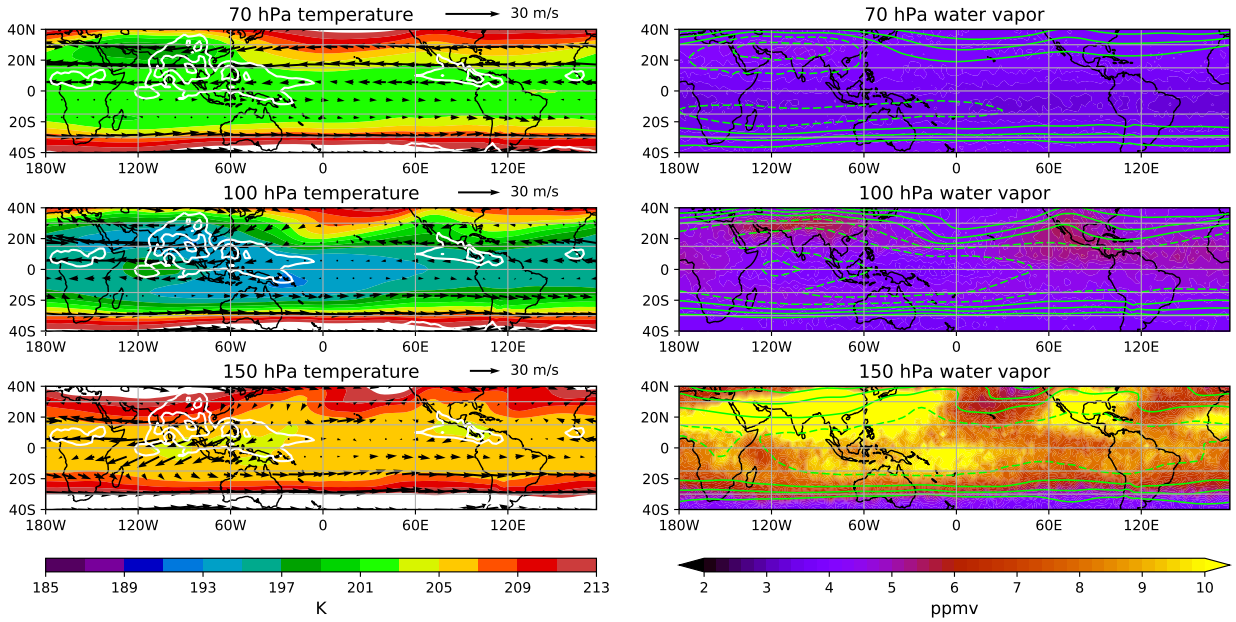

Figure 1.8 Same as Figure 1.7 except for July.

attributable to stationary equatorial waves in response to latent heating from convection (Matsuno 1966; Gill 1980). Latent heating centered on the equator induces a Kelvin wave response (as indicated through the easterly winds and cold temperatures east of convection) to the east of the heating and Rossby waves (indicated by the "tails" of the horseshoe which have anticyclonic winds and low temperatures) to the west. This is the subject matter of Chapter 2, which investigates how variations in the vertical distribution of latent heating affect this dynamical response. In July, a cold zone of similar shape is observed within 120°W and 0°, although the shape is not as symmetric since the majority of latent heating is from off-equatorial convection due to the South Asian Monsoon. Unlike at 150 hPa, the water vapor distribution is lower during January than July. The South Asian Monsoon is known to inject moist air into the lower stratosphere that become trapped in the monsoonal anticyclone over Asia (Park et al., 2007). As a result, water vapor mixing ratios larger than 6 ppmv are observed over Asia in July.

Water vapor at 70 hPa is much more zonally homogeneous compared to lower heights due to the uniformity of zonal winds in the lower stratosphere. This altitude is drier in July because we are actually observing the air originating from 100 hPa from the preceding winter. The temperature and wind patterns at 100 hPa, such as the cold horseshoe and the Asian monsoonal anticyclone, are also observed at 70 hPa, suggesting that the large-scale effects of convection can penetrate through the TTL into the lower stratosphere (Dunkerton 1995).

Vertical profiles of radiative heating rates estimated using tropical soundings are shown in Figure 1.9. Above 15 km, the positive heating rates balance the adiabatic cooling due to the large-scale upwelling forced by the BDC. For this reason, radiative heating rates in the TTL are related to the upwelling velocity in this region. In fact, it is standard practice for trajectories studies focusing on the TTL (e.g. Schiller et al., 2009) to use radiative heating as a proxy for

vertical motion in lieu of the vertical velocity from reanalyses. Although the radiative heating rates are important for diagnosing vertical motions in the TTL, there are large differences in radiative heating rates among reanalysis data sets (Randel et al., 2013). Variability of radiative heating is connected to variations in ozone, water vapor, temperature, and clouds. In particular, clouds are found to have a significant effect on the radiative balance of the TTL (Corti et al., 2005; Fueglistaler and Fu, 2006). This serves as motivation for the research presented in Chapter 4, which uses satellite data sets and reanalysis to investigate the effects of clouds on TTL radiative balance and the BDC.

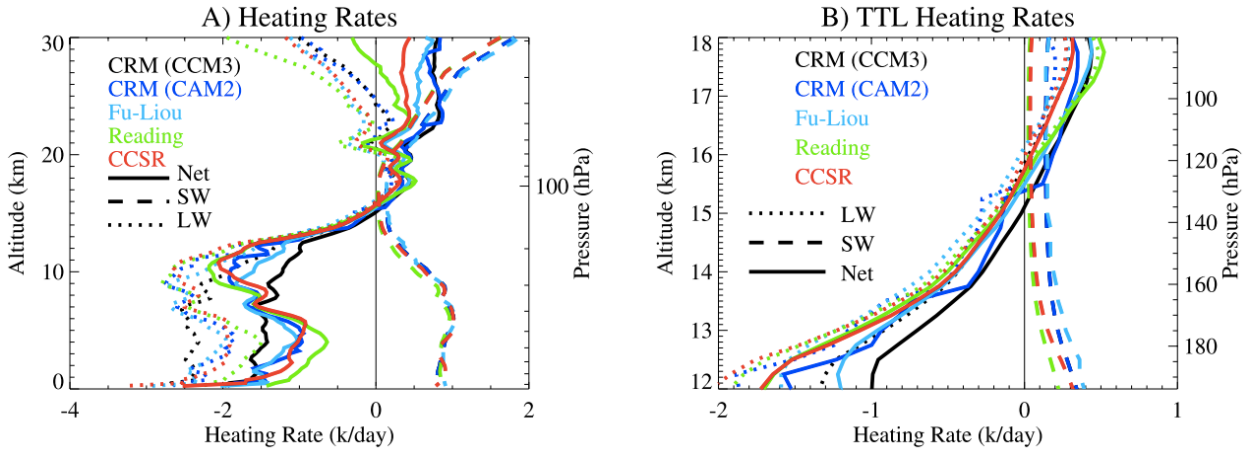

Figure 1.9 Radiative heating rates based on soundings at Galapagos Islands, estimated using various radiative transfer models. (Gettelman et al., 2004)

1.3 Cirrus clouds in the tropical tropopause layer

Low temperatures in the TTL facilitate ice formation and are responsible for the frequent occurrence of cirrus clouds. Figure 1.10 shows a global map and a height-latitude cross-section of cirrus cloud occurrence based on one year of observations from the Cloud-Aerosol Lidar and Infrared Pathfinder Satellite Observations (CALIPSO) satellite mission. The tropical belt has the

highest frequency of cirrus occurrence, and the vertical cross-section shows that a large amount of these clouds form in the tropical upper troposphere and near the tropopause. The global map shows three hot spots of cirrus occurrence: South Africa, Western Pacific, and South America, all of which have frequent convection as seen previously in Figure 1.7. For the latter two regions, the location and shape of the high cirrus frequency has good resemblance to the cold regions in Figure 1.7, indicating that the large-scale cooling of convection is associated with enhanced cirrus formation. On the other hand, over Africa there is no obvious cold region, so it may be likely that the cirrus clouds there are more associated with convective detrainment.

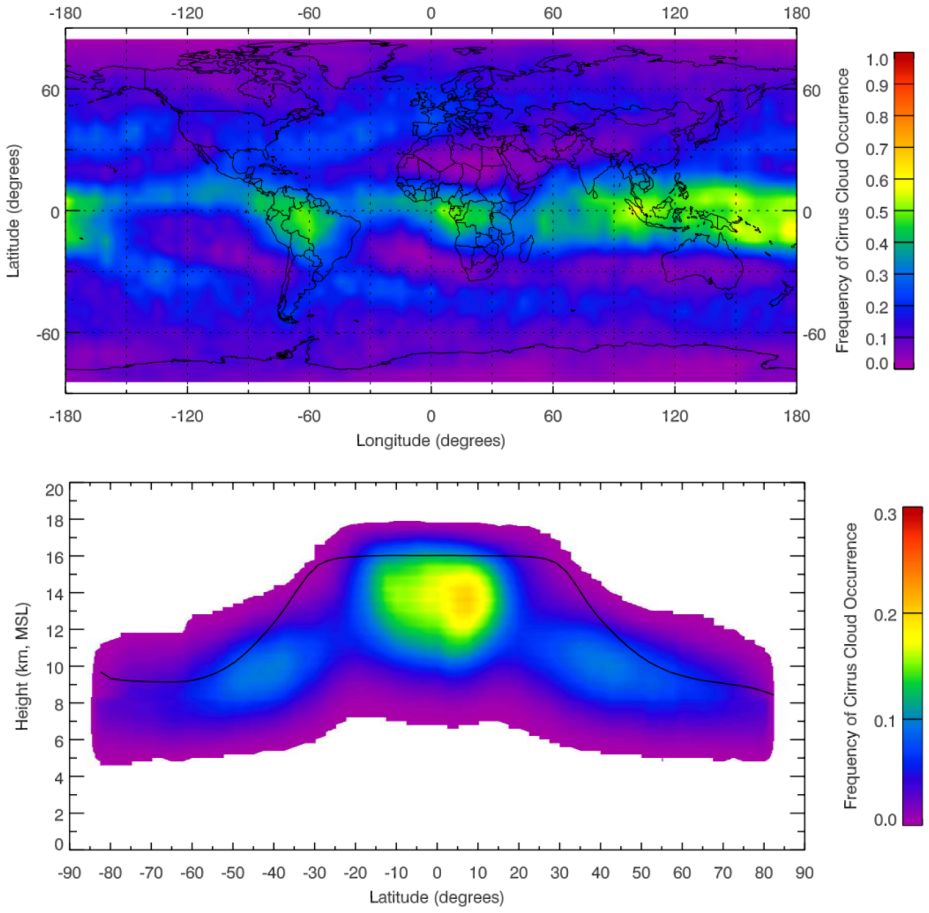

Figure 1.10 (Top) annual mean of cirrus occurrence based on one year of data from CALIPSO. (Bottom) Zonal mean cloud occurrence from the same data and time period. (Sassen et al., 2008)

A large portion of TTL cirrus clouds are optically very thin and are classified as "subvisual" when their optical depths are below 0.03. As this term suggests, these clouds are hard to detect with passive sensors such as radiometers and was not widely observed until lidar observations were available to confirm their pervasive presence throughout the tropics. The large horizontal scale of these clouds, as shown in Figure 1.11, indicates that the dehydration via cirrus formation can take place over a large area in the tropics (Luo et al., 2003).

Aside from the large-scale cooling due to the BDC and tropical convection, cold anomalies of gravity and Kelvin waves have also been found to facilitate cirrus formation. In Figure 1.12, cirrus clouds detected from ground-based lidar were often inside cold temperature anomalies due to Kelvin waves. Similarly, Boehm and Verlinde (2000) found that a majority of cirrus clouds observed during the Nauru99 Field Experiment (deployed by the Department of Energy) were found inside cold anomalies associated with Kelvin waves. Schoeberl et al. (2015) suggests that the rapid cooling due to gravity waves increases ice crystal concentration and enhances the dehydration caused by cloud formation. As such, wave-induced cirrus may be an important part of the TTL dehydration process. In addition, the importance of gravity waves in climate modeling is also demonstrated by Maloney et al. (2019), who added random temperature perturbations in the Community Atmosphere Model 5 (CAM5) to simulate the effects of wave temperature perturbations in the TTL. They found that adding these perturbations increased the amount of clouds with low extinction and improved the agreement between the model and aircraft observations.

Recently, Kim et al. (2016b) and Podglajen et al. (2018) presented relatively novel findings indicating that the vertical gradient of wave temperature perturbations plays an important role in the occurrence of TTL clouds. In Chapter 3 we further explore this topic using

satellite observations to understand how temperature perturbations from Kelvin and gravity waves influence TTL cirrus clouds.

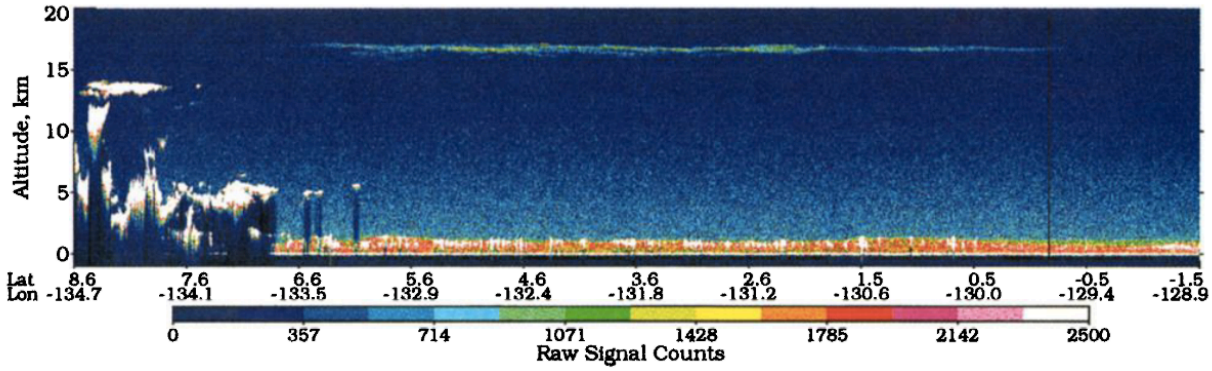

Figure 1.11 Cirrus with large horizontal scale observed by the Lidar In-space Technology Experiment (LITE). (Winker and Trepte, 1998)

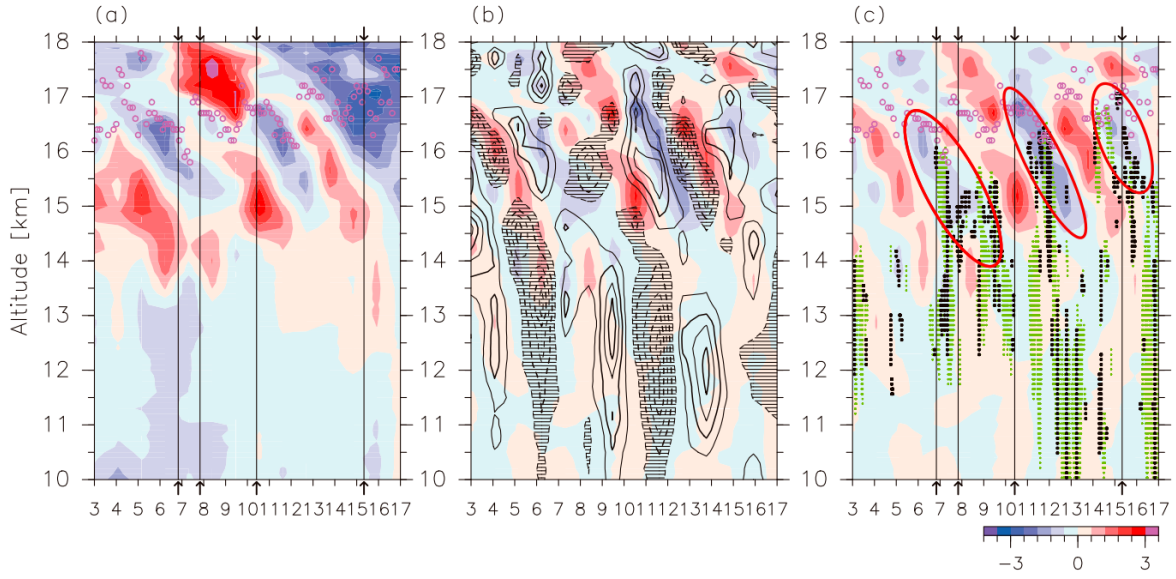

Figure 1.12 (a) Temperature anomalies observed at 8.0°S, 80.5°E. Purple dots indicate the location of the cold-point tropopause. (b) <7-day filtered temperature anomalies (colored) and wind velocities (contours and shading at intervals of 1.5 m/s). (c) Temperature anomalies (colored) overlaid by 1064 nm lidar attenuated backscatter coefficient (green dots for all cirrus and black dots for subvisual cirrus). Red circles indicate regions where observed cirrus clouds coincided with cold wave anomalies. (Suzuki et al., 2013)

1.4 Radio occultation

A brief overview of radio occultation (RO) is given here because RO data sets are used extensively in this dissertation. The RO technique is based on using low-earth-orbiting (LEO) satellites to receive radio signals from the Global Positioning System (GPS) or the Global Navigation Satellite System (GNSS). As depicted in Figure 1.13, the LEO satellite orbits the Earth, and the radio signal it receives from GPS satellites may pass through the atmosphere. Based on the atmosphere's thermodynamic state, the radio wave is bent and deviates from a straight path. This bending causes the received radio signal to have a slight shift in phase, compared to the scenario in which the radio signal is not attenuated at all. The observed phase shift can then be used to invert for the bending angle of the ray, the refractivity of the atmosphere, and subsequently atmospheric profiles of temperature and moisture. As the LEO satellite moves along its orbit, the radio wave passes the atmosphere at different altitudes, allowing vertical profiles of temperature and moisture to be obtained.

The feasibility of this technique for atmospheric observation was first demonstrated by the Global Positioning System/Meteorology (GPS/MET) mission (Rocken et al., 1997) conducted by the University Corporation of Atmospheric Research (UCAR). RO proved be a high-accuracy and high-precision source of temperature in the upper troposphere and stratosphere. The vertical resolution of ~1 km near the tropopause (Kursinski et al., 1997) is also finer than other satellite techniques offering temperature retrievals. The main limitation of RO is its coarse horizontal resolution of around 200 to 300 km (Kursinski et al., 1997). In addition, strong small-scale gradients of moisture or temperature along the path of the ray will cause significant bias in the retrieval (Healy, 2001). This primarily happens in the tropical lower troposphere where moisture can have large spatial variations.

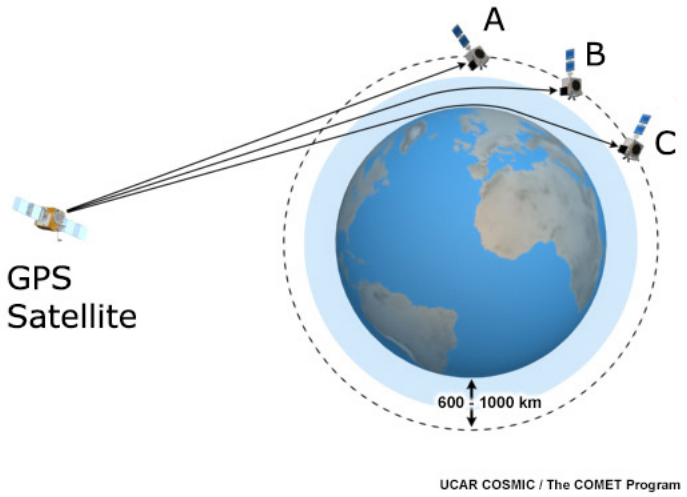

Figure 1.13 Diagram of the radio occultation technique. GPS/GNSS satellites send radio signals that penetrate the atmosphere and then are received by the LEO satellite. The amount of radio signal bending caused by the atmosphere can then be retrieved and used to infer the atmospheric state. As the LEO satellite moves from position A to C, the radio signal passes through the atmosphere at different altitudes, enabling the profiling of atmospheric thermodynamic conditions.

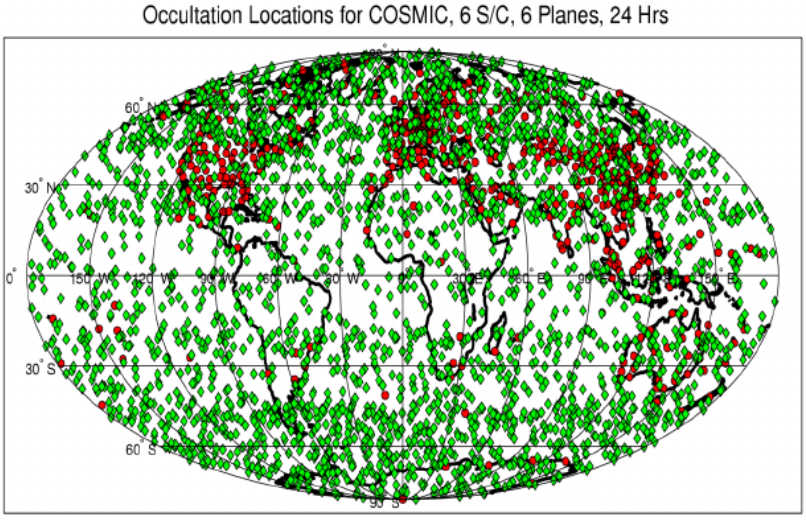

Figure 1.14 Distribution of RO profiles obtained by COSMIC in one day (green dots). Red dots denote stations deploying radiosondes.

Currently the largest data record of RO-derived profiles is from the FORMOSAT-3/Constellation Observing System for Meteorology, Ionosphere, and Climate (COSMIC) (Anthes et al., 2008) launched in April 2006. This US/Taiwan joint satellite mission comprises six LEO satellite providing up to 2500 profiles per day when all satellites were fully operational. Figure 1.14 shows a typical distribution of RO observation in one day. RO observations are distributed pseudo-randomly in time and space, since the occultations are based on the positions of GPS and LEO satellites. One of the unique features of the RO technique is that it does not suffer from inter-satellite calibration effects (Foelsche et al., 2011), and profiles from different RO satellite missions can be used together as long as they are processed with the same algorithm.

1.5 Outline of thesis and relevance of research

As mentioned in Section 1.1, tropopause temperature variability is imprinted onto lower stratospheric water vapor concentrations through the tape recorder effect. Understanding the processes responsible for these variabilities can improve our ability to predict future water vapor trends and also improve the representation of these processes in climate models. With this as a fundamental motivation, this thesis focuses on three distinct TTL processes that all influence the moisture budget of the lower stratosphere. Chapter 2, 3, and 4 present results from three separate research topics. A short overview of each is given below.

Chapter 2 investigates the relationship between tropical latent heating and temperatures in the tropical upper troposphere and lower stratosphere (UTLS). As mentioned in Section 1.2, TTL temperature variability is associated with equatorial waves due to latent heating. With the intent of understanding how variations in the vertical distribution of latent heating change the response of TTL temperatures, we analyze satellite-based estimates of latent heating and

temperature to assess the dependence of UTLS cooling and warming towards the altitude of latent heating.

Chapter 3 is focused on TTL cirrus clouds and is motivated by the results of Kim et al. (2016) who showed that the vertical gradient of gravity wave temperature perturbations is correlated with cirrus occurrence. We seek to further understand this connection between gravity waves and cirrus clouds and find whether their aircraft-based results are applicable to satellite observations and to the entire tropics.

Aside from temperature and clouds in the TTL, the rate of vertical transport also influences troposphere-to-stratosphere transport. Chapter 4 examines how clouds modify the radiative heating rate in the global UTLS, and how the radiative effect of clouds influences the BDC. We study this through a combination of satellite data sets as well as reanalysis.

The dissertation concludes with a summary of the results, discussions on the implication of our findings, and suggestions for future work. The appendix documents a study on the information content of the Atmospheric InfraRed Sounder (AIRS) towards tropical ice clouds, which may provide a useful framework for improving the retrieval of ice cloud properties using passive sensors.

Chapter 2

Role of latent heating vertical distribution in the formation of the boreal winter tropical cold trap

2.1 Introduction

TTL conditions near the Maritime Continent (MC) are particularly important since this region is a major pathway of troposphere-to-stratosphere transport (Fueglistaler, 2005). During boreal winter, a cold trap or temperature minimum resembling a horseshoe forms over the MC region, as seen in the climatological temperature distribution (Figure 2.1). It is clear that this cold pattern coincides with low water vapor concentration and high cirrus frequency, indicative of the dehydration process via cirrus formation (Jensen et al., 1996). The distributions of temperature, water vapor, and clouds are also dependent on the phase of ENSO, with the horseshoe shape shifted westward closer to the MC during La Niña phases. This dependence on ENSO phase depicts the influence of tropospheric circulation on the formation of the horseshoe cold region.

The horseshoe-shape morphology results from the Matsuno-Gill response to tropospheric diabatic heating (Highwood and Hoskins, 1998), which excites a stationary Kelvin wave (KW) to the east of the heating, and stationary equatorial Rossby wave (ERW) to the west of the heating (Figure 2.2 and 2.3) (Matsuno, 1966; Gill 1980). The cold region associated with the KW response is centered on the equator, while the ERW cooling responses are off the equator into each hemisphere, forming the tail of the horseshoe. Studies have demonstrated that intraseasonal variability of TTL temperature, especially in the MC region, is strongly modulated by ERW and KW associated with convective activity, for instance, through analysis of outgoing

longwave radiation (Zhou and Holton, 2002; Nishimoto and Shiotani, 2012) and cloud top height (Paulik and Birner, 2012; Kim et al., 2018a). Both are proxies of convective strength, but neither can resolve the vertical distribution of heating. Modeling studies (e.g. Ryu et al., 2008) imposing a heating source on atmospheric flow also show that planetary waves cause significant temperature perturbations in the MC region, but the role of variations in the heating vertical distribution has not been quantitatively assessed. Since the stationary planetary waves are caused by diabatic heating (Gill 1980) and mass flux into the layer (Matsuno 1966), physically it is plausible to expect that the horseshoe-shape cold region depends somewhat on the vertical distribution of heating. However, it remains poorly understood whether properties of these waves are related to the specific vertical configuration of heating.

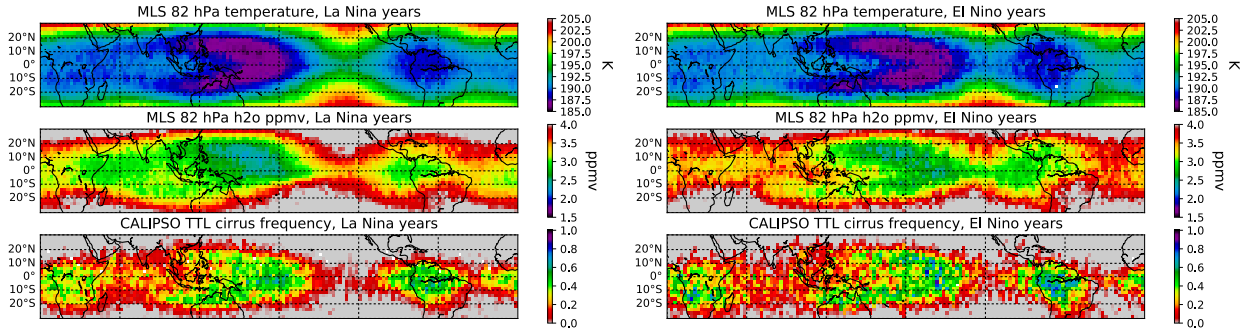

Figure 2.1 December-January-February (DJF) climatology of 82 hPa temperature (top row), water vapor mixing ratio retrieved by the Aura MLS (middle row), and frequency of cirrus clouds with cloud base above 15 km (bottom row) based on the CALIPSO 5-km cloud layer product. The left column shows composites on DJF periods with the Oceanic Niño Index < −0.5 (2008, 2009, 2011, and 2012), and those on the right correspond to DJF periods with Oceanic Niño Index > 0.5 (2007 and 2010).

Since tropospheric diabatic heating is dominated by latent heating from precipitation, it is reasonable to anticipate that the shape and intensity of the cold trap is linked to mesoscale convective systems (MCS), which contribute to more than half of tropical rainfall (Nesbitt et al.,

2006). Convective precipitation forms during the early stage of storm development, and as the MCS matures, a large area of outflow forms and in it the weak updrafts cause significant amounts of stratiform precipitation (Houze, 2004). The mean profiles of convective and stratiform LH over the MC region (Figure 2.4) show the typical vertical distribution of LH from these two precipitation regimes. While the LH from convective precipitation is positive throughout the atmosphere and peaks in the lower troposphere, stratiform precipitation forms higher in the troposphere, resulting in higher LH peaks. In addition to the heating aloft, stratiform LH is characterized by cooling below the melting layer due to evaporation. The combination of radar measurements and cloud-resolving models make it possible to separate the two components of heating (Tao et al., 2010), and we take advantage of this capability to investigate whether these two types of LH induce different temperature responses in the upper troposphere. Together with the high vertical resolution of temperature profiles from RO observations (Kursinski et al., 1997), these data sets also give insight into the vertical structure of the temperature responses.

To understand how the variability of tropical UTLS temperatures relate to the height of tropical LH, we study the time series of convective and stratiform LH extracted from the Tropical Rainfall Measurement Mission (TRMM) Spectral Latent Heating (SLH) product and temperature derived from RO observations. Cross-spectral analysis (CSA) is employed to analyze the coherence and time-lag relationship between LH and UTLS temperatures. Section 2.2 gives an overview of the data utilized in this chapter, and Section 2.3 describes the construction of LH and temperature time series, processing of the time series, the CSA, and significance testing. We present the results of the analysis in Section 2.4 and give a summary of this study in Section 2.5.

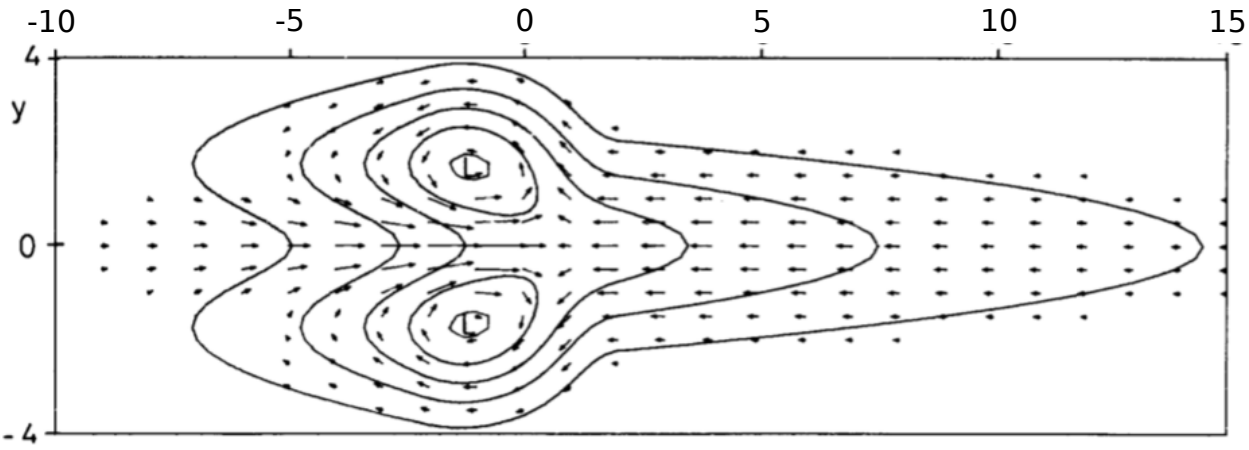

Figure 2.2 Lower tropospheric wind and pressure response of a resting atmosphere to latent heating centered at (0,0). The units of the x and y-axis are non-dimensional and roughly correspond to 10° per unit. (Gill 1980)

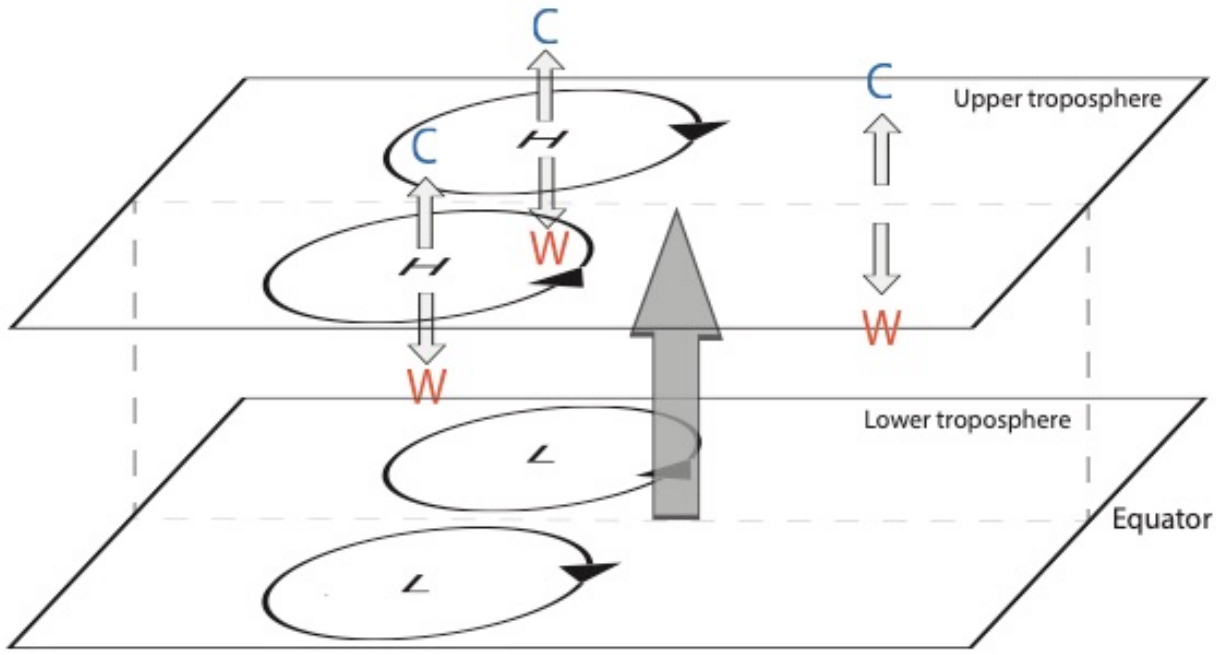

Figure 2.3 Schematic of circulation and temperature anomaly induced by tropospheric heating at the location indicated by the bold gray arrow in a resting atmosphere. High- and low-pressure anomalies are indicated by H and L, respectively, while cold and warm anomalies are indicated by blue C and orange W letters. The lower tropospheric response would be identical to Figure 2.2, while the upper tropospheric response would have the same pattern but opposing signs. Adapted from Highwood and Hoskins (1998).

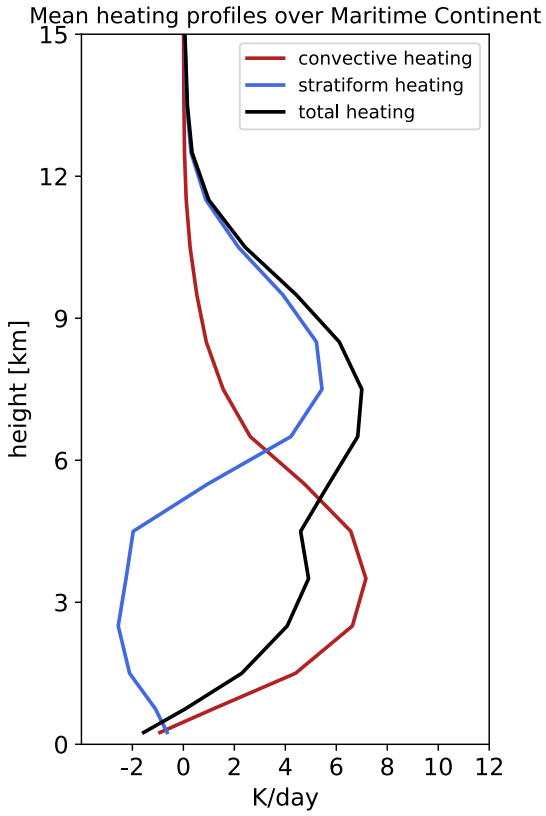

Figure 2.4 Mean convective (red), stratiform (blue), and total (black) latent heating profiles within a box over the Maritime Continent (10°N/S and 110–150°E), calculated using the TRMM SLH product over years 2006–2014.

2.2 Data sets

2.2.1 The wetPrf radio occultation data set

This study uses the reprocessed RO data sets processed by the Cosmic Data Analysis and Archive Center (CDAAC), which include occultations from the following satellite missions: Constellation Observation System for Meteorology, Ionosphere, and Climate (Anthes et al., 2008), Meteorological Operational Polar Satellite A/Global Navigation Satellite System Receiver for Atmospheric Sounding (Von Engeln et al., 2009), Meteorological Operational Polar Satellite B/Global Navigation Satellite System Receiver for Atmospheric Sounding, and the Challenging Minisatellite Payload (Wickert et al., 2001). Because the RO technique does not suffer from

inter-satellite calibration effects (Foelsche et al., 2011), profiles from different RO satellite missions can be used together as long as they are processed with the same algorithm. Temperatures from 500 to 70 hPa are extracted from the level 2 wetPrf products of the above missions. Although wetPrf profiles provide temperature every 100 m, the effective vertical resolution of the RO technique is around 1 km near the tropopause (Kursinski et al., 1997). Precision of temperature from RO is approximately 0.5 K within altitudes of 8 to 20 km (Anthes et al., 2008). Figure 2.5 show the daily count of wetPrf profiles available within 25° of the equator.

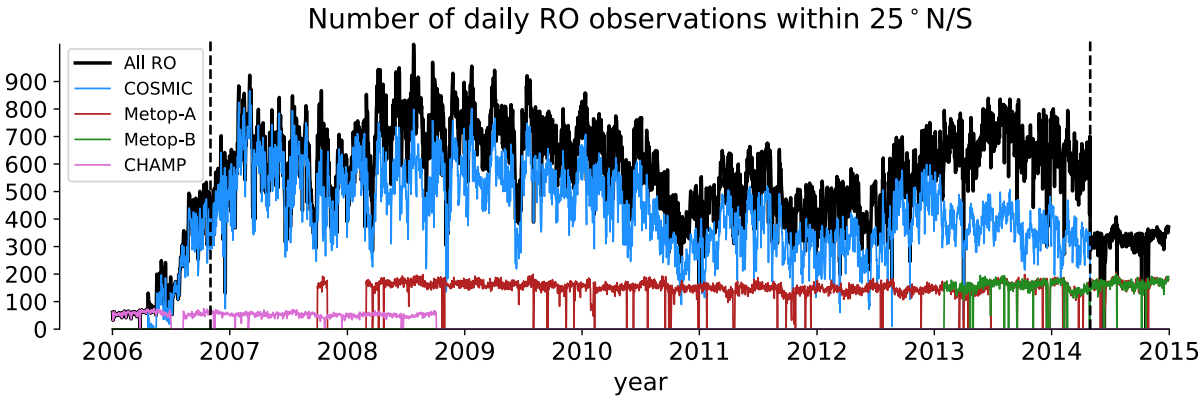

Figure 2.5 Daily count of wetPrf profiles within 25°N/S from each RO mission. Dashed lines indicate the beginning and end of the period used in this study. COSMIC = Constellation Observation System for Meteorology, Ionosphere, and Climate; Metop = Meteorological Operational Polar Satellite; CHAMP = Challenging Minisatellite Payload.

2.2.2 TRMM spectral latent heating

TRMM was launched in 1997 to improve our understanding of tropical precipitation and LH (Kummerow et al., 1998; Simpson et al., 1988). Its Precipitation Radar (PR) observes the vertical structure of clouds and enables the retrieval of vertically resolved LH in clouds. This study uses

the SLH product (Shige et al., 2004, 2007, 2008, 2009) within the time period of 2006 to 2014 when there was an abundance of RO observations.

The SLH algorithm employs a lookup table approach to retrieve LH. Lookup tables were generated with the Goddard Cumulus Ensemble model (Tao and Simpson, 1993) by simulating the LH structures based on observations of the Tropical Ocean and Global Atmosphere Coupled Ocean-Atmosphere Response Experiment (Shige et al., 2004). Global applicability of these lookup tables was evaluated with observations from various other campaigns (Shige et al., 2007). Simulated scenes are categorized as convective, shallow stratiform, or deep stratiform (anvil) based on precipitation rate, cloud water, and updraft velocity of the model grid point as well as surrounding grid points; details of the separation method are given in Section 3a of Shige et al. (2004). Inputs for the lookup table include precipitation-top height, precipitation rate, and precipitation type (convective or stratiform). To retrieve the LH of TRMM PR observations, the precipitation-top height and precipitation rates from the 2A25 product (Iguchi et al., 2000) and precipitation type from the 2A23 product (Awaka et al., 2002; Schumacher and Houze, 2003) were used. Identification of the precipitation type using the PR is based on the identification of the bright band from the melting layer and the vertical distribution of radar reflectivity.

Hagos et al. (2010) conducted a comparison of LH among reanalyses, various TRMM algorithms (including SLH), and sounding-based estimates. They show that the structure of the deep modes is similar across data sets, while the shallow modes differ significantly. Tao et al. (2016) show that the SLH better resolves shallow convection (see their Figure 2-4) compared to the Goddard Convective-Stratiform Heating (CSH) algorithm (Tao et al., 1993). Total heating estimates from existing TRMM LH algorithms generally compare well with sounding-based estimates (Figure 2-5 and 2-7 of Tao et al. (2016)), with some differences in amplitude and

vertical structure. However, we note that the reliability of the separate convective and stratiform components are not well documented, since validations using soundings have generally been focused on total heating.

SLH provides estimates of pure LH as well as $Q_1 - Q_r$, the difference between the apparent heating Q_1 (Yanai et al., 1973) and the radiative heating Q_r, which we will refer to as Q_{1r}. The Q_1 is the sum of LH, radiative heating, and vertical convergence of vertical eddy transport of heat flux. Since the last two terms are typically much smaller relative to LH, Q_{1r} is very close to LH (Shige et al., 2004). Since there are no Q_r estimates based on TRMM that covers the entirety of 2006-2014, in this study we use Q_{1r} in the main analysis and Q_r is treated separately as described below. In the following discussions we use the term LH in reference to Q_{1r}.

2.2.3 Radiative heating from CERES and its consistency with TRMM Estimates

To estimate Q_r, we use the Clouds and the Earth's Radiant Energy System (CERES) SYN1deg daily product (Doelling et al., 2016) which provides shortwave and longwave fluxes at 1000, 850, 500, 200, 70 hPa, and top-of-atmosphere. Q_r at layers between 1000 and 850 hPa, 850 and 500 hPa, 500 and 200 hPa, and 200 and 70 hPa are calculated from these fluxes. Cloud information in the SYN1deg algorithm comes from a combination of observations from the Moderate Resolution Imaging Spectroradiometer (MODIS) and geostationary satellites. Estimates of radiative heating from TRMM are also available from the Hydrologic Cycle and Earth's Radiation Budget (HERB) data set (L'Ecuyer and Mcgarragh, 2010) for the period 1998 to 2010. However, this overlaps with only about half of the COSMIC data record (2007–2014).

For this reason, we use HERB only to check the consistency of Q_r estimates between CERES and TRMM, as discussed below.

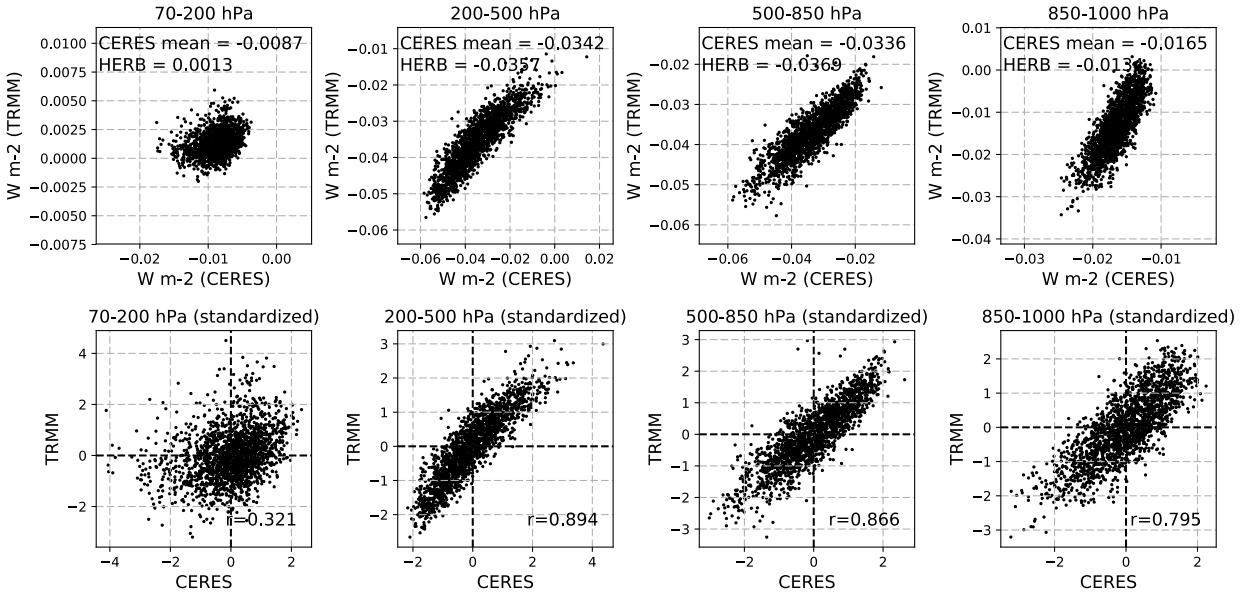

Figure 2.6 Scatterplot of vertically integrated $\boldsymbol{Q_r}$ inside the Indian Ocean Center box (Figure 2.8) estimated from the CERES SYN1deg and TRMM HERB product. Each dot represents daily mean values inside the box. Top row shows values in physical units (W/m2), with the mean value of each data set denoted in the legend. The bottom row is in standardized space, with the correlation coefficient *r* denoted.

Q_r is vertically integrated in the layers 1000–850, 850–500, 500–200, and 200–70 hPa for both the CERES SYN1deg and TRMM HERB data sets. Following Yanai et al. (1973), the vertically integrated heating of the *i*-th layer, $\bar{Q}_{(i)}$, is calculated as

$$\bar{Q}_{(i)} = \frac{1}{g}\int_{p_{top}^{(i)}}^{p_{base}^{(i)}} Q(p)dp \tag{2.1}$$

where g is the gravitational acceleration, $Q(p)$ is the LH profile as a function of pressure p, and $p_{top}^{(i)}$ and $p_{base}^{(i)}$ are the pressure of the top and bottom of the *i*-th layer. Figures 2.6 and 2.7 show

comparisons of integrated Q_r over the Indian Ocean (IO) and Maritime Continent (MC) region. Aside from the 200–70 hPa layer, correlation coefficients between the two data sets are high (0.795 or greater), showing the consistency of Q_r between CERES and TRMM estimates. The low correlation in the 200–70 hPa layer may be due to the effects of high clouds.

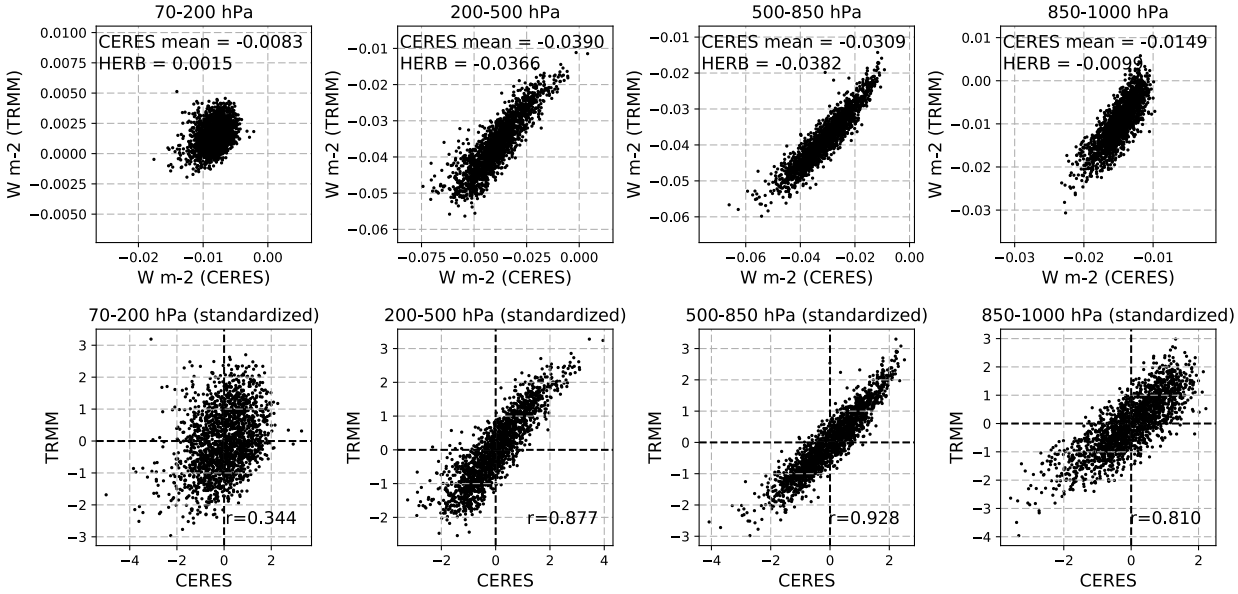

Figure 2.7 Same as Figure 2.6 except for the Maritime Continent Center box.

2.3 Time series processing and cross-spectral analysis

2.3.1 Construction and preprocessing of time series

Time series of daily mean temperature and LH from 1 November 2006 to 30 April 2014 are constructed in the boxes shown in Figure 2.8. We designate two areas of study, one over the Indian Ocean (IO) and another over the Maritime Continent (MC). In each area, one box centered on the equator is used to construct the LH time series, and the North, South, East, and Center boxes are used to construct time series of temperature. The locations of the North and South boxes coincide with the locations of the ERW response, while the East boxes coincides

with the KW response. Note that, as shown in Figure 2.3, the anticyclones are slight westward of heating. This is the pattern of the stationary ERW in a resting atmosphere, while Jin and Hoskins (1995) showed that in realistic atmospheric flow the anticyclones almost flank the heating directly north and south. For this reason, the North and South boxes are placed directly north and south of the heating boxes. The relationship between the temperature time series inside the (IO,MC) North, South, East, and Center boxes and the LH time series in the (IO,MC) Center boxes is analyzed through cross-spectral analysis.

Time series of temperature are made at 500, 400, 350, 300, 250, 200, 170 hPa and every 10 hPa between 150 and 70 hPa. For LH, we split the atmosphere into the following layers: 0–3, 3–6, 6–9, 9–12, and 12–15 km, and Q_{1r} is integrated in these layers using equation (2.1) to represent the vertically integrated LH.

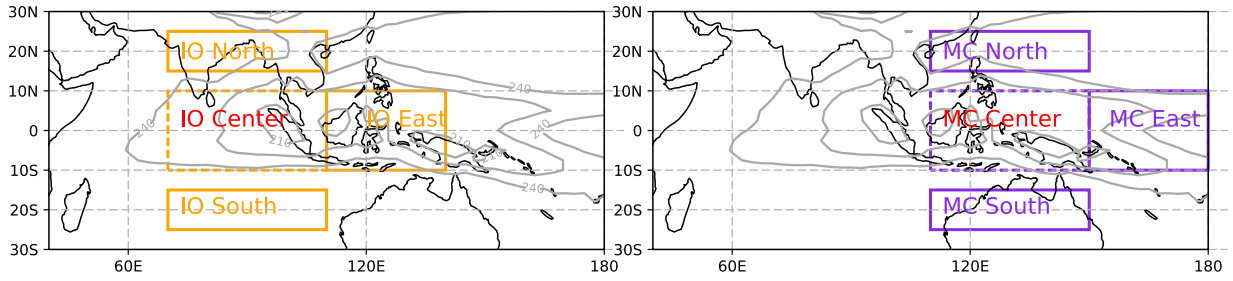

Figure 2.8 Boxes in which temperature and LH time series were constructed. LH time series are constructed inside the IO/MC Center boxes labeled in red, while temperature time series were constructed in the IO/MC North, South, East, and Center boxes. Contours at intervals of 15 W/m^2 are mean outgoing longwave radiation through 2006 –2014 derived from the National Oceanic and Atmospheric Administration Interpolated Outgoing Longwave Radiation daily data set. IO = Indian Ocean; MC = Maritime Continent.

Heating above 15 km is negligible (as seen in Figure 2.4) and is omitted. The same integrated quantity is calculated for convective, stratiform, and total (sum of convective and

stratiform) LH. All time series are first deseasonalized by removing the sinusoidal variations from the first three harmonics of the annual cycle and then standardized prior to performing the CSA.

Time series of Q_r based on CERES SYN1deg are constructed in the same manner as above, in the vertical layers 1000–850, 850–500, 500–200, and 200–70 hPa instead of the 3-km layers. Due to the differences in vertical resolution and spatial sampling between TRMM and CERES, Q_r is not added to the Q_{1r} term, and CSA is performed separately on Q_r and Q_{1r}.

2.3.2 Cross-spectral analysis

CSA is used to examine the relationship between two time series in the frequency domain. The coherence spectrum is analogous to the correlation coefficient and gives a measure of how closely two time series are varying together at a frequency f, while the phase spectrum tells whether one time series is leading or lagging the other at f. Given two time series x and y, their power spectral densities $P_{xx}(f)$ and $P_{yy}(f)$, and the cross-spectral density $P_{xy}(f)$, the coherence (or coherence-squared) spectrum is

$$Coh^2(f) = |r_{xy}(f)|^2 = \frac{|P_{xy}(f)|^2}{P_{xx}(f)P_{yy}(f)} \tag{2.2}$$

and the phase spectrum is

$$\theta_{xy}(f) = tan\left[\frac{Im(r_{xy})}{Re(r_{xy})}\right]. \tag{2.3}$$

The coherence falls between 0 and 1, where a value of 1 indicates that at f the amplitudes of the two time series are linearly related.

Cross-spectral densities are estimated using Welch's average periodogram method (Welch, 1967). Estimates of effective degree of freedom (eDOF) and the choice of window

length for the spectral density estimation follows Biltoft and Pardyjak (2009). The eDOF is calculated as $(8/3)N/\text{nfft}$ where N is the length of the time series and nfft is the width of window used to calculate the power densities. Although the length of each time series is $N = 2738$ days, each day cannot be seen as independent. The number of independent samples is calculated by (Bretherton et al., 1999)

$$N_* = N\left[\frac{1 - r_x r_y}{1 + r_x r_y}\right] \tag{2.4}$$

where r_x and r_y are the lag-one autocorrelation of x and y. Biltoft and Pardyjak (2009) recommends that the eDOF fall within 10 to 100 for reliable significance testing. By using values nfft = 128 and an overlap of 64, most of the eDOFs fall within 40 to 60, which is in the recommended range.

Significance testing of coherence also follows Biltoft and Pardyjak (2009). A coherence value is statistically significant at the $(1 - p) \times 100\%$ level if it is greater than the value calculated from

$$\chi_{1-p} = \frac{2F_p}{\text{eDOF} - 2 - 2F_p} \tag{2.5}$$

where F_p is the value of the F(2, eDOF − 2) distribution at $1 - p$. All significant levels shown in the results are calculated with p = 0.01 (99% significance).

2.4 Coherence and time-lag between latent heating and UTLS temperature

Figure 2.9 shows the coherence spectra between 100 hPa average temperature in IO South and convective, stratiform, or total LH inside the IO heating box in the five layers as defined in Section 2.3.1. Since Figure 2.9 shows only one altitude of temperature over one location (IO South), this plot serves simply as an example of the coherence and phase spectrum. The results

below are obtained by analyzing the gross features of the coherences and phases from all levels of temperature and all locations.

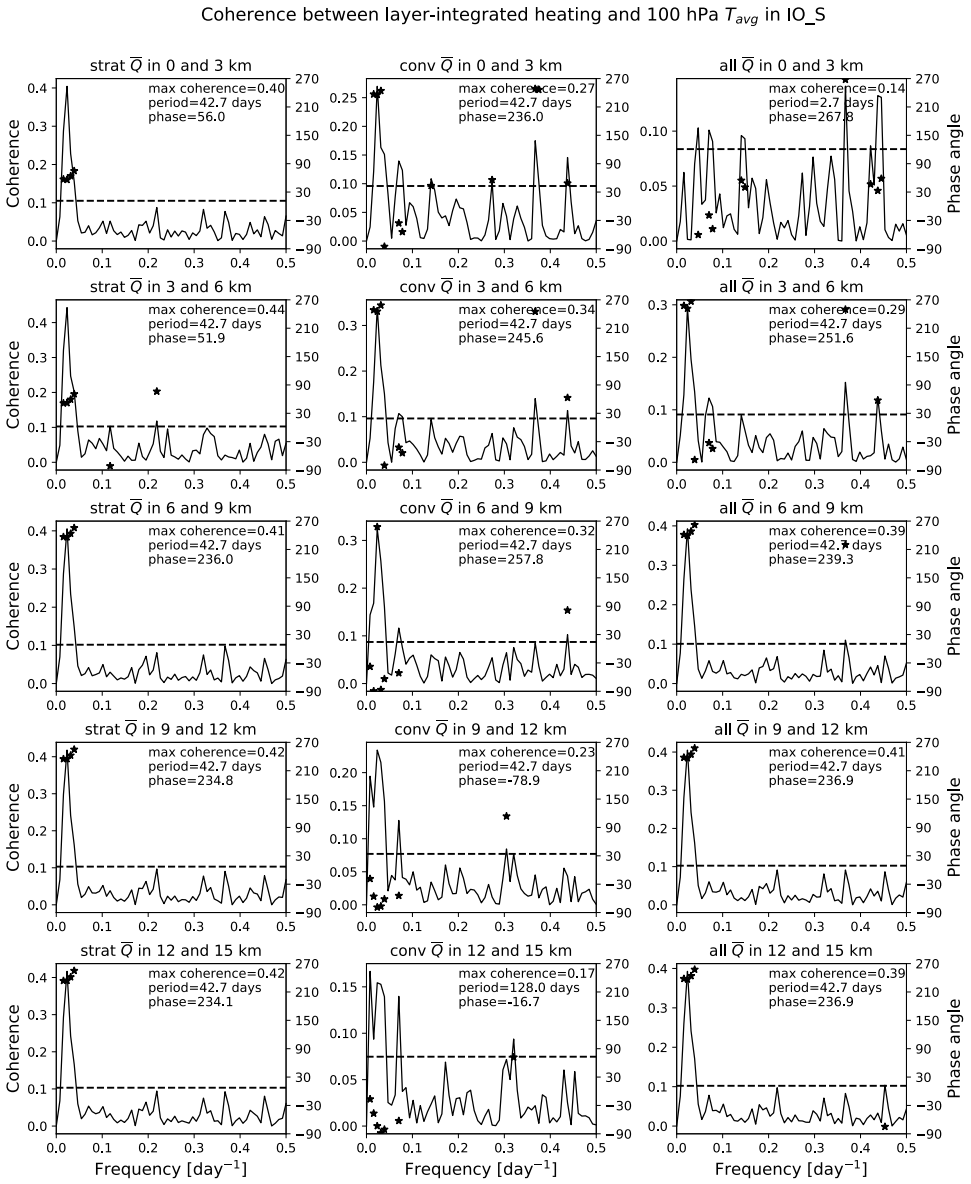

Figure 2.9 Coherence spectra between 100-hPa mean temperature inside Indian Ocean South box (see Figure 2.8) and stratiform (left column), convective (middle column), or total (right column) heating inside Indian Ocean Center in the five vertical layers defined in section 2.3.1. Dashed lines indicate 99% significance level. Phases for coherences above this level are plotted as stars. The max coherence in each case and the corresponding period and phase are summarized in the legends.

Although we evaluate the LH components separately, the atmosphere responds not to the individual components but rather to the total heating. As shown in Figure 2.10, the profile of maximum coherence from total heating tends to increase with altitude, with the exception of MC South and MC East for 100-hPa temperature. This suggests that, in general, both the warming (250 hPa) and cooling (100 hPa) signatures are more associated with heating aloft in the middle and upper troposphere. This implies that the temperature responses depend on the vertical distribution of heating, if the high coherences do, in fact, depict the temperature responses due to the stationary KW/ERW signature. In the following discussion, we show that the vertical structure of coherences and time lags agrees well with those of KW/ERW responses found in previous studies.

The phases corresponding to the statistically significant coherences from total LH are shown in the left panel of Figure 2.11. Note that the phase plots are largely the same for total LH in the three layers above 6 km, while the lower two layers have typically low coherence (Figure 2.10). Hence, we show the phases from total LH inside 9–12 km since they are representative of the phase distribution in general. One common feature across all boxes in both regions is the shift from phases between 0° to 90° below ~150 hPa to phases larger than 180° above ~150 hPa. A 180° phase difference indicates that when the LH time series reaches a maximum in amplitude (in the given frequency f), the temperature reaches a minimum. Phases slightly larger than 180° indicate that the temperature reaches a minimum shortly after a peak in LH. For this reason, we interpret the phases distributed around 180° as the cooling response. Likewise, phases within 0° to 90° are interpreted to be the warming response. The vertical structure of the phases indicates that the variability of LH tends to be associated with cooling above 150 hPa and warming below, physically consistent with the equatorial planetary wave structure as found by Dima and Wallace

(2007) who found that the largest geopotential height and wind anomalies due to equatorial planetary waves occur near 150 hPa.

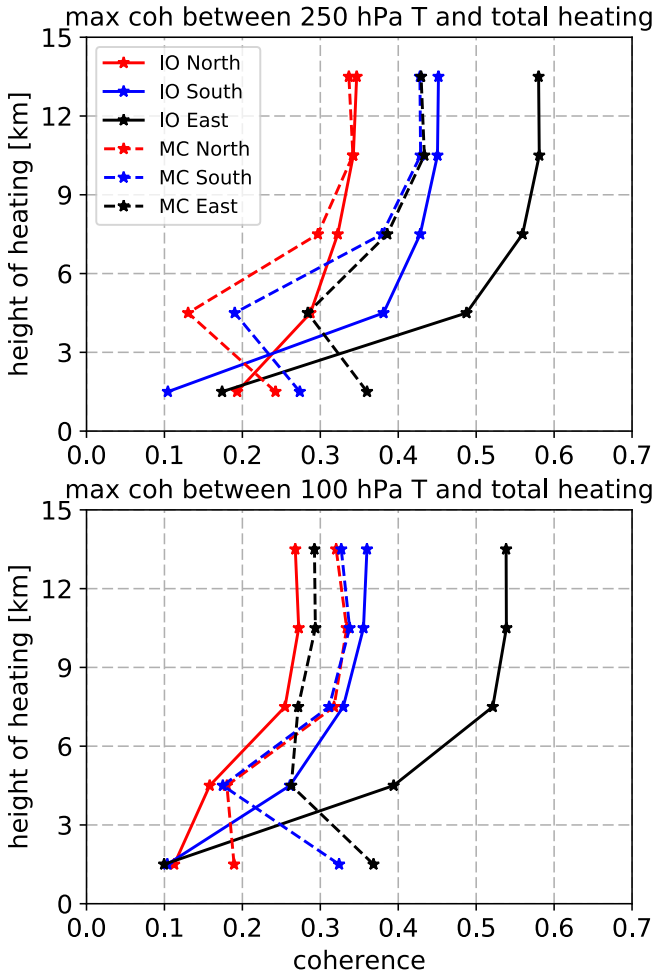

Figure 2.10 Maximum coherence between total heating at each of the five layers (y-axis) and temperature at 250 hPa (top) or 100 hPa (bottom). The maximum coherence represents the highest value of the coherence spectrum (see Figure 2.9) out of all frequencies. IO = Indian Ocean; MC = Maritime Continent.

The right panel of Figure 2.11 shows the time lag in days derived from the phase. Following the reasoning above, the lags above 150 hPa are calculated by assuming that day 0 is located at a phase of 180° in order to estimate the time lag of the cooling response, and below 150 hPa, the 0◦ phase is taken as day 0. In general, inside the North, South, and East boxes, the

lags fall within 0 to 12 days. Jin and Hoskins (1995) showed that in a model with prescribed heating, the ERW/KW response starts around day 3 after the onset of heating and ceases to change past 14 days. The lags found here are roughly consistent with this time range. In the North/South cases, the lags within 500–150 hPa are slightly larger than those above 150 hPa, suggesting that the upper-tropospheric warming response may be slightly slower than the TTL cooling response inside 150–80 hPa. Also, in IO North/South and MC South, the lags in the TTL clearly increase with height, although this feature is not present in MC North. This increase of lag with height may depict the upward propagation of the cold anomaly, which starts near 150 hPa where the geopotential anomalies occur.

The phases in the East boxes show signals of TTL cooling likely associated with KW, similar to the results of Zhou and Holton (2002) who concluded that intraseasonal cold temperature anomalies in these regions are likely due to KW excited by convection located west of cold anomalies. Due to the eastward movement of MJO convection together with the eastward tilt of KW, it is expected that the phase of TTL cooling descends with time. This is seen in the phases of IO East which has a downward trend of phase in the cooling response. The IO Center has in addition a downward propagation of warming response in 70–100 hPa. This vertical structure is consistent with the KW associated with MJO convection (Figure 4 of Virts and Wallace, 2014), where the warming phase of the KW lies above the cooling phase. On the other hand, the downward propagation in MC Center is not very evident, and the phases in MC East show no signs of downward phase propagation.

Although the range of time lags found here are consistent with the response times found by Jin and Hoskins (1995), the positive time lags could also be due to the effects of MJO convection moving eastward rather than representing the response times of the atmosphere to the

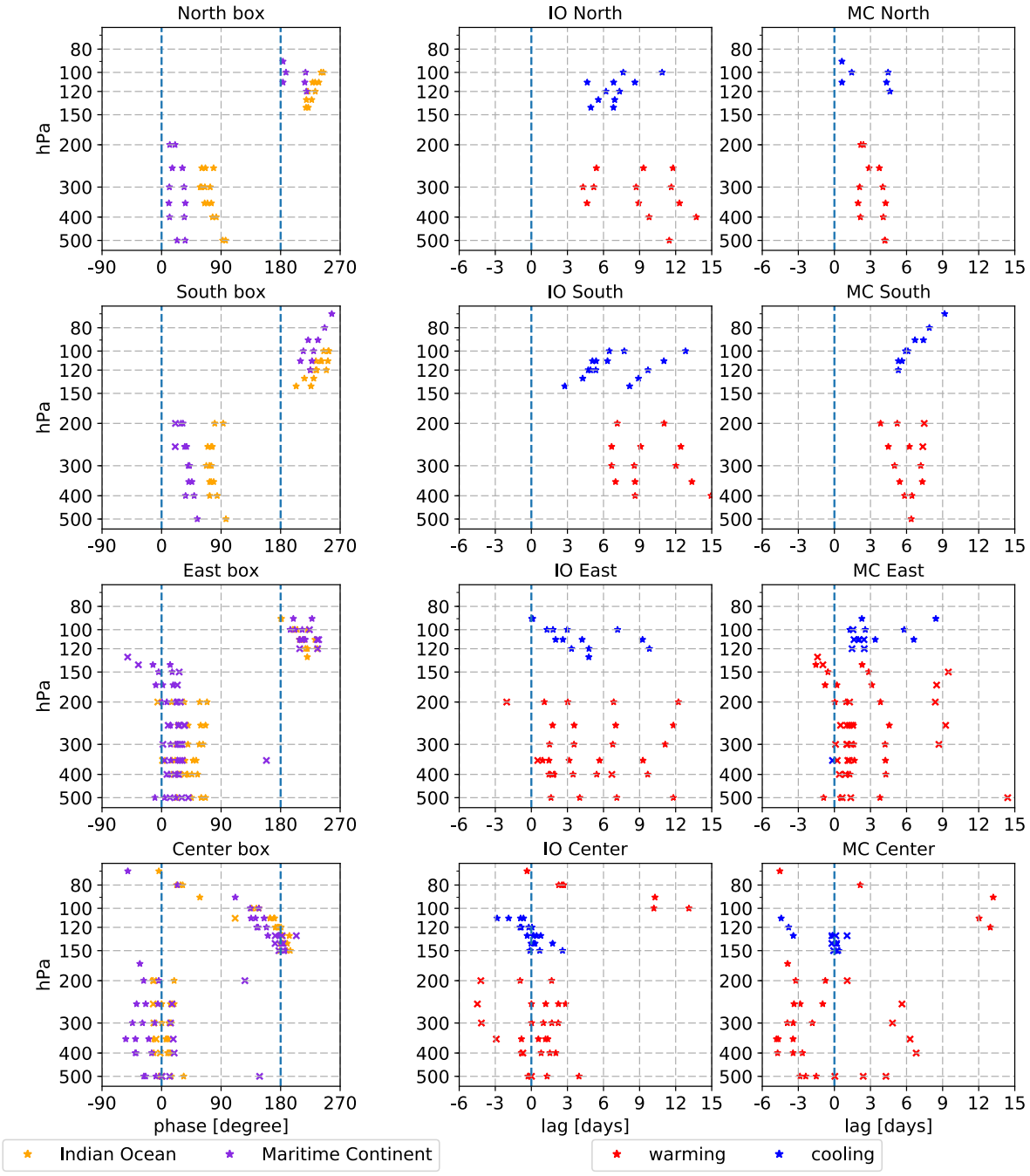

Figure 2.11 (Left) Phases corresponding to statistically significant coherences between 9–12 km total latent heating (LH) and temperature at the altitude indicated by the y-axis. Stars indicate that the time scale of the phase falls within 20–90 days, while the X marks phases outside this time scale. Positive phases indicate that the temperature lags LH. (Right) The lag in days, calculated from the phases in the left column. Positive lag indicates that temperature lags LH. Above 150 hPa, the 180° phase is assumed to be day 0 to estimate the lag of the cooling response (see text for explanation).

LH. The fact that anomalies associated with the MJO have a “swallowtail” shape (Zhang and Ling, 2011) means that the eastward movement of this anomaly may cause perturbations in the North/South boxes to lag that of the Center box. The East box would obviously be affected by eastward moving convection as well, as discussed above. Despite this possibility, the vertical structure of the warming and cooling is largely consistent with the known structure of equatorial waves, so the relationship between temperature and LH depicted in this study is most likely physical and still valuable for understanding which LH components are more highly associated with UTLS temperatures.

With this in mind, the distributions of these statistically significant coherences in all boxes are plotted in altitude and frequency space, as shown in Figure 2.12 for the IO region and Figure 2.13 for MC. In both regions, most statistically significant coherences fall within the time scales between 20 and 64 days, with many of the larger coherences (≥0.6) falling near 43 days. The maxima of coherences peak at time scales of~43 days and, vertically, lie between 500 and 200 hPa. There is also a group of high coherences between 150 and 80 hPa, especially over IO. Most of the highest coherences therefore occur on time scales consistent with the MJO (20 to 90 days), so the observed coupling between temperature and LH is largely associated with the MJO. The importance of MJO on the intraseasonal time scale has been shown by Mote et al. (2000) who found that MJO dominates the water vapor signal within 200 to 100 hPa and by Kim et al. (2018a) who showed, through compositing water vapor fields with respect to MJO and non-MJO convection, that the dehydration signal is much stronger from convection associated with MJO. The results presented here further link UTLS variability to LH linked to the MJO, since most statistically significant coherences occurs at MJO time scales. The collective results of this and

previous studies suggest that MJO-associated convection has properties that set it apart from other convection in its ability to affect the UTLS through the planetary wave pattern.

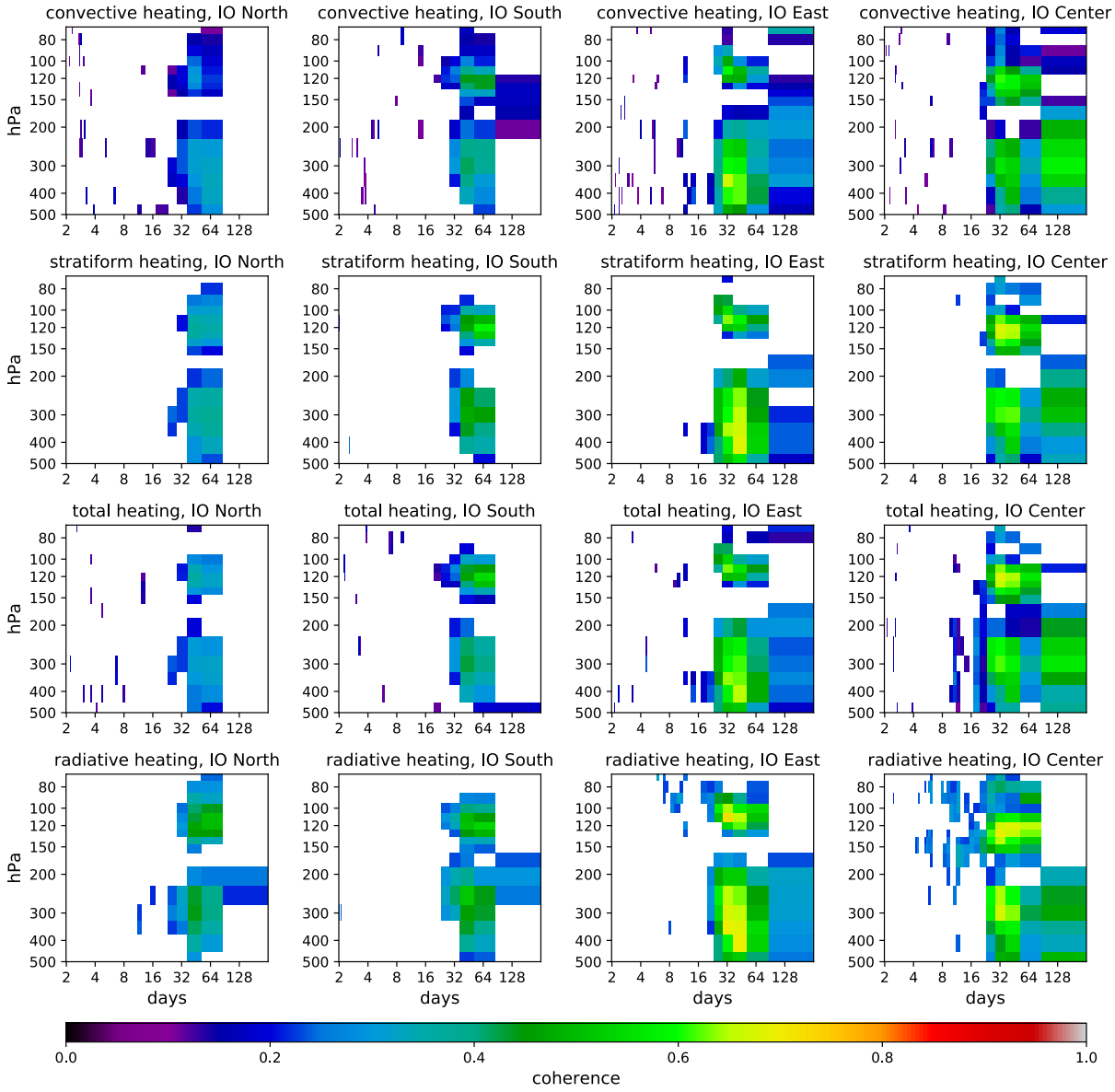

Figure 2.12 Highest coherence at each pressure level (ordinate) and frequency (absicca) for convective (first row), stratiform (second row), total heating (third row), and radiative heating (fourth row) for the IO North, South, East, and Center boxes. The ordinate axis denotes the altitude of the temperature time series. White spaces indicate pressures and frequencies at which no coherences passed the significance testing. IO = Indian Ocean.

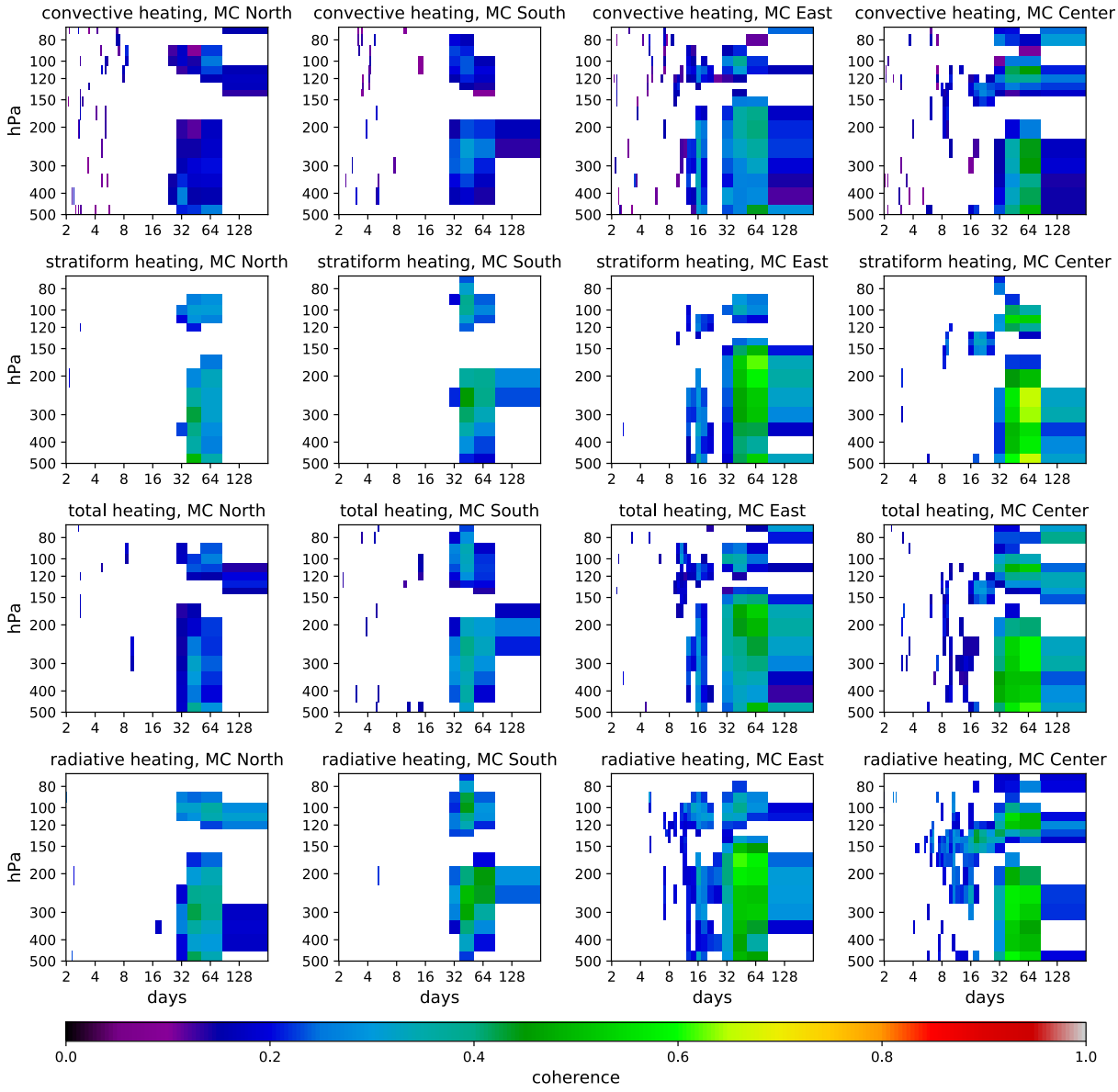

Figure 2.13 Same as Figure 2.12 except for the MC boxes. MC = Maritime Continent.

Figure 2.14 contrasts the vertical profiles of coherence between temperature at each pressure level and convective/stratiform LH. At each pressure level, the temperature time series is paired with the LH time series from each of the five layers, and the maximum coherence (out of the five possible pairings) is plotted. The vertical distribution of coherences of convective and stratiform LH is very similar, since the two are highly correlated; stratiform precipitation

typically comes after convection. In the North and South boxes, the stratiform LH varies more coherently with temperatures throughout most of the TTL and upper troposphere. Near the tropopause (~100 hPa), the coherence from stratiform LH is higher than that of convective LH in all the North/South cases. This indicates that the TTL cooling is more closely related to stratiform LH. Similarly, in the upper troposphere (500 to 150 hPa), the higher coherences from stratiform LH shows a closer relationship between upper-tropospheric warming and stratiform LH. Coherences over IO North is lower, possibly due to the strong influences of off-equator heating from the Asian Monsoon during boreal summer. Over the East boxes, coherences in the TTL are very close over IO, while over MC the convective LH coherences are slightly larger. Stratiform coherences are larger at most altitudes below 150 hPa over the East boxes. These

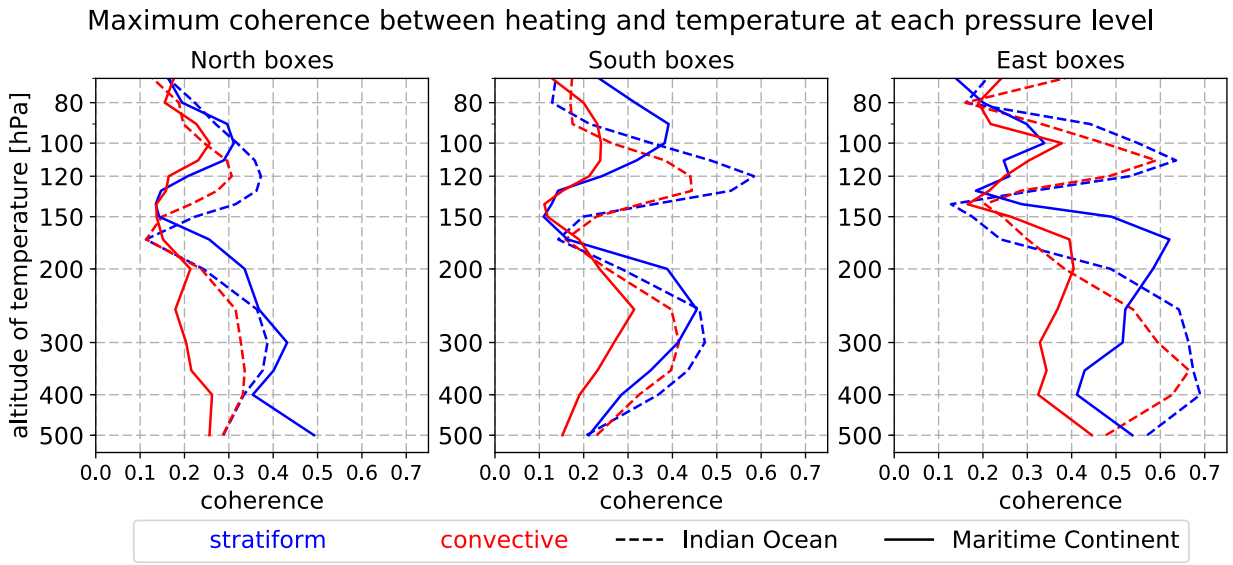

Figure 2.14 Profile of maximum coherence between temperature and latent heating for the North (left), South (middle), and East (right) boxes. The temperature time series from each pressure level (indicated by the ordinate axis) is paired with the latent heating time series from each of the five layers, and the coherence value plotted at each pressure represents the maximum coherence of the five possible pairings. Solid and dashed lines represent the Maritime Continent and Indian Ocean regions, respectively, while the colors distinguish the type of heating.

results show that upper-tropospheric warming has higher association with stratiform heating, and the same statement applies for TTL cooling, except for the MC East case.

In summary, results in this section show that (1) the upper-tropospheric warming and TTL cooling signal exhibit a dependence on heating altitude and (2) stratiform LH shares high coherences with TTL and upper-tropospheric temperature at MJO time scales.

2.5 Empirical orthogonal functions of latent heating and cross-spectral analysis of principal component time series

Empirical orthogonal functions (EOF) analysis (Wilks, 2011) is applied to the LH time series to find the dominant modes of variability. Figure 2.15 shows the first three EOFs of LH in the IO/MC Center boxes and the percentage of variance explained by the first five EOFs. In both IO and MC regions, the first EOF is a deep heating mode that peaks near 7.5 km. Compared to the mean convective heating profile in Figure 2.4 that peaks near 3.5 km, this EOF represents a much deeper heating mode. The second EOF is similar to the stratiform heating shown in Figure 2.4. Over IO, the first three EOFs explain 88.2%, 10.2%, and 1.2% of the total variance, while over MC the percentages are 87.5%, 11.0%, and 1.2%. The first two EOFs explain a large fraction of variability.

To evaluate how these EOFs relate to UTLS temperature, a similar CSA procedure is conducted here. In Section 2.4, the time series of LH at each of the five vertical layers are used to conduct CSA. Here we use the time series of principle components (PC) in place of the LH time series. The temperature time series are identical to those used in Section 2.4. Figure 2.16 shows the phase lags between UTLS temperatures and the PC time series of the first EOF (EOF1). The

time lags of EOF1 show high resemblance to Figure 2.11, indicating that the responses depicted in Figure 2.11 is mostly associated with the deep heating of EOF1.

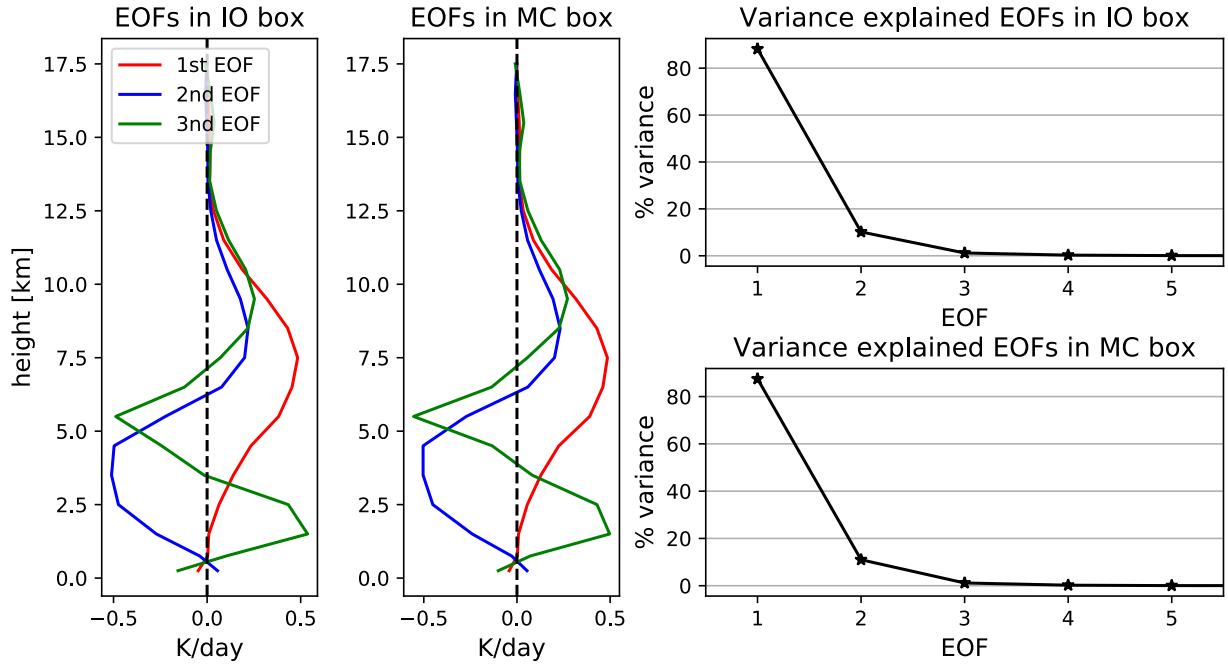

Figure 2.15 The first three EOFs of latent heating the IO and MC box (left), and the variance explained by the first five EOFs (right).

On the other hand, the time lags of EOF2 (Figure 2.17) exhibit several differences with those of the EOF1. The cooling responses in the North and South boxes still exist, although the time lags in these boxes are shifted closer to day 0. In the East boxes, the cooling response in the TTL is less apparent since there are much fewer blue markers between 150–70 hPa compared to Figure 2.11. In the Center box, instead of having primarily heating below 150 hPa, there are lags associated with cooling. This most likely indicates the lower-level evaporative cooling of the stratiform heating profile. The existence of TTL cooling in the North/South boxes but the lack thereof in the East box indicates that EOF2 is linked to the ERW response but less so to the KW response.

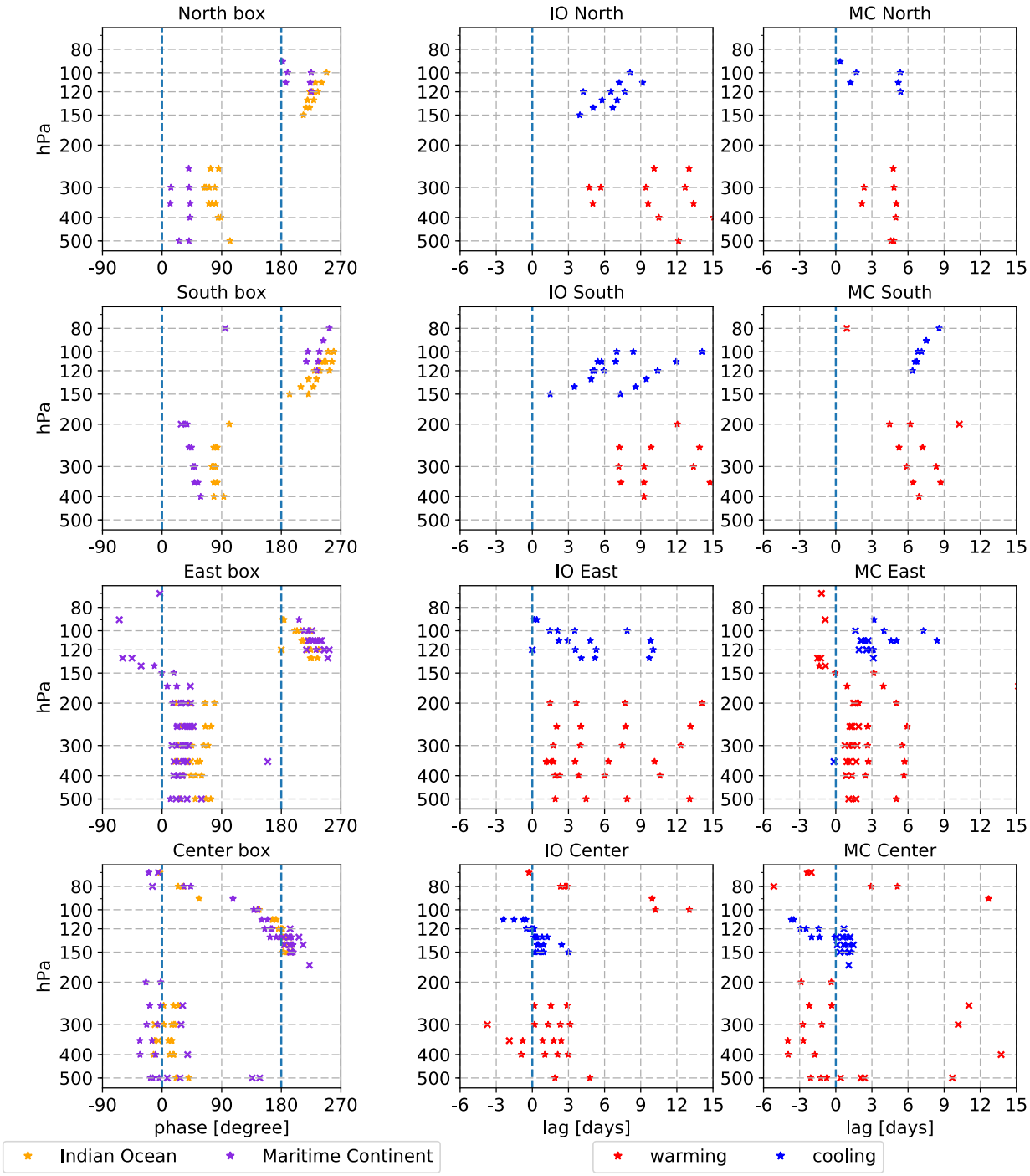

Figure 2.16 Same as Figure 2.11 except for the first EOF.

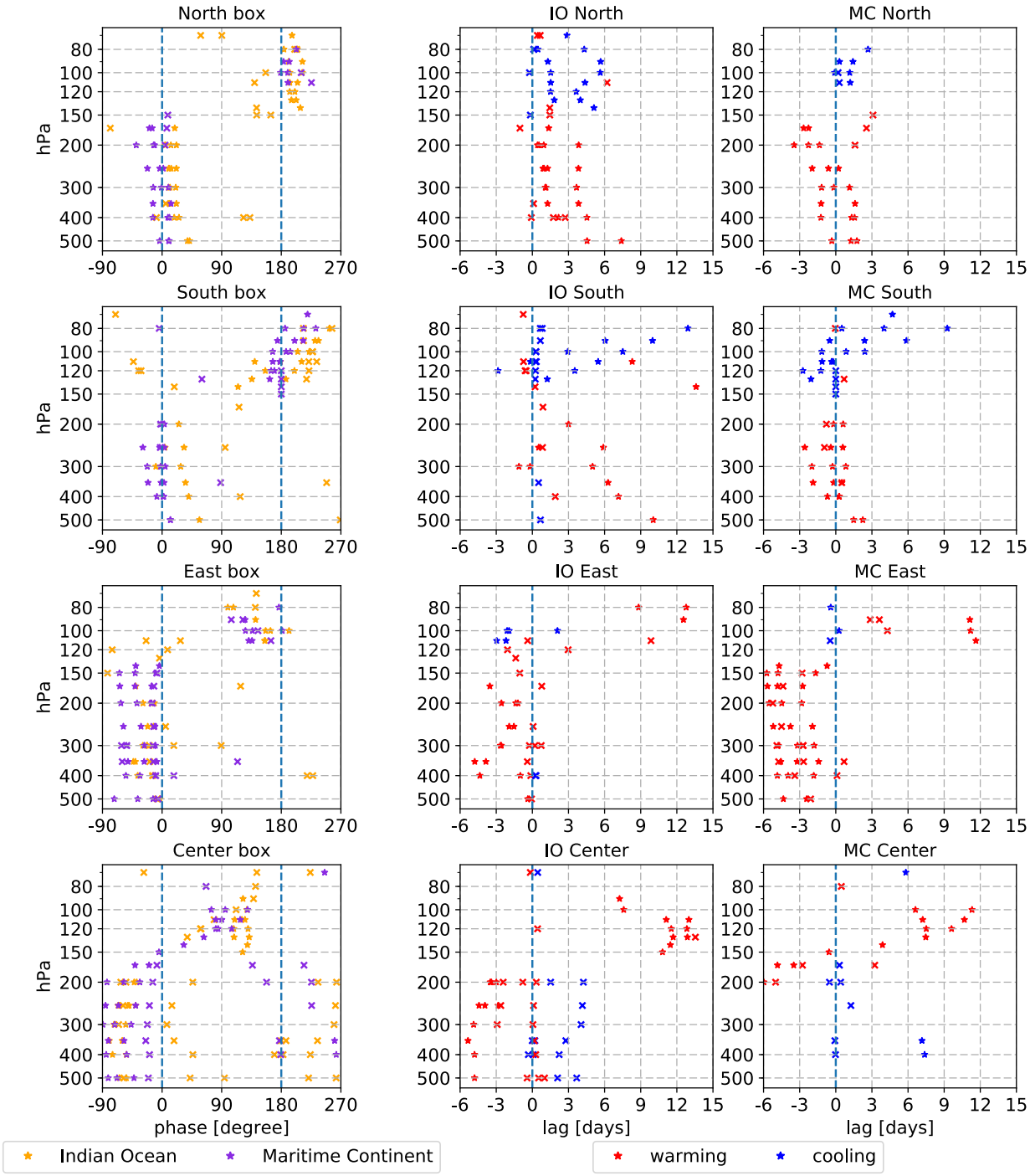

Figure 2.17 Same as Figure 2.11 except for the second EOF.

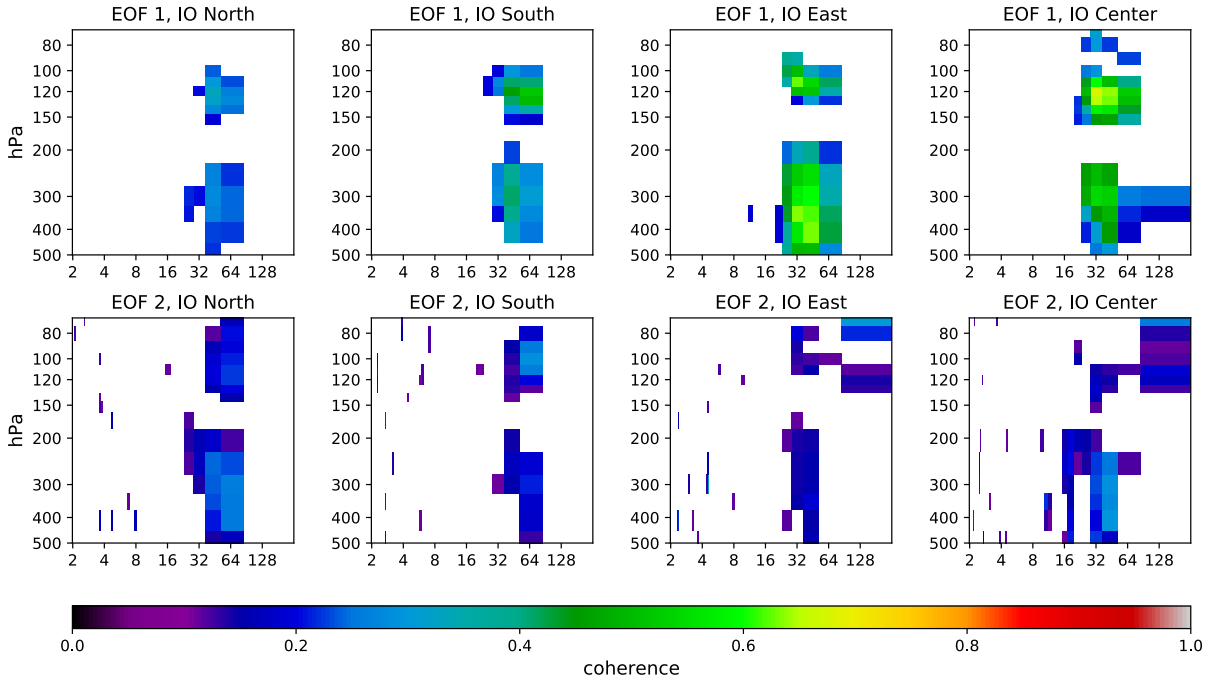

Figure 2.18 (Top row) Coherence between the first EOF and time series of temperature at each pressure level. (Bottom row) Same as top row except for the second EOF.

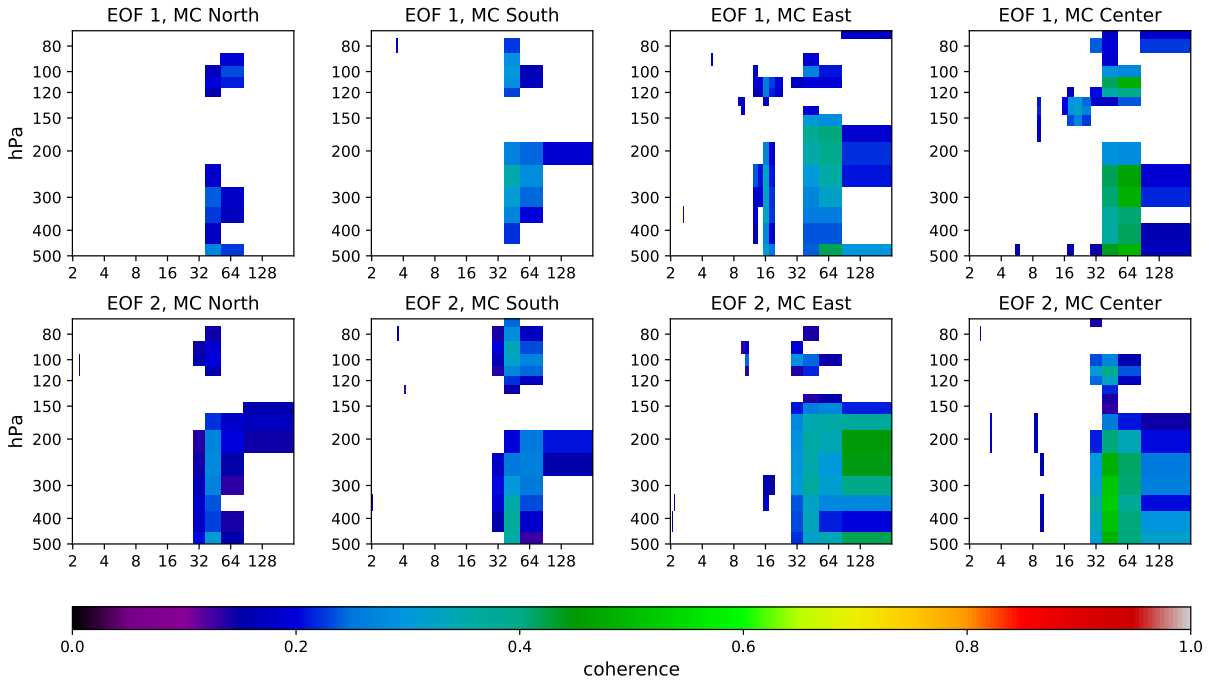

Figure 2.19 Same as Figure 2.18 except for the MC boxes.

The distribution and magnitude of coherences are shown in Figure 2.18 and 2.19, for IO and MC, respectively. Over IO, the first EOF generally has larger coherences with temperature. Over MC, the coherence values are comparable between the first and second EOF. The structure of the coherences is similar to those in Figure 2.12 and 2.13; significant coherences mostly fall near the MJO timescale, and vertically there are statistically significant coherences between 70-120 hPa and 150-500 hPa.

The results in Section 2.4 demonstrate that (1) the upper-tropospheric warming and TTL cooling signal exhibit a dependence on heating altitude and (2) stratiform LH shares high coherences with UTLS temperatures. Results in this section are arguably consistent with first point. Based on Figure 2.10 we suggested that heating needs to reach above 6 km before it has strong association with UTLS temperatures. The EOF1 peaks at 7.5 km and is therefore representative of heating from deep convection. The similarity between Figure 2.16 and 2.11 suggests that variability of deep heating is sufficient to capture the temperature variability associated with the Matsuno-Gill pattern. However, this seems to be at odds with the finding that stratiform LH shares high coherences with UTLS temperatures. Here we give a possible explanation. If the deep heating mode represented by EOF1 is primarily responsible for the planetary wave pattern, then this may reconcile the results in this section and the previous section. Since stratiform precipitation only forms after deep convection (and not shallow convection), Figure 2.14 shows higher coherence between stratiform LH and UTLS temperatures because deep convective heating always precedes stratiform precipitation. This interpretation is consistent with most results in the chapter, so it may be that the deep heating mode of EOF1 is the primary driver of the Matsuno-Gill pattern. However, this interpretation is not perfect as it does not directly explain why EOF2 is not associated with cooling in the East box. Since

stratiform heating and the deep mode both have high heating altitudes and are closely related to each other, we suggest that future research is necessary to delineate the role of these two LH sources in modulating tropical UTLS temperatures.

2.6 Chapter summary

This study examines the coupling between UTLS temperatures to equatorial LH over the Indian Ocean and Maritime Continent. With the goal of understanding whether the temperature perturbations depend on the vertical distribution of diabatic heating, we analyzed time series of LH spanning from 0 to 15 km in altitude and time series of temperature from 500 to 70 hPa. The spectral coherence and phase, derived from cross-spectral analysis, were studied to understand the role of heating altitude and the contribution of convective/stratiform heating to UTLS temperature variations. Statistically significant coherences between total heating and temperature are generally higher when total heating occurred above 6 km, signifying that the TTL cooling and upper-tropospheric warming are related to the heating altitude. Analysis of the phase and lag between temperature and LH shows that the vertical structure and time scale of the lags between LH and temperature agree well with previous studies of equatorial waves, suggesting that the coherence observed between LH and UTLS temperatures likely depict the coupling through planetary waves. The coherence between temperatures and total LH increases with the altitude of LH. This increase of coherence magnitude with height suggests that LH occurring at higher altitudes may favor the formation of the horseshoe cold trap over the MC, or that the UTLS temperature perturbations are coupled to circulations that form stratiform precipitation.

Stratiform LH, which is characterized by a higher heating peak altitude, was found to have higher coherences overall with UTLS temperatures. In all the studied cases, the stratiform

LH coherences associated with the TTL cooling in the tail region (North/South boxes) of the horseshoe are higher than those of convective LH. On the other hand, the coherences associated with the KW cooling showed negligible difference between convective and stratiform LH. EOF analysis suggests that UTLS cooling and warming are mostly associated with the deep convective heating mode. A plausible interpretation is that stratiform LH has higher coherences than the shallow convective LH because stratiform LH is preceded by deep convective heating.

In the frequency domain, most statistically significant coherences between UTLS temperature and LH fall within the time scale of 20 to 64 days, which corresponds roughly to the MJO time scale of 20 to 90 days. The fact that most high coherence values occurred at MJO time scales, together with the findings of Kim et al. (2018a) indicating that MJO convection causes more pronounced dehydration than non-MJO convection, suggests that MCS in the MJO exert strong influence on TTL cooling and subsequent dehydration processes. This study provides additional evidence that the mechanism behind these effects is linked to the vertical structure of diabatic heating in the MJO. A distinct feature of MJO convection is its top-heavy heating profile as found in campaign observations (Lin et al., 2004; Kim et al., 2018b) and cloud-permitting simulations (Wang et al., 2015). Based on our results, we suggest that the top-heaviness of heating in the MJO at least partially plays a role in its prominent signal in TTL and upper-tropospheric water vapor and temperature found here and in previous studies.

Aspects of the problem unaddressed with our approach include the dependence of the atmosphere's response on background flow varying with season. Since this study uses fixed box locations, it is unable to account for possible shifts in the position or vertical/horizontal tilt of the temperature perturbations. In addition, the coexistence of MJO and MCS makes it hard to separate the effects of moving convection and the dynamical response to diabatic heating,

complicating the interpretation of the results. Our results show a significant statistical relationship between LH and UTLS temperatures but cannot confirm whether this connection is causal.

Finally, based on the analysis presented here it is difficult to evaluate whether it is deep convective heating (EOF1) or stratiform heating that is most responsible for the temperature perturbations. It would be valuable to impose stratiform or deep convective heating in an idealized model simulation to evaluate how the atmospheric responses differ.

Chapter 3

Influence of gravity wave temperature anomalies on cirrus clouds in the tropical tropopause layer

3.1 Introduction

Cirrus formation by cold temperatures in the TTL is regarded as the primary mechanism dehydrating air entering the stratosphere (Holton et al., 1995). Studies have shown that cirrus cloud occurrence strongly relates to Kelvin waves (Immler et al., 2007; Fujiwara et al., 2009) and gravity waves (Suzuki et al., 2013; Kim et al., 2016b), and that these waves can enhance the dehydration occurring inside the TTL (Schoeberl et al., 2015).

Previous studies on waves and cirrus clouds generally show that enhanced cirrus cloud occurrence tend to coincide with the gravity wave phases having negative temperature anomalies. Through aircraft observations of the NASA Airborne Tropical TRopopause EXperiment (ATTREX) campaign (Jensen et al., 2013), Kim et al. (2016b) (K16 hereafter) show that ice was found most frequently where the temperature anomaly (T') and vertical slope of temperature anomaly (dT'/dz) were both negative, bringing the latter quantity into attention as a possible control on cirrus formation. Since K16 showed that the occurrence of convectively-coupled cirrus clouds had no preference towards the sign of T' or dT'/dz, the tendency of TTL clouds to occur in negative T' and dT'/dz likely depicts a connection between clouds and gravity wave perturbations. They suggest that the negative rate of change in temperature (positive cooling rate) inside where $dT'/dz < 0$, due to the downward phase propagation of gravity waves, may facilitate cloud formation and explain the abundance of clouds in the phase with $T' < 0$ and

$dT'/dz < 0$. Another explanation of high cloud frequency in this phase is given by Podglajen et al. (2018) (P18 hereafter) who used a simplified set of equations to model the interaction between ice crystal growth, sedimentation, and gravity wave perturbations of temperature and vertical motion. P18 argues that in this phase the upward vertical motion acts in concert with the sedimentation rate of crystals with certain sizes, suspending crystals inside this wave phase as it descends with the downward phase propagation of the wave. Motivated by these studies, we aim to further explore this connection between gravity waves anomalies and cirrus clouds through satellite data sets.

This chapter utilizes temperature profiles from the RO technique which has been widely used to study gravity and Kelvin waves (Randel et al., 2005; Alexander et al., 2008; Scherllin-Pirscher et al., 2017). We collocate RO profiles to cirrus cloud observations from the Cloud-Aerosol Lidar and Infrared Pathfinder Satellite Observations (CALIPSO) (Winker et al., 2010) to study the relationship between gravity/Kelvin wave phases and cirrus occurrence. Especially within 2006 to 2014, there is a high spatial and temporal density of RO soundings from COSMIC, allowing a large number of collocations between RO profiles and cirrus cloud retrievals.

Collocations that are temporally close in time are used to evaluate wave perturbations T' and dT'/dz in relation to cloud occurrence and properties. In addition, since the sampling of RO is pseudo-random in both space and time, it is possible to obtain RO profiles that are spatially close to CALIPSO footprints but precede or accede the time of the footprint. Using collocations of various time separations, we build composite time series of wave anomalies and cloud frequency to understand how waves are influencing TTL clouds. Finally, we use the Aura Microwave Limb Sounder (MLS) water vapor retrievals (Read et al., 2007) and cloud effective

radius (r_e) retrievals from the CloudSat/CALIPSO 2C-ICE product (Deng et al., 2013) to evaluate whether relative humidity and r_e have connections to gravity waves as shown by P18.

3.2 Data sets

As mentioned in Section 1.4, RO data from multiple satellite missions can be used together as long as they are processed by the same algorithm. Here we use the re-processed atmPrf data set processed by the CDAAC. We use occultations from the following satellite missions: COSMIC (Anthes et al., 2008), Meteorological Operational Polar Satellite A/Global Navigation Satellite System Receiver for Atmospheric Sounding (Metop-A/GRAS) (Von Engeln et al., 2009), Metop-B/GRAS, and the Challenging Minisatellite Payload (CHAMP) (Wickert et al., 2001). The level 2 atmPrf data set provides "dry" profiles of atmospheric temperature derived by neglecting moisture, which is appropriate for TTL altitudes. The atmPrf provides temperature estimates at 30-meter vertical spacing, but the effective resolution of RO is around 200 meters in the tropical tropopause layer (Zeng et al., 2019). The precision of temperature is approximately 0.5 K within 8 to 20 km (Anthes et al., 2008).

CALIPSO is a sun-synchronous, polar-orbiting satellite along the NASA A-Train formation, overpassing the equator at 0130 and 1330 local solar time. Its main instrument, the Cloud-Aerosol Lidar with Orthogonal Polarization (CALIOP), is a dual-wavelength lidar capable of detecting thin clouds with optical depths less than 0.01. We use the Level 2 V4.10 5-km Cloud Layer product for estimates of cloud top and base altitude and the V4.10 5-km Cloud Profile product for detection of clouds in 60-meter vertical bins. The CAD Score in these products is a measure of confidence that the detected feature is correctly classified as cloud. To ensure high confidence that all analyzed features are clouds, our analysis only includes CALIPSO layers and

bins with CAD score at or above 80 (where 100 means complete confidence in the feature being a cloud). Corresponding to the dates when RO data were available, we use nighttime CALIPSO data between 2006 and 2014. Daytime CALIPSO data were excluded due to the lower lidar signal-to-noise ratio of daytime CALIOP observations.

Estimates of r_e come from the 2C-ICE product (Deng et al., 2013, 2015) which is derived jointly using the CloudSat radar and CALIPSO lidar observations. This product provides r_e retrievals at 1-km footprints in 250-m vertical bins. The r_e estimates from 2C-ICE compare well to in-situ flight measurements with a retrieval-to-flight ratio of 1.05 (Deng et al., 2013). For quality control, we only use r_e with uncertainty (given by the re_uncertainty variable) less than 20%. Due to a battery failure, CloudSat left the A-Train formation in 2011. After that it only operated in daytime and its footprint was no longer collocated to CALIPSO. For this reason, we limit our analysis using 2C-ICE to 2007–2010 when nighttime data was available.

The Aura MLS H_2O product provides retrievals of water vapor mixing ratio at pressures at and above 316 hPa with a precision of ~0.2-0.3 ppmv (4-9%) in the stratosphere (Lambert et al., 2007). We use the water vapor mixing ratio to estimate relative humidity with respect to ice (RH_i) using collocated RO temperature. Criteria for data screening follows all recommendations in section 3.9 of the product documentation (Livesey et al., 2017). Although Aura was launched in 2004, the scan of MLS did not align with that of CALIOP until May 2008. For this reason, all analysis involving this product uses data from 2008 to 2014.

3.3 Methodology

3.3.1 Extraction of gravity wave temperature anomalies

Our method for obtaining temperature perturbations (T') due to gravity waves is based on Alexander et al., 2008. Mean temperature profiles are calculated on grid boxes of 20° longitude × 5° latitude × 7 days centered on each day of year. Mean maps are made for each day between 1 Nov 2006 and 30 April 2014. For an arbitrary RO temperature profile, the mean map centered on the same day as the RO profile is used to derive the corresponding mean-state profile through bilinear interpolation of the four grid boxes surrounding the location of the RO profile. T' is then obtained by removing the mean-state from the temperature profile. Since we use a 7-day mean as background, the resulting T' can be thought of as representing variability on timescales less than seven days. After T' is obtained, its vertical gradient is calculated to get dT′/dz. Figure 3.1 shows one example of temperature profile, its corresponding mean-state, and the resulting anomalies T' and dT′/dz.

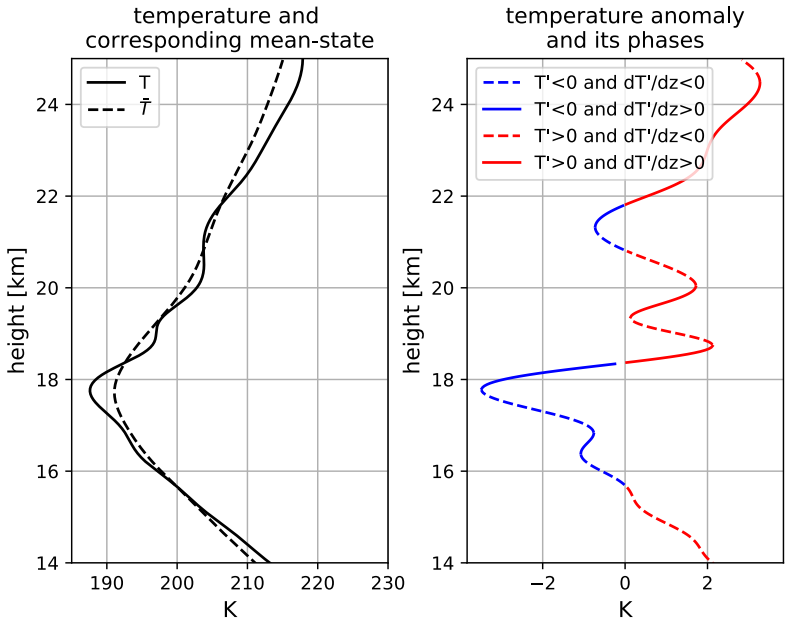

Figure 3.1 (Left) Temperature profile (solid line) from COSMIC at 155° 43' W, 18° 16' N on 1 Jan 2007 and its corresponding mean-state (dashed). (Right) T' of the given profile and its four phases based on the sign of T' and dT'/dz.

3.3.2 Collocation of CALIPSO observations to RO profiles

The primary goal of this work is to study cirrus occurrence and properties in relation to the four gravity wave phases defined in Figure 3.1 To accomplish this we collocate CALIPSO cloud observations to RO temperature profiles. The horizontal weighting of RO retrievals is mostly centered within 200 to 300 km of the perigee (tangent) point (Kursinski et al., 1997) where the ray experiences most bending. For this reason, we use the spatial location of the perigee point as basis for collocation. Since our interest lies strictly inside the TTL and the perigee point of each occultation ray changes with height, we determine the perigee point at the middle of the TTL by

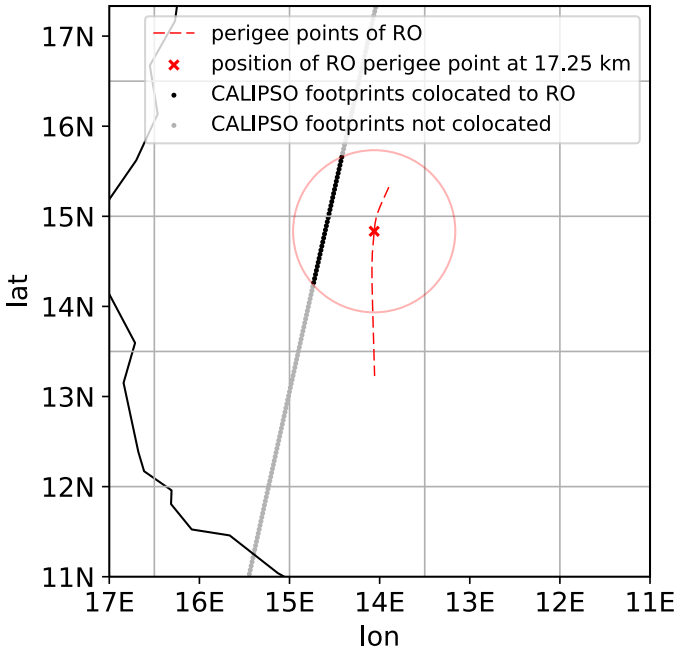

Figure 3.2 Schematic of collocation between RO profile and CALIPSO footprints. The perigee points of the RO profile throughout all altitudes are shown in the red dashed line, while the position of the perigee point in the middle of the TTL (17.25 km) is denoted by the red X. The CALIPSO 5-km product provides estimates of cloud properties at 5-km footprints, and all footprints within 100 km of the red X are collocated to the RO profile, as indicated by the black dots. Gray dots are CALIPSO footprints considered too far from the RO profile and not collocated. The shown RO profile was taken at approximately 0120UTC 2 Jan 2009.

interpolating the longitude and latitude of RO profiles to 17.25 km (middle of TTL defined as the average of 14.5 km and 20 km). Any CALIPSO observations within 100 km of this point are collocated to the RO profile for analysis. Figure 3.2 gives an example of one RO profile, its perigee point at 17.25 km, and the collocated CALIPSO 5-km footprints.

We collocate RO profiles to 2C-ICE cloud retrievals in a similar manner. Unlike the CALIPSO 5-km products, 2C-ICE provides cloud properties at 1-km footprints and vertical bins of approximately 250 m. Other than this difference, the collocation method is identical to that of CALIPSO and RO. In May 2008 the Aura MLS was aligned to within ±10 km of CALIOP. For analysis involving RH_i, for each CALIPSO footprint with a RO collocation, we find the closest MLS footprint to that CALIPSO footprint to calculate RH_i.

3.4 Population of clouds in wave phases

All results below were derived from data within 20° of the equator. For convenience we will refer to the four gravity wave phases as follows. Phase 1: $T'<0$ and $dT'/dz<0$, Phase 2: $T'<0$ and $dT'/dz>0$, Phase 3: $T'>0$ and $dT'/dz<0$, and Phase 4: $T'>0$ and $dT'/dz>0$. Cold and warm phases refer to where $T'<0$ and $T'>0$, respectively. For the analysis presented in this section, the temporal requirement for collocation is that all the collocated data must be within two hours of each other.

As previously mentioned, K16 (their Figure 5) found that a majority of TTL clouds in the ATTREX data were observed in the cold phase and that in the 2014 flight legs over the Western Pacific there was a higher frequency of ice inside $dT'/dz<0$ than in $dT'/dz>0$. Figure 3.3 shows the population of CALIPSO Cloud Profile vertical bins detected as clouds in each wave phase

extracted from collocated RO profiles. Throughout the entire TTL, over 50% of clouds were found in Phase 1. When the cloud population is examined in 1-km vertical layers (14.5 – 15.5 km, 15.5 – 16.5 km, etc.), there is no obvious change with height and most clouds are found in Phase 1 followed by Phase 2 at all heights. Above 16.5 km there is a smaller fraction of clouds in the warm phase. A possible explanation for this may be that there are less convectively detrained clouds as altitude increases, increasing the likelihood of clouds having been formed by gravity waves. In addition, the population in Phase 2 tends to increase with height, with 38% of clouds above 17.5 km in Phase 2. For comparison, using K16's Figure 5 one can infer that for clouds above 16.5 km the cloud fraction in Phase 1, 2, 3, and 4 are 56.25%, 31.25%, 9.375%, and 3.125% (calculated as the percentage in that phase divided by the sum all four phases), and for clouds below 16 km the percentages are 49.3%, 28.17%, 14.08%, and 8.45%. These ratios are similar to our findings, though we find less clouds in Phase 2 below 16 km.

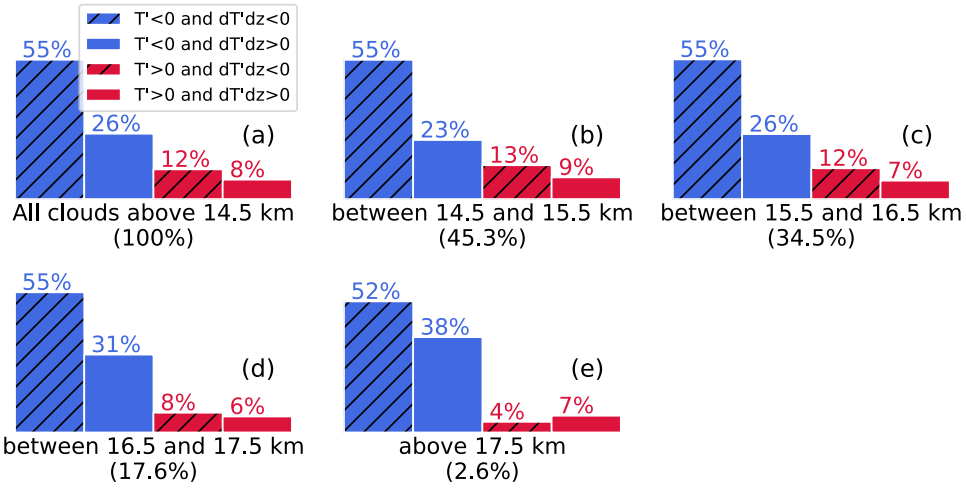

Figure 3.3 Population of CALIPSO Cloud Profile cloud bins inside each wave phase from 1 November 2006 to 30 April 2014. Plot (a) shows the cloud fraction for all of TTL (14.5 to 20 km), while (b)–(e) show the population in four different 1-km layers. The percentage in parenthesis denote the portion of clouds found in that vertical layer relative to all TTL clouds.

Cloud fractions in each phase are separated into six longitudinal belts in Figure 3.4. During December-January-February (DJF), the 120E-180E belt, which covers the Maritime Continent and Western Pacific, has the lowest cloud population in Phase 1 (52%) as well as the most clouds inside the warm phase (24%). Although this region is known for very low tropopause temperatures and high TTL cirrus frequency during boreal winter (Highwood and Hoskins, 1998; Sassen et al., 2009), there is also frequent deep convection (Ramage, 1968) which may generate clouds unrelated to gravity waves. This could partly explain the higher cloud population in warm phases. The influence of convection could also explain the high warm phase population during June-July-August (JJA) in 60E-120E where the Asian Monsoon occurs. In this period and region, 28% of clouds are in the warm phase and 47% is in Phase 1.

Over 180W-120W, which approximately covers the Eastern Pacific, 56% (25%) of clouds fall in Phase 1 (Phase 2) during DJF. This is at odds with K16 who found that in the 2011 and 2013 ATTREX flight legs over the Eastern Pacific there were more clouds in Phase 2 than in Phase 1. The 2011 flights were conducted in October and November while the 2013 flights were in February and March. Plots similar to Figure 3.4 made from data in Oct–Nov yielded Phase 1/2 populations of 63%/24% while Feb-Mar yielded 58%/20%. Over this region we were not able to find Phase 2 having more clouds as K16 did. It is not clear what causes this difference. Their T' were calculated as the difference between aircraft in-situ temperature and 30-day mean temperature derived from RO. Since the vertical resolution of in-situ temperature measurements is different than that of RO, this may be one cause of the contrasting findings. Their choice of 30-day instead of the 7-day mean implemented here may also cause differences.

Using the cloud top and base heights from the CALIPSO Cloud Layer product we calculate the vertical cloud fraction in each wave phase, defined as the amount of vertical

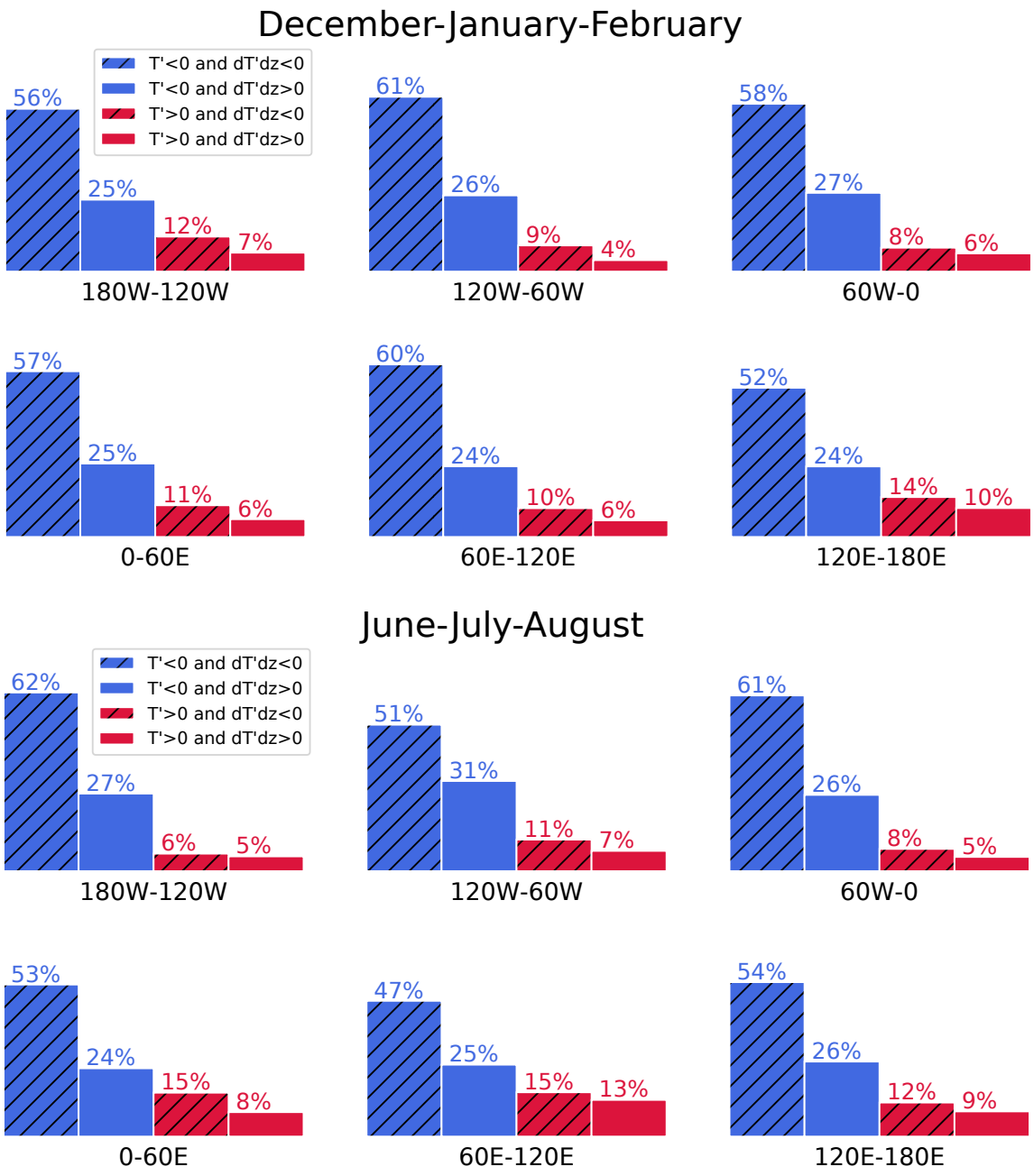

Figure 3.4 Same as Figure 3.3(a) except for different longitudinal belts. Top six plots are for December-January-February and bottom six plots are for June-July-August.

overlap between the cloud boundaries and the temperature profile segments in Figure 3.1 corresponding to each phase. The distributions of vertical cloud fraction are shown in Figure 3.5. In this figure we only consider clouds with base above 14.5 km and wave phase segments whose

base height lie within 14.5 and 18.5 km. In phases of positive dT'/dz, the number of samples tend to decrease as cloud fraction increases. This trend doesn't apply for negative dT'/dz, and in Phase 1 there is a clear increase of samples with increasing cloud fraction. The difference in trend is rather large since the ordinate is in log-scale. It is interesting that even in the warm phase, regions of negative dT'/dz are more likely to take on larger values of cloud fraction compared to regions of positive dT'/dz, though in comparison the role of dT'/dz seems to be stronger in the cold phase. Overall, Phase 1 is most distinct as it has most samples with cloud fractions of unity and it significantly favors higher values of vertical cloud fraction.

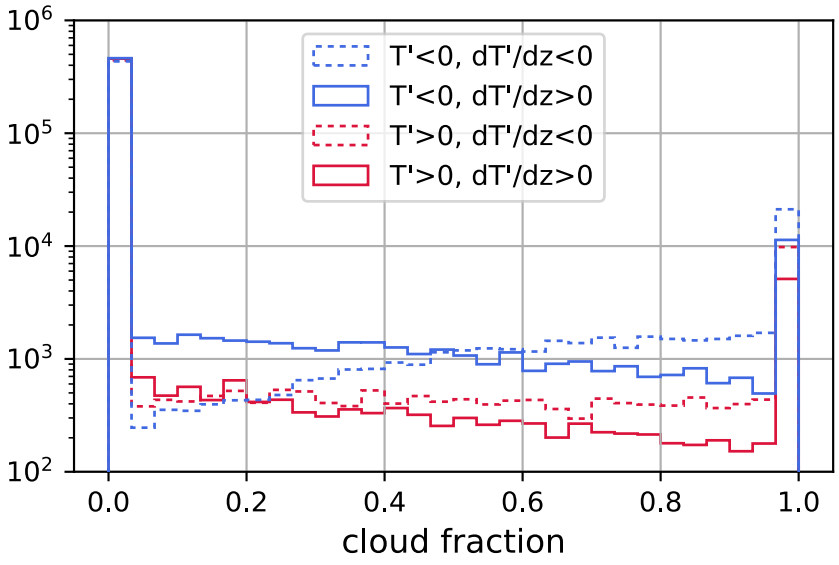

Figure 3.5 Distribution of vertical cloud fraction in each gravity wave phase. Note that the ordinate is in log-scale. Blue and red colored lines indicate the cold and warm phase, respectively, while the solid and dashed lines represent dT'/dz>0 and dT'/dz<0.

3.5 Composite time evolution of wave anomalies and cirrus occurrence

Since COSMIC observations are pseudo-random in time and space, it is possible to collocate CALIPSO observations with RO soundings close by but having varying offsets in time. By binning the temperature profiles according to the time offsets, we can make a composite of T' showing the mean time evolution of wave anomalies relative to the cloud observation. Such an approach of creating composite time series has been used to study the thermodynamic budget before and after tropical convection (Masunaga, 2012; Masunaga and L'Ecuyer, 2014) and temperature anomalies associated with tropical deep convection (Paulik and Birner, 2012).

Unlike Section 3.4, where we require that the collocated RO and CALIPSO observations be within two hours of each other, in this section the time difference between the two can be up to 35 hours. We bin RO profiles in time bins of -35 – -33, ..., -1 – 1, ... 33 – 35 hours relative to the CALIPSO observations, where a negative value indicates that the collocated RO profiles precede the CALIPSO overpass. Composites of T', dT'/dz, and buoyancy frequency (N^2) anomaly for all collocations in 2006 to 2014 are shown in Figure 3.6. In making these composites we only include clouds with base above 14.5 km. Also, for statistical testing, we need the RO profiles used in each time bin to be unique. For this reason, only the CALIPSO footprint closest to the RO profile is used so that there is a one-to-one pairing between the cloud and RO profile. If this is not done, then the same RO profile may be reused several times due to the multiple collocated CALIPSO footprints as shown in Figure 3.2.

In the T' composite of Figure 3.6, the strongest cold anomaly is found close to the cloud top and is coldest near hour 0. The cold anomaly contour with value below -0.6 K lasts approximately from -15 to +6 hours and migrates downward with time, consistent with the

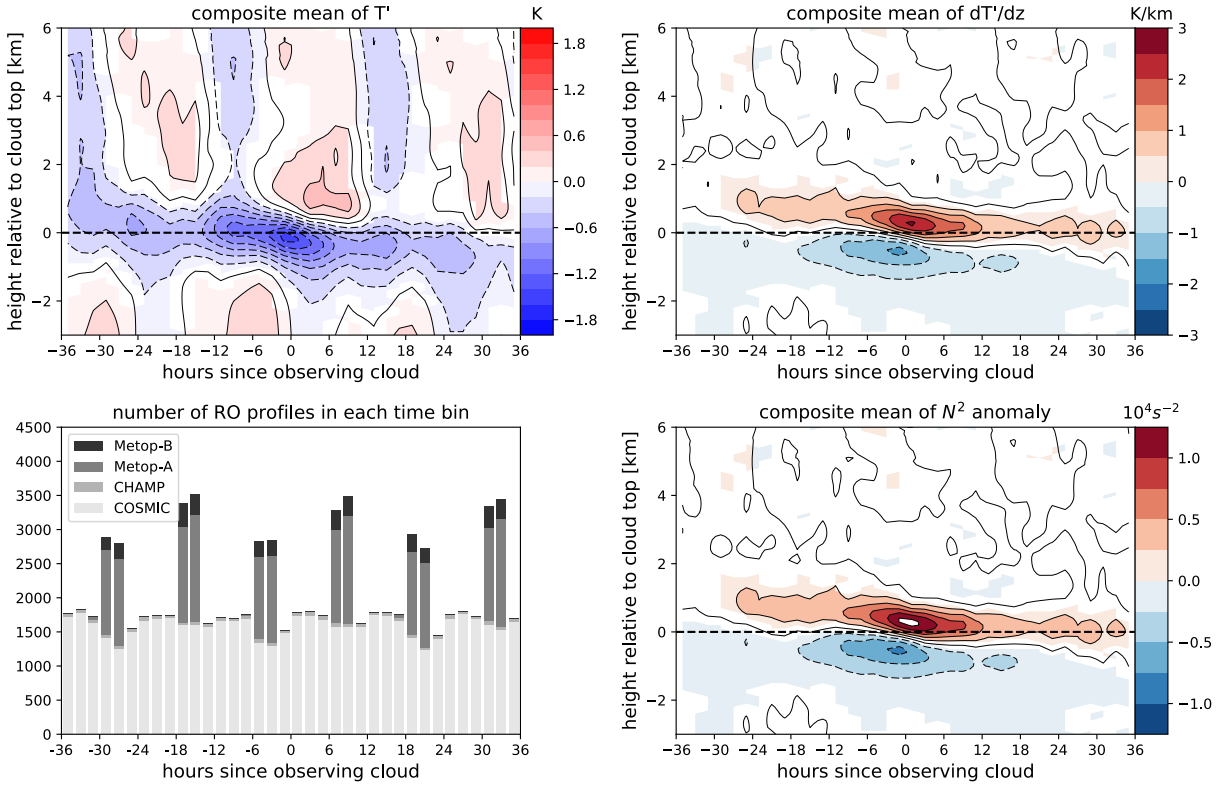

Figure 3.6 Composite of T' (top left), dT'/dz (top right), and buoyancy frequency (N^2) anomaly (bottom right) in height coordinate relative to cloud top. Colored contours in these three plots are at or above the 95% significance level according to the Student's t-test. Solid (dashed) contours represent positive (negative) anomalies and are at the same intervals as the colored contours. The abscissa denotes the time offset between the CALIPSO observation and RO sounding. The bottom left plot shows the number of unique RO profiles in each 2-hour time bin used to calculate the composites.

property of gravity and Kelvin waves with upward group velocity. The alternating cold-warm anomaly at heights of 2 to 6 km should be due to the diurnal tide (Zeng et al., 2008; Pirscher et al., 2010) since we are compositing only on nighttime data from CALIPSO which always overpasses the equatorial region at similar local times. The number of samples in each time bin has a 12-hour periodicity mainly due to Metop-A/B. When only using COSMIC observations to make Figure 3.6 the anomaly patterns are largely the same, so the periodicity does not affect the composites.

It is noteworthy that the mean cold anomaly is centered on cloud top and not inside the cloud. This leads to a dipole structure in dT'/dz and buoyancy frequency anomalies with positive anomalies just above the cloud top and negative anomalies below. This structure shows that the inside of clouds (below cloud top) is likely to have negative dT'/dz, corollary to the finding by K16 and Figure 3.3 that a majority of clouds are found in Phase 1. Although this structure implies weakened stability (negative N^2 anomaly) inside the cloud, it is unclear whether this decreased stability has connections to cloud formation or maintenance. Since negative dT'/dz also corresponds to upward vertical motion anomalies (assuming that these anomalies are from gravity waves), further study is required to separate the role of vertical motion and stability in how gravity and Kelvin waves influence TTL clouds.

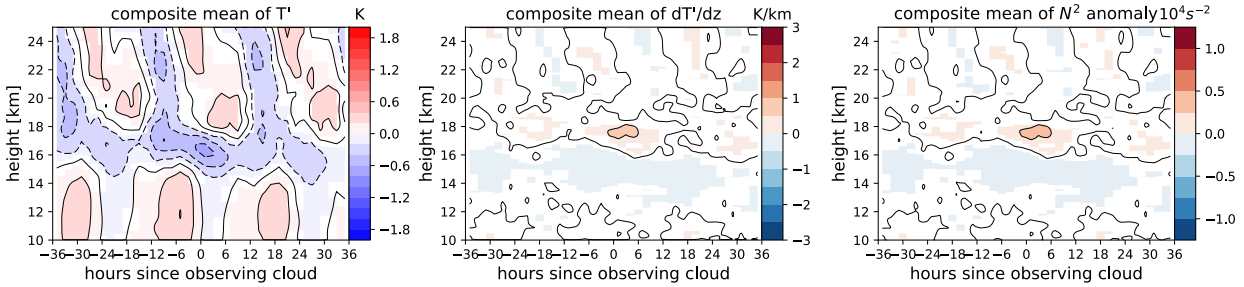

Figure 3.7 Same as Figure 3.6, except the composites are evaluated with respect to height above mean sea level instead of cloud top. Colored contours are at or above the 95% significance level according to the Student's t-test. Contour levels are identical to Figure 3.6.

Figure 3.7 is similar to Figure 3.6 except the anomalies are not composited relative to cloud top but rather on height above mean sea level. In this composite, there are cold anomalies within 16 to 18 km, but the magnitude is weaker than that of Figure 3.6. This leads to weak anomalies in dT'/dz and N^2. We conclude that gravity wave anomalies in Figure 3.6 are physically significant and have a close association with the vertical position of TTL cloud tops.

According to the relationship between vertical velocity and temperature anomalies based on linear wave theory, dT'/dz<0 corresponds to where the vertical velocity anomaly is positive. P18 argues that the upward vertical velocity in Phase 1 slows down the descent of ice crystal and suspends them inside Phase 1. Since Figure 3.6 depicts a downward propagation of wave anomalies, it is of interest to investigate whether the phase propagation of gravity waves also "carries'" clouds downward. We can explore this possibility through a similar compositing technique employed above. Instead of centering on the CALIPSO footprint, we centered on the time of RO sounding, and use the CALIPSO cloud product to calculate the cloud frequency in each 2-hour time bin. And instead of compositing relative to cloud top height, we composite on the altitude of the *local* minima or maxima of T'. A schematic of this compositing approach is given in Figure 3.8.

In the example shown in Figure 3.8(a), at day i there is a collocated RO sounding that occurred within 100 km of the CALIPSO footprint but Δt_i hours after. The position of the cloud top and base is evaluated relative to a local T' minimum, as shown by the magenta lines. Since the CALIPSO overpass occurred before this RO profile, in the compositing (shown in Figure 3.9(b)) the observed cloud position is used to calculate the cloud fraction at Δt_i hours *before* the RO sounding. The cloud fractions are calculated on a grid of 50-m height and 2-hour time bins. For the collocation pair in Figure 3.8(a), the cloud fraction in the time bin corresponding to $t = -\Delta t_i$ is calculated according to how much each vertical bin overlaps with the interval $[h_i^{(b)}, h_i^{(t)}]$. If the collocated CALIPSO footprint has no clouds with base above 14.5 km, cloud fractions of zero are still tabulated in the appropriate time bin at all heights. Since any RO profile most likely has multiple local minima, the tabulation of cloud fraction is repeated for each local minimum in a T' profile. The exact same procedure is also conducted for local maxima to create a separate

cloud frequency composite. To focus on TTL clouds we only include clouds with base at or above 14.5 km. Also, we only consider local T' extrema within 14.5 to 18.5 km since a majority of TTL clouds are inside this height range.

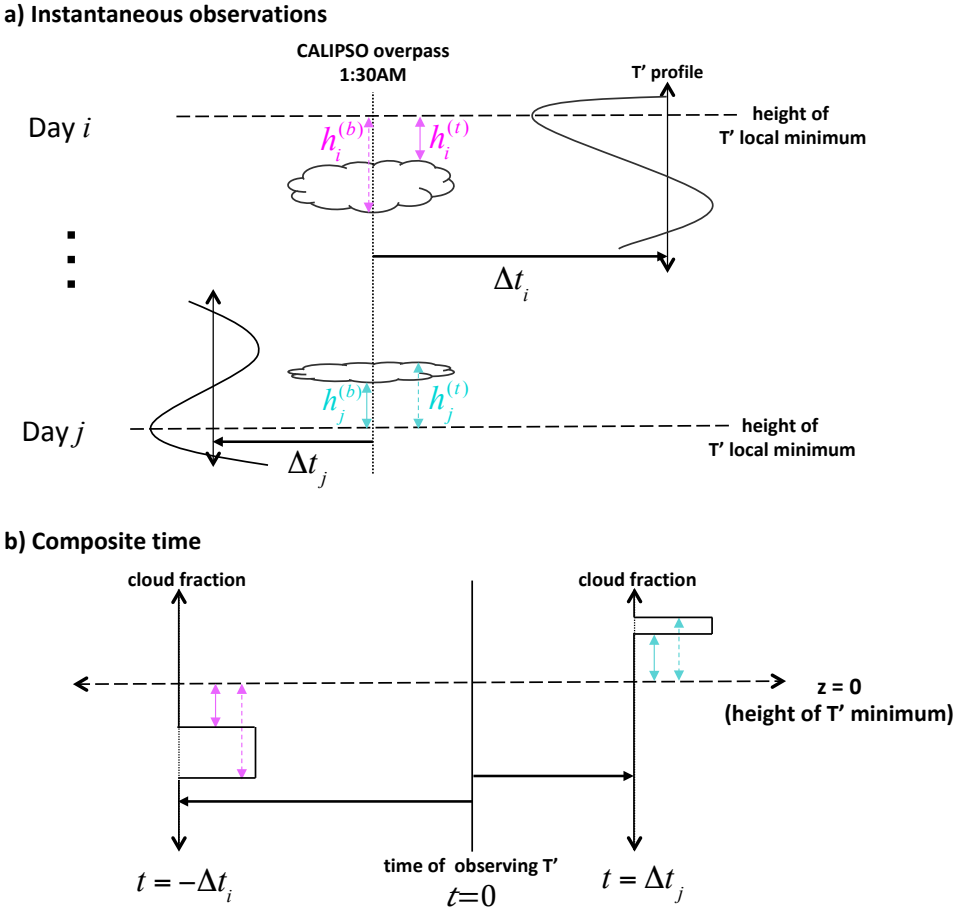

Figure 3.8 Schematic for creating the composite temporal evolution of cloud frequency with respect to T' minima. In this example, as shown in (a), during day *i* there is a collocated pair of CALIPSO and RO observations. The RO observation occurs Δt_i hours after that of CALIPSO, and the vertical distance between the height of local T' minimum (dashed horizontal line) and the cloud top (base) is depicted by the dashed (solid) magenta lines with length $h_i^{(t)}$ ($h_i^{(b)}$). For the temporal compositing (b), inside the time bin corresponding to Δt_i hours before observing T', the cloud fraction is calculated according to how much each vertical bin overlaps with the interval $[h_i^{(b)}, h_i^{(t)}]$. The same procedure is carried out for the collocated pair at day *j*. Also see text for explanation.

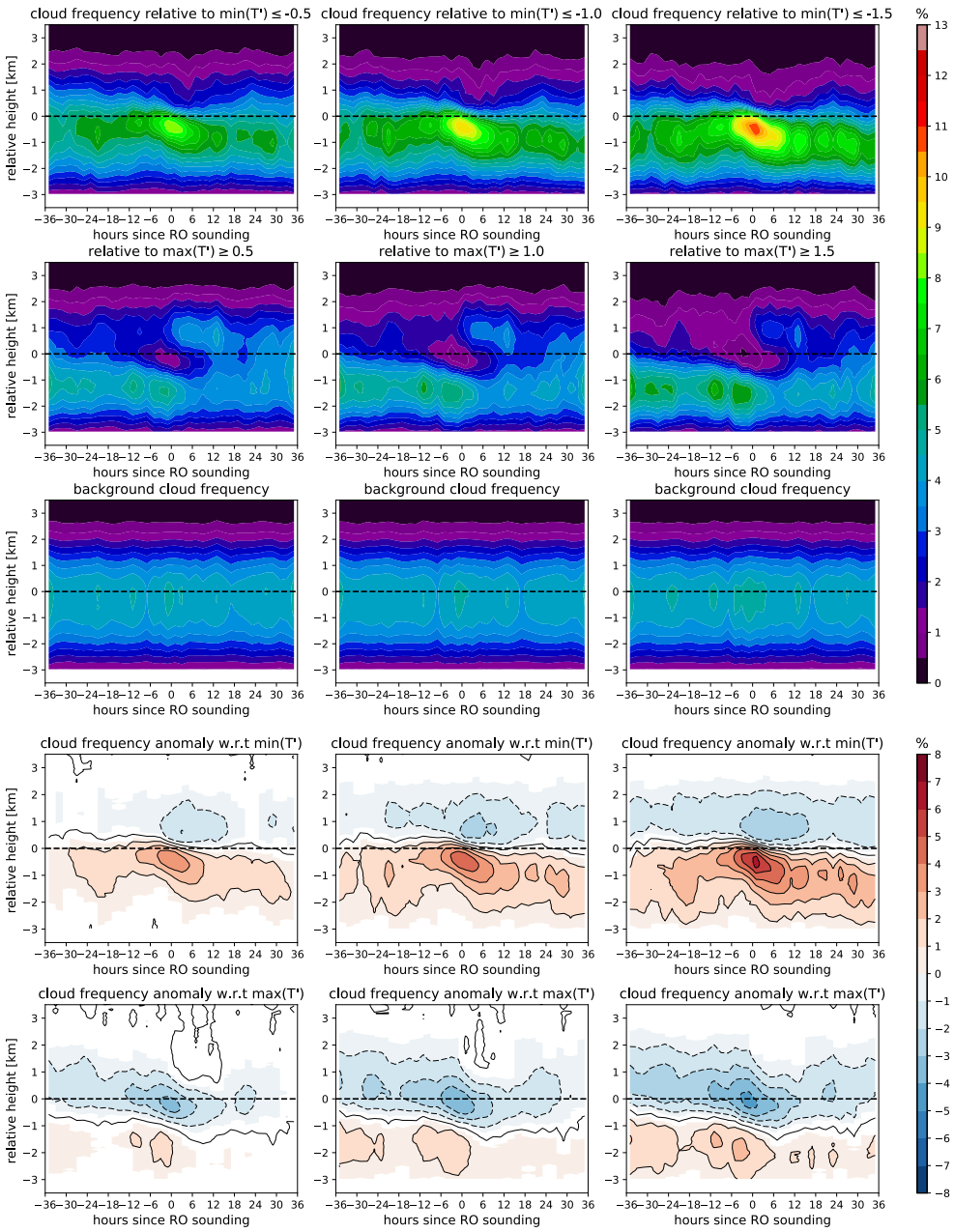

Figure 3.9 Composite of cloud frequency with respect to local minima (first row) or maxima (second row) of T'. The columns correspond to composites made from subsets of T' extrema with magnitudes greater or equal to 0.5 K (left column), 1.0 K(middle), and 1.5 K (right). Dashed horizontal indicates the position of the local T' extrema. The third row shows the background frequency (see text for explanation). The fourth and fifth rows are the cloud frequencies anomalies associated with cold or warm anomalies, calculated as the difference between the cloud frequency composites and the background cloud frequency. Contours in the bottom two rows are at intervals of 1% (dashed negative), matching the filled color contours which show values at or above the 95% significance level.

The composites of cloud frequency made this way, shown in the top two rows of Figure 3.9, can be interpreted as the likelihood of finding clouds in the vicinity of local T' extrema. The plotted values represent the mean cloud fraction in each time-height bin. The first and second row are the cloud frequencies relative to min(T') and max(T') (local minima and maxima), respectively, and each column is produced from a different subset of T' extrema based on magnitude ($|T'| > 0.5$, 1.0, or 1.5). Beneath the vertical position of min(T') minima we find a lobe of enhanced cloud frequency and this becomes more evident as min(T') decreases. Likewise, in the vicinity of max(T') the cloud frequency is reduced, and this reduction also shows dependence on the magnitude of max(T'). Both the increased and decreased cloud frequencies have a downward trend consistent with the expectation that wave phases propagate downward with time. However, it is hard to quantitatively know which parts of these plots are true anomalies. For this reason, we devise a way for extracting the anomalies in these patterns and for statistical testing, as described below.

The cloud frequency composites in the top two rows of Figure 3.9 are made using the altitude of the T' extrema as the zero height. To generate a composite where the vertical position of T' extrema has no relationship with the cloud top/base height, for each T' extremum we generate a random altitude using uniform distribution unif(14.5,18.5) and make a separate cloud frequency time-height section with the random altitude as zero height, shown in the third row of Figure 3.9. These plots can be interpreted as the cloud frequency distribution one would expect if the vertical position of T' extrema has no connection to cloud top/base height. Then the statistically significant differences between the first/second row and the third row may signify a connection between wave anomalies and cloud occurrence. The distribution of cloud fraction in each time-height bin is similar to those shown in Figure 3.5 and therefore is not Gaussian, so the

Student's t-test cannot be used here. We use the two-sided two-sample Kolmogorov-Smirnov test (K-S test) (Hollander et al., 2015) which does not make any assumptions about the data distributions. This test can be used to evaluate whether two continuous or discrete probability distributions differ from each other. The K-S test is employed to compare the discrete cloud fraction distribution in each time-height bin of the first/second row to the same bin in the third row. The null hypothesis is that the first/second row is not different than the randomly generated cloud frequency pattern in the third row.

The fourth row of Figure 3.9 is the first row minus the third row, depicting the anomalies associated with min(T'), and similarly the fifth row shows the anomalies associated with max(T'). Colored portions of the contour denote regions with $p<0.05$ (95% confidence) as estimated from the K-S test. In these anomaly patterns it is confirmed that there is enhanced cloud occurrence below min(T'), and, in addition, a weak reduction of cloud occurrence above it. For the subset of min(T')<0.5, the positive cloud frequency anomaly peaks at 3% whereas for min(T')<1.5 it peaks at 6%. The anomaly patterns due to max(T') also exhibit a dipole structure with negative anomalies centered on the altitude of max(T') and a weak positive anomaly below. The negative anomalies associated with max(T') show dependence on the magnitude of max(T'), although the variation is not as large compared to that of min(T'). Both positive/negative anomalies associated with min(T')/max(T') tend to migrate downward in time, although this trend is slightly more apparent in the enhanced cloud occurrence of min(T').

A notable difference between min(T') and max(T') is that the positive anomalies in min(T') occur below the altitude of min(T') while the negative anomalies in max(T') are centered on it. Despite Figure 3.5 suggesting that positive dT'/dz may favor clouds even in the warm phase, such an effect is not apparent in these composites and the eroded cloud frequency due to

the warm phase appears more or less symmetric about max(T'). In the cold phase, Phase 1 statistically dominates the signal in the increased likelihood of finding TTL clouds. Although the predictions of P18 suggests that it may be more likely to find clouds in Phase 2 under low background RH_i, this global analysis suggests that on average the role of Phase 1 in facilitating TTL clouds is dominant.

3.6 Comparing satellite-observed features to theoretical predictions

We want to evaluate whether P18's theoretical predictions are consistent with satellite observations. P18 suggests that (1) ice crystals within a confined range of r_e are suspended mostly in Phase 1 and partially in Phase 2, and (2) *background* relative humidity with respect to ice (RH_{ic}) influences the phase at which ice crystals are suspended. These two features are depicted in their Figure 2. We examine r_e and RH_{ic} in observations to see whether these quantities exhibit any connections to gravity waves. Although here we present analysis motivated by P18, we note that their study assumes no background wind in their derivations and simulations.

Figure 3.10 shows normalized r_e distributions in the four wave phases as well as their mean and standard deviation. The collocated r_e and temperature data are within two hours of each other. In making this plot we only use nighttime 2C-ICE data, since the information toward thin cirrus are mostly from lidar backscatter. Clouds above 17.5 km were omitted in this plot due to the low samples (~0.6% of all TTL clouds). The distributions for all phases are very similar regardless of height. At 14.5–15.5 km and 15.5–16.5 km, the r_e distribution of Phase 1 has a higher peak near 16 μm. Above 16.5 km this peak is not evident, but the Phase 1 distribution has

higher values around 15 μm and lower values between 20 to 25 μm, slightly differentiating Phase 1 from the other phases. The mean r_e of Phase 1 is lower than all other three phases at all vertical layers, but the differences are small. In summary, characteristics of r_e found here are qualitatively consistent with P18's findings, as Phase 1 tends to have a relatively larger number of ice particles localized around a certain r_e value (~16 μm in this case). However, we note that retrieving r_e of thin cirrus is difficult and more research is needed to explore the r_e distribution in gravity waves phases using a variety of observations.

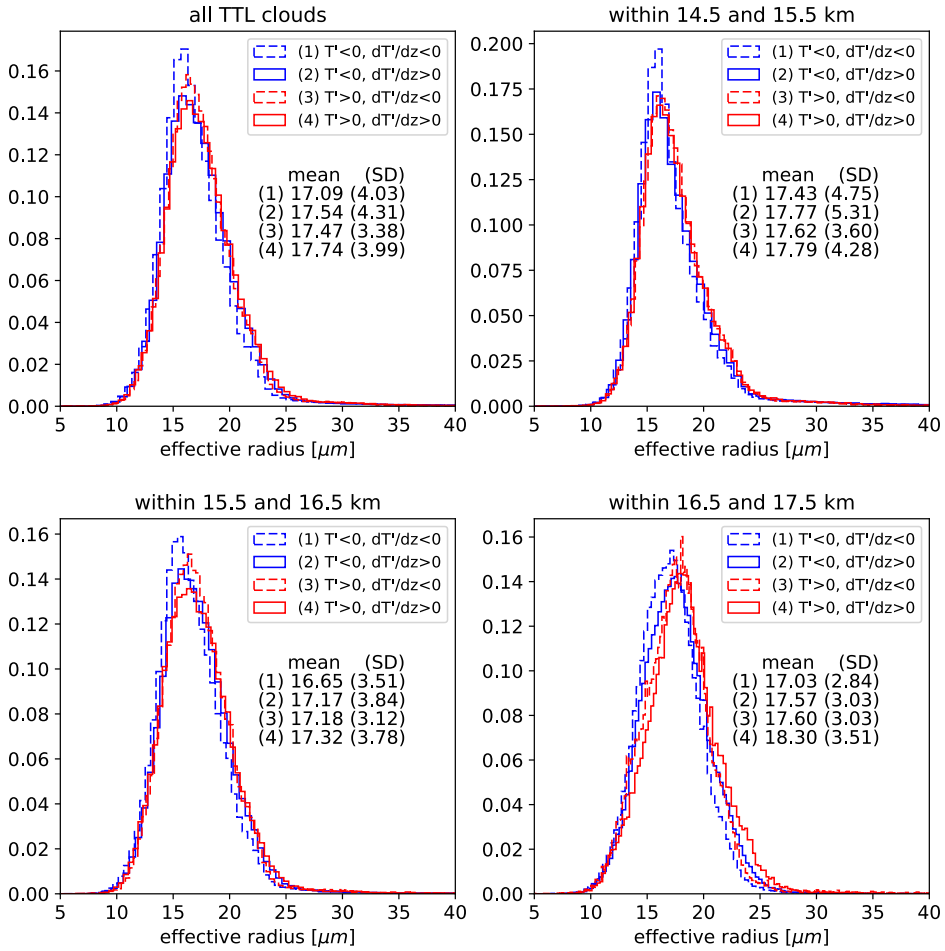

Figure 3.10 Normalized density function of r_e in each gravity wave phase for all of TTL (top left) and 1-km vertical layers (top right and bottom row). The mean and standard deviation (SD) are given in the legend.

As discussed in Section 3.4, K16 found that in the 2011 and 2013 ATTREX flight legs over the Eastern Pacific there were slightly more clouds in Phase 2 than Phase 1, whereas in the 2014 flights over the Western Pacific Phase 1 contained the majority of clouds. P18 argues that this may be due to the relatively low RH_{ic} of the TTL over the Eastern Pacific. P18 solved a simplified set of equations describing the interaction of gravity wave perturbations and ice particle growth/sedimentation. Comparison of the solution using values of RH_{ic}=0.85 or 0.64 (to represent Western and Eastern Pacific, respectively) showed that the former results in the ice crystals being suspended in Phase 1 where in the latter ice particles were situated closer to the T' minimum which may result in a portion of particles to be inside Phase 2. Motivated by these results we collocate the MLS water vapor retrieval to CALISPO and RO data to evaluate whether observations suggest a similar dependence on RH_{ic}.

For each CALIPSO Cloud Profile vertical bin identified as cloud, the water vapor mixing ratio from the Aura MLS product is log-interpolated (as suggested by the product documentation) to the height of the cloud bin. To evaluate the background saturation mixing ratio, we interpolate the *7-day mean temperature* to the cloud height since we are interested in the RH_{ic} instead of the actual RH_i (which would include wave influence). The Goff-Gratch equation (Goff and Gratch, 1946) is used to get the saturation vapor pressure, and subsequently the saturation mixing ratio and then RH_{ic}. Figure 3.11 shows the cloud population in each phase partitioned by RH_{ic} values. The subsets with RH_{ic} below 60%, 60% –80%, and above 180% tend to have less clouds in Phase 1 compared to the other RH_{ic} categories. The intermediate values of RH_{ic} (between 80% to 140%) yielded the highest fraction in Phase 1. Qualitatively, this is somewhat consistent with P18 since there are more clouds in Phase 2 for the lowest two RH_{ic} categories, but the dependence on RH_{ic} has no clear trend. We conclude that our analyses on r_e

and RH_{ic} has some qualitative consistency with P18 but does not prove or disprove P18's assertions.

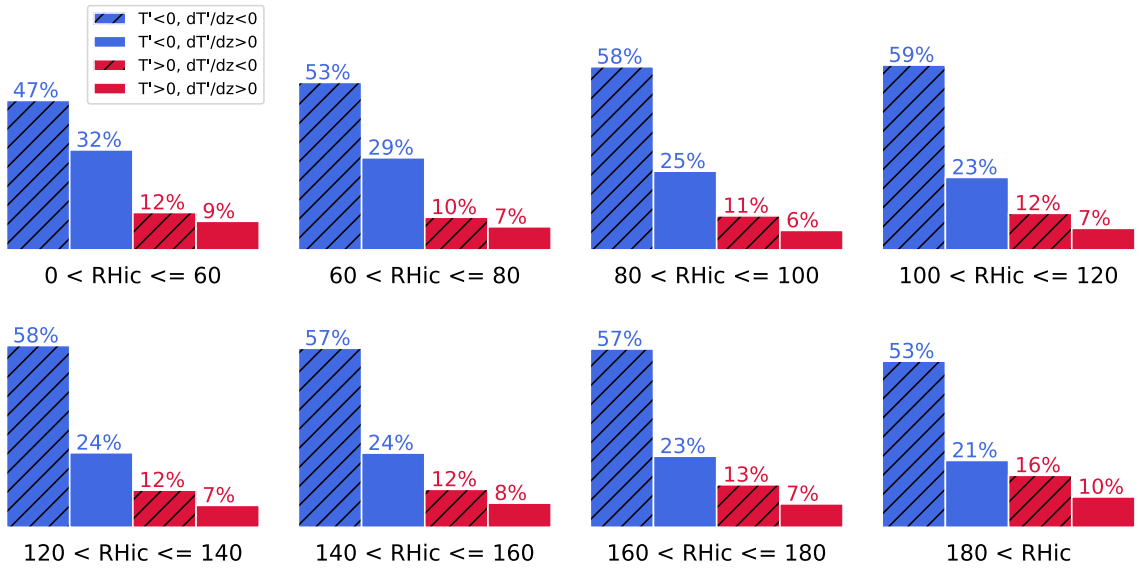

Figure 3.11 Fraction of TTL clouds inside each wave phase categorized by background relative humidity with respect to ice (RH_{ic}).

3.7 Chapter summary

This study uses multiple satellite data sets to evaluate the influence of gravity wave perturbations on TTL cirrus clouds. With a focus on understanding the role of dT'/dz, the vertical gradient of the gravity wave temperature perturbation T', we extract T' and dT'/dz from RO observations and collocate them to clouds observed by CALIPSO to evaluate cloud occurrence relative to wave anomalies. Similar to the results of K16, we find that the phase where T' and dT'/dz are both negative (Phase 1) is most frequently occupied by TTL clouds. The second most populous phase is where T'<0 and dT'/dz>0 (Phase 2), followed by where T'>0 and dT'/dz<0 (Phase 3) and then

T'>0 and dT'/dz>0 (Phase 4). We show that this relation among the four phases is more or less invariant with height or longitude.

A mean view of the temporal evolution of wave anomalies with respect to clouds is constructed by taking advantage of RO's pseudo-random distribution in time and space. We collocate CALIPSO cloud observations to RO soundings that occur before and after the CALIPSO observation, and by averaging a large number of observations with different time separations, a composite time series of wave anomalies is presented. These composites illustrate that, on average, the strongest cold anomaly due to gravity waves tends to be centered on the height of cloud top, and this cold anomaly descends with time consistent with the downward phase propagation of gravity and Kelvin waves having upward group velocity.

In the cloud frequency composites made with respect to local T' minima or maxima, we find that the decrease of cloud likelihood in the warm phase does not show clear dependence on the sign of dT'/dz. This is distinct from the cold phase, where cloud likelihood is increased mainly below min(T') where dT'/dz is negative. In terms of wave vertical velocity anomalies (w'), this portion has positive w' and is just above where the w' is at a maximum. Together with existing studies, this result adds support to the idea that Phase 1 facilitates cloud formation and/or maintenance. Although the downward migration of the increased cloud frequency may be due to ice sedimentation, this cannot be the case for the decreased cloud frequency associated with the warm phase. Hence the downward migration of increased/decreased cloud frequency in the temporal composites is most likely due to waves with downward phase propagation. We also show that the positive or negative cloud frequency anomalies strengthen with increasing magnitude of T' minima or maxima, giving evidence on a global scale that the wave amplitude is connected to the probability of cloud occurrence.

Finally, an assessment of the theoretical predictions by P18 is attempted here using satellite estimates of r_e from 2C-ICE and RH_{ic} based on the Aura MLS H_2O product. Among all phases, r_e are distributed similarly but the distribution of Phase 1 had a slightly sharper peak than the other three phases and also a slightly smaller mean r_e. The partitioning of cloud population among the four phases showed some variation with different values of RH_{ic}, with Phase 1 having less clouds at very low or very high RH_{ic}, but no clear trend is identified. In summary, our satellite-based analysis has some qualitative consistency with the results of P18 but is insufficient for verifying their conclusions.

This study adds to previous findings showing that Phase 1 has a distinct connection to TTL clouds. The results of K16, based on aircraft data limited to specific regions and time span, have been extended by our study which shows that the large amount of clouds in Phase 1 is a general characteristic of the TTL. Based on our composite analysis, the connection between wave anomalies and cloud occurrence is evident: cold anomalies are associated with the position of cloud top, and the amplitude of T' influences the increase or decrease in cloud frequency. The purpose of constructing a composite temporal evolution by piecing together collocated temperature and cloud observations is an attempt to study processes occurring on a timescale typically unobserved by satellites. Although the resulting composites are not true time series, the anomalies patterns depict signatures consistent with wave propagation and enhances our understanding of how waves are connected to TTL clouds.

Due to the spatial and vertical resolution of the RO technique, the waves analyzed here have relatively large wavelengths and low frequencies. It remains to be explored whether the Phase 1 of high-frequency waves are also distinct from other phases. Also, possible explanations for Phase 1 favoring clouds remain an open question. Since negative dT'/dz corresponds to a

positive cooling rate (due to downward phase propagation as explained by K16), weakened stability, as well as upward vertical motion wave anomalies (according to the polarization relationships), whether one has a stronger role in favoring clouds needs to be better understood.

Chapter 4

Influence of clouds on the radiative heating and residual circulation of the upper troposphere and lower stratosphere

4.1 Introduction

Wave breaking in the midlatitude middle atmosphere leads to a "suction pump" effect that causes ascent in the tropics and descent in the polar regions. Since the resulting tropical ascent is adiabatic, air cannot cross isentropes purely due to this process. However, upward transport through the TTL is evident in the "tape recorder" of water vapor demonstrated by Mote et al (1996) (Figure 1.3). This is possible because radiative heating in the tropical lower stratosphere balances the ascent due to the Brewer-Dobson circulation (BDC). The relationship between radiative heating and vertical motion of the BDC can be seen in Figure 4.1. The spatial pattern of heating is very similar to that of the BDC vertical velocity. At both 70 hPa and 100 hPa there is a belt of upwelling centered on the tropics, representing the upwelling portion of the BDC. The location and seasonal cycle of the upwelling belt correspond well to the region of positive radiative heating. The rate of radiative heating or cooling is determined by the local air composition, temperature, and also by the presence of clouds in the atmospheric column. This chapter focuses on the effects of clouds on the UTLS radiative heating and how these effects may imprint onto the shallow branch of the BDC, which consists of the tropical upwelling and meridional transport in the lower stratosphere (as seen in Figure 1.4).

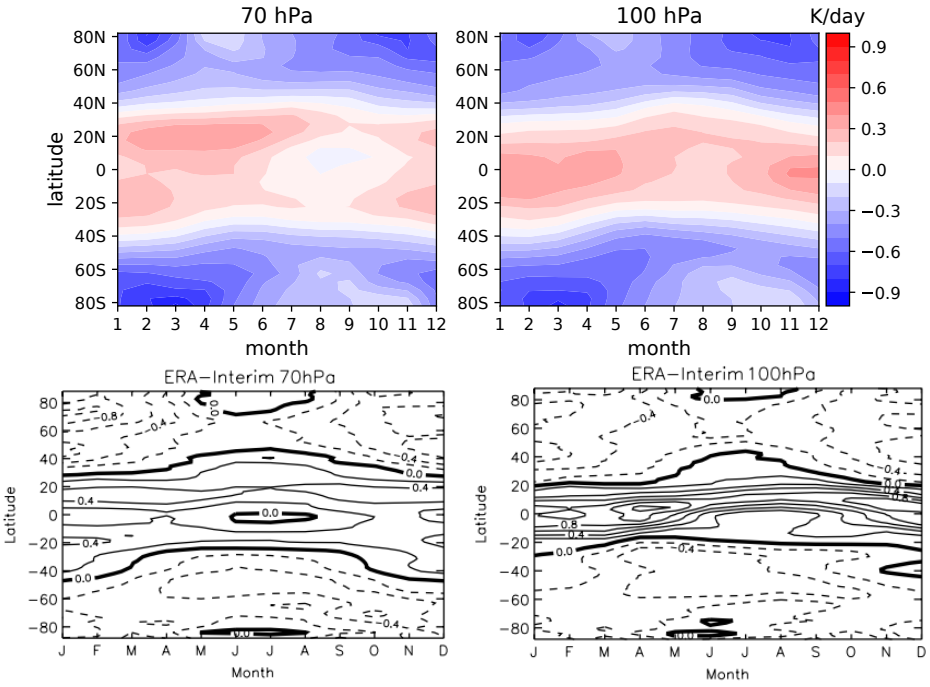

Figure 4.1 (Top row) Mean radiative heating rates at 70 hPa (left) and 100 hPa (right) in 2007–2010 calculated using 2B-FLXHR-LIDAR**.** (Bottom row) Vertical velocity of the Brewer Dobson circulation diagnosed using ERA-Interim data in 1989-2009 (Seviour et al., 2012); contours are in mm/s, dashed negative.

4.2 Data sets

4.2.1 2B-CLDCLASS-LIDAR and 2B-FLXHR-LIDAR

CloudSat (Stephens et al., 2008) flies along the NASA A-Train satellite formation and profiles clouds using its 94-GHz Cloud Profiling Radar (CPR) with a minimum sensitivity of -30 dBZ. From 2007 to 2010, CloudSat and CALIPSO footprints were collocated, observing the same locations within 15 seconds of each other. While CALIPSO is able to detect thin clouds, its lidar signal cannot penetrate cloud layers with optical thickness greater than ~3. On the other hand, CloudSat cannot observe very thin clouds but can completely profile very thick clouds such as deep convective clouds. Multiple retrieval data sets take advantage of this synergy to characterize the atmospheric column. Due to a battery failure CloudSat left the A-Train

formation in early 2011. After that it only operated in daytime and its footprints were no longer collocated to CALIPSO. For this reason, in all chapters we limit the usage of CloudSat/CALIPSO to the period of 2007–2010. Also, due to the orbit of the A-Train, CloudSat/CALIPSO do not obtain observations above 82°N/S.

The 2B-CLDCLASS-LIDAR algorithm (Sassen et al., 2008; Sassen et al., 2009) classifies cloud scenes into eight types: cirrus, altostratus, altocumulus, stratus, stratocumulus, cumulus, nimbostratus, and deep convective clouds. The classification is based on a fuzzy-logic approach taking in account the cloud altitude, temperature, optical properties, as well as the clouds' horizontal and vertical morphology.

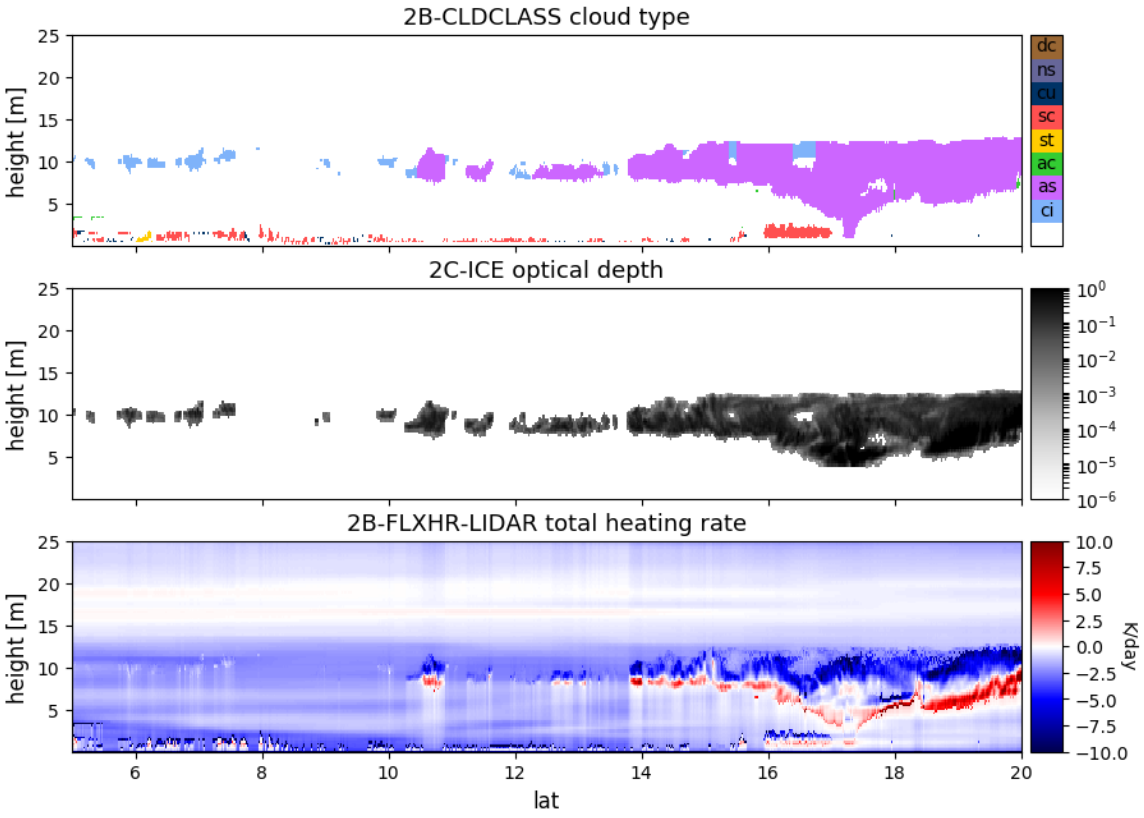

Figure 4.2 Height-latitude sections of 2B-CLDCLASS-LIDAR cloud classification (top), 2C-ICE ice cloud optical depth (middle), and 2B-FLXHR-LIDAR radiative heating rates.

The 2B-FLXHR-LIDAR (Henderson et al., 2013) product provides estimates of vertically-resolved radiative heating in 250-meter vertical bins as well as radiative fluxes at the top-of-atmosphere and surface. This algorithm ingests cloud properties derived from CPR and CALIOP and meteorological variables from ECMWF analysis to perform radiative transfer calculations with the BugsRad model. Figure 4.2 shows an example of radiative heating rates from 2B-FLXHR-LIDAR and the corresponding cloud types from 2B-CLDCLASS-LIDAR and cloud optical depth from 2C-ICE.

4.2.2 Radio occultation temperature profiles

Solving for the residual circulation through radiative heating rates requires the global distribution of potential temperature. In this chapter, the level 2 atmPrf RO temperature profiles are used to obtain the potential temperature in the UTLS. A description of RO can be found in Section 1.5. Corresponding to the CloudSat/CALIPSO data, RO profiles from 2007 to 2010 are used here.

4.2.3 MERRA-2 reanalysis

The Modern-Era Retrospective analysis for Research and Applications, Version 2 (MERRA-2) is generated from the NASA Goddard Earth Observing System (GEOS) version 5 and is available for all dates between 1 January 1980 and the current date. The model-level fields of MERRA-2 are available on 72 vertical layers between 0.01 hPa and the surface, and the native horizontal resolution is 0.5° × 0.625°. We use the radiative diagnostics *tavg3_3d_rad_Nv* for air temperature tendencies due to shortwave and longwave radiation. In addition, we use the daily average of model-level pressure, temperature, and winds, which are available from the

inst3_3d_asm_Nv data collection. To match the 2B-FLXHR-LIDAR data set we use MERRA-2 reanalysis from 2007 to 2010.

4.3 Effect of clouds on TTL radiative heating rates

Gettelman et al. (2004) has shown that clouds tend to reduce the upwelling longwave radiation, resulting in a weaker radiative heating rate in the TTL. Although the high shortwave albedo of clouds also increases the upwelling shortwave and in turn increases the UTLS shortwave radiative heating rate, this effect can only partially compensate for the longwave cooling (Fueglistaler and Fu, 2006). Figure 4.3 and 4.4 show the mean radiative heating rates as a functions of cloud top height for various cloud types. The effect of clouds on radiative heating, calculated as the difference between cloudy and clear-sky radiative heating rates, is shown in the right column of Figure 4.3 and 4.4. These figures are calculated using the radiative heating profiles from 2B-FLXHR-LIDAR when the labeled cloud type from 2B-CLDCLASS-LIDAR is within the CloudSat footprint. Only footprints within 20° N/S were used in making these two figures. Generally, the presence of clouds tends to reduce the radiative heating rate at altitudes above cloud tops. This reduction is more apparent for altostratus, nimbostratus and deep convective clouds. For these three cloud types, the cooling effect at TTL altitudes is apparent when the cloud top height reaches 15 km or higher. On the other hand, cumulus, stratocumulus, and altocumulus are observed to have a weak effect at these heights. Cirrus clouds also has a weak effect when their cloud tops are below TTL altitudes. However, as summarized in Chapter 1, most tropical cirrus occur within the TTL, and they tend to increase the local radiative heating rate.

One parameter of interest is the level of net zero radiative heating (LZRH). As Figure 1.9 shows, in the middle and upper troposphere there is negative radiative heating, and at around 15

km the signs of radiative heating transitions from negative to positive. This level marks the LZRH. The LZRH is a quantity of interest since above this level, the positive heating rate implies slow ascent. In Figure 4.3 and 4.4 the mean clear-sky LZRH is marked by the dotted line while the LZRH in the presence of clouds is denoted by the solid lines. For altostratus, nimbostratus, and deep convection, the separation between cloudy and clear-sky LZRH becomes larger as cloud top height increases. When the cloud top reaches 14 km, the separation is close to 1 km. The reduction of heating rate due to the presence of these clouds tends to elevate the LZRH.

Clouds at low altitudes, such as cumulus, stratocumulus and altocumulus, have a minute effect on the LZRH, and in general they impose a very slight reduction on UTLS heating rates. On the other hand, the effects of cirrus clouds on the LZRH is harder to interpret. Since they are optically thin, cirrus clouds have little influence on the LZRH when their cloud top height is below it. When the cloud top height reaches 15 km and above, cirrus clouds locally impose additional radiative heating on the order of 1 K/day, and in the vertical structure of mean radiative heating rates there is a transition from radiative cooling to heating at around 14 km (indicated by the green solid line). This indicates that, in the presence of TTL cirrus clouds, the mean LZRH lie below the cirrus clouds and tend to be below the mean clear-sky LZH. In summary, the effects of cirrus clouds below the TTL on the LZRH is negligible, while cirrus situated at TTL altitudes tend to lower the LZRH significantly due to its radiative heating effect. In the latter case, the LZRH could be depressed to heights lower than the TTL base (~14.5 km), implying mean upwelling throughout all TTL altitudes.

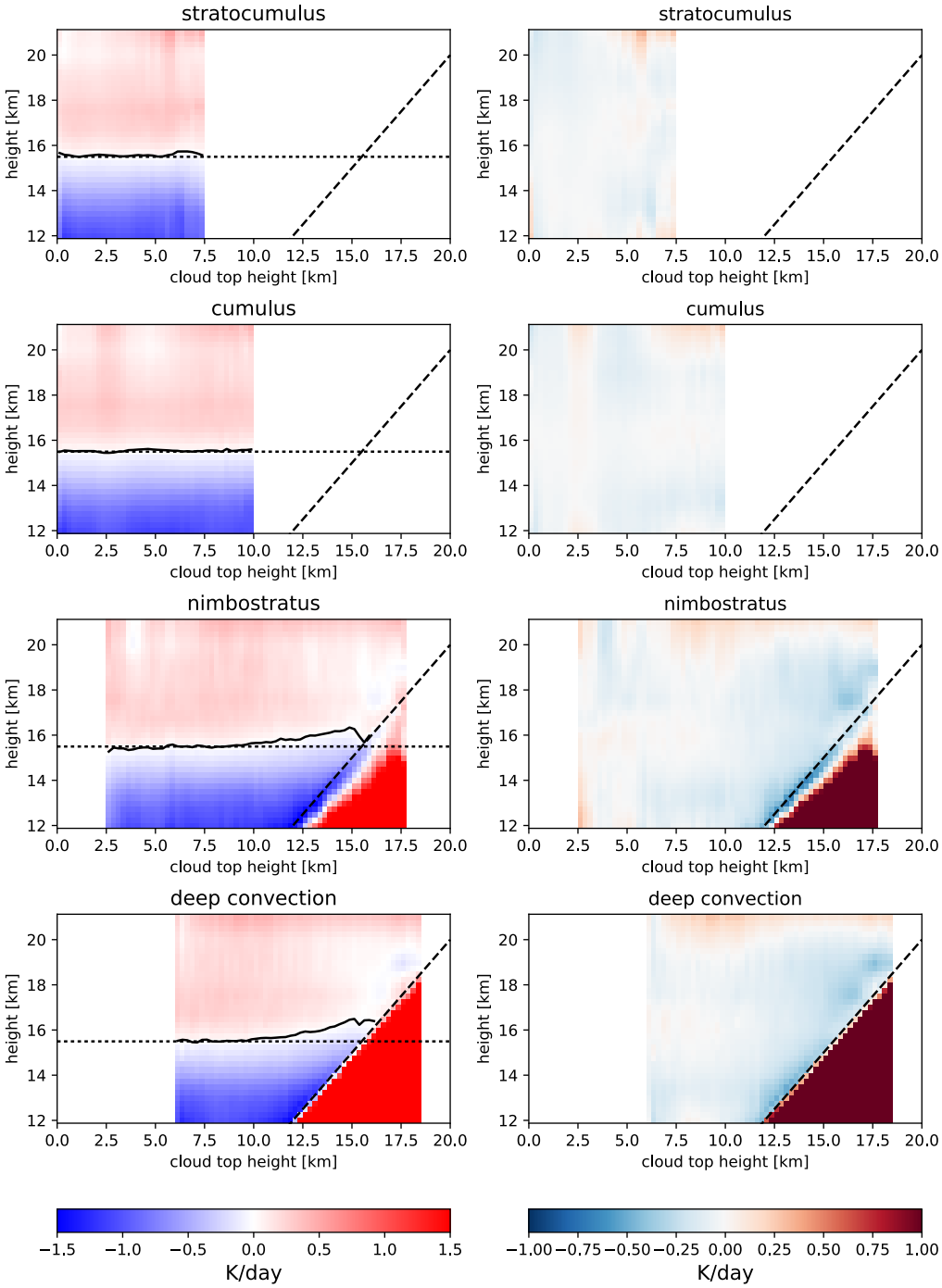

Figure 4.3 (Left column) Mean radiative heating rates calculated from 2B-FLXHR-LIDAR footprints containing the labeled cloud type. Horizontal dotted lines indicate the level of mean clear-sky LZRH, solid lines denote the mean cloudy-sky LZRH, and the dashed line is where the y-axis height is equal to the cloud top height. Calculated from data with 20° of the equator. (Right column) Difference between cloudy-sky and clear-sky radiative heating rates. Positive values mean that the presence of clouds increase the radiative heating rate.

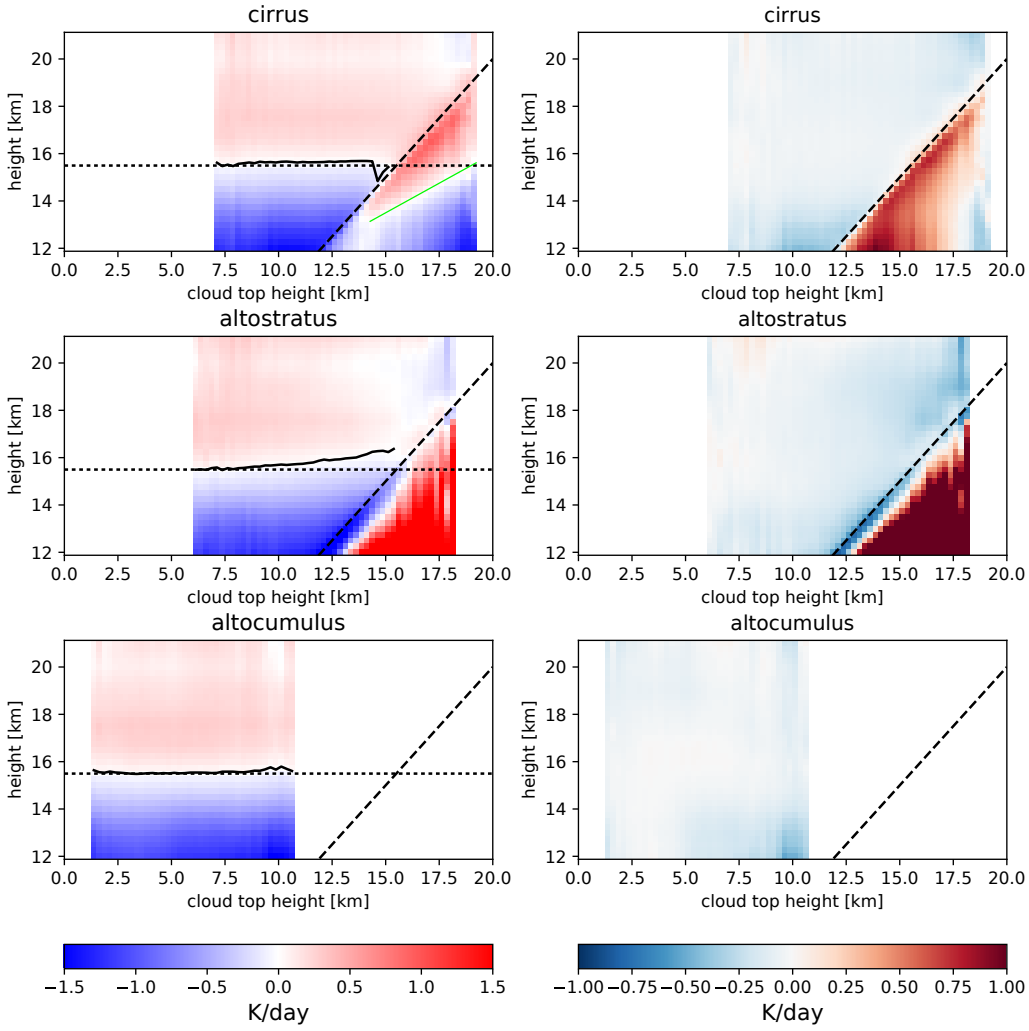

Figure 4.4 Same as Figure 4.3 except for cirrus, altostratus, and altocumulus clouds. In the left plot for cirrus, the green line indicates the mean LZH when cirrus clouds are inside the TTL.

4.4 Global UTLS radiative heating rates under clear-sky and all-sky conditions

Hereafter the all-sky radiative heating rate will be referred to as Q, and the clear-sky and cloudy-sky radiative heating rates will be Q_{clear} and Q_{cloud}, respectively. For 2B-FLXHR-LIDAR, Q_{clear} is calculated by averaging the radiative heating rates from clear-sky CloudSat footprints, Q_{cloud} uses only cloudy footprints, and Q uses all footprints. In MERRA-2, at every grid point the reanalysis

provides both Q and Q_{clear} where the latter is calculated through radiative calculations assuming no clouds in the column. The abbreviation FLXHR will be used to refer to 2B-FLXHR-LIDAR.

The monthly average radiative heating rates are calculated using FLXHR by binning the data onto 5° × 5° bins. The resulting zonal averages are shown in Figure 4.5. The MERRA-2 zonal averages (Figure 4.6) are calculated by first interpolating the values onto the pressure levels of interest, and then averaged on the reanalysis native horizontal resolution. At 70 hPa, approximately the top of the TTL, there is a belt of positive radiative heating centered on the equator. In all the 70 hPa distributions, there is a lobe of maximum centered near 20°N from February to May. Inside the belt of heating, the clear-sky heating rates are higher than those of all-sky or cloudy-sky. This is the case in both MERRA-2 and FLXHR. The Q and Q_{clear} from these two data sets are qualitative similar and exhibit similar seasonal cycles. The equatorial radiative heating belt in MERRA-2 is positive throughout the year, while in FLXHR Q there is weak cooling during August near 0°. Outside the tropics, MERRA-2 exhibits heating around 80°N during May and June, while this heating is not present in FLXHR.

At 100 hPa, the equatorial belt of heating is narrower than at 70 hPa. In FLXHR Q and Q_{cloud}, from November to May there is a region of enhanced heating centered on the equator. This region is not present in Q_{clear}. It is also not in MERRA-2. Unlike FLXHR, the Q_{clear} equatorial heating of MERRA-2 is stronger than its Q, indicating that in MERRA-2 clouds tend to weaken the heating in the TTL. The belt of heating is also significantly wider in MERRA-2. At middle and high latitudes, FLXHR has stronger cooling in both the southern and northern hemisphere.

The heating anomalies due to clouds, calculated as Q - Q_{clear}, are shown in Figure 4.7. At 70 hPa, FLXHR and MERRA-2 show a similar cloud effect at low latitudes — there is a strip of

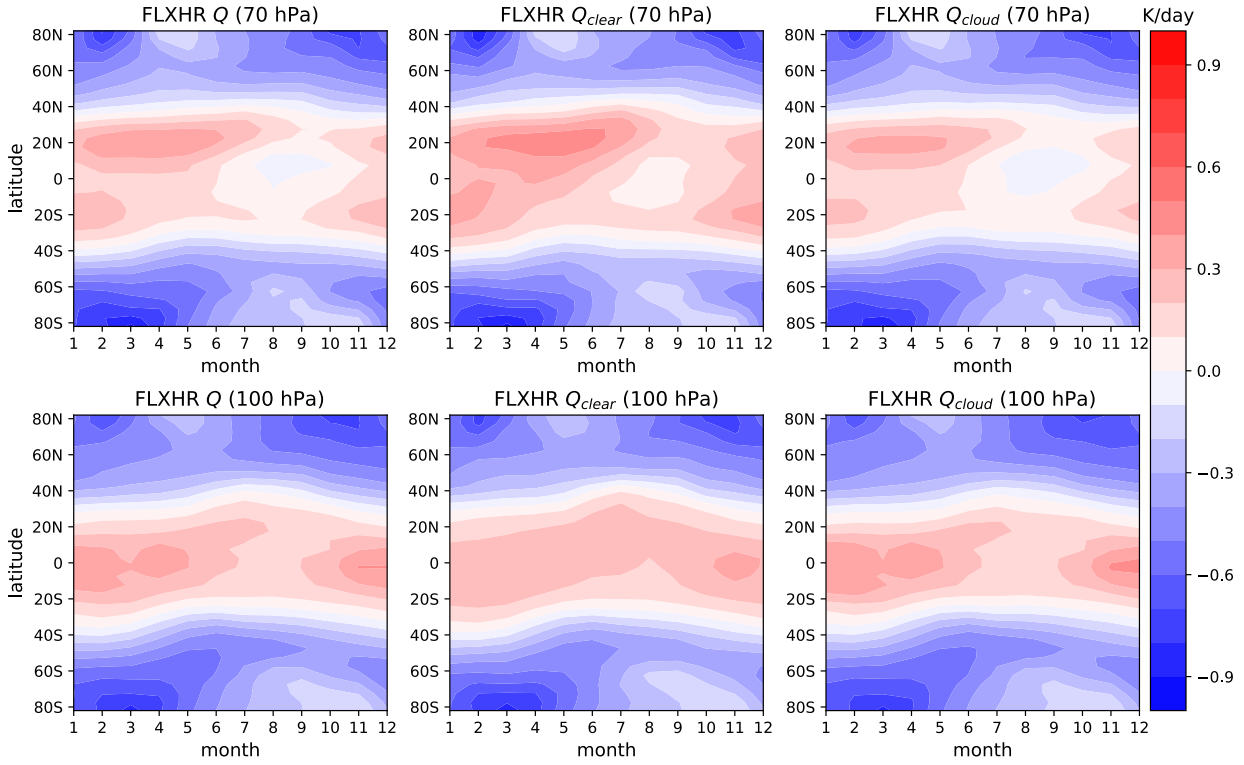

Figure 4.5 2B-FLXHR-LIDAR monthly zonal averages of radiative heating rate at 70 hPa (top row) and 100 hPa (bottom row) through 2007–2010. Q refers to all-sky radiative heating rates, while Q_{clear} and Q_{cloud} are the clear-sky and cloudy-sky heating rates. Contours intervals are 0.1 K/day.

reduced heating around 0° to 20°N. In MERRA-2 this reduction peaks at -0.16 K/day around August and September, while in FLXHR it peaks at -0.14 K/day around June and July. During these two months there is also reduced heating from 20°N to 40°N in FLXHR but not in MERRA-2. The high-latitude clouds in FLXHR increases the 70 hPa heating rates, whereas clouds in MERRA-2 have no such effect. At 100 hPa, these two data sets exhibit significant differences in their cloud effects. Tropical clouds in FLXHR significantly increase the radiative heating at 100 hPa, peaking at +0.10 K/day. This heating is not present in MERRA-2. For MERRA-2, the patterns of cloud effects are quite similar between 70 and 100 hPa, with the former having stronger reductions in heating rates. On the other hand, the patterns at these two

levels are quite different in FLXHR especially inside the tropics and subtropics. At the poles, FLXHR has a similar pattern and magnitude of increased heating at both pressure levels.

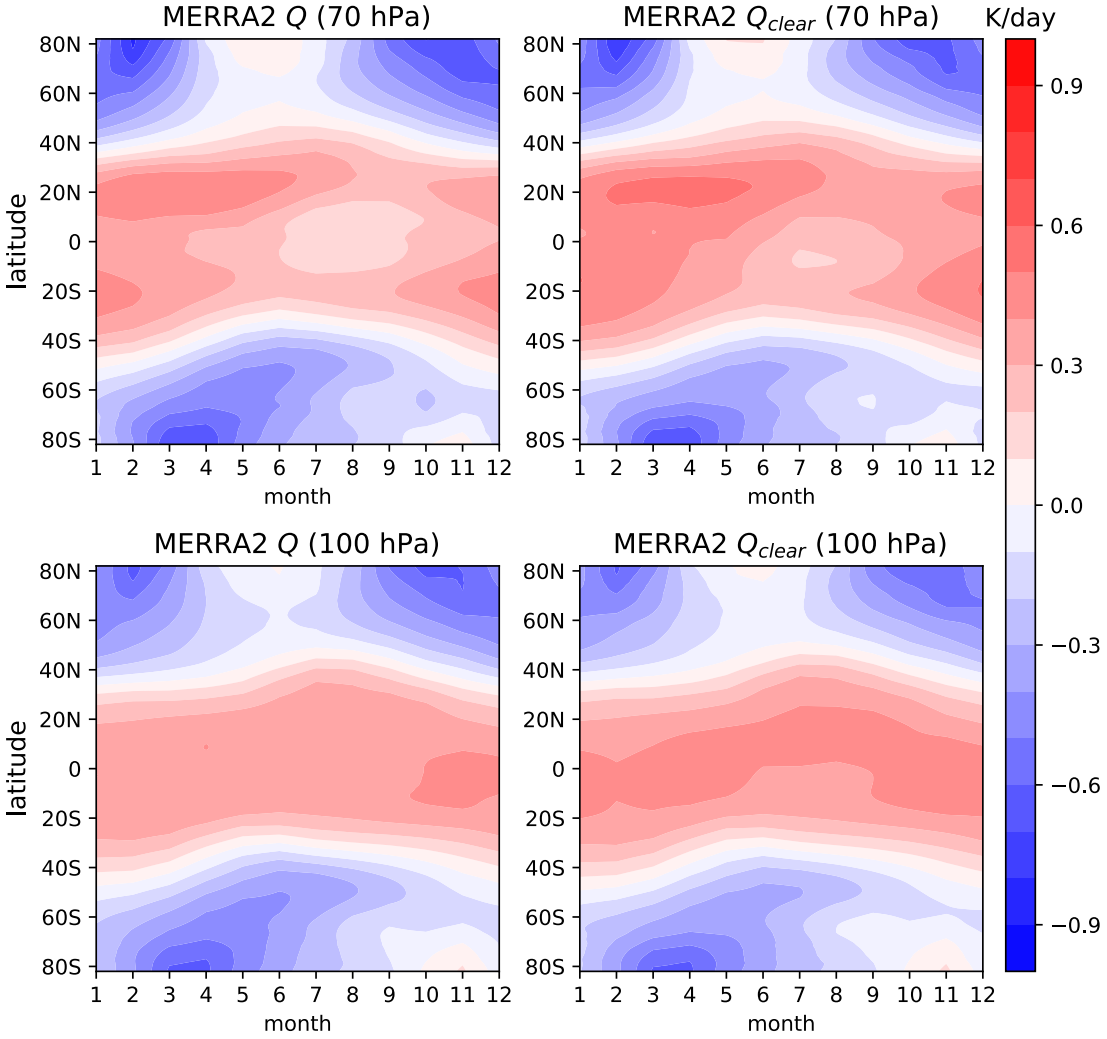

Figure 4.6 Same as Figure 4.5 except for MERRA-2.

Vertical cross-sections of zonal-mean heating rates during January and July are shown in Figure 4.8 and 4.9 for FLXHR and MERRA-2. Overall, MERRA-2 has higher heating rates in the equatorial UTLS, and the belt of positive heating is wider at most heights when compared to FLXHR. This is true during both January and July. The polar cooling in MERRA-2 exhibits a

stronger seasonal cycle with winter hemisphere having stronger cooling. During July, FLXHR Q shows weak cooling between 50 and 60 hPa centered on the equator. This region of cooling is small in Q_{clear} but large in Q_{cloud}, illustrating the cooling effect of clouds. This is similar to the findings of Fueglistaer and Fu (2006) who found that thick clouds can cause cooling in the lower stratosphere. In comparison, both Q and Q_{clear} of MERRA-2 is positive throughout 110–40 hPa within 20°S to 20°N.

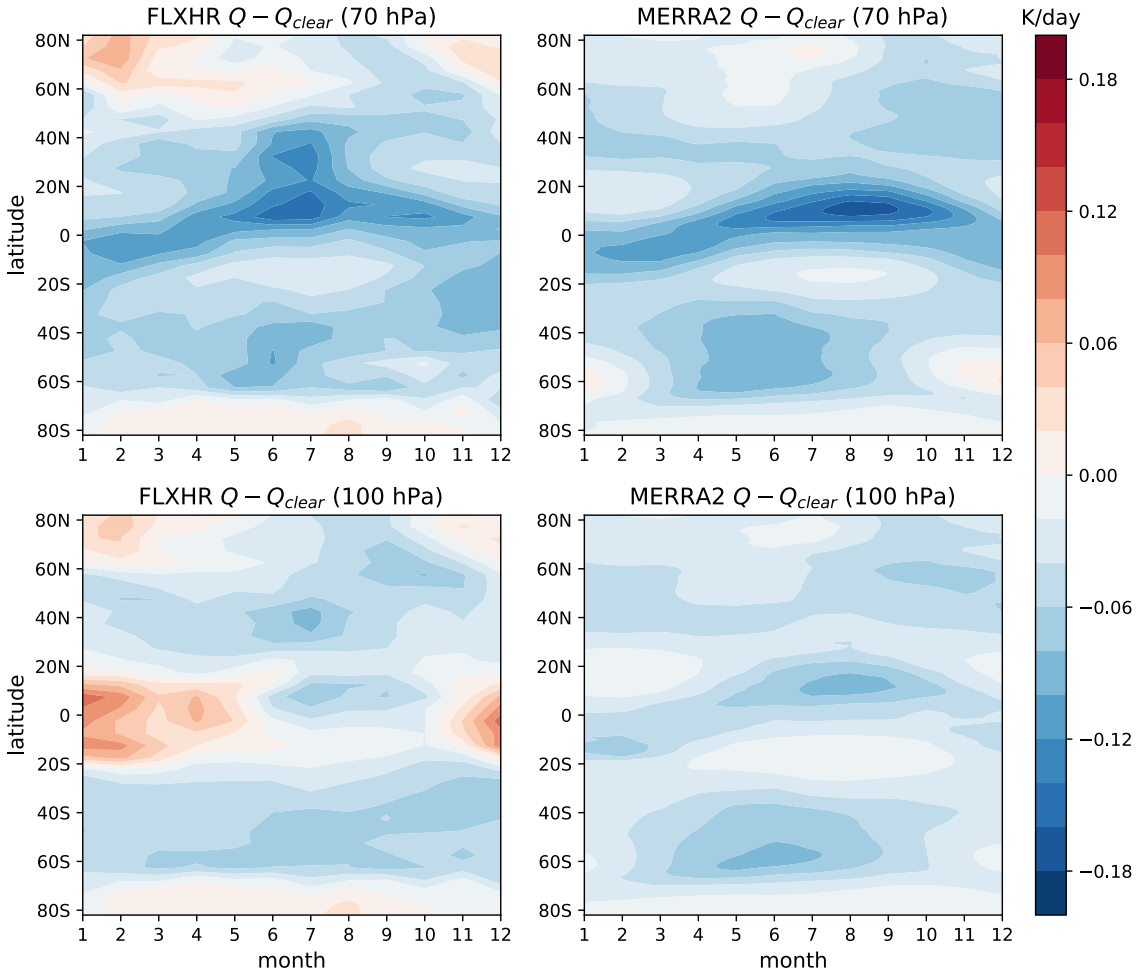

Figure 4.7 Difference between the all-sky (Q) and clear-sky radiative heating rate (Q_{clear}) for FLXHR (left column) and MERRA-2 (right column) at 70 (top row) and 100 hPa (bottom row). Contour intervals are 0.02 K/Day.

The cloud effects (Figure 4.10) in July is similar between FLXHR and MERRA-2. Like Figure 4.7, there is a region of reduced heating between 0° to 20°N. However, in FLXHR this region extends downward both towards the equator as well as towards ~40°N. In MERRA-2 the reduced heating is localized between 0° to 20°N. In the northern hemisphere, there is a positive cloud effect at high latitudes in both FLXHR and MERRA-2, although the former exhibits increased heating at around 60°N while the latter is at 80°N. In January, FLXHR has increased heating at and below 90 hPa. Based on Figure 4.4 it can be inferred that TTL cirrus clouds are responsible for the increased heating rate near the tropopause. Above 90 hPa, both MERRA-2 and FLXHR suggest that clouds on average enhance the cooling rate of the tropical lower stratosphere. This cooling is positioned roughly within 20°S–0° during January and 0°–20°N in July. Outside the tropics, the main difference between MERRA-2 and FLXHR is that in the latter clouds increase the north pole radiative heating rate while the former has increased cooling around 60°S.

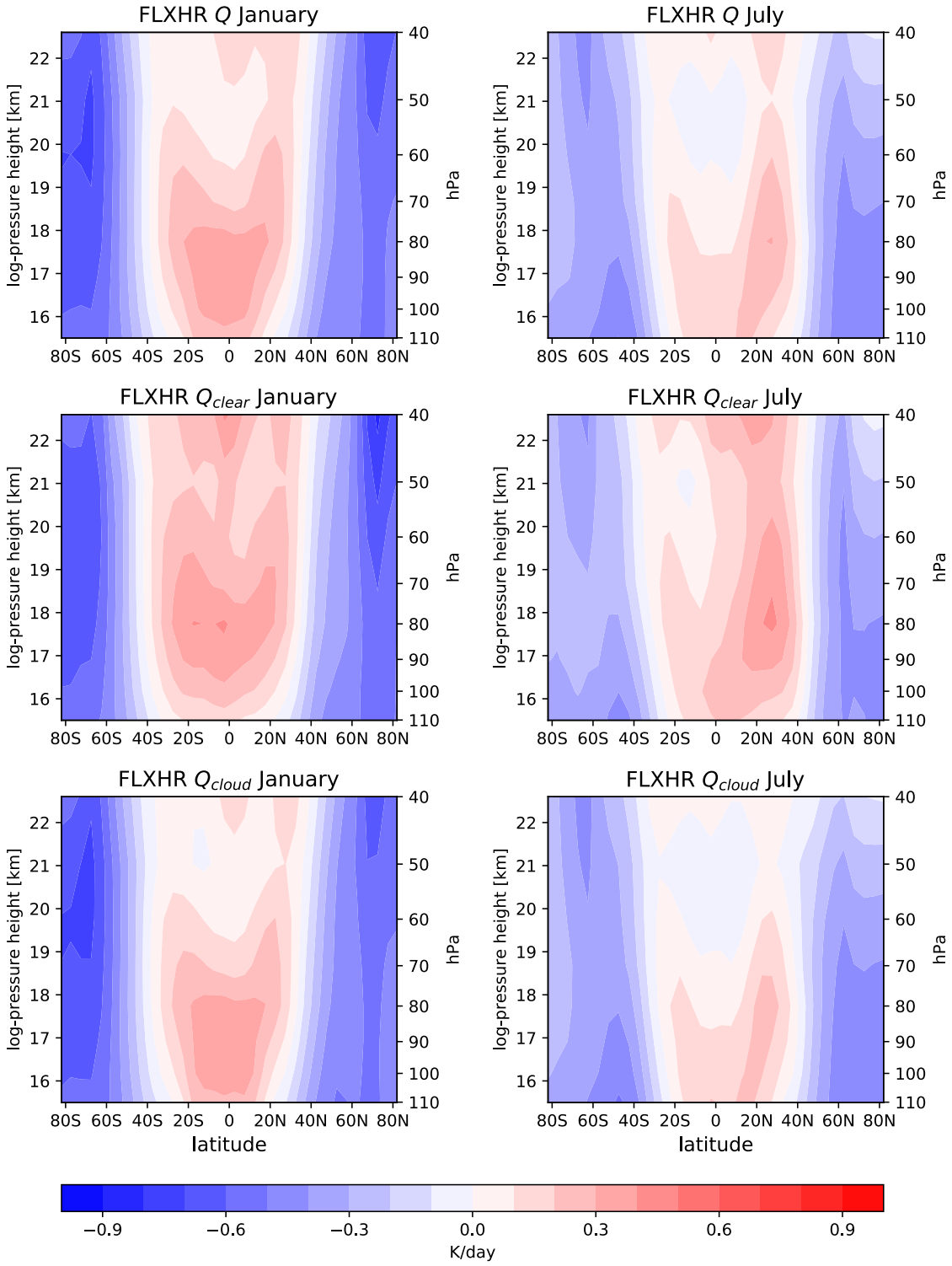

Figure 4.8 Height-latitude cross-section of monthly mean all-sky (Q, top row), clear-sky (Q_{clear}, middle row), and cloudy-sky (Q_{clear}, bottom row) radiative heating rates from 2B-FLXHR-LIDAR. Left column is for January and right column is for July. Contour intervals are 0.1 K/day.

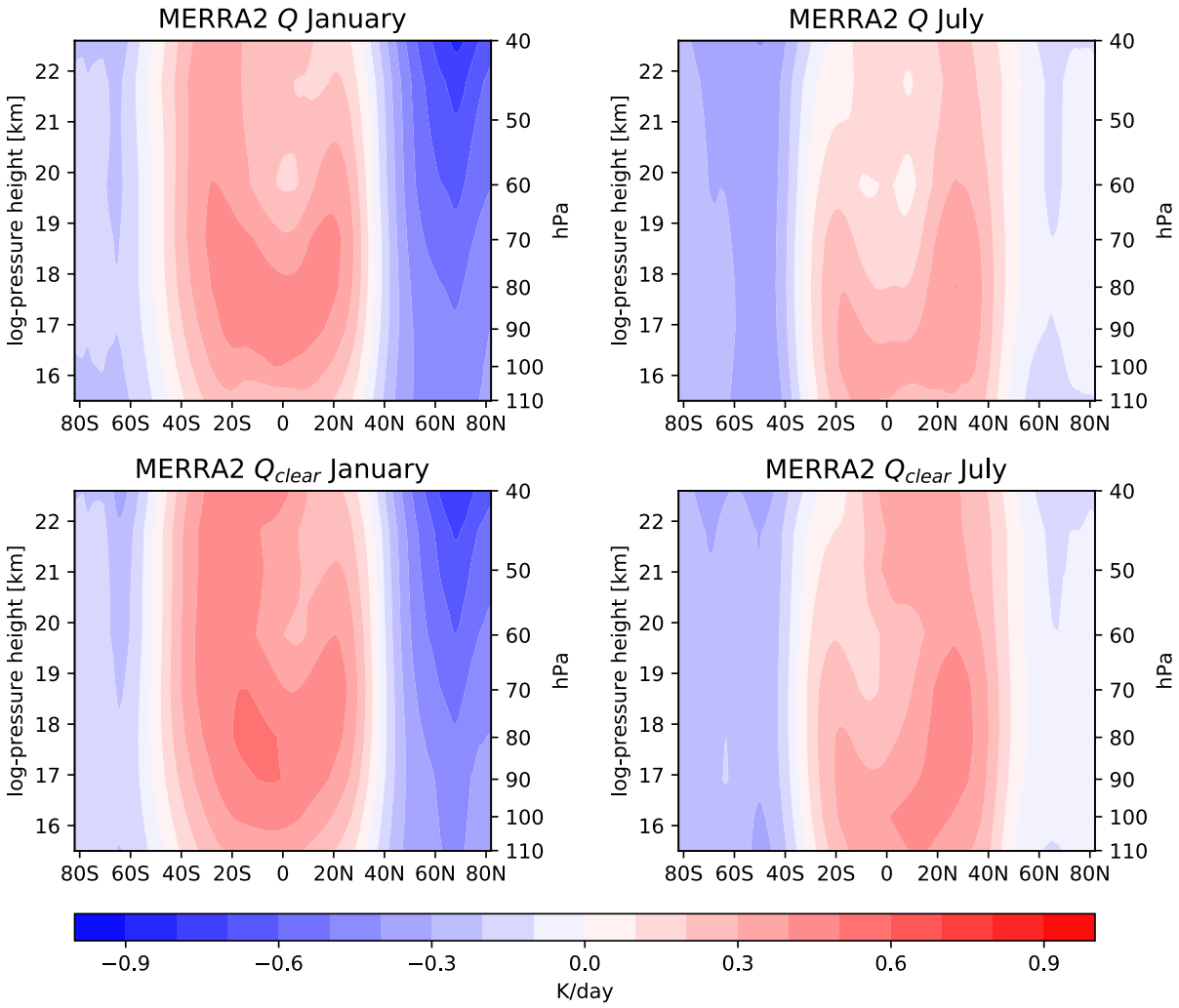

Figure 4.9 Same as Figure 4.8 except for MERRA-2.

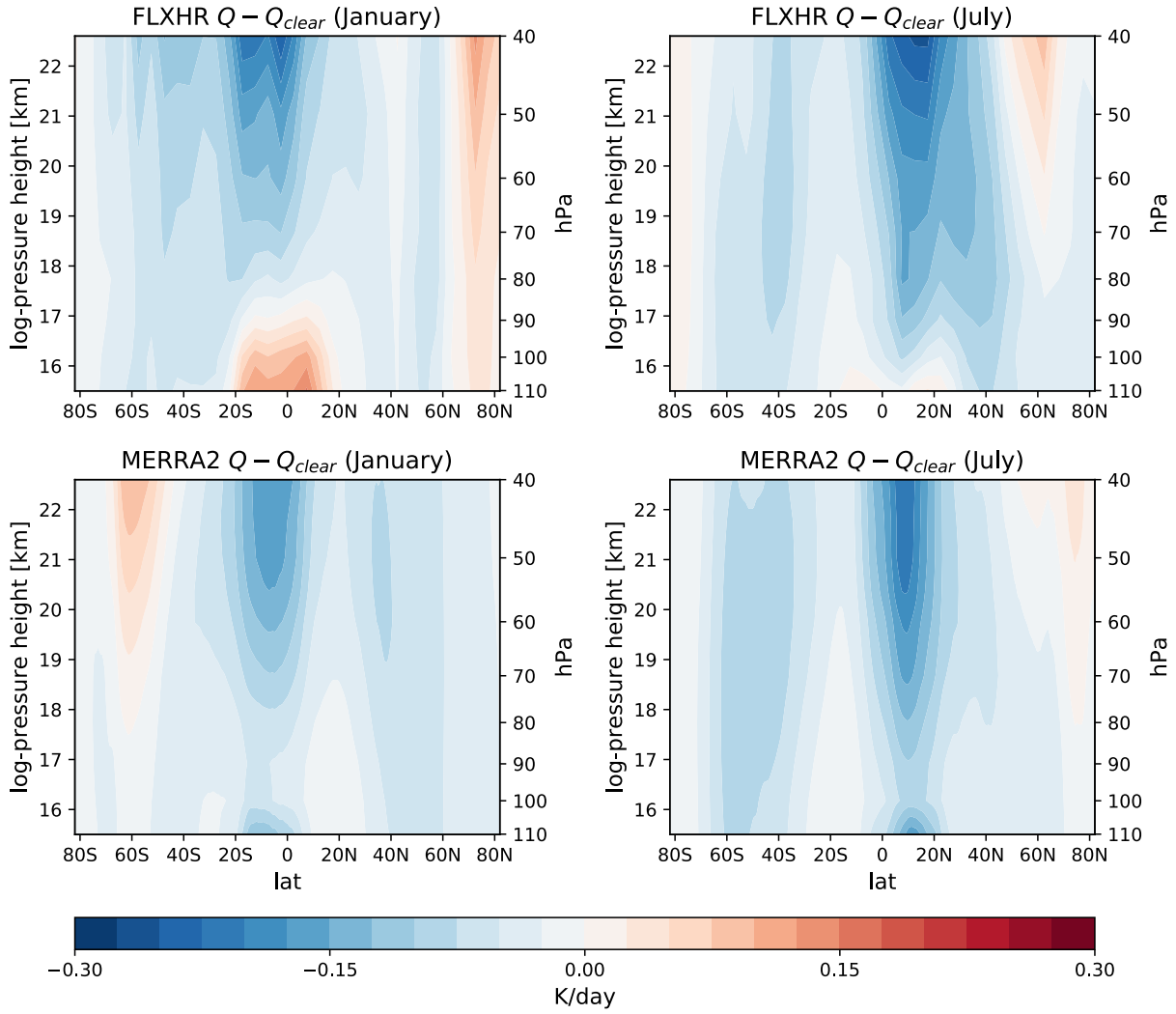

Figure 4.10 Difference between the all-sky (Q) and clear-sky radiative heating rate (Q_{clear}) from FLXHR (top row) and MERRA-2 (bottom row). Left column is for January and right column is for July. Contour intervals are 0.025 K/Day.

4.5 Residual velocities diagnosed from satellite data sets and MERRA-2

After the Brewer (1949) proposed the BDC, subsequent studies found that the mean circulation in the stratosphere and mesosphere did not agree with the schematic shown in Figure 1.2. It was suggested by Andrews and McIntyre (1976) and others that the transport of tracers follows Lagrangian motions. Andrews and McIntyre (1976,1978) proposed the transformed Eulerian-mean (TEM) framework which approximates the Lagrangian circulation in the latitude-height plane. In log-pressure coordinates, the TEM thermodynamic equation is

$$\frac{\partial\bar{\theta}}{\partial t} = -\frac{\bar{v}^*}{a}\frac{\partial\bar{\theta}}{\partial\phi} - \bar{w}^*\frac{\partial\bar{\theta}}{\partial z} + \bar{Q} - \frac{1}{\rho_0}\frac{\partial}{\partial z}\left(\rho_0\overline{v'\theta'}\frac{\partial\bar{\theta}/\partial\phi}{a(\partial\bar{\theta}/\partial z)} - \rho_0\overline{w'\theta'}\right) \tag{4.1}$$

where the overbars indicate zonally averaged quantities, θ is potential temperature, ϕ is latitude, Q is total diabatic heating, a is the Earth radius, $\rho_0 = \rho_s \exp(-z/H)$, and $\bar{v}^*$ and $\bar{w}^*$ are the mean residual meridional and vertical velocities under the TEM framework. The residual velocities are defined as

$$\bar{v}^* \equiv \bar{v} - \frac{1}{\rho_0}\frac{\partial}{\partial z}\left(\frac{\rho_0\overline{v'\theta'}}{\partial\bar{\theta}/\partial z}\right), \quad \bar{w}^* \equiv \bar{w} + \frac{1}{a\cos\phi}\frac{\partial}{\partial\phi}\left(\cos\phi\frac{\overline{v'\theta'}}{\partial\bar{\theta}/\partial z}\right) \tag{4.2}$$

and the mass continuity equation is

$$\frac{1}{a\cos\phi}\frac{\partial}{\partial\phi}(\bar{v}^*\cos\phi) + \frac{1}{\rho_0}\frac{\partial}{\partial z}(\rho_0\bar{w}^*) = 0. \tag{4.3}$$

In Equation (4.1), the last term on the right-hand side is small under quasi-geostrophic scaling. Also, for heights at and above the tropopause, diabatic heating is approximately equal to radiative heating. Hence Equation (4.1) is usually well approximated by

$$\frac{\partial\bar{\theta}}{\partial t} + \frac{\bar{v}^*}{a}\frac{\partial\bar{\theta}}{\partial\phi} + \bar{w}^*\frac{\partial\bar{\theta}}{\partial z} = \left(\frac{p_s}{p}\right)^K \bar{Q}_r \tag{4.4}$$

where $\bar{Q}_r = (\partial\bar{T}/\partial t)_r$ is the zonally-averaged radiative heating rate. Since the satellite and reanalyses data sets used in this chapter provide radiative heating rates of air temperature (instead of potential temperature), $\bar{Q}_r$ needs to be multiplied by the factor $(p_s/p)^K$ where $K = 2/7$, $p_s = 1000$ hPa is the reference pressure, and p is pressure,. Using Equation (4.3), it can be shown that

$$\bar{v}^*(\phi)cos\phi - \bar{v}^*(\phi_0)cos\phi_0 = -\frac{1}{\rho_0}\int_{\phi_0}^{\phi}\frac{\partial}{\partial z}(\rho_0\overline{w}^*)acos\phi' d\phi'. \tag{4.5}$$

From fields of radiative heating rates and potential temperature, $\bar{v}^*$ and $\overline{w}^*$ can be solved for by iterating Equation (4.4) and (4.5). First, as in Hitchman and Leovy (1986), we smooth $\partial\bar{\theta}/\partial\phi$ in latitude using a 1-2-1 weighting. We assume $\bar{v}^* = 0$ everywhere and use (4.4) to solve for $\overline{w}^*$. Since the total vertical mass flux across a pressure surface between the northmost and southmost latitude must be zero, a uniform correction is applied to $\overline{w}^*$ according to Shine (1989) to satisfy this constraint. The corrected $\overline{w}^*$ is then used in (4.5) is used to solve for $\bar{v}^*$ by assuming $\bar{v}^*(-\pi/2) = 0$ (zero meridional velocity at the south pole). A correction to $\bar{v}^*$ based on Murgatroyd and Singleton (1961) is applied so that the meridional velocities at the poles are zero. The resulting $\bar{v}^*$ is then smoothed in latitude using 1-2-1 weighting and used in (4.4) again to solve for new estimates of $\overline{w}^*$. We found that convergence is quick, and five iterations is sufficient to obtain a solution.

The residual mean velocities can also be calculated directly using the definitions in equation (4.2). We will refer to the velocities derived from equation (4.4) and (4.5) as radiative $\bar{v}^*$ and $\overline{w}^*$, and velocities from (4.2) as dynamic $\bar{v}^*$ and $\overline{w}^*$.

Model-level MERRA-2 fields are first interpolated onto every 1 hPa between 1 and 10 hPa, every 5 hPa between 10 and 60 hPa, and every 10 hPa between 60 and 110 hPa. The

dynamic residual circulation is calculating with Equation (4.2) using daily fields of winds and temperature from MERRA-2. The $\partial\bar{\theta}/\partial z$ term is evaluated with one-sided finite difference at 1 hPa and 110 hPa, and with central finite difference at the interior vertical levels. The radiative residual circulation of MERRA-2 is calculated by iterating Equation (4.4) and (4.5) using daily fields of radiative heating rates and potential temperature. The $\partial\bar{\theta}/\partial t$ term is calculated using central finite difference on the daily fields. Monthly averages of the residual circulations are then calculated by averaging the daily circulation in each month. Since our focus in this dissertation is on the UTLS, in the subsequent discussions we show the solutions between 110 and 40 hPa. The solutions at all heights are available at the end of this chapter for reference (Figure 4.20 and 4.21).

To obtain the radiative residual circulation using FLXHR, the zonal-mean radiative heating rates are calculated in 5° latitude bins for each month. Potential temperature calculated from the RO atmPrf temperature profiles are also binned the same way. Both radiative heating and potential temperature are interpolated to every 10 hPa between 40 and 110 hPa. Then the radiative residual circulation is solved for by iterating equation (4.4) and (4.5). The $\partial\bar{\theta}/\partial t$ term is calculated using central finite difference on the monthly fields.

Figure 4.11 shows the dynamic and radiative residual velocities at 70 and 100 hPa from MERRA-2. Two different solutions of radiative residual velocities are shown: one obtained using Q and another using Q_{clear}. At 70 hPa, the dynamic $\bar{w}^*$ and $\bar{v}^*$ are in good agreement with the radiative $\bar{w}^*$ and $\bar{v}^*$. In the dynamic $\bar{w}^*$ there are two belts of upwelling, one in each hemisphere. This feature is also visible in the radiative $\bar{w}^*$ although it is not as obvious. From November to March, near 20°N the dynamic $\bar{v}^*$ has a maximum of 20 cm/s while the radiative $\bar{v}^*$ maximum is around 30 cm/s. Similarly, from April to June there is a southward $\bar{v}^*$ of about -

20 cm/s in the dynamic $\bar{v}^*$ and -30 cm/s in the radiative $\bar{v}^*$. These subtropical $\bar{v}^*$ maxima represent the meridional component of the shallow BDC. Above 60°N/S, the dynamic and radiative $\overline{w}^*$ have similar amplitudes and seasonal cycles. The dynamic and radiative circulation overall are consistent with each other at 70 hPa. At 100 hPa however the difference is more apparent. The equatorial belt of upwelling is narrower in the dynamic field, and the magnitude of dynamic $\overline{w}^*$ is weaker at most latitudes and months except for at the north pole during boreal winter. The poleward $\bar{v}^*$ in the subtropics is more confined near the equator compared to the radiative $\bar{v}^*$ where the maxima are higher in latitude. Although the position of the $\bar{v}^*$ maxima are

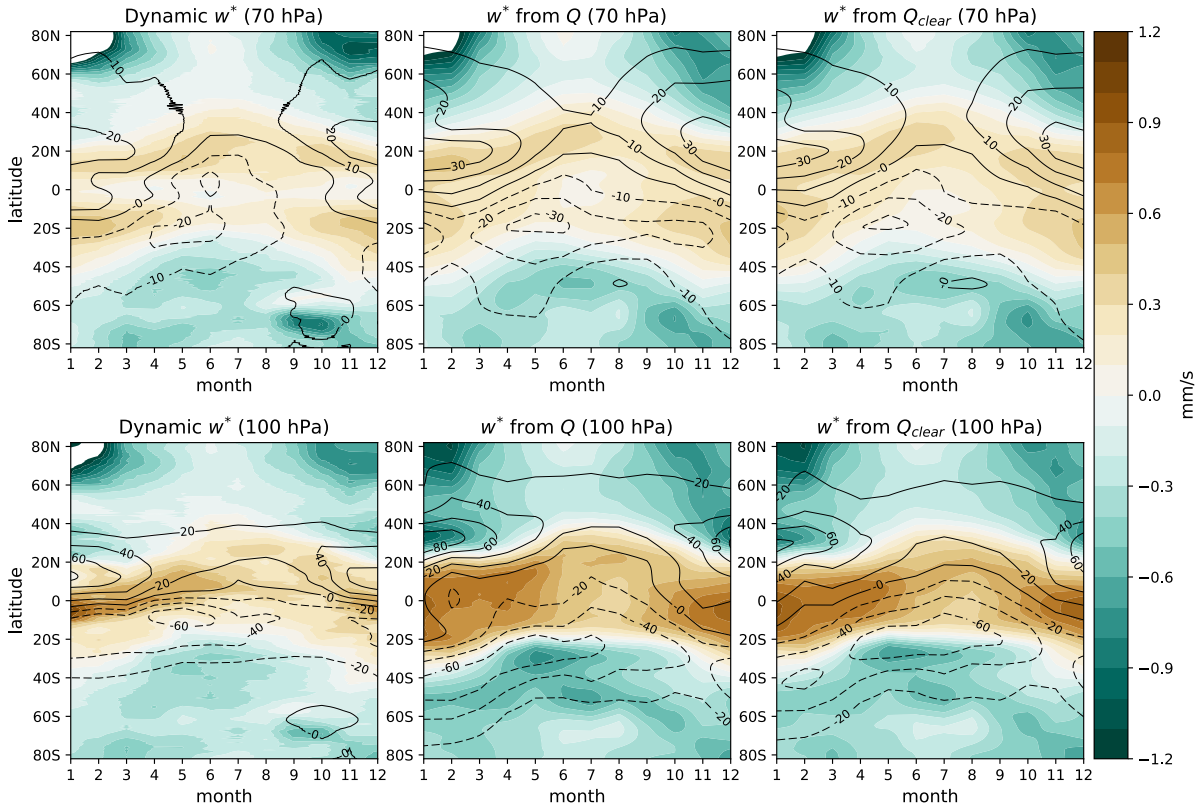

Figure 4.11 (Left column) MERRA-2 dynamic residual vertical and meridional velocities ($\overline{\boldsymbol{w}}^*$ and $\overline{\boldsymbol{v}}^*$), (middle column) radiative $\overline{\boldsymbol{w}}^*$ and $\overline{\boldsymbol{v}}^*$ solved using all-sky radiative heating Q, and (right column) radiative $\overline{\boldsymbol{w}}^*$ and $\overline{\boldsymbol{v}}^*$ solved using clear-sky radiative heating Q_{clear}. Colored contours are for $\overline{\boldsymbol{w}}^*$ at intervals of 0.1 mm/s. Black contours are for $\overline{\boldsymbol{v}}^*$ at intervals of 20 cm/s; dashed negative.

different, the magnitude of $\bar{v}^*$ between dynamic and radiative calculations are consistent. Despite some differences, comparison between the dynamic and radiative circulations shows that the radiative solution is consistent with the dynamic counterpart.

The solutions from Q and Q_{clear} are very similar at 70 hPa, suggesting that at this level the cloud effect on the BDC is minor. The ascent in the tropics and descent at the poles are similar in magnitude, as are the positions and magnitudes of the subtropical $\bar{v}^*$ maxima. At 100 hPa the differences between $\bar{w}^*$ derived from Q and Q_{clear} are more apparent, indicating the stronger influence of clouds at this level. Above 50°N/S, these two solutions are similar. The main differences lie near the equator, where the $\bar{w}^*$ from Q has a wider belt of equatorial upwelling especially from October to May. Despite the wider $\bar{w}^*$, the magnitude is similar between the solutions of Q and Q_{clear}.

The corresponding residual velocities derived from FLXHR are shown in Figure 4.12. The subtropical $\bar{v}^*$ maxima at 70 hPa has similar magnitudes to those of MERRA-2, and the latitude of these maxima are also similar. At 100 hPa the $\bar{v}^*$ maxima are weaker than MERRA-2, and the latitude and timing of the maxima are also different. Comparing the solutions from FLXHR Q and Q_{clear}, we find that, similar to MERRA-2, the cloud effect at 70 hPa is minor. The solution from Q_{clear} has stronger subtropical $\bar{v}^*$ maxima but its $\bar{w}^*$ is very similar in value and distribution to the Q solution. The discrepancy between Q and Q_{clear} solutions is apparent at 100 hPa. Unlike MERRA-2, the presence of clouds significantly increases the upwelling strength and the poleward $\bar{v}^*$ flanking the upwelling belt. Especially in the northern hemisphere, the regions of subtropical $\bar{v}^*$ maxima are much more diffuse in the Q_{clear} solution. Comparison of Figure 4.11 and 4.12 suggests that the clouds observed by CloudSat/CALIPSO has a significantly different effect on UTLS heating rates and BDC than the clouds in MERRA-2.

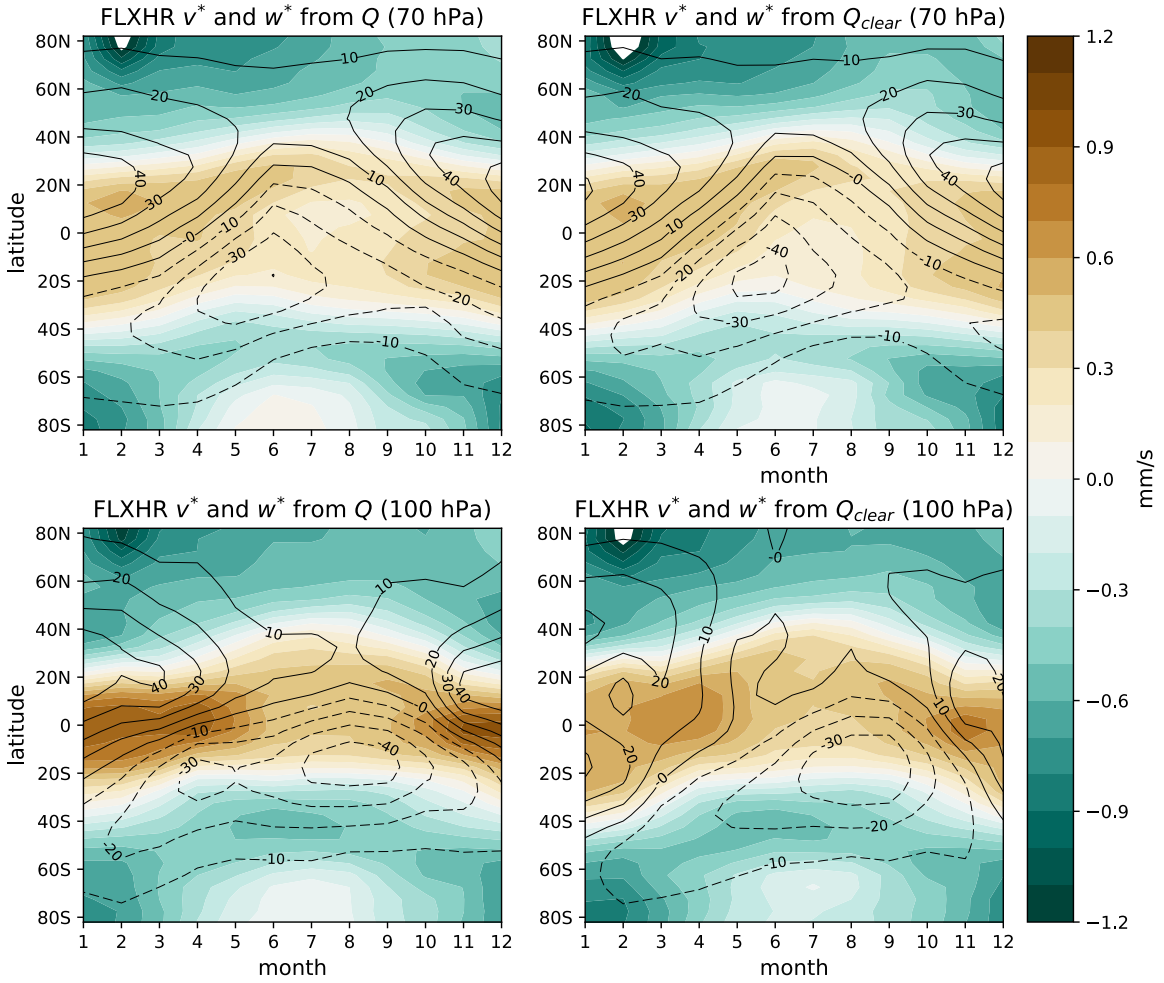

Figure 4.12 2B-FLXHR-LIDAR radiative $\overline{w}^*$ and $\overline{v}^*$ calculated using Q (left column) and Q_{clear} (right column) at 70 (top) and 100 hPa (bottom). Colored contours are for $\overline{w}^*$ at intervals of 0.1 mm/s. Black contours are for $\overline{v}^*$ at intervals of 10 cm/s; dashed negative.

The difference between solutions from Q and Q_{clear} is shown in Figure 4.13. We interpret this difference as the radiative cloud effect on $\overline{v}^*$ and $\overline{w}^*$. At 70 hPa, the plots derived from MERRA-2 and FLXHR both indicate that the cloud effect on v^* is on the order of 1 cm/s and the effect on $\overline{w}^*$ is on the order of 0.1 mm/s. At the north and south poles both MERRA-2 and FLXHR show an increased $\overline{w}^*$ which implies that clouds in both data sets tend to slightly dampen the polar descent of the BDC. This effect is also visible at 100 hPa, with FLXHR having

a higher amplitude. At low latitudes, the cloud effects at 70 hPa on $\overline{w}^*$ are similar in that both data sets have an enhanced upwelling centered around 20°S from June to August.

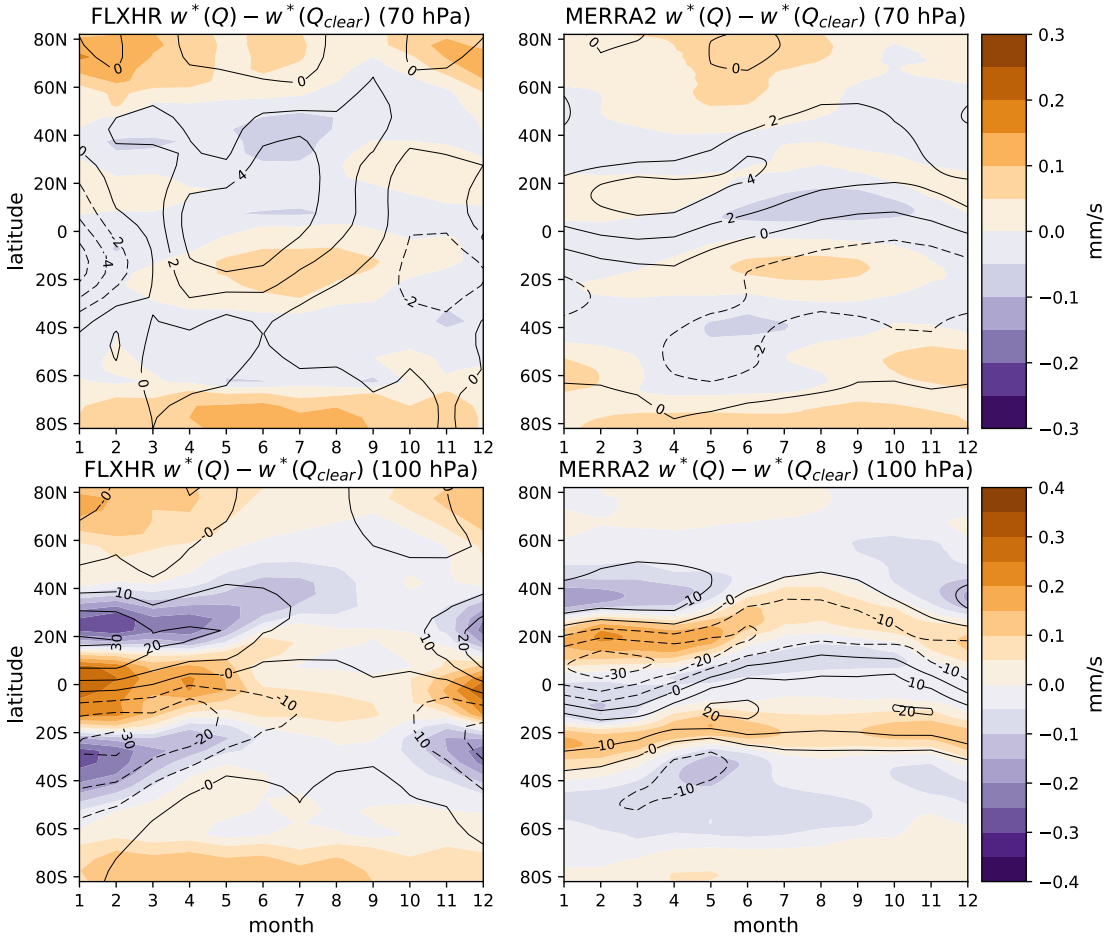

Figure 4.13 The difference between $\overline{\boldsymbol{w}}^*/\overline{\boldsymbol{v}}^*$ solved using Q and Q_{clear} at 70 (top row) and 100 hPa (bottom). Left column is for FLXHR and right column is for MERRA-2. Colored contours are for $\overline{\boldsymbol{w}}^*$; note that the top and bottom rows have the same contour intervals (0.05 mm/s) but different color scales. Black contours are for $\overline{\boldsymbol{v}}^*$ at intervals of 2 cm/s for the top row and 10 cm/s for the bottom row; dashed negative.

The cloud effects at 100 hPa are larger in magnitude and significantly different between MERRA-2 and FLXHR. In FLXHR, clouds increase the upwelling near 0° and reduce the upwelling at the north and south flanks of the upwelling belt from November to May. This effect

narrows the equatorial upwelling belt while enhancing the upwelling rate in the center of the belt. The associated residual meridional motions are also increased due to the presence of clouds. On the other hand, MERRA-2 exhibits a very different cloud effect in the tropics and subtropics. Instead of increasing upwelling centered on the equator, there is a weak reduction of upwelling around 0° and two narrow belts of increased upwelling at 20°N/S. Throughout the year, $\bar{v}^*$ anomalies are towards the equator in both the tropical northern hemisphere and tropical southern hemisphere. In comparison, the cloud effect in FLXHR on tropical and subtropical $\bar{v}^*$ is minor from August to October. Tracing back to the cloud radiative heating rate anomalies in Figure 4.7, it could be said that this discrepancy between FLXHR and MERRA-2 can be attributed to the enhanced radiative heating near the equator in FLXHR. Since the source of this heating is most likely TTL cirrus, these results suggest that the radiative heating effect of TTL cirrus, combined with the radiative cooling effect of subtropical clouds, tends to increase the strength of equatorial ascent through the tropopause, narrow the belt of upwelling, and also increase the meridional residual poleward transport in the shallow branch of the BDC.

Figure 4.14 and 4.15 show the vertical cross-sections of $\overline{w}^*$ and $\bar{v}^*$ from MERRA-2 and FLXHR, respectively. The dynamic and radiative residual velocities from MERRA-2 have reasonable agreement, although below 100 hPa there are significant differences. One possible cause of the discrepancy is that below 100 hPa latent heating still contributes to total diabatic heating, so the approximation in Equation (4.4) is not appropriate at lower levels. At and above 100 hPa, $\overline{w}^*$ and $\bar{v}^*$ are similar in direction and magnitude though the location of the subtropical $\bar{v}^*$ maxima is farther from the equator in the radiative solution. The equatorial upwelling in January is also stronger and narrower in the dynamic $\overline{w}^*$, as seen earlier in Figure 4.11. Compared to the MERRA-2 Q solution, the subtropical $\bar{v}^*$ maxima from FLXHR Q is slightly

higher in altitude in both January and July. The vertical depth of the subtropical $\bar{v}^*$ maxima in FLXHR is also larger.

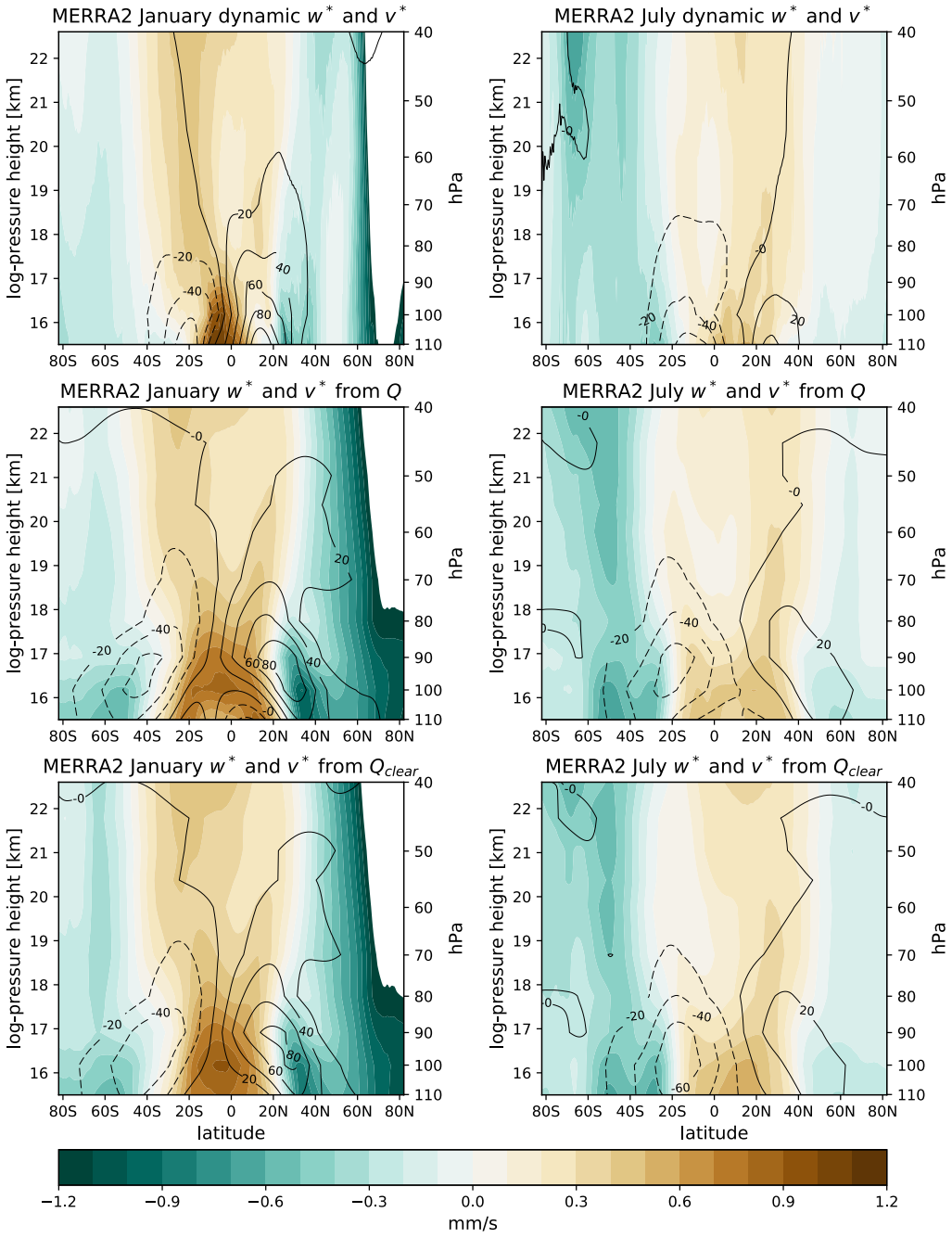

Figure 4.14 MERRA-2 January (left column) and July (right column) mean residual circulation calculated from dynamical fields (top), Q (middle), and Q_{clear} (bottom). Colored contours are for $\bar{\boldsymbol{w}}^*$ at intervals of 0.1 mm/s. Black contours in units of cm/s are for $\bar{\boldsymbol{v}}^*$ at intervals of 20 cm/s; dashed negative.

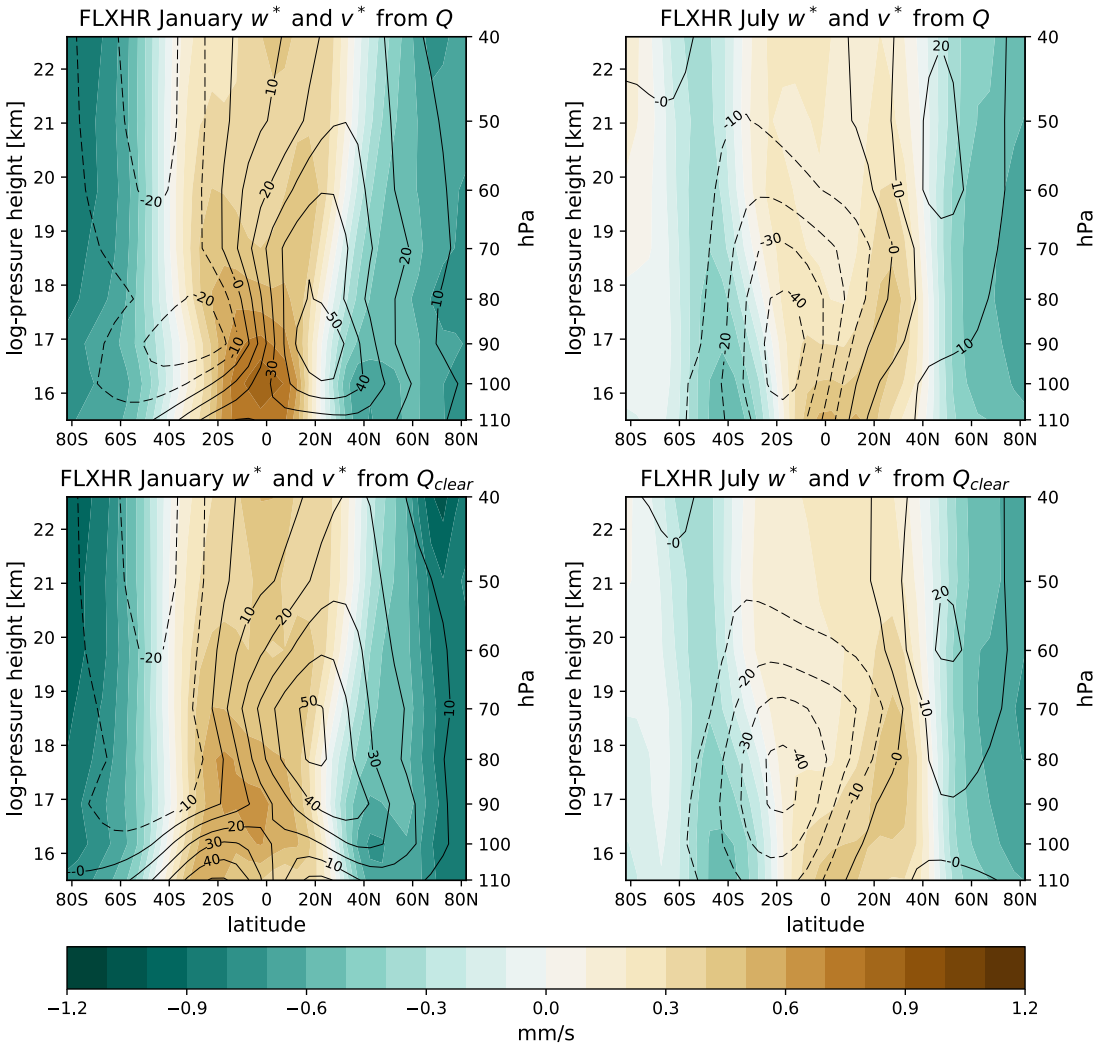

Figure 4.15 FLXHR January (left column) and July (right column) mean residual circulation calculated from Q (top row) and Q_{clear} (bottom). Colored contours are for $\overline{w}^*$ at intervals of 0.1 mm/s. Black contours in units of cm/s are for $\overline{v}^*$ at intervals of 10 cm/s; dashed negative.

The vertical cross-sections of cloud effects on $\overline{v}^*$ and $\overline{w}^*$ are presented in Figure 4.16. As discussed previously, in January the cloud effect of MERRA-2 and FLXHR are almost opposite in sign at tropopause altitudes (~100 hPa). Significant cloud effects are mostly found below 80 hPa. At the north pole, FLXHR suggests that clouds increase $\overline{w}^*$, but MERRA-2 only exhibits a very weak increase. There is also a discrepancy at 60°S where an increase in $\overline{w}^*$ during January and October is found in MERRA-2 but not FLXHR. The cloud effect in April is qualitatively

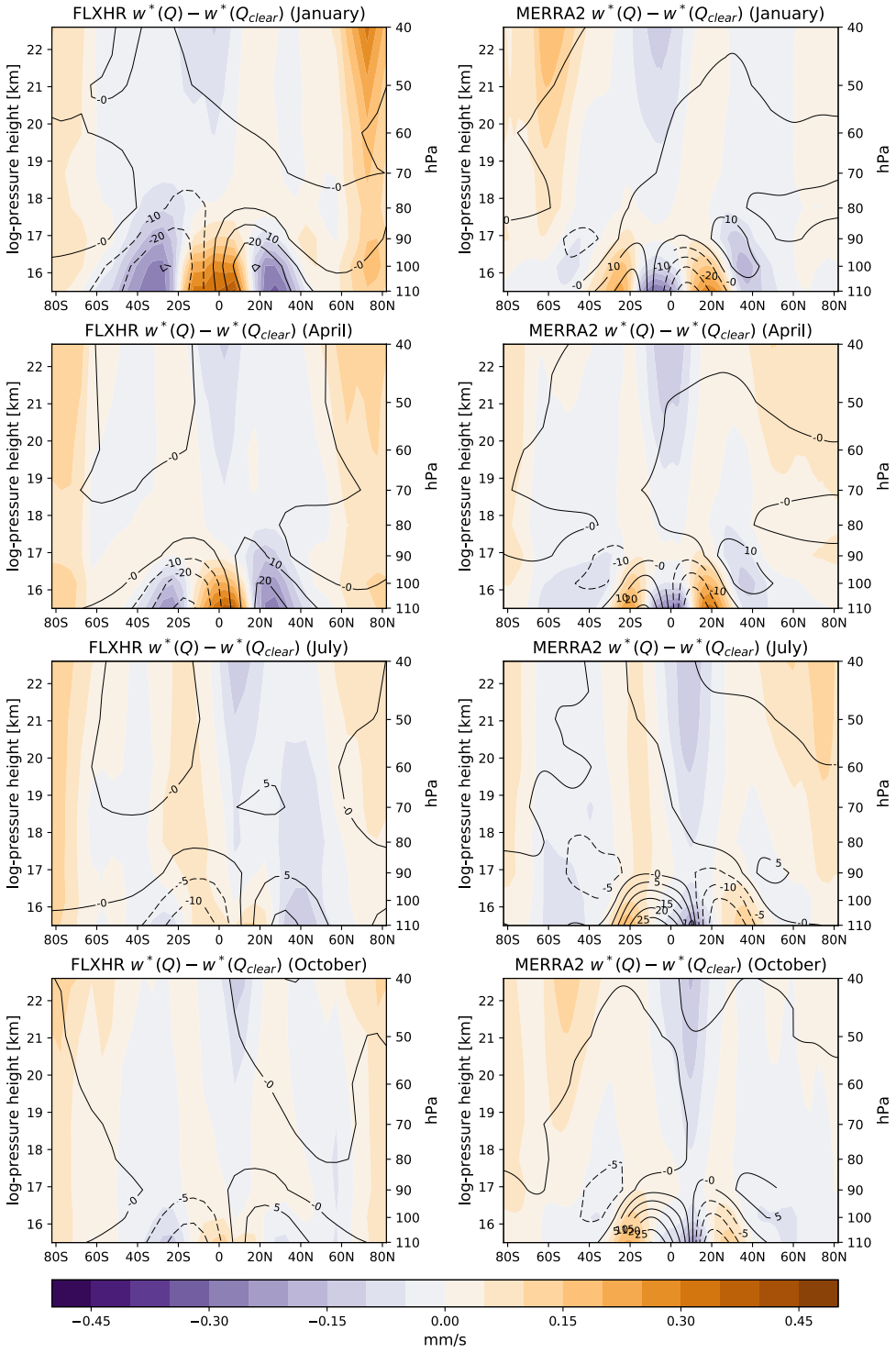

Figure 4.16 Differences between $\overline{\boldsymbol{w}}^*/\overline{\boldsymbol{v}}^*$ solved using Q and Q_{clear} for January (top row), April (second row), July (third row), and October (bottom row). Left column is for FLXHR and right column is for MERRA-2. Colored contours are for $\overline{\boldsymbol{w}}^*$ at intervals of 0.05 mm/s. Black contours are for $\overline{\boldsymbol{v}}^*$ at intervals of 10 cm/s for the top two rows and 5 cm/s for the bottom two rows; dashed negative.

similar to January. In July and October, the cloud effect in FLXHR is weak compared to January and April. MERRA-2, in contrast, has stronger cloud effects on $\bar{v}^*$ during July and October.

4.6 Radiative influence of cirrus on the residual circulation

Figure 4.17 shows the cloud fraction at 100 hPa derived from the 2B-CLDCLASS-LIDAR and MERRA-2. Apparently, in CLDCLASS there is a higher occurrence of clouds from November to March near the equator, most likely due to TTL cirrus clouds. In this chapter, we show that the tropopause level cloud effect on $\bar{v}^*$ and $\bar{w}^*$ is due to the lack of TTL cirrus clouds in MERRA-2. Although outside the scope of this chapter, a high occurrence of clouds at the south pole around July to September is found in MERRA-2. During these months there is a high probability of finding polar stratospheric clouds over Antarctica (Poole and Pitts, 1994). However, these clouds seem to have no obvious signature in the cloud effect on radiative heating rates (Figure 4.7).

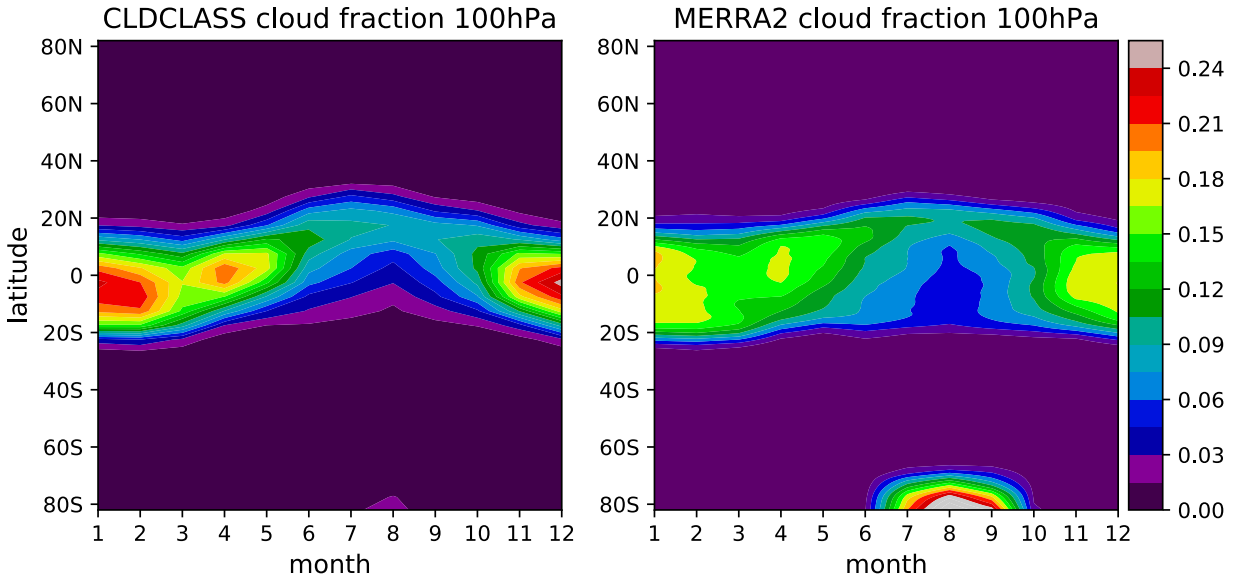

Figure 4.17 Cloud fraction at 100 hPa from 2B-CLDCLASS-LIDAR (left) and MERRA-2 (right) in 2007–2010.

In Section 4.6, the FLXHR all-sky solutions came from Q calculated using CloudSat footprints containing all types of clouds as well as clear-sky footprints. Alternatively, we can construct Q while excluding certain cloud types. By solving Q made this way, it is possible to examine how specific cloud types radiatively influence the BDC. Using the cloud type identification from 2B-CLDCLASS-LIDAR, in this section we calculate Q without footprints that contain cirrus; this field will be referred to as Q_{noci}. It is then used to solve for the residual circulation in the same manner as Section 4.5.

Previously we have demonstrated that clouds tend to increase the tropical upwelling near the tropopause (in FLXHR) and suggested that the radiative heating from cirrus clouds plays a vital role in the enhanced upwelling. Figure 4.18 and 4.19 show the difference in radiative heating between Q_{noci} and Q_{clear}, as well as the difference between the residual velocities obtained from them. Without cirrus clouds the tropopause-level heating is no longer present. At 100 hPa, the radiative heating anomaly due to all clouds but cirrus (left column of Figure 4.18) now resemble the heating anomaly of MERRA-2 (Figure 4.7). The cloud effects on $\bar{v}^*$ and $\bar{w}^*$ are now more similar to those of MERRA-2 (Figure 4.13), with a narrow belt of reduced $\bar{w}^*$ near the equator and equatorward $\bar{v}^*$ anomalies. The vertical cross-sections of cloud effects on $\bar{v}^*$ and $\bar{w}^*$, shown in Figure 4.19, also more closely resemble those of MERRA-2, especially in January. Without cirrus clouds, the bulk radiative effect of clouds on the BDC in boreal winter is to weaken the equatorial upwelling and also weaken the poleward $\bar{v}^*$ in the shallow branch of the BDC. In contrast, TTL cirrus clouds have the opposite effect on the residual circulation in the UTLS.

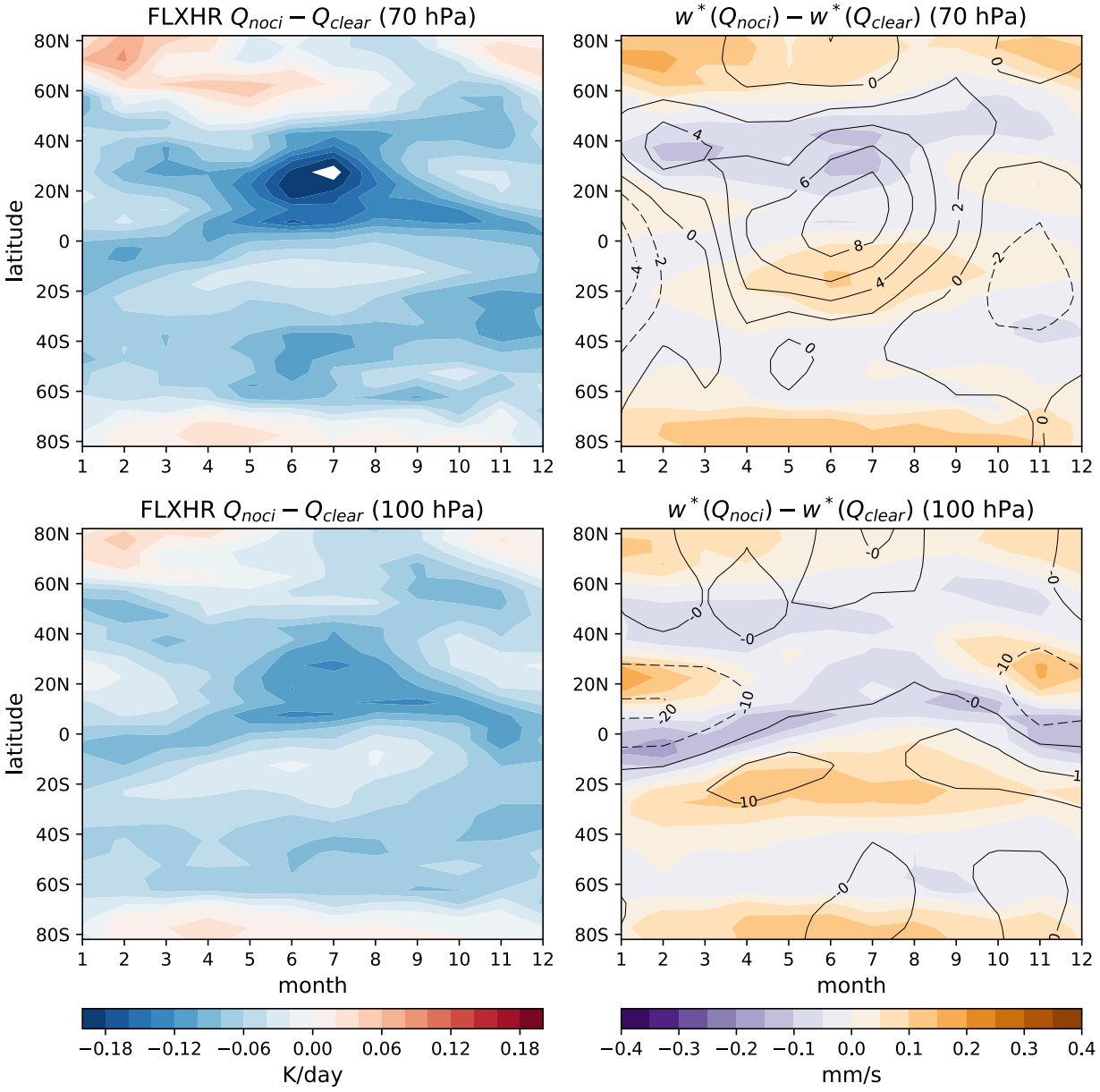

Figure 4.18 (Left column) Difference in mean radiative heating rates calculated from cloudy CloudSat footprints without cirrus (Q_{noci}) and from only clear-sky footprints (Q_{clear}). Contour intervals are 0.02 K/Day. (Right column) Difference between solutions of $\overline{\boldsymbol{w}}^*/\overline{\boldsymbol{v}}^*$ using Q_{noci} and Q_{clear}. Contour intervals are 0.05 mm/s.

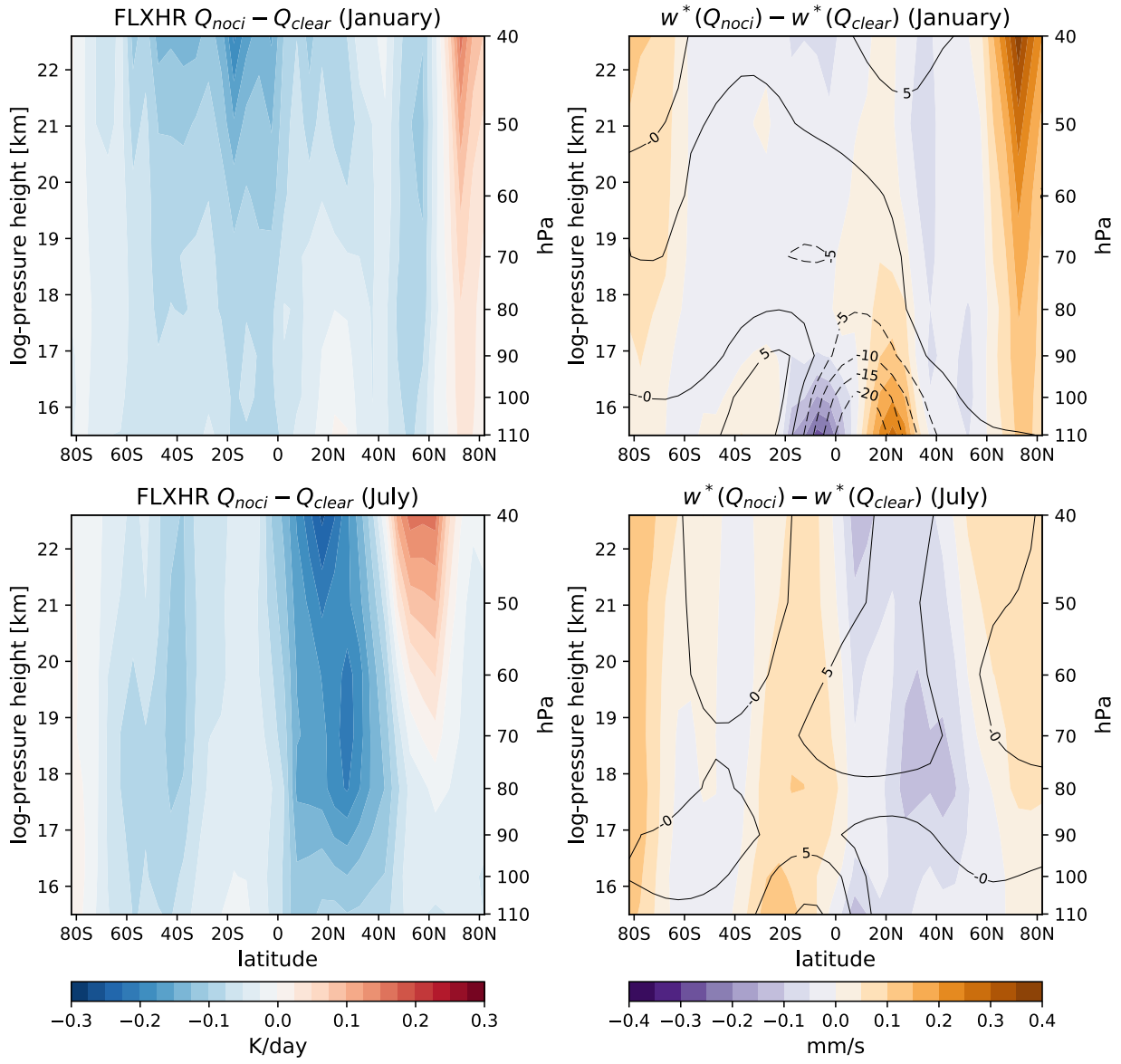

Figure 4.19 (Left column) Vertical cross sections of the difference in mean radiative heating rates calculated from cloudy CloudSat footprints without cirrus (Q_{noci}) and from only clear-sky footprints (Q_{clear}). (Right column) Difference between solutions of $\overline{w}^*/\overline{v}^*$ using Q_{noci} and Q_{clear}. Contour intervals are 0.05 mm/s.

4.7 Chapter summary

In this study we utilize satellite data sets and reanalysis to assess the effect of clouds on global UTLS heating rates and on the shallow branch of the BDC. Similar to previous studies, we found that at middle and low latitudes most clouds tend to reduce the radiative heating rates of the UTLS. In the tropics, TTL cirrus increase the radiative heating rates within the cirrus layer. We found that near the poles, clouds tend to increase the UTLS radiative heating. This may be explained by the inversion of temperature near the surface, which imply that cloud top temperatures may be warmer than the surface temperature. The increased longwave upwelling would then explain why the polar UTLS heating rates are increased. The radiative heating anomalies due to clouds as represented by MERRA-2 and FLXHR were similar at the lower stratosphere (70 hPa) but not at 100 hPa where FLXHR contains significant positive heating anomalies near the equator.

The fields of radiative heating rates from MERRA-2 and FLXHR were used to diagnose the BDC by calculating the mean residual velocities under the TEM framework. The method of calculation was validated through the good agreement of residual velocities derived from the dynamical field (winds) and from radiative heating rates. By solving for the residual velocities using all-sky and clear-sky radiative heating, we examined the features of the BDC circulation in the global UTLS and how clouds radiatively influence the circulation. In both the residual velocities derived from FLXHR and MERRA-2, we showed that the influence of clouds is strongest during boreal winter where the $\overline{w}^*$ and $\bar{v}^*$ below 80 hPa exhibit differences on the order of 0.1 mm/s and 10 cm/s, respectively. At higher heights, the radiative influence of clouds on $\overline{w}^*$ is slightly weaker in magnitude, and significantly weaker on $\bar{v}^*$ (on the order of 1 cm/s). While, on average, the cloud effects represented by FLXHR is to increase the tropical upwelling

and also increase the poleward motion in the shallow branch of the BDC, we found the cloud effects in MERRA-2 to have an opposite effect. By solving for $\overline{w}^*$ and $\overline{v}^*$ using FLXHR footprints without cirrus clouds, the cloud effects become similar to that of MERRA-2. This finding suggests that clouds other than cirrus tend to weaken the shallow BDC. However, the effect of TTL cirrus heating is strong and more than compensates for the weakening due to other cloud types. At the poles, both MERRA-2 and FLXHR showed that clouds increase $\overline{w}^*$, implying that the polar descent of the BDC may be weakened by the increased UTLS radiative warming due to clouds.

A possible direction of future work is to account for the feedback effect of cloud radiative heating on atmospheric temperature. Since changes in cloud radiative heating will change the distribution of temperature, the meridional temperature gradients will be modified and there may be significant changes to the BDC. The method in this study cannot account for this, so our results can only be interpreted as the "radiative" influence of clouds on the BDC and not the total influence. Studies such as Li et al. (2017, 2019) have investigated the role of cloud radiative effects on midlatitude jets shifts and the tropospheric circulation by rendering clouds radiatively transparent in climate models. A study using this method to evaluate the interaction between cloud radiative effects and the BDC would be valuable, and results from our study can serve as a useful complement in decoupling the mechanisms through which clouds can contribute to the large-scale middle atmosphere circulation.

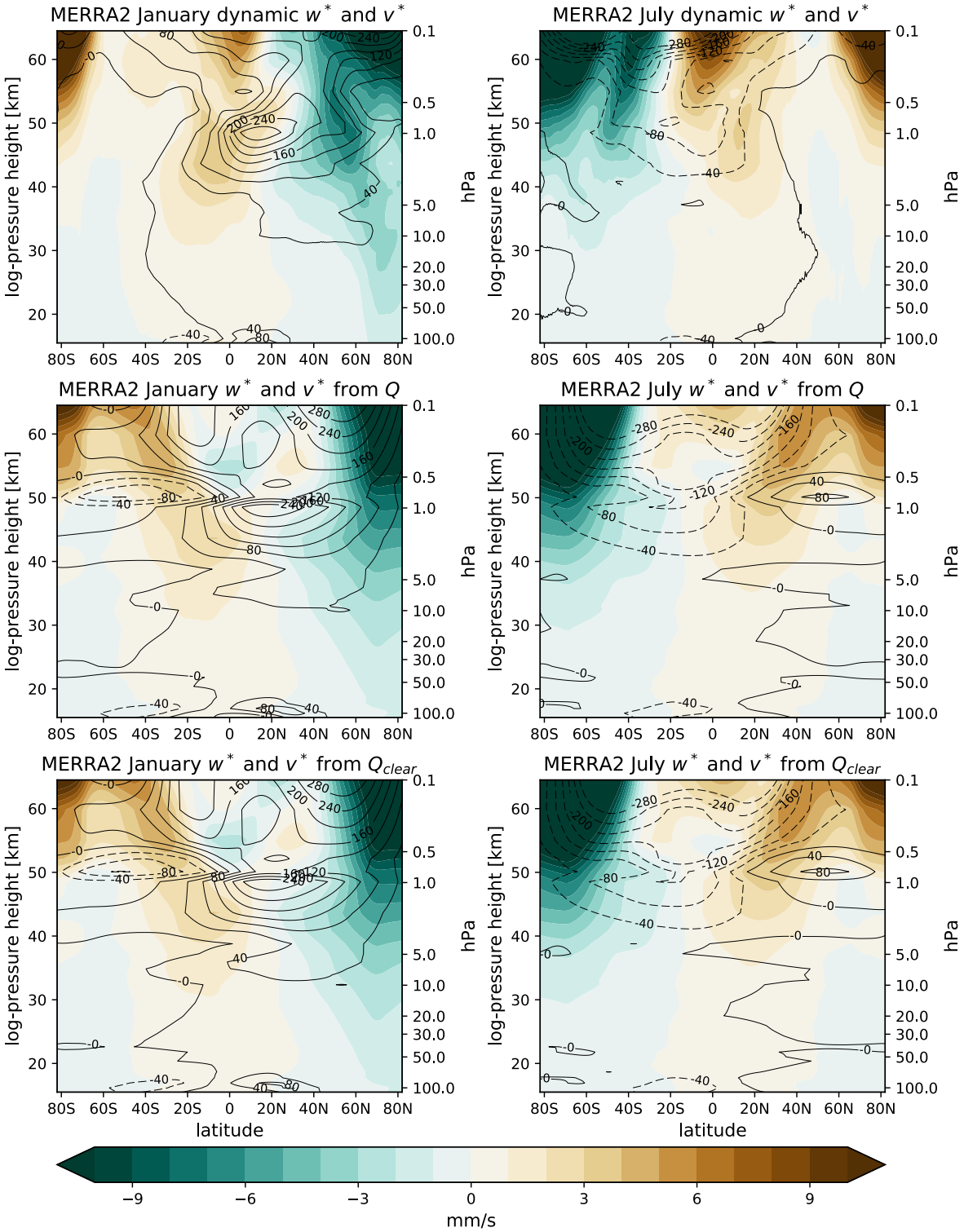
MERRA2 January dynamic w^* and v^*
MERRA2 July dynamic w^* and v^*
MERRA2 January w^* and v^* from Q
MERRA2 July w^* and v^* from Q
MERRA2 January w^* and v^* from Q_{clear}
MERRA2 July w^* and v^* from Q_{clear}
log-pressure height [km]
hPa
latitude
80S 60S 40S 20S 0 20N 40N 60N 80N
mm/s

Figure 4.20 Same as Figure 4.14 except for 100 to 0.1 hPa. Colored contours are for $\overline{w}^*$ at intervals of 1 mm/s. Black contours in units of cm/s are for $\overline{v}^*$at intervals of 40 cm/s; dashed negative.

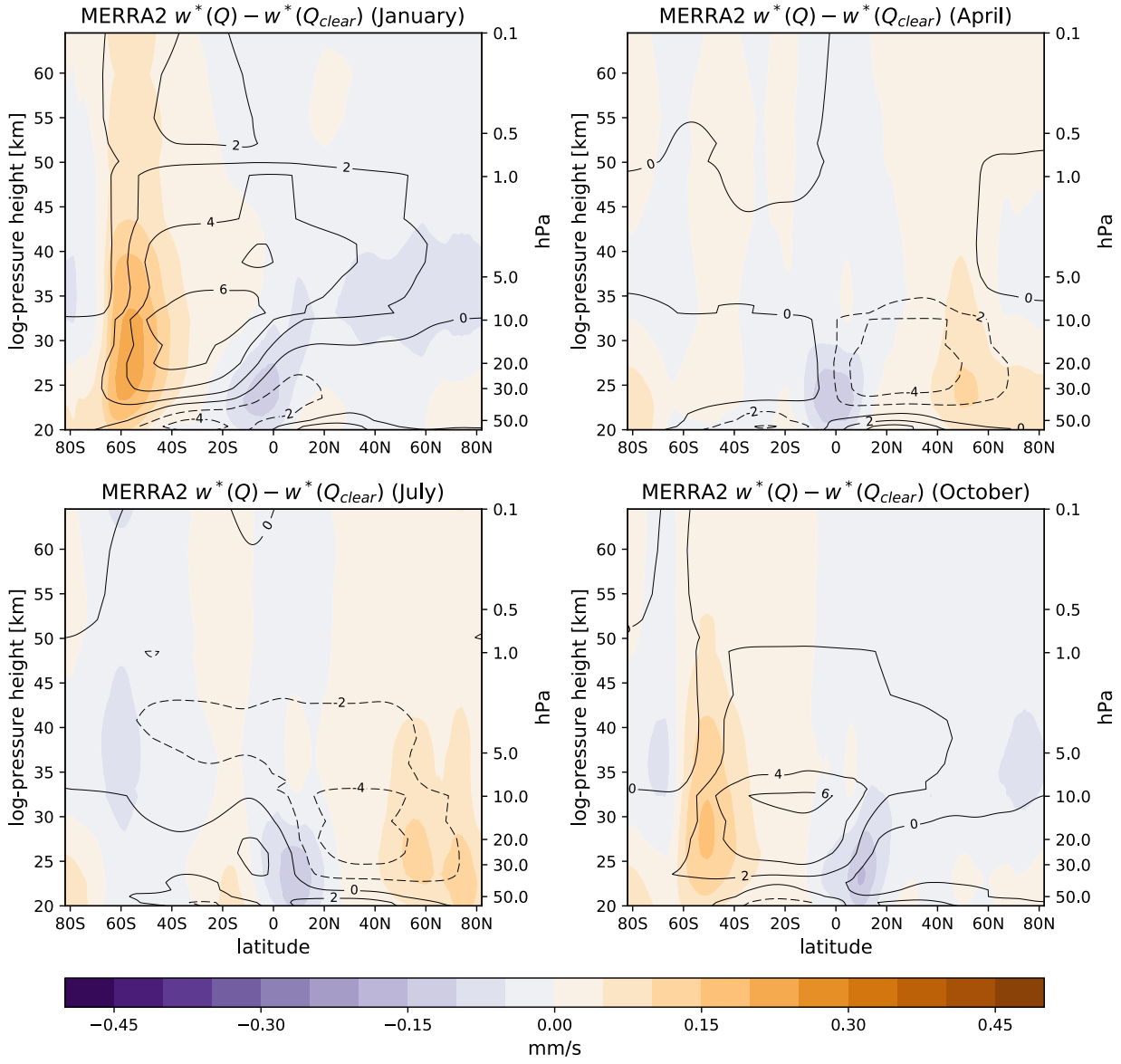

Figure 4.21 Difference between $\overline{w}^*/\overline{v}^*$ solved from Q and Q_{clear}, calculated from MERRA-2. Colored contours are for $\overline{w}^*$ at intervals of 0.05 mm/s, and black contours are for $\overline{v}^*$ at intervals of 2 cm/s.

Chapter 5
Summary

The distribution of trace gases in the UTLS is determined largely by the BDC, which contains descending branches at the poles, poleward motion in the midlatitudes, and an upwelling branch through the TTL. Because of this, the TTL is a vital pathway of troposphere-to-stratosphere transport. Its temperature variability modulates the moisture of upwelling air, and cloud formation in the TTL is a requisite process in the dehydration of air prior to entering the stratosphere. The tracer transport in the TTL, and also in the global UTLS, is balanced by the distribution of radiative heating at these altitudes. This dissertation investigates dynamical and radiative processes related to the TTL and UTLS through a combination of remote sensing and reanalysis data sets.

Moisture in the tropical lower stratosphere is strongly correlated to temperatures at the tropical tropopause. Since a significant portion of irreversible troposphere-to-stratosphere transport occurs over the Maritime Continent and Western Pacific region, tropopause temperatures in this region play a key role in determining the amount of water vapor entering the stratosphere. During boreal winter, there is a large temperature minimum over this region that resembles the shape of a horseshoe, attributable to the stationary Rossby and Kelvin waves generated from tropical latent heating. Chapter 2 discusses these wave responses to tropical latent heating and how they may relate to the vertical distribution of latent heating and to the convective and stratiform components of latent heating. Using temperature and latent heating

retrievals from satellite observations, we show that latent heating below 6 km has weak influence on temperatures in the tropical UTLS. Also, we found that the stratiform component of latent heating has higher association with UTLS temperatures. A possible explanation for this may be that stratiform latent heating has a higher heating peak and therefore is more effective at perturbing the UTLS. However, the PCA analysis suggested that a large amount of variability is associated with the deep convective mode of heating. As an alternative explanation, it is possible that the stratiform latent heating is highly correlated with UTLS temperatures not because it causes the UTLS temperature anomalies through its own latent heating but because it precedes deep convective heating that is strong and deep enough to cause the stationary wave patterns.

The main contribution of this study, in our view, is demonstrating through observations that variations in latent heating altitude will also change the response of the TTL temperatures. However, it is difficult to disentangle the exact roles of stratiform or deep convective heating. As future work, experiments using idealized model would be valuable for studying the atmospheric response to heating of different depths and also different modes (i.e. convective, stratiform, and deep convective). In addition, our study focuses on equatorial heating. Examining the characteristics of off-equatorial heating from sources such as the Southern Pacific Convergence Zone or the Asian Monsoon, would provide useful insight for further understanding the processes that connect latent heating to UTLS temperature variability.

Cirrus formation in the TTL is an active field of research and is difficult to represent accurately in climate models. Gravity and Kelvin wave cause temperature perturbations (T') that facilitate cloud formation through cooling and increasing the relative humidity with respect to ice. A recent study found that, in addition to T', the vertical gradient of wave temperature perturbations (dT'/dz) may be important for cirrus formation and maintenance. We explore the

connection of TTL cirrus clouds to T' and dT'/dz in Chapter 3 using lidar observations of TTL cirrus and temperature soundings from RO. Clouds detected by CALIPSO were collocated to temperature profiles from RO to analyze the altitude of clouds in relation to wave anomalies. Four phases of waves were defined according to the sign of T' and dT'/dz. We found that 57% of all TTL clouds were observed within the phase where T'<0 and dT'/dz<0. In contrast, 24% of TTL clouds were within where T'<0 and dT'/dz>0. Evidently, there is a strong association of cloud occurrence to dT'/dz. Our work suggests that the results of Kim et al. (2016b), who showed through in-situ aircraft observations that a large fraction of clouds over the Pacific were found in T'<0 and dT'/dz<0, is a general feature of the TTL, and the role of dT'/dz is significant throughout the tropics and in all seasons. Aside from confirming the importance of dT'/dz, one of the main contributions of this work is demonstrating that the amplitude of T' is related to cloud occurrence. Regions with higher (lower) values of T' is associated with a lower (higher) probability of finding clouds.

Due to the vertical resolution of RO, the waves included in this study have relatively long wavelengths and low frequencies. It is possible that, due to the different time scales of the wave cooling, fast and slow waves facilitate cloud formation and maintenance in different ways. As such, it is currently unclear whether dT'/dz is also important for fast gravity waves. Also, how dT'/dz<0 is favorable for clouds remains an active subject of research. A possible approach to separate the roles of vertical velocity and temperature perturbations could be to impose two variations of gravity wave fluctuations in a numerical model. One would have the full gravity wave perturbation including temperature and winds, while the other would only have the temperature perturbations. Through this experimental setup, the behavior of the modeled cirrus

cloud could yield insight on whether the importance of dT'/dz comes from the vertical wind perturbations or from dT'/dz itself, or possibly from other factors.

Clouds absorb, emit, and scatter radiation, and as a result contribute to the radiative heating and cooling of the atmosphere. Although the effects of clouds on radiative heating are typically strongest near or within the cloud, they can also modify the radiative heating at greater heights by increasing or decreasing upwelling radiation. The final study in this dissertation examines how clouds influence the radiative heating rates in the UTLS and in turn the shallow branch of the BDC. Using radiative heating rates from the CloudSat/CALIPSO 2B-FLXHR-LIDAR algorithm and potential temperature fields from RO, we diagnose the shallow branch of the BDC at UTLS altitudes by solving for the residual meridional and vertical velocities under the TEM framework. The same method was applied to MERRA-2 radiative heating. Residual velocities obtained from clear-sky and cloudy-sky radiative heating rates were compared to assess the influence of clouds on the BDC. In 2B-FLXHR-LIDAR, enhanced radiative heating due to TTL cirrus was found to enhance the tropical upwelling strength and also the poleward velocities in the subtropics. In contrast, MERRA-2 lacks the increased heating from TTL cirrus and as a result the effect of clouds were to reduce the tropical upwelling and weaken the subtropical poleward transport. Both 2B-FLXHR-LIDAR and MERRA-2 suggests that clouds near the poles slightly slow the descent of the BDC. Below 80 hPa, differences of the residual velocities solved from clear-sky and cloudy-sky radiative heating rates are on the order of 0.1 mm/s (vertical velocity) and 10 cm/s (meridional velocity), which are comparable to the magnitude of the residual velocities. Results from this study illustrate that the modulation of radiative heating rates by clouds can have a significant influence in the upward mass transport through the TTL and meridional mixing of tracers in the lower stratosphere.

Appendix

Information Content of Visible and Mid-Infrared Radiances for Retrieving Tropical Ice Cloud Properties

A.1 Introduction

Clouds regulate the Earth's climate or energy balance through interactions with solar and terrestrial radiation (Liou, 1986). Cirrus on average cover 16.7% of the globe, and about 35% of cirrus clouds are found in the tropics within 15° of the equator (Sassen et al., 2008, 2009). In addition to radiatively influencing the climate, tropical cirrus is also linked to the amount of water vapor entering the stratosphere (Brewer, 1949; Jensen et al., 1996). Accurate representations of ice clouds are, therefore, necessary to accurately constrain climate processes in models. Furthermore, the manner in which clouds interact with the radiation field depends on their macrophysical and microphysical properties, including water path, particle size, geometric thickness, and height. These properties define the cloud's shortwave albedo, longwave emissivity and optical thickness which are fundamental to its radiative impacts. For this reason, much effort has been devoted to retrieving these parameters from a variety of satellite remote sensors, as well as surface-based observations and aircraft in-situ sampling.

Passive sensors such as the Atmospheric InfraRed Sounder (AIRS) (Aumann et al., 2003) and the Moderate Resolution Imaging Spectroradiometer (MODIS) (Barnes et al., 1998) have accumulated over a decade-long record of observations that is particularly valuable for

evaluating clouds in the context of climate processes and inter-annual variations. Several retrieval techniques have been developed to make use of these observations for estimating cloud properties. For example, the split-window technique (Inoue, 1985) retrieves cloud optical thickness and effective size by a lookup-table approach using brightness temperatures in the window region. For optically thicker clouds, the Nakajima-King approach (Nakajima and King, 1990) also retrieves optical thickness and effective particle size using a non-absorbing channel in the visible band and an absorbing channel in the near-infrared (NIR) region. For retrieving cloud top temperature, the CO_2 slicing method (Smith and Platt, 1978) utilizes channels within 13-15 μm to vertically position the cloud and is effective particularly for optically thin clouds. More recently, a number of approaches have also been developed for retrieving cloud macrophysical and microphysical properties simultaneously. One technique that is often adopted for this purpose is optimal estimation (OE) (Rodgers, 1976), which obtains an estimate that maximizes the *a posteriori* probability of the joint probability distribution between *a priori* estimates and the observations. OE has been effectively applied to global cloud retrievals using independent observations from MODIS (Cooper et al., 2007; Wang et al., 2016b), and AIRS (Kahn et al., 2014).

Maximizing the value of combining MODIS and AIRS observations requires careful consideration of the synergies between these instruments to improve and refine the state of passive retrieval techniques. In principle, OE provides a framework for optimally combining information from multiple instruments since it allows for any number of observations, or bands/channels, given that one can appropriately model the observations, their Jacobians, and the associated uncertainties. However, in practice, modeling the satellite-observed radiances and their Jacobians can be computationally expensive. As such, it is desirable to restrict the retrieval

to use only the channels most sensitive to the desired atmospheric state. Such channel selection is particularly important for hyperspectral sensors like AIRS, due to the large number of channels (2378), additional computational expense to calculating radiances at finer resolution (~1 cm^{-1}), and the varying influence of other parameters such as atmospheric temperature and humidity on each channel. There is, therefore, a need for objectively selecting optimal channel sets for cloud retrievals that maximize information while minimizing computation time. An objective way of determining the most crucial channels is through quantifying changes in information content (IC).

IC can be understood by recognizing that the problem of retrieving cloud properties is an inverse problem in which the range of possible states is characterized by a probability distribution. Upon obtaining a measurement, the range of probable states is generally reduced. Assuming the probability density of the states are Gaussian, the IC represents the magnitude of such reduction. More specifically, given a set of Jacobians that represent the sensitivity of the observations (radiances) to the retrieval variable, and the observation errors (noise, bias, etc.), IC represents the capability of an observation to reduce the width of the *a priori* PDF of possible states. Applied to spectral channels of spectrometers, this quantity naturally represents the impact of each channel on the retrieval. For this reason, IC plays a central role in channel selection methodologies (Rodgers, 1996). Sofieva (2003) demonstrated an IC channel selection approach on measurements from the GOMOS stellar occultation instrument for finding optimal channel combinations to retrieve atmospheric optical thickness. The selections of optimal MODIS channels for the retrieval of liquid or ice clouds, respectively, were reported in L'Ecuyer et al., (2006) and Cooper et al. (2006). Sourdeval et al. (2015) utilized IC to analyze the feasibility of retrieving cloud properties in multi-layer cloud configurations. An IC channel analysis was

employed by Wang et al. (2016a, 2016b) to diagnose MODIS channels in an optimal estimation retrieval.

Several sensitivity studies have examined the effectiveness of infrared radiances for retrieving ice cloud properties. Chung et al. (2000) analyzed the sensitivity of high-resolution mid-infrared IR radiances to ice cloud particle size, ice water path, cloud top position and thickness by varying these cloud properties in radiative transfer simulations, while Huang et al. (2004) adopted a similar approach to examine the sensitivity of IR radiances towards cloud optical thickness and particle size. Kahn et al. (2004) employed a statistical approach using empirical orthogonal function (EOF) analysis to examine the variance of mid-infrared radiances due to varying ice crystal shape, effective radius, ice water path, as well cloud height and thickness. Similar to such approaches, IC analysis also considers the channel sensitivities through the Jacobian but has the added advantage of including multiple error sources, especially those associated with forward modeling. In addition, IC analysis is especially compatible with optimal estimation, as it considers the error covariances of the *a priori* estimates.

In this study we apply an IC-based channel selection to identify the optimal set of AIRS channels for cloud property retrievals under three scenarios: a stand-alone AIRS algorithm, a combined AIRS-MODIS algorithm, and a combined active/passive retrieval that further utilizes cloud boundary information from CloudSat and CALIPSO. AIRS is a hyperspectral infrared spectrometer onboard the Aqua satellite with 2378 channels over wavelengths of 3.74–4.61 μm, 6.20–8.22 μm and 8.8–15.4 μm (Aumann et al., 2003). Its spatial resolution is 13.5 km by 13.5 km at nadir and 41 km by 21.4 km at the scan extremes. The AIRS version 6 ice cloud retrieval product is derived from an OE algorithm, providing estimates of the cloud thermodynamic phase, effective diameter (D_e), cloud optical thickness (COT), and cloud top temperature (T_c) at

the AIRS footprint resolution (Kahn et al., 2014). The OE algorithm is applied to the 27% of AIRS FOVs that are identified as containing an ice cloud thermodynamic phase (Jin and Nasiri, 2014; Kahn et al., 2015). This algorithm uses 59 channels located within 8–15 μm, selected to include three spectral regions: CO_2 slicing channels within 13.2–14.5 μm, and the window regions between 10–12 μm and 8.8–9.15 μm, manually picked by avoiding strong absorption lines and noisy channels. Although these spectral regions have been shown to have sensitivity to the aforementioned cloud properties (Huang et al., 2004), the channels were not optimized through a rigorous objective channel selection methodology. Also, it is known that some channels are specifically useful for certain types of clouds. For instance, the 13–15 μm region is effective for obtaining cloud top temperature of optically thin clouds (Smith and Platt, 1978), whereas for optically thick clouds, such as anvil tops, the 11 μm brightness temperature is often used as a proxy for its physical temperature.

Here we apply a formal channel selection process to a variety of ice clouds objectively extracted using a clustering algorithm on a database of cloud retrievals from observations of ground radar/lidars deployed by the U. S. Department of Energy Atmospheric Radiation Measurement (ARM) program (Ackerman and Stokes, 2003). This diverse collection of cloud states spans a wide range of optical and geometrical thicknesses, particle size distributions, and heights, allowing optimal channels to be selected for a range of scenes appropriate for retrievals over the tropics. Satellite viewing geometry is considered through simulations at seven different viewing angles. Ocean, vegetation, and bare soil surfaces are examined separately to quantify the difference in optimal channel configuration over distinct land and ocean surfaces. Through considerations of the above factors and appropriate representations of forward model uncertainties, it is anticipated that the resulting AIRS channel set will be optimal for ice cloud

retrievals in most scenarios. In addition to AIRS, IC channel selection is also applied to MODIS, to gain insight into how the two instruments can be jointly used for ice cloud retrievals.

While the wide swaths of AIRS and MODIS provide important sampling, it has been demonstrated that passive cloud retrievals can benefit from the more precise delineation of cloud boundaries afforded by active sensors. Cooper et al. (2003) for example showed that having accurate cloud boundary information (cloud top temperature or height) can reduce the error in retrieved particle size and COT. Conversely, the lack of accurate boundary information can cause large errors. Thus, in addition to exploring an optimized AIRS channel selection, this study also explores the scenario where passive retrievals may further leverage cloud boundary information from active radar/lidar measurements. Both AIRS and MODIS fly aboard the Aqua satellite in the A-Train constellation, which includes CloudSat and CALIPSO. These sensors have obtained multiple years of collocated observations valuable for extracting high quality estimates of cloud properties. In this study, we examine the impacts of having CloudSat cloud top boundary on the optimal passive channels for ice cloud retrievals.

A.2 Ice cloud database construction

To account for the dynamic range of ice cloud properties found in the tropics, the IC of all AIRS and MODIS channels must be evaluated over a wide range of ice cloud types. The ARM program has deployed active ground-based sensors at multiple stationary sites in the tropical western pacific (TWP), Lamont, Oklahoma, and in Barrow, Alaska. For the three TWP sites, the "Cloud Properties and Radiative Heating Rates for TWP" (CPRHR henceforth) data set (Comstock et al., 2013) provides cloud microphysical properties and heating rate profiles retrieved from ground-based measurements by the millimeter wavelength cloud radar (Moran et

al., 1998) and the micropulse lidar (Spinhirne, 1993). This study uses vertical profiles of generalized effective ice particle size (D_{ge}) (Fu, 1996), ice water content (IWC), and cloud phase provided in CPRHR. The retrieval method used by CPRHR to determine cloud microphysical properties depends on which of the two instruments detect clouds (radar, lidar, or both). If only radar detects clouds, an empirical relation based on Hogan et al. (2006) is used to obtain IWC and D_{ge} from the radar reflectivity. If only lidar detects clouds, the retrieval follows the method outlined by Heymsfield et al., 2005. If both instruments detect clouds, the retrieval algorithm of Wang and Sassen (2002) is used. Uncertainties in the CPRHR data set are evaluated in Comstock et al. 2013 but it is noted that the analysis conducted here is not sensitive to the accuracy of this input data set. It merely serves to provide a realistic distribution of cloud scenes that spans the range of regimes expected in the tropics.

For the TWP site at Darwin, Australia, the CPRHR covers approximately six years from 2005 to 2011. Performing IC analysis on all clouds available is not feasible and redundant, as many clouds may have similar features. To reduce redundancy and provide a tractable set of unique cloud types that span the range of clouds observed in nature, we use the k-means clustering algorithm, which partitions the data into k (user-specified) clusters. The k-means algorithm initializes k centroids, assigns each data point to the closest centroid, and then perturbs the centroid positions to minimize the sum of Euclidean distance between all data points and their respective centroids (Wilks, 2011). For clustering the cloud profiles, we define five features that describe each cloud: mean D_e, mean IWC, cloud top height, T_c, and cloud geometric thickness. The clustering analysis is limited to single-layer ice clouds whose T_c is below 253.15 K; clouds not meeting these criteria are excluded.

The choice of k is based on the criterion that the intra-cluster spread of COT should be small, so that all clouds in the cluster are well-represented by the cluster center. This is to ensure that the channels selected for each cloud type can be associated with its occurrence frequency in

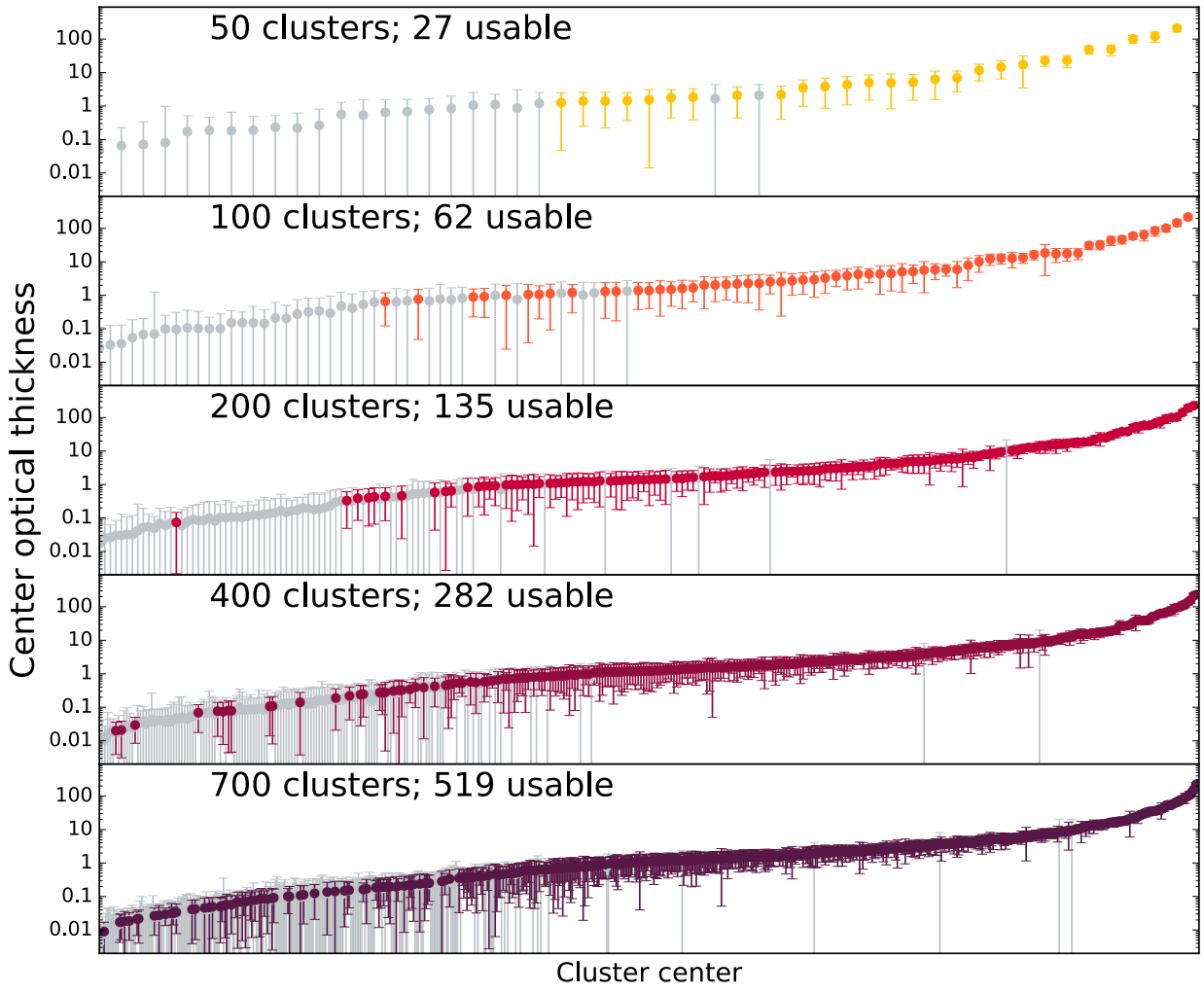

Figure A.1 Distribution of cluster center COTs from k = 50, 100, 200, 400 and 700 clusters. Error bars represent the intra-cluster standard deviation. Gray dots indicate clusters deemed unusable, due to its standard deviation being greater than the center value.

the channel selection process. As a simple quantitative test of this requirement, we require that the standard deviation of COT be less than the center value. Figure A.1 shows the application of this criterion onto clusters resulting from various choices of k. With relatively smaller numbers

of clusters (k=50, 100, 200), many clusters have a large standard deviation, and are therefore too broad for our analysis. Furthermore, choosing a smaller k leaves very few thin cloud clusters, which are among the most populous and important ice cloud types. Even at k=400, clusters with narrow COT ranges remain quite sparse. Through experimentation it was determined that k=700 adequately represents the spectrum of ice clouds in the composite ARM TWP data set.

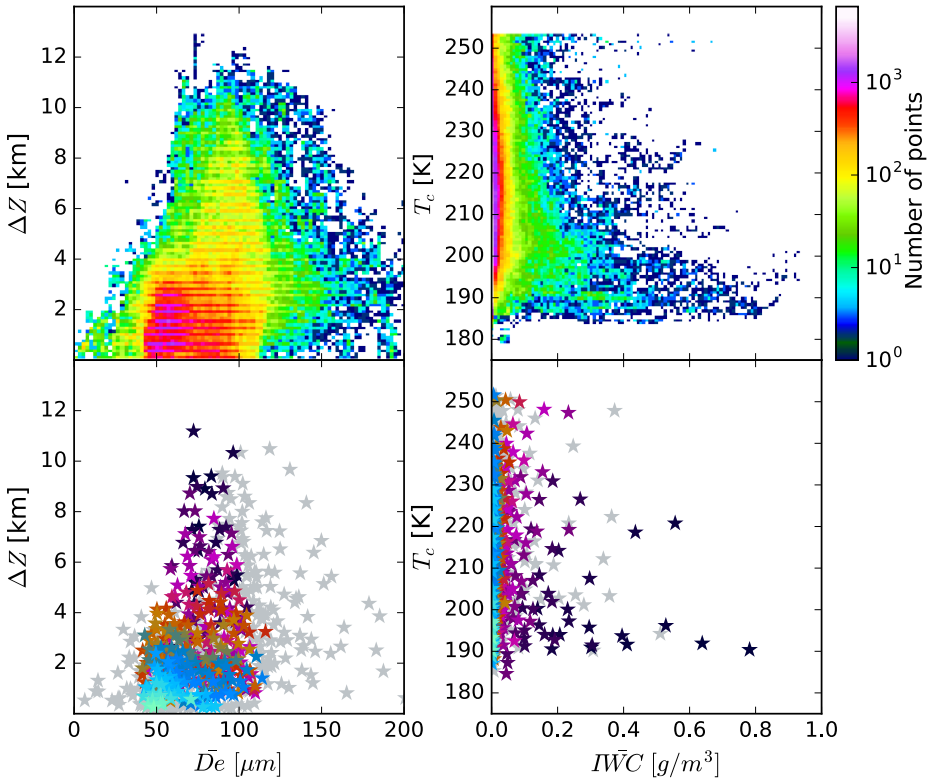

Figure A.2 Top row: Density plots of all data before clustering, for geometric thickness versus mean D_e (top left), and T_c versus mean IWC (top right). Bottom row: Scatter plot of cluster centers; gray stars indicate clusters not used in the simulations due to particle size being outside the valid range of the ice crystal scattering properties. Cluster used in the IC analysis are represented as stars colored by COT.

Figure A.2 compares the raw data (before clustering) to the clustering result. Before clustering, there were approximately $4.14*10^5$ single-layer clouds of ice phase with temperatures

below 253.15 K. After clustering using k=700, the resulting cluster centers span the complete range of cloud properties present in the raw data set. Due to the limitations of the ice crystal scattering property data set (Baum et al., 2014), which is limited to D_e between 10 and 120 μm, 348 out of the 700 clusters were usable (shown as colored stars in the bottom row of Figure A.2). The number of clouds included by the 348 clusters is approximately $2.19*10^5$. Scatter plots of cluster centers show that the centers cover a dynamic range comparable to the raw data set in every cloud property aside from particle size.

A.3 Channel selection using information content

A.3.1 Radiative transfer model

A model based on the Vector Linearized Discrete Ordinate Radiative Transfer model (VLIDORT) (Spurr, 2006) is used to simulate radiances and Jacobians. The High-Resolution Transmission Molecular Absorption (HITRAN; Rothman et al., 2009) database was used for gas attenuation, and the treatment of Rayleigh scattering follows the methodology of Bodhaine et al. 1999. Line-by-line radiances and Jacobians simulated with this model were convolved with AIRS and Aqua MODIS spectral response functions (SRF) in order to simulate the satellite-observed radiances. It is assumed that all simulated AIRS and MODIS radiances are overcast (100% cloud fraction), and that AIRS and MODIS pixel sizes are the same.

Time-collocated temperature and humidity profiles for the CPRHR data set are obtained from the Merged Sounding (MERGESONDE) product (Troyan, 2012) also available from ARM. Trace gas profiles come from two sources: Air Force Geophysics Laboratory atmospheric constituent profiles (Anderson et al., 1986), and the Monitoring Atmospheric Composition and Climate (MACC) reanalysis (Inness et al., 2013). The vertical resolution of input profiles for

each simulation was approximately 250 m inside clouds, and 1 km outside of clouds for pressure levels below 50 hPa; above 50 hPa, levels are specified at 30, 20, 10, and 1 hPa.

Radiances and Jacobians were simulated over three surface types: ocean, vegetation, and bare soil. The former uses ocean spectral emissivities derived from Hale and Querry (1973) and Sidran (1981), while the vegetation and bare soil are represented by grass and loamy sand spectral emissivities from the Advanced Spaceborne Thermal Emission Reflection Radiometer (ASTER) spectral library (Baldridge et al., 2009). Spectral emissivities of these three surface types are shown in Figure A.3. All simulations assume daytime conditions with a solar zenith angle of 20°, at seven different viewing angles ±45°, ±30°, ±15°, and 0°, where negative angles indicate that the sensor is on the same side of the sun.

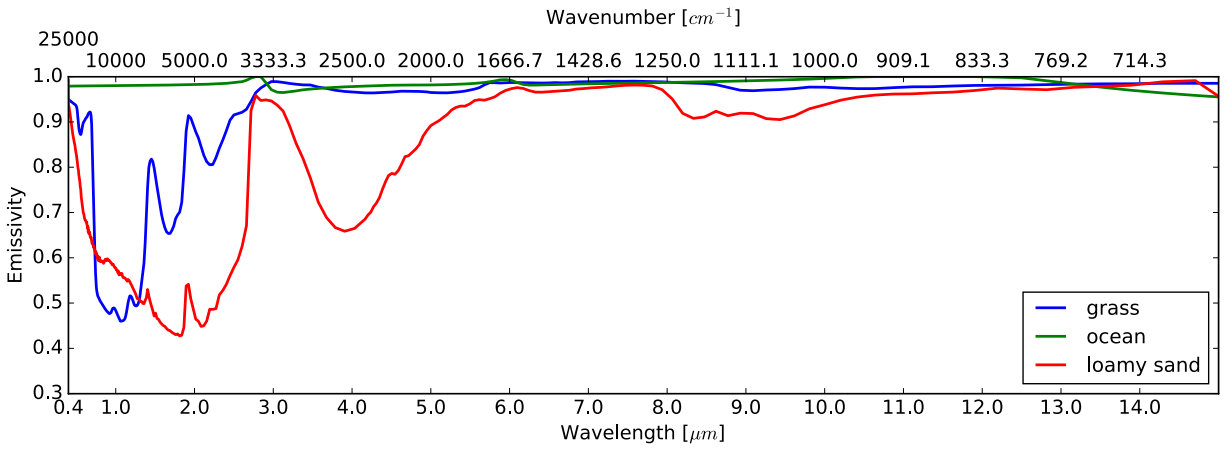

Figure A.3 Spectral emissivities of ocean, vegetation (grass), and bare soil (loamy sand).

A.3.2 Information content

The information content analysis conducted here is rooted in the concept of Shannon entropy introduced by Shannon and Weaver (1949):

$$S(P) = -\sum_i P(x_i) log_2\big(P(x_i)\big). \tag{A1}$$

The Shannon entropy (SE) is related to the number of possible states of any random variable. Specifically, the SE in bits is the number of binary digits required to represent the possible range of outcomes. For example, the outcome of a coin can be represented by one bit since there are only two possible outcomes (heads or tails). In this case, the SE would be 1. With two coins, the SE increases to 2, and so on. The concept of SE has been frequently used in remote sensing to quantify the extent to which measurements reduce the SE, or, equivalently, the possible solution space of a retrieved variable. This represents a reduction of uncertainty or increased knowledge of the variable so it is desirable to find measurements that can offer the greatest reduction in SE, i.e. the most IC. One implied assumption here is that the retrieved variables follow Gaussian distributions. Otherwise, the Shannon entropy may not be an appropriate measure of information (Petty, 2018).

Let the probability density function (PDF) of the cloud property, x, to be retrieved be $P_0(x)$ and $P_1(x)$ before and after making a measurement, respectively. The IC of the measurement H can be formally defined as the difference in entropy S of the two PDFs:

$$H = S(P_0) - S(P_1). \tag{A2}$$

Rodgers (2000) has shown that the multivariate Gaussian distribution for a vector of retrieved variables is

$$S\big(P(x)\big) = c + \frac{1}{2}\ln\ |\boldsymbol{S_x}| \tag{A3}$$

where c is a constant and $\boldsymbol{S_x}$ is the error covariance matrix of the retrieved variables. It follows that the IC of a measurement can be expressed as

$$H = \frac{1}{2}\ln|\boldsymbol{S_a}| - \frac{1}{2}\ln|\widehat{\boldsymbol{S}}| = \frac{1}{2}\ln|\boldsymbol{S_a}\widehat{\boldsymbol{S}}^{-1}| \tag{A4}$$

where $\boldsymbol{S_a}$ and $\widehat{\boldsymbol{S}}$ are the prior and posterior error covariance matrices of the retrieved variables, respectively. In our analysis, $\boldsymbol{S_a}$ is obtained from the climatological standard deviation of the retrieved cloud properties in the ARM TWP data set. Given the Jacobian $\boldsymbol{K}$ of the measurement with respect to the retrieved variables and the total error covariance of the measurements, $\boldsymbol{S_\epsilon}$, $\widehat{\boldsymbol{S}}$ can be expressed as

$$\widehat{\boldsymbol{S}} = (\boldsymbol{K^T S_\epsilon^{-1} K} + \boldsymbol{S_a^{-1}})^{-1} \tag{A5}$$

which is used in Equation A4 to calculate the IC of the measurements. We define the Jacobian $\boldsymbol{K}$ as

$$\boldsymbol{K} = \begin{pmatrix} \frac{\partial I_{v_1}}{\partial \ln(\mathrm{COT})} & \frac{\partial I_{v_1}}{\partial \ln(D_e)} & \frac{\partial I_{v_1}}{\partial \ln(T_c)} \\ \frac{\partial I_{v_2}}{\partial \ln(\mathrm{COT})} & \frac{\partial I_{v_2}}{\partial \ln(D_e)} & \frac{\partial I_{v_2}}{\partial \ln(T_c)} \\ \vdots & \vdots & \vdots \\ \frac{\partial I_{v_N}}{\partial \ln(\mathrm{COT})} & \frac{\partial I_{v_N}}{\partial \ln(D_e)} & \frac{\partial I_{v_N}}{\partial \ln(T_c)} \end{pmatrix} \tag{A6}$$

where I_{v_i} is the radiance of channel i at wavelength v_i, COT is cloud optical thickness, D_e is effective diameter, T_c is cloud top temperature, and N is the total number of channels.

To apply equation A4 to a single channel, we take the row of $\boldsymbol{K}$ corresponding to the channel number i, $\boldsymbol{k_i}$, and assume the observation error covariance is diagonal, so that each channel has an associated error variance σ_i^{-2}. Then the IC of a single channel can be written as

$$H = \frac{1}{2}\ln\left|\boldsymbol{S_a}\left(\boldsymbol{k_i^T}\sigma_i^{-2}\boldsymbol{k_i} + \boldsymbol{S_a^{-1}}\right)\right| \tag{A7}$$

$$= \frac{1}{2}\ln\left|\sigma_i^{-2}\boldsymbol{S_a}\boldsymbol{k_i^T}\boldsymbol{k_i} + \boldsymbol{I}\right|.$$

We use a sequential selection procedure similar to that described by Sofieva (2003) to identify the optimal set of channels for retrieving the properties of each cluster at all seven viewing angles over three surface types. Figure A4 depicts the process graphically. To begin, Equation A7 is used to calculate the IC of each channel (shown as the magenta line in Figure A4). When the IC of all channels are determined, we select the channel with highest IC (shown as the magenta star). After this first selection, the selected channel is "added" to the *a priori* error covariance matrix by

$$\boldsymbol{S_{a,new}} = (\boldsymbol{k_i^T}\sigma_i^{-2}\boldsymbol{k_i} + \boldsymbol{S_a^{-1}})^{-1} \quad \text{(A8)}$$

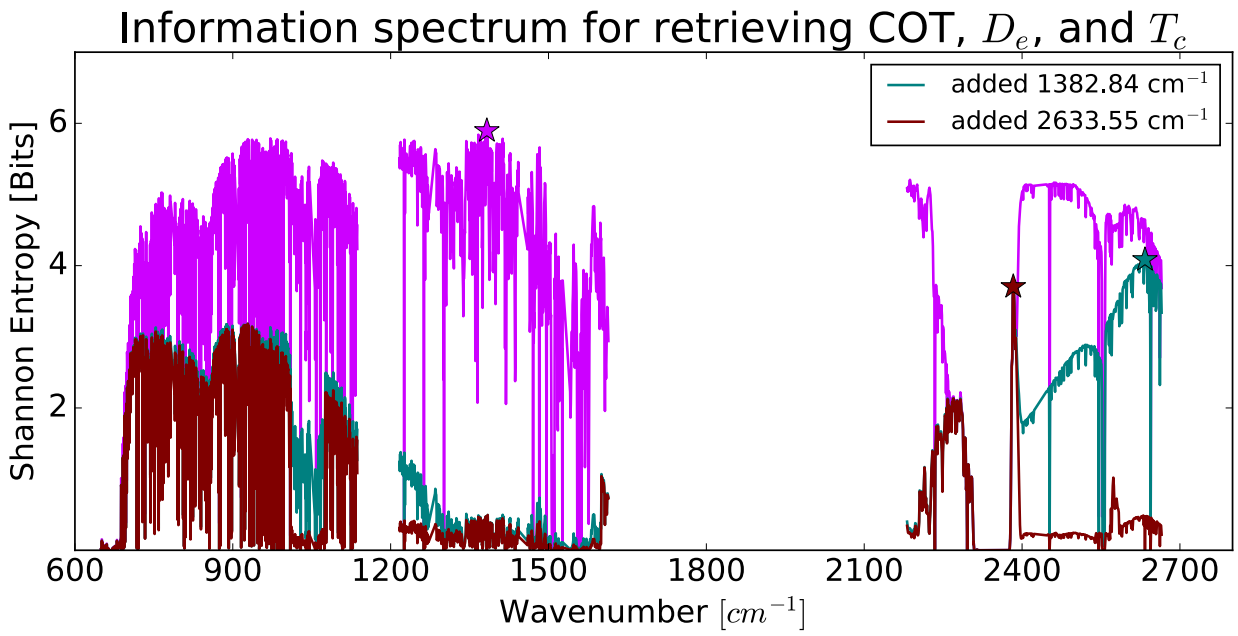

Figure A.4 Demonstration of channel selection using IC: AIRS Information spectrum before channel selection (magenta), after adding the 936.78 cm^{-1} channel to the a priori error covariance matrix (teal), and after adding both 936.78 cm^{-1} and 2616.38 cm^{-1} channels (maroon). Stars indicate the channel with highest IC during each step.

We can now calculate the IC of every channel again (teal line in Figure A4) with respect to the updated *a priori* error covariance matrix. From the new IC spectrum we can select a channel that yields the most complimentary information to the first. This process is then repeated to select the desired number of channels.

The number of channels to select may be determined from the degree of freedom for signal (DOF), which can be calculated as

$$d_s = tr([\widetilde{\boldsymbol{K}}^{\boldsymbol{T}}\widetilde{\boldsymbol{K}} + \boldsymbol{I}]^{-1}\widetilde{\boldsymbol{K}}^{\boldsymbol{T}}\widetilde{\boldsymbol{K}}) \quad \text{(A9)}$$

where $\widetilde{\boldsymbol{K}} = \boldsymbol{S}_{\boldsymbol{\epsilon}}^{-\frac{1}{2}}\boldsymbol{K}\boldsymbol{S}_{\boldsymbol{a}}^{\frac{1}{2}}$. The DOF cannot be larger than the number of retrieved variables, which is three in our case (COT, D_e, T_c). We found that the DOF of most clusters were typically slightly above 2. Since more than two channels are needed to take advantage of a DOF above 2, for each cluster we make three channel selections.

A.3.3 Uncertainty sources

Channel selection depends on the uncertainties of each channel (L'Ecuyer et al., 2006), as described by the total error covariance $\boldsymbol{S}_{\boldsymbol{\epsilon}}$. This matrix includes the measurement error covariance matrix, which characterizes the uncertainty in the observed radiances, as well as systematic forward modeling uncertainties, i.e. uncertainties in the simulated radiances caused by inherent errors in the parameters used in the forward model. For instance, atmospheric thermodynamic profiles taken from any source, whether they derive from radiosondes, reanalyses, or satellite retrievals, all have associated errors. Radiances forward-modeled using these profiles will unavoidably deviate from the actual observations. Uncertainties of this type can be estimated for each input source by randomly perturbing the input profiles and using the

resulting radiances to estimate the error covariance matrix. The resulting magnitudes of each forward model uncertainty are summarized as a percentage relative to the mean radiances in Figure A.5. Other error sources, such as spatial inhomogeneity and three-dimensional effects, are much harder to estimate and are not treated in this study.

The separate error covariance matrices can by combined as a sum if we assume all sources are uncorrelated with each other. The total error covariance matrix, which contains all uncertainties, is

$$\boldsymbol{S}_{\boldsymbol{\epsilon}} = \boldsymbol{S}_{\mathbf{y}} + \boldsymbol{S}_{\mathbf{T}} + \boldsymbol{S}_{\mathbf{wv}} + \boldsymbol{S}_{\mathbf{habit}} + \boldsymbol{S}_{\mathbf{aerosol}} \tag{A10}$$

where $\boldsymbol{S}_{\mathbf{y}}$ is the instrument error covariance matrix, $\boldsymbol{S}_{\mathbf{T}}$ represents the uncertainty due to temperature, $\boldsymbol{S}_{\mathbf{wv}}$ due to humidity, $\boldsymbol{S}_{\mathbf{habit}}$ due to ice crystal assumptions, and $\boldsymbol{S}_{\mathbf{aerosol}}$ due to aerosols.

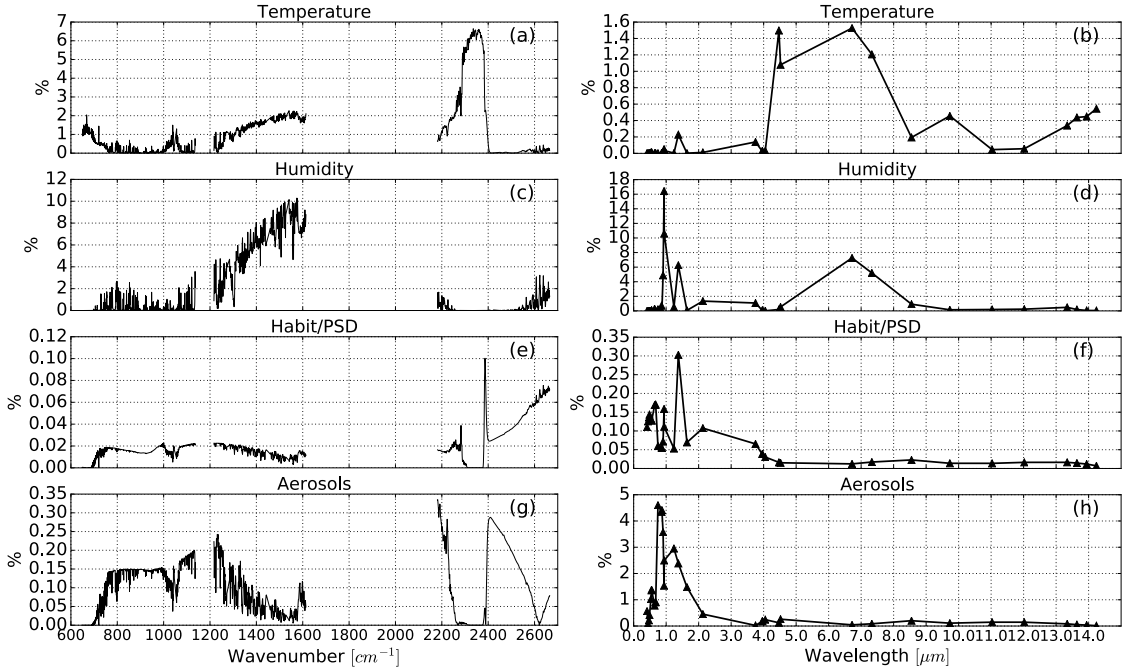

Figure A.5 Uncertainty due to the specified source for AIRS (left column) and MODIS (right column) channels. Percentages indicate the magnitude of the error standard deviation relative to the mean radiance of the simulations used to generate each uncertainty.

To generate the uncertainties due to temperature, we assume that for every temperature profile, the temperature at each layer is a Gaussian-distributed random variable with an associated standard deviation. It is also assumed that errors in different layers are uncorrelated. We assume that the temperature error standard deviation at each layer is 1.5 K, consistent with documented errors in AIRS temperature profile retrievals at 1-kilometer resolution (Divakarla et al., 2006). A temperature profile from the MERGESONDE data set at Darwin, Australia was used to generate 600 profiles by randomly sampling temperatures at each layer from the appropriate Gaussian distributions. A set of AIRS and MODIS radiances was generated for each of these profiles and the covariance matrix of the resulting radiances was then used as the error covariance matrix due to temperature profile errors. The error covariance matrix includes off-diagonal elements that represent covariances between errors in different channels.

Figures A.5a and A.5b show the diagonal elements of this error covariance matrix that represents the uncertainty due to temperature profile errors. Uncertainties due to temperature are typically less than 3% of the mean radiance for most AIRS channels. Temperature uncertainties are highest around 2200–2400 cm−1 (4.5–4.2 μm), approaching almost 7% at around 2300 cm^{-1} (4.35 μm). Uncertainties across all MODIS bands are less than 2% with the highest values reaching 1.5% at 4.5 and 6.7 μm (2200 and 1492 cm^{-1}).

The temperature error covariance matrices, together with the others that have off-diagonal elements, are visualized in Figure A.6. For ease of interpretation, the matrices are plotted in terms of percentages relative to the mean radiances. Each element is calculated as

$$c_{i,j} = \begin{cases} \sqrt{\dfrac{\sigma_{i,j}}{\bar{I}_i \bar{I}_j}} & \sigma_{i,j} > \mathbf{0} \\ -\sqrt{\dfrac{\sigma_{i,j}}{\bar{I}_i \bar{I}_j}} & \sigma_{i,j} < \mathbf{0} \end{cases} \tag{A11}$$

where $c_{i,j}$ is the plotted value, $\sigma_{i,j}$ is the (i, j) element in the covariance matrix, and $\bar{I}_i$, $\bar{I}_j$ are the mean radiances of channel i and j. Plotted this way, the diagonals will have identical values to Figure A.5. For the temperature error covariance matrices, covariances are strongest between the region near 2300 cm^{-1} (4.3 μm) and 650 cm^{-1} (15.4 μm).

The diagonals of the error covariance matrix due to uncertainty in the assumed humidity profile were constructed using water vapor Jacobians from the RTM. Given the specific humidity weighting functions $\partial I_v / \partial \ln\, q(z_i)$ at each wavelength v the standard deviation can be calculated using

$$\begin{aligned} \sigma_{q,v} &= \sum_{\boldsymbol{i}}^{\boldsymbol{N_{\text{layer}}}} \frac{\partial I_v}{\partial q(z_i)} \left(\frac{\mathrm{UNC}(z_i)}{100\%} q(z_i) \right) \\ &= \sum_{\boldsymbol{i}}^{\boldsymbol{N_{\text{layer}}}} \frac{\partial I_v}{\partial \ln q(z_i)} \left(\frac{\mathrm{UNC}(z_i)}{100\%} \right) \end{aligned} \tag{A12}$$

where $\mathrm{UNC}(z_i)$ is the uncertainty in specific humidity in percentage relative to the specific humidity at height z_i. Based on Divakarla et al. (2006), the uncertainty in specific humidity was assumed to be 20% at the surface and linearly increases to 50% at 250 hPa. At all altitudes above 250 hPa, the uncertainty was assumed to be 50%. The standard deviations at all wavelengths, calculated by equation A12, make up the diagonal of the error covariance matrix. To obtain the off diagonals, a method similar to the temperature uncertainty is used, where 600 profiles were generated by randomly sampling humidity at each layer using the appropriate standard deviation.

The correlation matrix of the radiances was then used to construct the off-diagonal elements of the error covariance matrix.

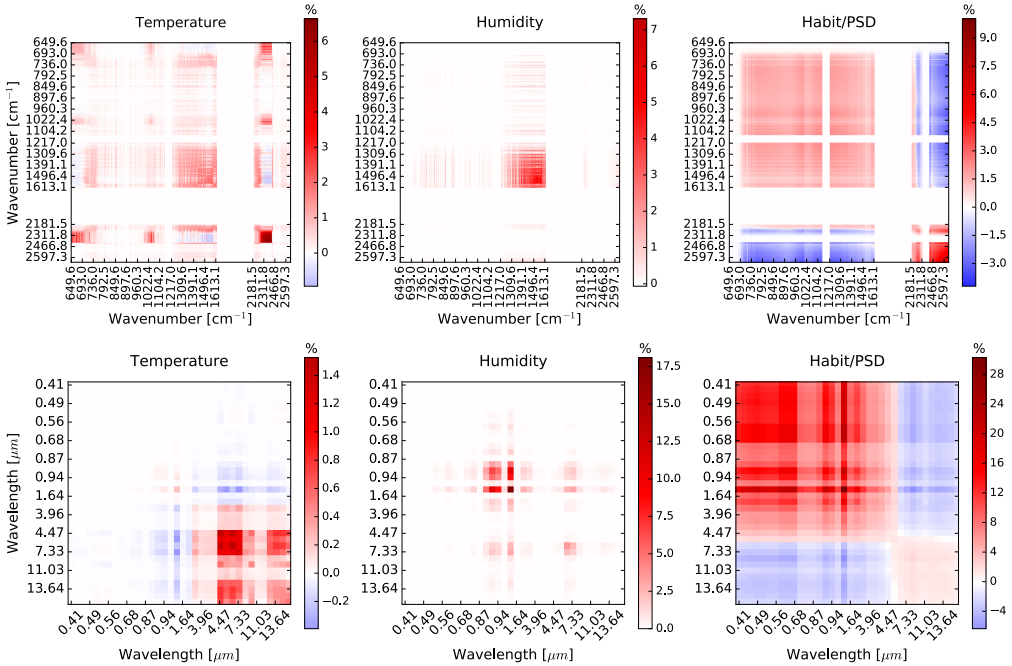

Figure A.6 Visualization of (top row) AIRS and (bottom row) MODIS error covariance matrices for temperature, humidity, and assumptions in the ice crystal habit and particle size distribution, calculated using equation (11). In the top row, the white gaps are regions where AIRS does not have channels.

The relative magnitudes of humidity uncertainties are shown in Figures A.5c and A.5d. As expected, humidity errors induce the largest uncertainty in AIRS channels within the water vapor absorption regions between 1200 and 1600 cm^{-1} (8.3 and 6.3 μm), peaking at around 10%. In the same spectral region, MODIS uncertainties increase to 8%, but the maximum is 16% at 0.9 μm where water vapor has low transmission (Eldridge, 1967). Covariances among channels are localized in the water vapor absorption bands, for example, within 1200 and 1600 cm^{-1} for AIRS (Figure A.6). In MODIS channels, these wavelengths have high covariances as well, although the magnitudes are higher in the near-infrared water vapor absorption bands, such as 1.38, 0.94, and 0.91 μm.

Another source of uncertainty is the assumption of ice crystal habit and particle size distribution (PSD). To estimate these uncertainties, 30 different clouds ranging from optically thin (0.009) to thick (7.4) from the clustering analysis were used to simulate radiances. For each cluster, nine different habit and PSD combinations were assumed, as listed in Table A.1. The first three habit/PSD types were adopted from Baum et al. (2014), where the PSD was based on a collection of in situ campaigns. For the last six types, whose scattering properties are described by Yang et al. (2013), an exponential distribution and two different gamma distributions were specified. The gamma distributions are based on equation (2.56) of Hansen and Travis (1974):

$$n(r) = n_0 r^{\frac{1-3b}{3}} e^{\frac{r}{br_e}} \tag{A13}$$

where b is a unitless factor controlling the shape of the distribution. To obtain the covariance matrix, the intracluster mean was first removed from the simulated radiances for every cluster.

Habit Type	PSD Type	Source of Scattering Properties
General habit mixture	Fit to campaign data [1]	*Baum et al.* [2014]
Solid columns	Fit to campaign data [1]	*Baum et al.* [2014]
Aggregate columns	Fit to campaign data [1]	*Baum et al.* [2014]
Droxtals (lightly roughened)	Exponential	*Yang et al.* [2013]
Droxtals (lightly roughened)	Hansen-Travis Gamma, $b = 0.2$	*Yang et al.* [2013]
Droxtals (lightly roughened)	Hansen-Travis Gamma, $b = 0.4$	*Yang et al.* [2013]
10-element plates (severely roughened)	Exponential	*Yang et al.* [2013]
10-element plates (severely roughened)	Hansen-Travis Gamma, $b = 0.2$	*Yang et al.* [2013]
10-element plates (severely roughened)	Hansen-Travis Gamma, $b = 0.4$	*Yang et al.* [2013]

Table A.1 List of Habit and PSD Combinations for Obtaining the Habit/PSD Uncertainties.

The resulting radiances can be then interpreted as the perturbations about the mean due to the assumed habit and PSD, resulting in 270 sets of radiance perturbations that define the uncertainty covariance matrix.

As shown in Figures A.5e and A.5f, uncertainties are under 2% for AIRS channels within 650 cm^{-1} to 1630 cm^{-1} (15.4 to 6.1 μm). Above 2200 cm^{-1} (4.55 μm), the uncertainty becomes significantly higher in many channels, notably at 2390 cm^{-1} (4.2 μm) where the uncertainty peaks at 10%. MODIS channels in the NIR and visible suffer more notably from this type of uncertainty. Below 4 μm, all uncertainties are above 5%, exceeding 10% in many of the visible bands, with the highest value being 30% at 1.375 μm. The magnitude of these uncertainties is mostly consistent with Cooper et al. (2006) who reported that uncertainties of this type are typically less than 5% in the infrared and grow to around 20–30% in the visible. By comparing the habit/PSD error covariance matrices of AIRS and MODIS (Figure A.6), it is apparent that habit/PSD errors covariances are more significant in MODIS visible and near-infrared channels.

Since visible and NIR channels are sensitive to aerosols, the presence of aerosols in cloudy scenes should also be considered a source of uncertainty. We estimated this uncertainty by extracting the mean aerosol optical thickness (AOT) in the tropics (20°N–20°S) during 2007 from the MACC reanalysis for four different aerosol types: sea salt, organic carbon, soot, and sulfate. The sum of these four average AOTs was around 0.14. These AOTs were distributed vertically by assuming an exponential distribution with an *e*-folding height of 3 km. The mean radiance perturbation due to aerosols over all clusters were assumed to be the standard deviations for the diagonal of the aerosol error covariance matrix. Aerosol uncertainties in AIRS channels are less than 0.5% in all channels. Aerosols have a much more prominent effect on MODIS radiances, peaking at around 4.5% at the 0.74 μm band. One source of aerosol that we have not included is dust, which can be a major source of aerosols in North Africa and the Middle East. However, the AOT value used here (0.14) should be representative of the mean AOT in the tropics outside of these areas (Hsu et al., 2012). As such, the aerosol uncertainty used in this

study should be adequate for most scenarios, and the addition of dust is unlikely to significantly impact the magnitude and spectral characteristics of aerosol uncertainty.

The instrument uncertainty matrix $\boldsymbol{S_y}$ is assumed to be diagonal. The error variances of MODIS solar reflective bands were derived using the instrument signal-to-noise ratio provided by Xiong et al. (2003a), and the error variances of MODIS thermal bands were derived from nedT values from Xiong et al. (2003b). Error variances of AIRS channels were derived using the nedT values provided in the channel property files available at https://disc.gsfc.nasa.gov/AIRS/documentation/v6_docs/v6releasedocs-1/v6-chan-prop-files.zip.

A.4 Optimal channels for ice cloud retrievals

Using the IC approach, we select optimal channels for retrieving COT, D_e, and, T_c. All three parameters are fundamental to the radiative characteristics, as COT and D_e controls the scattering and absorption characteristics of the cloud, and T_c is an indicator of outgoing longwave radiation. The channel selection process described in the previous section was carried out for every cluster, over all viewing angles, over three surfaces types: ocean, vegetation, and bare soil.

A.4.1 Stand-alone AIRS retrievals

Results from simulations over ocean are presented as a baseline, since retrievals over ocean are less problematic than over land surfaces. Figure A.7 shows the number of times that AIRS channels in each 5 cm^{-1} spectral bin are selected from all retrieval simulations over an oceanic surface. The results clearly identify a small sub-set of preferred spectral ranges for AIRS ice cloud retrievals around 930, 2400, and 2630 cm^{-1} (10.75, 4.17, and 3.80 μm). These regions contain the most information overall, independent of COT, but some channels around 700 cm^{-1}

(14.3 μm) become important for retrieving thinner clouds. The IC selections favored CO_2 slicing channels near 2400 cm^{-1} (4.2 μm) in the shortwave infrared (SWIR) over the midinfrared channels around 700 cm^{-1}. Although in the SWIR region (2380 to 2600 cm^{-1}) the uncertainties due to habit/PSD are higher than those at other wavelengths, there is less absorption from other gases that could increase uncertainties at longer wavelengths causing retrievals to favor the SWIR.

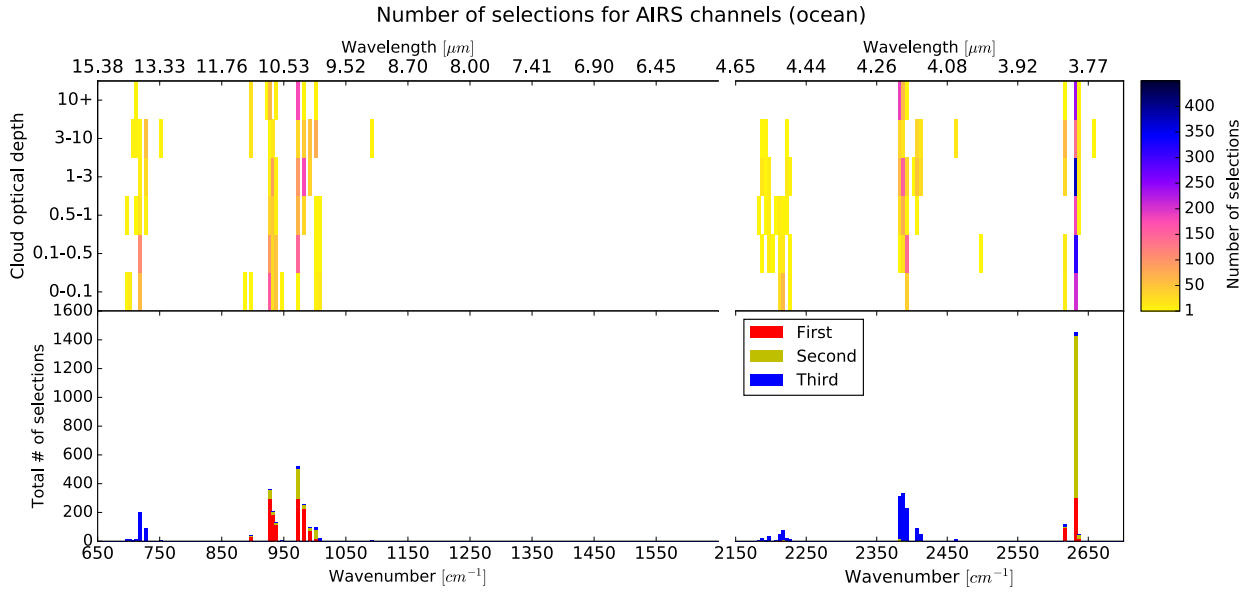

Figure A.7 (Top) Number of AIRS channel selections within each 5 cm^{-1} bin for ocean surface simulations, over all clusters and all viewing angles, categorized by COT. (Bottom) Total number of AIRS channel selections within each 5 cm^{-1} bin.

It is known that the usage of SWIR radiances includes some complications, such as solar contamination and non-LTE effects. However, the AIRS version 6 temperature retrieval has experienced improvement in temperature retrievals over version 5 after including and appropriately preprocessing SWIR channels (Susskind et al., 2014). Given that temperature sounding retrievals have benefited from the addition of SWIR channels, it is plausible that these channels can potentially improve cloud temperature retrievals as well.

The order in which the channels were selected is also shown in Figure A.7, indicating the relative importance of each spectral region. CO_2 slicing channels were rarely selected first; most of the first selections occurred in the 2600 and 930 cm^{-1} (3.8 and 10.8 μm) regions, which suggests that overall the AIRS measurements carry more information for COT and D_e than T_c. To verify this, a singular value decomposition (SVD) is applied to $\widetilde{\boldsymbol{K}}$, revealing why each channel is selected.

Analysis of $\widetilde{\boldsymbol{K}}$ is valuable because it determines the effective rank of the problem (Rodgers, 2000). SVD is similar to eigenvalue decomposition but can also be applied to non-square matrices such as $\widetilde{\boldsymbol{K}}$. SVD decomposes a matrix into a set of singular values and singular vectors. In this application, the singular values give a relative estimate of precision, while the singular vectors indicate which retrieved variables are being measured. Also, since the singular vectors are orthogonal, SVD can show whether retrieved variables can be measured independently. For this reason, using SVD to decompose $\widetilde{\boldsymbol{K}}$ reveals what spectral regions were most impactful toward retrieving COT, D_e,or T_c. In conjunction with the IC channel selection, SVD gives insight into why the channels were selected and which variables the select channels help retrieve. Singular value decomposition of the matrix $\widetilde{\boldsymbol{K}}$ can be expressed as

$$\widetilde{\boldsymbol{K}} = \boldsymbol{U}\boldsymbol{\Lambda}\boldsymbol{V}^{\boldsymbol{T}}. \tag{A14}$$

Each column vector of $\boldsymbol{U}$ is the basis in the measurement space and can be interpreted to be "measuring" the retrieved variables as indicated by the corresponding singular vectors (column vectors of $\boldsymbol{V}$). The singular values in $\boldsymbol{\Lambda}$ represent the weighting of the corresponding basis (Rodgers, 2000). Figure A.8 shows an example of SVD applied to a cloud with COT of about 1.36. The highest weighted singular vector (first column of $\boldsymbol{V}$) shows highest magnitudes for COT and then D_e, indicating that the corresponding measurement basis contributes most to these

two variables, while its contribution to T_c is much smaller. It is expected that the channels with highest values in the most heavily weighted basis were the ones picked first in the channel selection process.

In most cases, the singular vectors do not point to just one retrieval variable, making it hard to interpret which channels impact each variable. However, since the singular vectors are orthogonal, it is possible to apply transformations so that the singular vectors point to one retrieval variable only. Let $\overrightarrow{v_1}, \overrightarrow{v_2}, \overrightarrow{v_3}$ be the column vectors of $\boldsymbol{V}$ so that $\boldsymbol{V} = [\overrightarrow{v_1}, \overrightarrow{v_2}, \overrightarrow{v_3}]$. We would like to find coefficients $\vec{c} = [c_1, c_2, c_3]$ such that

$$c_1\overrightarrow{v_1} + c_2\overrightarrow{v_2} + c_3\overrightarrow{v_3} = \begin{bmatrix}1\\0\\0\end{bmatrix} \text{ or } \begin{bmatrix}0\\1\\0\end{bmatrix} \text{ or } \begin{bmatrix}0\\0\\1\end{bmatrix} \tag{A15}$$

where the vector $[1 \quad 0 \quad 0]^T$ represents a singular vector with a nonzero component only in the direction of COT, $[0 \quad 1 \quad 0]^T$ one with nonzero component only for D_e, and so on. Equivalently,

$$\boldsymbol{V}\vec{c} = \begin{bmatrix}1\\0\\0\end{bmatrix} \text{ or } \begin{bmatrix}0\\1\\0\end{bmatrix} \text{ or } \begin{bmatrix}0\\0\\1\end{bmatrix}. \tag{A16}$$

Then $\vec{c}$ can be solved by

$$\vec{c} = \boldsymbol{V^{-1}} * \left(\begin{bmatrix}1\\0\\0\end{bmatrix} \text{ or } \begin{bmatrix}0\\1\\0\end{bmatrix} \text{ or } \begin{bmatrix}0\\0\\1\end{bmatrix}\right). \tag{A17}$$

By multiplying $\vec{c}$ onto $\boldsymbol{U}$, we get $\overrightarrow{u'} = \boldsymbol{U}\vec{c}$, where $\overrightarrow{u'}$ is a measurement basis that corresponds to a singular vector of $[1 \quad 0 \quad 0]^T$ or $[0 \quad 1 \quad 0]^T$ or $[0 \quad 0 \quad 1]^T$. The measurement basis $\overrightarrow{u'}$ isolates each individual retrieval variable. The weightings (singular values) of each transformed basis may be also calculated by

$$\lambda' = |c_1|\lambda_1 + |c_2|\lambda_2 + |c_3|\lambda_3 \tag{A18}$$

where λ_1, λ_2, and λ_3 are the singular values (diagonal elements of $\boldsymbol{V}$) corresponding to the untransformed bases. Figure A.9 shows the result of applying the transformation onto the vectors of Figure A.8. After this transformation, it is now seen that, for this particular cloud, channels near 2600 cm^{-1} (3.85 μm) primarily constrain COT. Also, the transformed basis corresponding to COT and D_e have higher weights relative to that of T_c, indicating that the channel constraining T_c is likely to have been selected last.

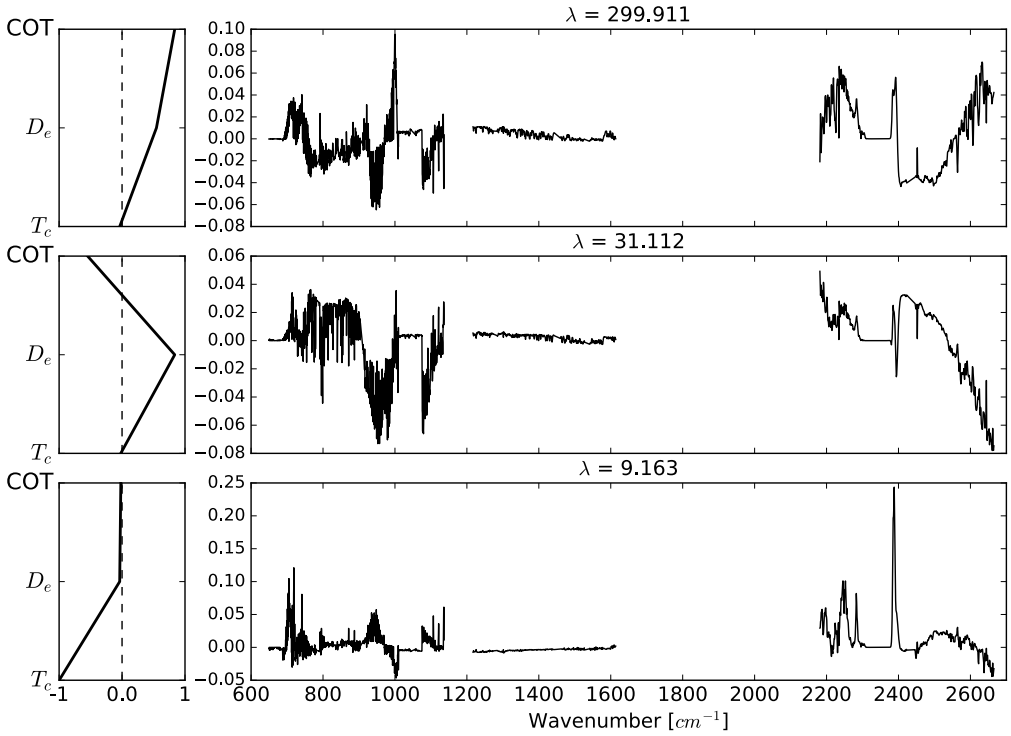

Figure A.8 (Left column) Singular vectors and (right column) their corresponding basis in measurement space for a cloud with a COT of 1.36. The singular vectors indicate which retrieved variables the measurement bases help constrain. In the top row, for instance, since the singular vector value for T_c is near zero, the measurement basis on the right does not help retrieve Tc but rather contribute most to COT and then, to a lesser magnitude, to D_e. The values shown on the top part are the singular value from **Λ** of equation (A14).

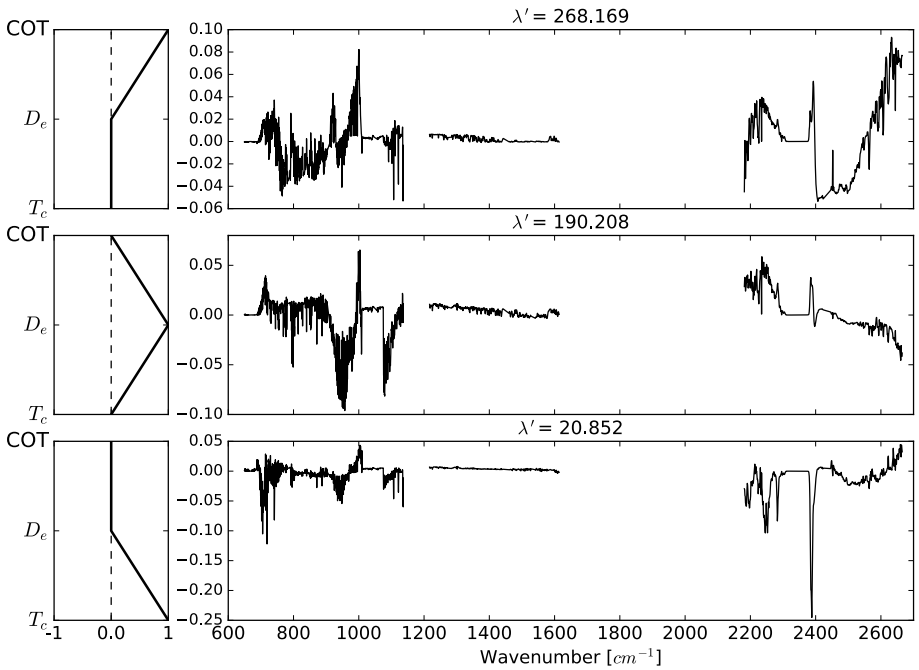

Figure A.9 (Left column) Transformed singular vectors and (right column) their corresponding measurement basis after applying the transformation of equation (A17) onto the same cloud as used in Figure A.8. After the transformation, the singular vectors point only to one retrieval variable, and the measurement basis can be interpreted to be contributing to one variable only.

Using the weights calculated from equation (A18), the weighted average of measurement bases over all clusters and viewing angles were calculated, as shown in Figure A.10. The average bases of AIRS for D_e and T_c both have high magnitudes in the SWIR, explaining the tendency of IC to select channels in this spectral region. In particular, the peak near 2640 cm^{-1} (3.79 μm) coincides with the most selected channel in Figure A.7. Highest values in the average AIRS basis for COT occur in the window region near 1000 cm^{-1} (10 μm). In the AIRS basis for D_e, channels throughout the 800–1000 cm^{-1} (12.5-10 μm) have peak magnitudes of around 0.02, while the largest magnitude (−0.07) occurs around 2640 cm^{-1} (3.79 μm). This indicates that although the window channels are potent for retrieving D_e, the SWIR channels may be a better alternative. Another feature of the AIRS D_e basis is that the thin cloud basis overall has larger magnitudes than the thick cloud basis, implying that most AIRS channels perform better for retrieving D_e of

thinner clouds. The average AIRS basis for temperature has peaks at 700, 1000, 2200, 2245, 2380, 2630, and 2660 cm^{-1} (14.3, 10, 4.55, 4.45, 4.2, 3.80, and 3.76 μm). The spectral regions near 700, 2200, 2245, and 2380 cm^{-1} corresponds to the frequent third channel selections in Figure A.7, which confirms that these channels were selected for their sensitivity to temperature.

Differences between thin and thick clouds are also evident in the bases. The AIRS temperature basis for thin clouds has larger magnitudes near 700 and 2400 cm^{-1}, while the thick clouds basis has peaks at 1000 and 2600 cm^{-1} which are windows channels.

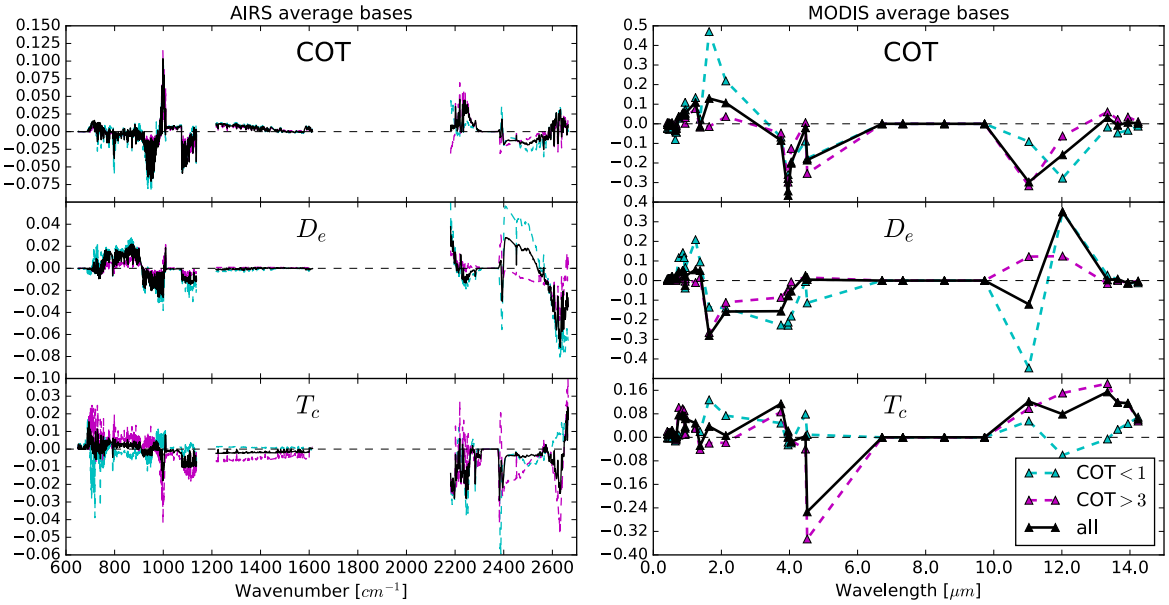

Figure A.10 Weighted average of (left column) AIRS and (right column) MODIS measurement bases corresponding to (top row) COT, (middle row) D_e, and (bottom row) T_c, for thin clouds (cyan), thick clouds (magenta), and all clouds (black).

A.4.2 Stand-alone MODIS retrievals

MODIS selections were also performed over ocean, as shown in Figure A.11. In contrast with AIRS results, the selected MODIS channels exhibit clear dependence on COT. For instance, the 0.65 μm channel is increasingly favored as COT increases; the 1.38 μm channel is selected only

for very thin clouds; the 13.9 μm (720 cm^{-1}) channel was most selected for optically thin clouds while the 11.0 μm (909 cm^{-1}) is selected more as COT increases. The most frequently selected MODIS channel, 3.96 μm (2525.3 cm^{-1}), however, is independent of COT, like the most selected AIRS channels. Note that MODIS has two channels, channels 21 and 22, centered at 3.96 μm. Since the latter obtained more selections, all subsequent mentions of the 3.96 μm channel is meant to refer to channel 22. The second most popular MODIS channel, 12 μm (833 cm^{-1}) is generally selected for clouds with a COT between 0.1 and 3. These results generally agree with the current understanding on sensitivity of these bands to cloud properties. For instance, 1.38 μm has been used for cirrus detection (Gao et al., 1993), the 1.64 and 3.96 μm channels have been shown to be sensitive to particle size (Lensky and Rosenfeld, 2008), and the 0.65 μm is a nonconservative band often used in Nakajima-King-type retrievals (Nakajima and King, 1990).

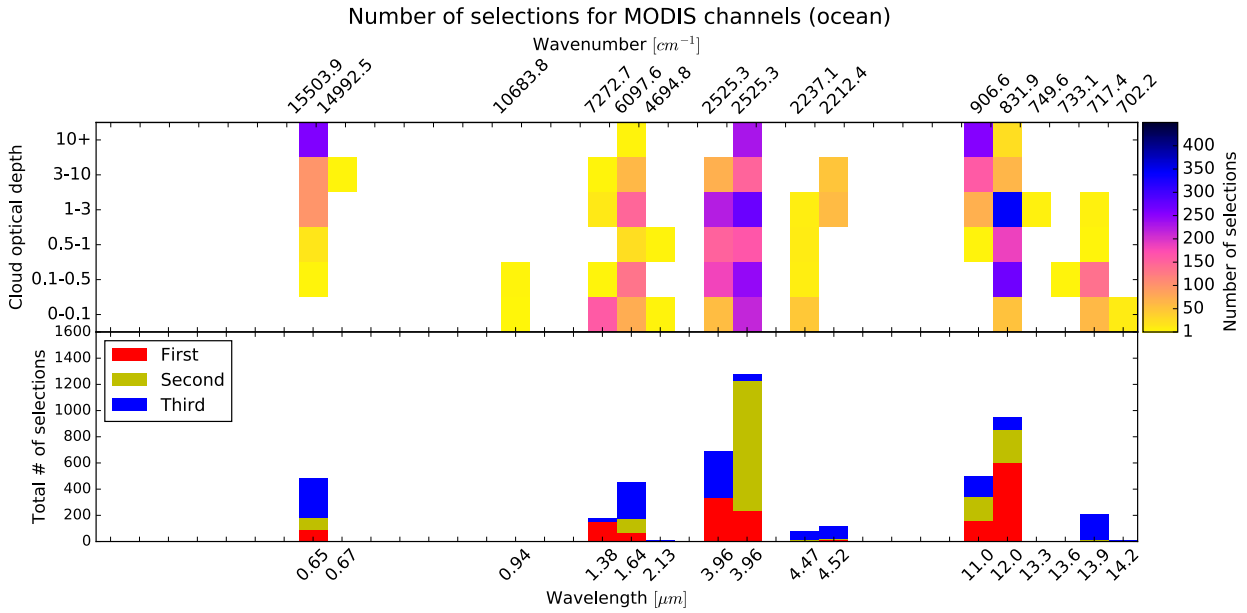

Figure A.11 (Top) Number of MODIS band selections for ocean surface simulations, over all clusters and all viewing angles, categorized by COT. (Bottom) Total number of MODIS band selections. Note that MODIS has two channels, channels 21 and 22, with center wavelengths at 3.96 μm.

Revisiting the SVD results in Figure A.10, the average bases of MODIS also explain the channel selections made in Figure A.11. The three most selected MODIS channels, which are 3.96, 12, and 11 μm, have large values in the average SVD basis for COT and D_e. The 3.96 μm channel contributes to both COT and D_e, while 11 μm channel contributes mostly to COT and 12 μm channel mostly to D_e. In the basis for D_e, 1.64 μm also stands out, indicating the band's utility for retrieving particle size. Finally, the average basis for T_c, having high values at 4.5 and 13.3 μm, peaks near 4.5 μm, showing why IC analysis favors SWIR channels for temperature retrieval, a result similar to the AIRS selections. Also, similar to the AIRS selections, we found that temperature retrieval channels were rarely selected in the first iteration (Figure A.11).

A.4.3 Surface and viewing angle dependence

Equivalent results for both AIRS and MODIS retrievals over a grass surface are presented in Figures A.12 and A.13. Overall, the differences between selections over grass and ocean are very subtle, suggesting that the spectral reflectance differences between these two surface types did not alter the IC significantly. Differences in the AIRS selections between the two surfaces were negligible, while for MODIS, the only notable change is that over vegetation there are fewer selections at 0.65 and 1.64 μm, and more frequent selections at 4.52 μm. The loss of 1.64 μm channels may be due to the stronger reflectivity of grass in this region (Figure A.3). Overall, as both AIRS and MODIS analyses over vegetation were largely similar to the ocean case, we conclude that there is no need to consider separate channel sets over these two surfaces.

Simulations over bare soil, however, results in some notable differences relative to ocean and vegetation. For AIRS (Figure A.14), the 2620 cm^{-1} (3.82 μm) channel is almost always

selected first over bare soil as opposed to over grass and ocean where the window region near 1000 cm^{-1} (10 μm) is preferred. Second, while selections over grass and ocean favored channels near 2640 cm^{-1} (3.79 μm), retrievals over bare soil favor slightly longer wavelengths at 2620 cm^{-1} (3.82 μm) and channels near 2640 cm^{-1} were selected mostly for thicker clouds. Despite these differences in the selection process, the spectral distribution of the optimal AIRS channels remains largely similar to the two previous surfaces.

In the case of MODIS (Figure A.15), IC analysis over bare soil yielded results similar to the grass simulations, where 0.65 and 1.64 μm have fewer selections compared to over ocean, and infrared channels such as 4.52 μm were favored slightly more. Again, no new channels appeared in the bare soil selections, implying that one set of channels is suitable for both AIRS and MODIS retrievals over most of the tropical region.

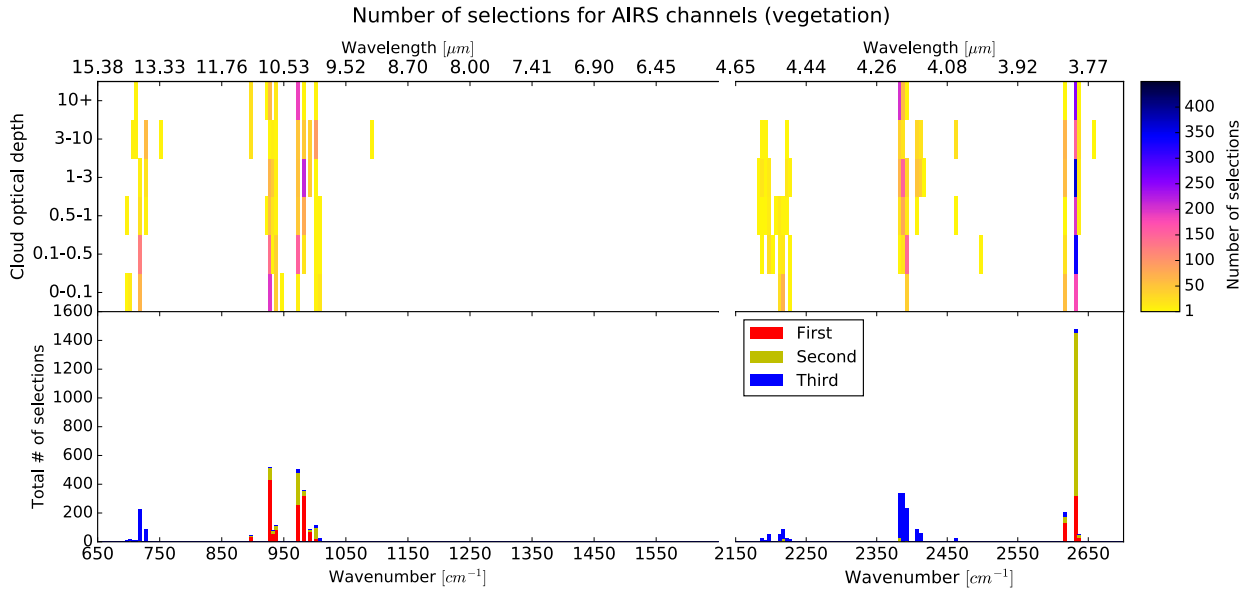

Figure A12. Same as Figure A.7, except over grass.

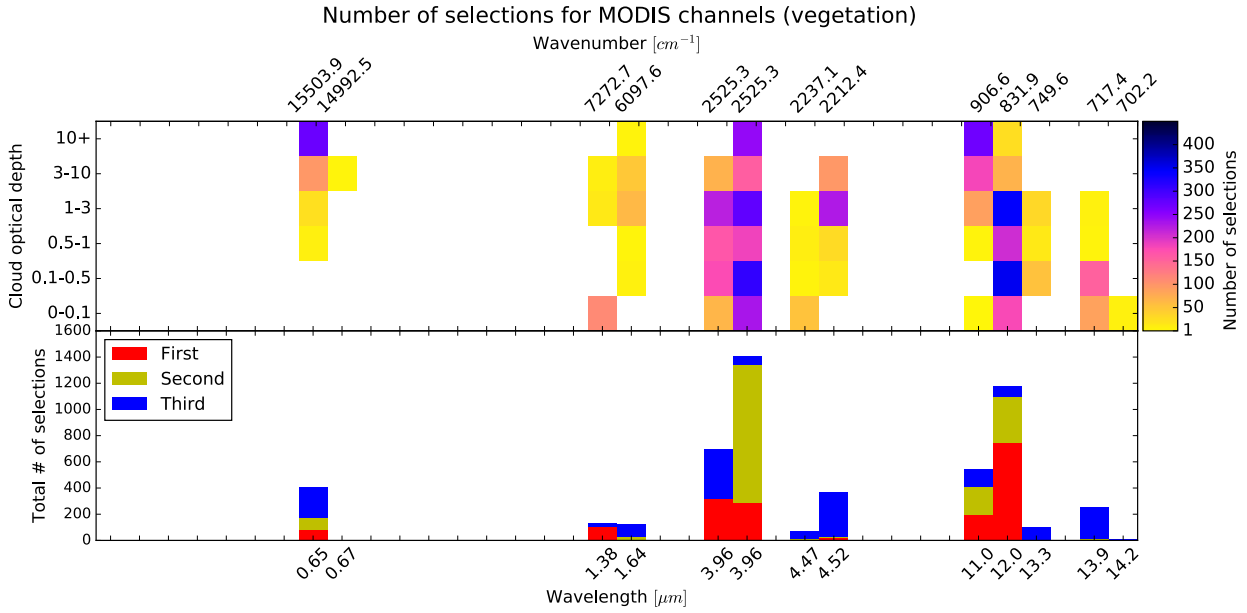

Figure A.13 Same as Figure A.11, except over grass.

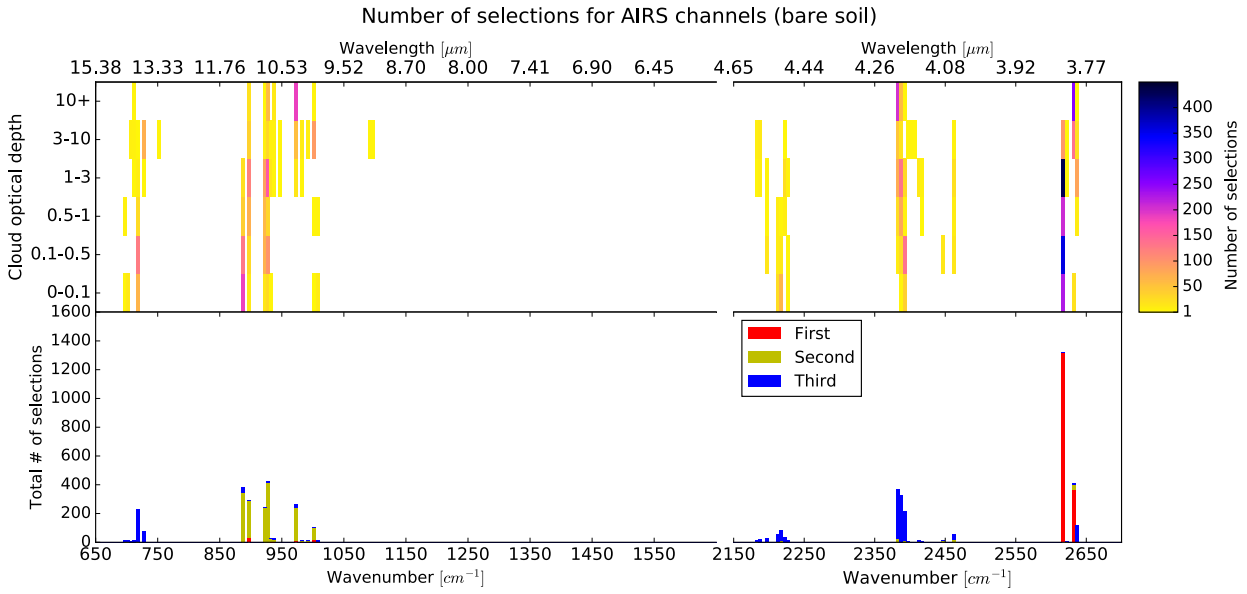

Figure A.14 Same as Figure A.7, except over bare soil.

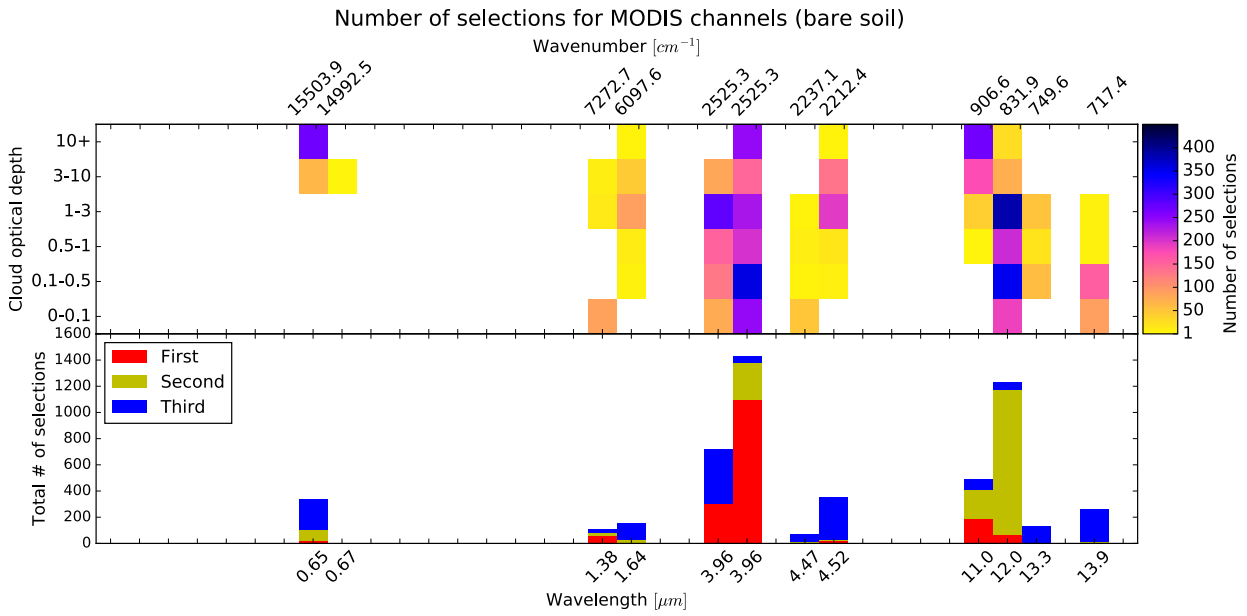

Figure A.15 Same as Figure A.11, except over bare soil.

Finally, we found that differences due to varying viewing angles were largely negligible in both AIRS and MODIS selections. The only notable difference is that in MODIS selections over bare soil, the 0.65 μm channel is selected more frequently at the expense of the 4.52 μm channel when viewed at 45 ° off nadir.

A.4.4 Combined AIRS+MODIS retrievals

By virtue of their distinct spectral coverage and spectral resolution, there is good reason to expect that AIRS and MODIS may provide complementary information for improved cloud property retrievals. Since these sensors are both on board the Aqua satellite, their spatially and temporally colocated observations are suitable for a joint retrieval. Here we perform channel selection assuming that both AIRS and MODIS channels are available to retrieve an observed cloud. In practice, such a retrieval will be complicated by differences in the AIRS and MODIS

fields of view, but for simplicity here we assume that the observed cloud is spatially homogeneous to facilitate the IC analysis.

Optimal channels for combined AIRS+MODIS ice cloud retrievals over ocean are shown in Figure A.16. Both AIRS and MODIS channels were selected, the latter being selected first more often, especially at 11 and 12 μm (909 and 833 cm^{-1}). MODIS longwave window channels were favored over the equivalent AIRS channels, but the AIRS SWIR channels near 2640 cm^{-1} (3.79 μm) outnumber those of MODIS. Of the channels that were previously found to contribute to T_c in Figure A.10, which are the 4.47 and 4.52 μm (2237 and 2212 cm^{-1}) MODIS channels and the AIRS channels near 2200 and 2400 cm^{-1} (4.6 and 4.2 μm), AIRS are selected more

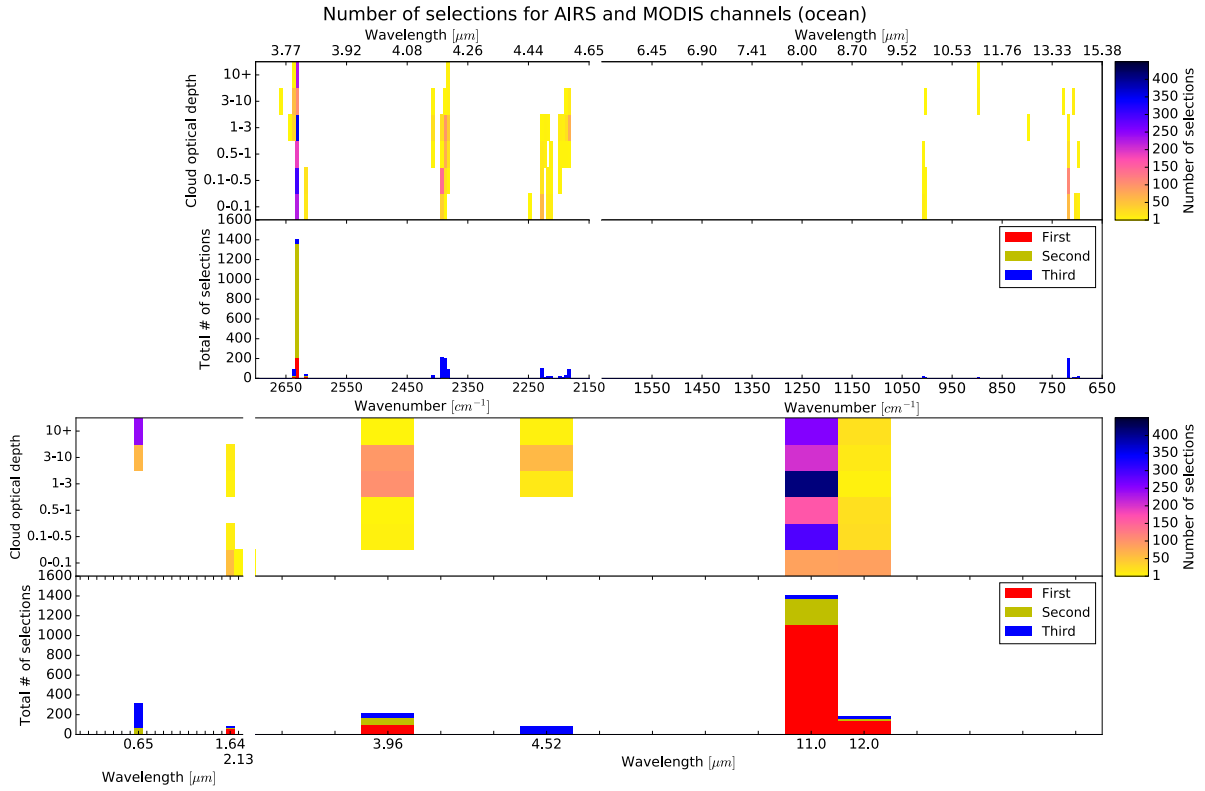

Figure A.16 Number of channel selections when simultaneously selecting from AIRS and MODIS for ocean surface simulations. (top plot) The number of AIRS selections in 5 cm^{-1} bins and (bottom plot) the number of selections for each MODIS channel. Note that the wave number axis of the top plot has been reversed to facilitate comparison between AIRS and MODIS.

often. This is expected as the finer resolution of AIRS channels can vertically locate the cloud more accurately. Finally, among the visible and NIR MODIS channels, the 0.65 and 1.64 μm are chosen for combined retrievals with the former being selected frequently for thick clouds. From these results and the previous SVD analysis, it can be concluded that in a combined retrieval, most of the COT and D_e information will come from MODIS, while T_c will almost exclusively be constrained by AIRS.

A.4.5 Combined active+passive retrievals

As suggested by Cooper et al. (2003), there is incentive to combine active and passive observations for cloud retrievals because large cloud boundary uncertainties can induce large biases in COT and D_e retrievals particularly for thin clouds. Active sensors provide the capability to significantly reduce the uncertainty in cloud top heights. The CloudSat Cloud Profiling Radar (CPR) (Stephens et al., 2008) has a vertical resolution of 240 m, which roughly corresponds to a Tc retrieval error of 2 K. To assess IC channel selection while having accurate cloud top boundary, we adopt the methodology of Cooper et al. (2006), where the T_c error standard deviation is reduced to simulate the presence of accurate cloud boundary information. We assume the *a priori* error standard deviation in T_c to be 2 K instead of the 16.2 K (derived from the ARM data set) assumed in the previous analyses and perform the channel selection process as outlined in Section A.3.

Having accurate *a priori* cloud boundary significantly influences the channel selection, as can be seen in Figures A.17 and A.18. All channels sensitive to cloud height, such as the CO_2 slicing channels, are now scarcely selected. Instead, channels previously not selected, such as the AIRS channels near 920 cm^{-1} (10.9 μm) and 2640 cm^{-1} (3.8 μm) now frequently become the

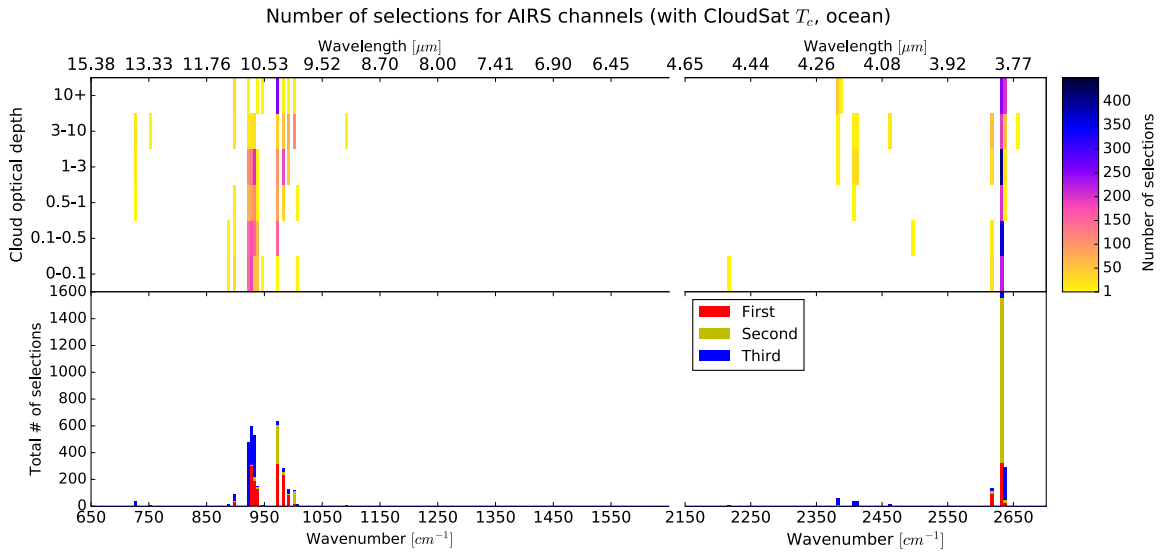

Figure A.17 AIRS channel selection over ocean assuming a temperature a priori standard deviation of 2K.

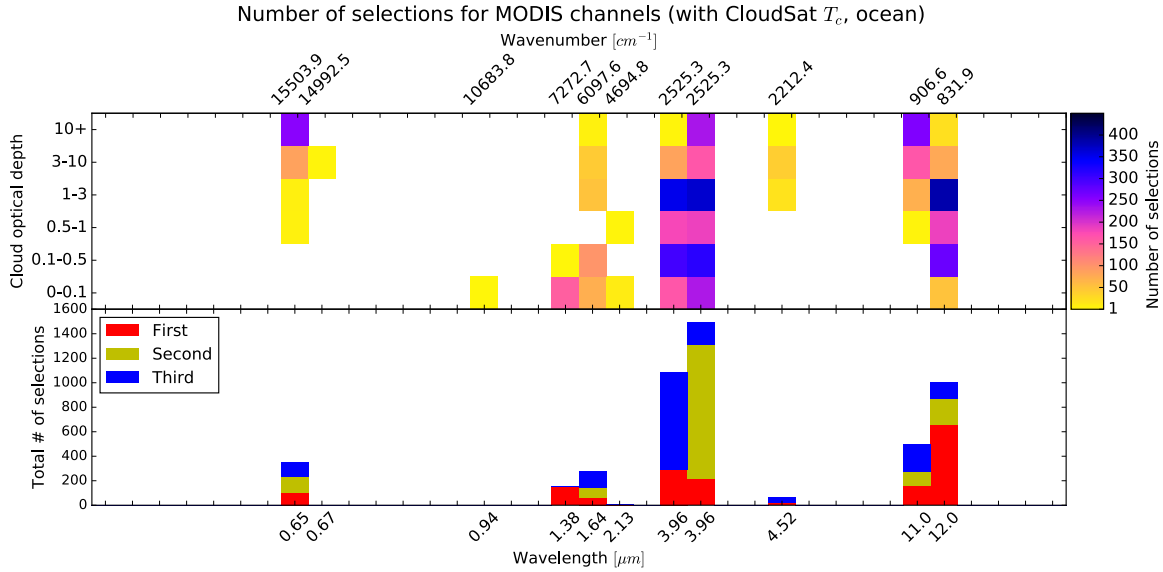

Figure A.18 MODIS channel selection over ocean assuming a temperature a priori standard deviation of 2K.

third channel, with the latter primarily selected for thicker clouds. No new MODIS channels are selected, and most temperature-related channels shift to the 3.96 channel as the third selection. This shows that more accurate a priori cloud boundary can help extract additional COT and D_e information from extra channels especially for AIRS.

A.5 Conclusion

This study applied an objective channel selection methodology utilizing IC to iteratively select optimal channels with the most IC, for tropical ice cloud retrievals under a range of conditions. The complete range of ice cloud types sampled in multiple years at the ARM TWP site is used to extract a set of cloud clusters expected to represent the full dynamic range of optical thickness, effective diameter, cloud top height, and geometric thickness in the tropics. This ensures that the selected channels will be appropriate for most ice clouds found in the tropics. While issues due to cloud inhomogeneity are important in actual retrievals, for this study the simulated radiances were assumed to be overcast through a plane-parallel RTM, and pixel sizes of AIRS and MODIS are assumed to be the same. Analysis of stand-alone AIRS retrievals favors SWIR channels, which were shown to be sensitive to COT and T_c through SVD analysis. AIRS SWIR and long-wave CO_2 slicing channels are selected with comparable weight. Because of this, it is suggested that one should favor the longwave CO_2 slicing channels, in order to avoid non-LTE effects around 4.3 μm. However, it has been shown that the inclusion of SWIR CO_2 slicing channels aid AIRS temperature retrievals, which suggests that it might be worthwhile to include these

channels for cloud temperature retrievals, provided that the proper correction for non-LTE effects are applied.

In the AIRS-only, MODIS-only, as well as AIRS+MODIS channel selections, the channel with highest IC rarely corresponds to cloud temperature information, echoing the finding of Cooper et al. (2003) which suggests that large errors in cloud boundaries will lead to significant uncertainties in other retrieved variables. Adding accurate cloud top boundary information from active sensors allows additional channels to be selected to improve COT and D_e retrievals. The results suggest that channel choices in presence of accurate cloud boundaries may not be as simple as taking away temperature retrieval channels but rather may allow new channels to contribute to COT and D_e retrievals owing to reduce uncertainty in cloud placement.

Having considered various permutations of satellite retrieval scenarios through varying surface type, viewing geometry, and cloud type, it is worthwhile to compile an optimal channel set from these IC analyses. Since the purpose of this study is to find the optimal channels for the most frequent cloud scenes, it is desirable to pick channels that contain the greatest information for clouds with larger populations, i.e., that are more common. Clustering analysis gives the occurrence frequency of each cloud type, which is used as weighting for the channel selection. Each cloud cluster center (used to represent a cloud type) has an associated population N_k representing the number of cloud profiles belonging to cluster k. We weight each channel by the number of clouds in each cluster,

$$W_v = \sum_{k}^{K} N_k f_v(k) \tag{A20}$$

where

$$f_v(k) = \begin{cases} 1 & \text{if channel } v \text{ is selected for cluster k} \\ 0 & \text{if channel } v \text{ is not selected for cluster k} \end{cases} \quad \text{(A21)}$$

W_v is the weighting of the channel at wavelength v, and K is the number of cloud types obtained from the clustering analysis. Such a weighting scheme gives preference to channels useful for clouds that occur more frequently. By using this weighting in conjunction with the channels selected objectively through IC analysis, we propose a recommended set of channels based on the IC channel selection.

The list of channels most heavily weighted for ice clouds retrievals is shown in Table A.2, for three different retrieval scenarios, and Figure A.19, categorized by COT. We find that for clouds with COT greater than 3, the CO2 slicing channels around 700 and 2200 cm^{-1} (14.3 and 4.55 μm) have less weight than that of thinner clouds, indicating that these channels are useful mostly for thinner clouds. Conversely, within the window regions between 900 to 1000 cm^{-1} (11.1 to 10 μm) have larger weights for COT > 3. Aside from these differences, the spectral distribution of weighting is largely the same between the two COT categories. Based on this weighting, Table A.2 provides a succinct channel set that is applicable to ice cloud retrievals over a wide range of scenes. Relative to the 59 channels used in the AIRS version 6 ice cloud retrieval (Kahn et al., 2014), the channel set presented in Table A.2 could potentially reduce computational expense, provided that retrieval experiments show that these channels can retrieve ice cloud properties with comparable accuracy to the retrievals done using the version 6 channel set.

This study employs the use of Shannon entropy reduction as a measure of information content, which has been shown to be inappropriate for non-Gaussian variables. Petty (2018) has shown that Shannon entropy can remain constant or increase in situations where an observation provides benefit to the retrieval. As an example, the effective radii of cloud droplets or ice

crystals tend to follow Gamma distributions, and the information content as evaluated using Shannon entropy may not be representative of how observations may give improved knowledge regarding the variable. A alternative approach is to instead use the Kullback-Leibler divergence as a measure of information, a method that could yield new insight regarding the retrieval of cloud properties whose distributions vary widely and are generally not well understood.

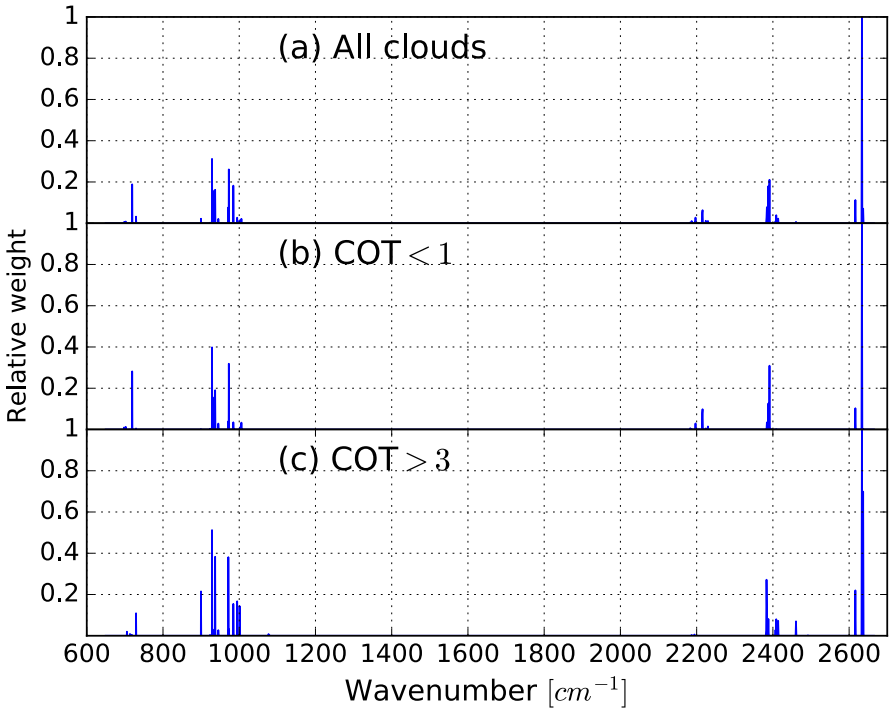

Figure A.19 Relative weight of AIRS channels for (a) all clouds, (b) clouds with optical thickness less than 1, and (c) clouds with optical thickness larger than 3.

In summary, this study has incorporated a large collection of observed ice cloud morphologies, together with varying satellite geometry and surface types, to obtain optimal channel sets for tropical ice cloud retrievals under three scenarios: a stand-alone AIRS algorithm, a combined AIRS-MODIS algorithm, and a combined active/passive retrieval that further utilizes

	AIRS Stand-Alone			AIRS+MODIS			AIRS+Active	
	cm^{-1} (μm)	Relative Weight		cm^{-1} (μm)	Relative Weight		cm^{-1} (μm)	Relative Weight
1	2633.55 (3.80)	1.000	1	2633.55 (3.80)	1.000	1	2633.55 (3.80)	1.000
2	928.59 (10.77)	0.312	2	11.03 μm (MODIS)	0.937	2	928.59 (10.77)	0.425
3	972.67 (10.28)	0.261	3	719.17 (13.90)	0.181	3	930.07 (10.75)	0.401
4	2391.09 (4.18)	0.211	4	2391.09 (4.18)	0.144	4	923.46 (10.83)	0.325
5	719.17 (13.90)	0.189	5	2388.15 (4.19)	0.139	5	972.67 (10.28)	0.247
6	984.50 (10.16)	0.182	6	12.02 μm (MODIS)	0.129	6	984.50 (10.16)	0.153
7	2388.15 (4.19)	0.180	7	3.96 μm (MODIS)	0.102	7	936.78 (10.67)	0.136
8	936.78 (10.67)	0.162	8	2390.11 (4.18)	0.089	8	971.46 (10.29)	0.104
9	930.07 (10.75)	0.159	9	0.65 μm (MODIS)	0.085	9	2636.79 (3.79)	0.080
10	2616.38 (3.82)	0.113	10	2229.59 (4.49)	0.075	10	2616.38 (3.82)	0.056
11	2384.25 (4.19)	0.078	11	1.64 μm (MODIS))	0.067	11	899.62 (11.12)	0.049
12	971.46 (10.29)	0.077	12	2183.31 (4.58)	0.061	12	994.56 (10.05)	0.045
13	2636.79 (3.79)	0.071	13	2384.25 (4.19)	0.054	13	1000.96 (9.99)	0.031
14	2215.50 (4.51)	0.063	14	2636.79 (3.79)	0.040	14	729.266 (13.71)	0.015
15	2214.57 (4.52)	0.051	15	2616.38 (3.82)	0.031	15	2383.280 (4.20)	0.014

Table A.2 Channel sets obtained from IC channel selection, weighted by cloud cluster populations. Leftmost column denotes channel selection and weights for stand-alone AIRS retrievals; middle column denotes selection and weights for combined AIRS-MODIS retrievals; rightmost column is for retrievals combining active sensors and AIRS. The weights are relative to the highest weighted channel in each category, so that the channel with highest weight has a relative weight of unity. Only the first 15 highest weighted channels are shown. Channels colored green indicate weights favoring thin clouds (COT < 1), blue indicates those favoring clouds with 1 < COT < 3, and orange indicates those favoring thick clouds (COT >3).

cloud boundary information from CloudSat and CALIPSO. Although this paper has demonstrated the utility of IC for channel selection and analysis, one of the drawbacks of IC channel selection is the difficulty of properly representing uncertainties. While some uncertainties, such as ones due to temperature and humidity, are relatively straightforward to model, other error sources, such as non-LTE (Strow et al., 2006), spatial inhomogeneity (Kahn et al., 2015), and 3-D effects (Fauchez et al., 2015) present significant challenges. Despite this drawback, IC channel selection provides a more robust assessment of optimal retrieval channels than simpler sensitivity analyses because it considers multiple sources of forward model

uncertainties and prior knowledge of retrieved variables. The channel sets we have presented can serve as a guideline for optimal estimation ice cloud retrievals and will soon be tested in the AIRS version 6 algorithm.

References

Ackerman, T. P., and G. M. Stokes, 2003: The atmospheric radiation measurement program. *Physics Today*, **56** (1), 38–44, https://doi:10.1063/1.1554135.

Alexander, S. P., T. Tsuda, Y. Kawatani, and M. Takahashi, 2008: Global distribution of atmospheric waves in the equatorial upper troposphere and lower stratosphere: COSMIC observations of wave mean flow interactions. *J. Geophys. Res.*, **113**, 1–18, https://doi.org/10.1029/2008JD010039.

Anderson, G., S. Clough, and F. Kneizys, 1986: AFGL atmospheric constituent profiles. *Environ. Res. Pap*., **954**, 1–46.

Andrews, D. G., and M. E. McIntyre, 1976: Planetary Waves in Horizontal and Vertical Shear: The Generalized Eliassen-Palm Relation and the Mean Zonal Acceleration. *J. Atmos. Sci.,* **33**, 2031–2048, https://doi.org/ 10.1175/1520-0469(1976)033,2031:PWIHAV.2.0.CO;2.

Andrews, D. G., and M. E. McIntyre, 1978: Generalized Eliassen-Palm and Charney-Drazin Theorems for Waves in Axismmetric Mean Flows in Compressible Atmospheres. *J. Atmos. Sci.*, **35**, 175–185, https://doi.org/10.1175/1520-0469(1978)035<0175:GEPACD>2.0.CO;2.

Anthes, R. A., and Coauthors, 2008: The COSMIC/FORMOSAT- 3 Mission: Early Results. *Bull. Amer. Meteor. Soc.*, **89**, 313–334, https://doi.org/10.1175/BAMS-89-3-313.

Aumann, H. H., and Coauthors, 2003: AIRS/AMSU/HSB on the aqua mission: Design, science objectives, data products, and processing systems. *IEEE Trans. Geosci.*, 41, 253–263, https://doi.org/10.1109/TGRS.2002.808356.

Awaka, J., T. Iguchi, H. Kumagai, and K. Okamoto, 2002: Rain type classification algorithm for TRMM precipitation radar. *IGARSS'97. 1997 IEEE International Geoscience and Remote Sensing Symposium Proceedings. Remote Sensing - A Scientific Vision for Sustainable Development*, IEEE, **4**, 1633–1635, https://doi.org/10.1109/IGARSS.1997.608993.

Baldridge, A. M., S. J. Hook, C. I. Grove, and G. Rivera, 2009: The ASTER spectral library version 2.0. *Remote Sens. Environ.*, **113**, 711–715, https://doi.org/10.1016/j.rse.2008.11.007.

Barnes, W., T. Pagano, and V. Salomonson, 1998: Prelaunch characteristics of the Moderate Resolution Imaging Spectroradiometer (MODIS) on EOS-AM1. *IEEE Trans. Geosci*, **36**,1088–1100, https://doi.org/10.1109/36.700993.

Baum, B. A., P. Yang, A. J. Heymsfield, A. Bansemer, B. H. Cole, A. Merrelli, C. Schmitt, and C. Wang, 2014: Ice cloud single-scattering property models with the full phase matrix at

wavelengths from 0.2 to 100μm. *J. Quant. Spectrosc. Radiat. Transfer*, **146**, 123–139, https://doi.org/10.1016/j.jqsrt.2014.02.029.

Biltoft, C. A., and E. R. Pardyjak, 2009: Spectral Coherence and the Statistical Significance of Turbulent Flux Computations. *J. Atmos. Oceanic Technol.*, **26**, 403–409, https://doi.org/10.1175/2008JTECHA1141.1.

Bodhaine, B. A., N. B. Wood, E. G. Dutton, and J. R. Slusser, 1999: On Rayleigh Optical Depth Calculations. *J. Atmos. Oceanic Technol.*, **16**, 1854–1861, https://doi.org/10.1175/1520-0426(1999)016<1854:ORODC>2.0.CO;2.

Boehm, M. T., and J. Verlinde, 2000: Stratospheric influence on upper tropospheric tropical cirrus. *Geophys. Res. Lett.*, **27,** 3209–3212, https://doi.org/10.1029/2000GL011678.

Bretherton, C. S., M. Widmann, V. P. Dymnikov, J. M. Wallace, and I. Blade, 1999: The effective number of spatial degrees of freedom of a time-varying field. *J. Climate*, **12**, 1990–2009, https://doi.org/ 10.1175/1520- 0442(1999)012<1990:TENOSD>2.0.CO;2.

Brewer, A. W., 1949: Evidence for a world circulation provided by the measurements of helium and water vapour distribution in the stratosphere. *Quart. J. Roy. Meteor. Soc.*, **75**, 351–363, https://doi.org/10.1002/qj.49707532603.

Butchart, N., 2014: The Brewer-Dobson circulation. *Rev. Geophys.*, **52**, 157–184, https://doi.org/10.1002/2013RG000448.

Charney, J. G., and P. G. Drazin, 1961: Propagation of planetary-scale disturbances from the lower into the upper atmosphere. *J. Geophys. Res.*, **66**, 83–109, https://doi.org/10.1029/JZ066i001p00083.

Chen, B., and Z. Liu, 2016: Global water vapor variability and trend from the latest 36 year (1979 to 2014) data of ECMWF and NCEP reanalyses, radiosonde, GPS, and microwave satellite. *J. Geophys. Res. Atmos.*, **121**, 11442– 11462, https://doi.org/10.1002/2016JD024917.

Chung, S., S. Ackerman, P. F. van Delst, and W. P. Menzel, 2000: Model Calculations and Interferometer Measurements of Ice-Cloud Characteristics. *J. Appl. Meteor.*, **39**, 634–644, https://doi.org/ 10.1175/1520-0450-39.5.634.

Comstock, J. M., A. Protat, S. A. McFarlane, J. Delanoe, and M. Deng, 2013: Assessment of uncertainty in cloud radiative effects and heating rates through retrieval algorithm differences: Analysis using 3 years of ARM data at Darwin, Australia. *J. Geophys. Res. Atmos.*, **118**, 4549–4571, https://doi.org/10.1002/jgrd.50404.

Cooper, S. J., T. S. L'Ecuyer, P. Gabriel, A. J. Baran, and G. L. Stephens, 2006: Objective Assessment of the Information Content of Visible and Infrared Radiance Measurements

for Cloud Microphysical Property Retrievals over the Global Oceans. Part II: Ice Clouds. *J. Appl. Meteor.*, **45** 42–62, https://doi.org/ 10.1175/JAM2327.1.

Cooper, S. J., T. S. L'Ecuyer, P. Gabriel, A. J. Baran, and G. L. Stephens, 2007: Performance assessment of a five-channel estimation-based ice cloud retrieval scheme for use over the global oceans. *J. Geophys. Res.*, **112**, D04207, https://doi.org/10.1029/ 2006JD007122.

Cooper, S. J., T. S. L'Ecuyer, and G. L. Stephens, 2003: The impact of explicit cloud boundary information on ice cloud microphysical property retrievals from infrared radiances. *J. Geophys. Res*, **108**, 4107, https://doi.org/10.1029/2002JD002611.

Corti, T., B. P. Luo, T. Peter, H. Vomel, and Q. Fu, 2005: Mean radiative energy balance and vertical mass fluxes in the equatorial upper troposphere and lower stratosphere. *Geophys. Res. Lett.*, **32**, 1–5, https://doi.org/10.1029/2004GL021889.

Deng, M., G. G. Mace, Z. Wang, and E. Berry, 2015: Cloudsat 2C- ICE product update with a new Ze parameterization in lidar-only region. *J. Geophys. Res.*, **120**, 12,198–12,208, https://doi.org/10.1002/2015JD023600.

Deng, M., G. G. Mace, Z. Wang, and R. Paul Lawson, 2013: Evaluation of several A-Train ice cloud retrieval products with in situ measurements collected during the SPARTICUS campaign. *J. Appl. Meteor.*, **52**, 1014–1030, https://doi.org/ 10.1175/JAMC-D-12-054.1.

Dessler, A. E., M. R. Schoeberl, T. Wang, S. M. Davis, and K. H. Rosenlof, 2013: Stratospheric water vapor feedback. *Proc. Natl. Acad. Sci. U.S.A.*, **110**, 18087–18091, https://doi.org/10.1073/pnas.1310344110.

Dima, I. M., and J. M. Wallace, 2007: Structure of the Annual- Mean Equatorial Planetary Waves in the ERA-40 Reanalyses. *J. Atmos. Sci.*, **64**, 2862–2880, https://doi.org/10.1175/JAS3985.1.

Divakarla, M. G., C. D. Barnet, M. D. Goldberg, L. M. McMillin, E. Maddy, W. Wolf, L. Zhou, and X. Liu, 2006: Validation of Atmospheric Infrared Sounder temperature and water vapor retrievals with matched radiosonde measurements and forecasts. *J. Geophys. Res.*, **111**, 1–20, https://doi.org/10.1029/2005JD006116.

Dobson, G. M. B., D. N. Harrison, and J. Lawrence, 1929: Measurements of the Amount of Ozone in the Earth's Atmosphere and Its Relation to Other Geophysical Conditions. Part III. *Proceedings of the Royal Society A: Mathematical, Physical and Engineering Sciences*, **122**, 456–486, https://doi.org/10.1098/rspa.1929.0034.

Doelling, D. R., M. Sun, L. T. Nguyen, M. L. Nordeen, C. O. Haney, D. F. Keyes, and P. E. Mlynczak, 2016: Advances in Geostationary-Derived Longwave Fluxes for the CERES Synoptic (SYN1deg) Product. *J. Atmos. Oceanic Technol.*, **33**, 503–521, https://doi.org/10.1175/JTECH-D-15-0147.1.

Dunkerton, T., 1978: On the Mean Meridional Mass Motions of the Stratosphere and Mesosphere. *J. Atmos. Sci.*, **35**, 2325–2333, https://doi.org/10.1175/1520-0469(1978)035<2325: OTMMMM>2.0.CO;2.

Dunkerton, T. J., 1995: Evidence of meridional motion in the summer lower stratosphere adjacent to monsoon regions. *J. Geophys. Res.*, **100**, 16 675, https://doi.org/10.1029/95JD01263.

Eldridge, R. G., 1967: Water Vapor Absorption of Visible and Near Infrared Radiation. *Applied Optics*, **6**, 709, https://doi.org/10.1364/AO.6. 000709.

Fauchez, T., P. Dubuisson, C. Cornet, F. Szczap, A. Garnier, J. Pelon, and K. Meyer, 2015: Impacts of cloud heterogeneities on cirrus optical properties retrieved from space-based thermal infrared radiometry. *Atmos. Meas. Tech.*, **8**, 633–647, https://doi.org/10.5194/amt-8-633-2015.

Foelsche, U., B. Scherllin-Pirscher, F. Ladstadter, A. K. Steiner, and G. Kirchengast, 2011: Refractivity and temperature climate records from multiple radio occultation satellites consistent within 0.05%. *Atmos. Meas. Tech.*, **4**, 2007–2018, https://doi.org/10. 5194/amt-4-2007-2011.

Fu, Q., 1996: An Accurate Parameterization of the So- lar Radiative Properties of Cirrus Clouds for Climate Models. *J. Climate*, **9**, 2058–2082, https://doi.org/ 10.1175/1520-0442(1996)009<2058:AAPOTS>2.0.CO;2.

Fueglistaler, S., 2005: Stratospheric water vapor predicted from the Lagrangian temperature history of air entering the stratosphere in the tropics. *J. Geophys. Res.*, **110**, D08107, https://doi.org/10.1029/2004JD005516.

Fueglistaler, S., a. E. Dessler, T. J. Dunkerton, I. Folkins, Q. Fu, and P. W. Mote, 2009: Tropical tropopause layer. *Rev. Geophys.*, **47**, RG1004, https://doi.org/10.1029/2008RG000267.

Fueglistaler, S., and Q. Fu, 2006: Impact of clouds on radiative heat- ing rates in the tropical lower stratosphere. *J. Geophys. Res. Atmos.*, **111**, 1–13, https://doi.org/10.1029/2006JD007273.

Fujiwara, M., and Coauthors, 2009: Cirrus observations in the tropical tropopause layer over the western Pacific. *J. Geophys. Res. Atmos.*, **114**, 1–23, https://doi.org/10.1029/2008JD011040.

Gao, B.-C., A. F. H. Goetz, and W. J. Wiscombe, 1993: Cirrus cloud detection from Airborne Imaging Spectrometer data using the 1.38 μm water vapor band. *Geophys. Res. Lett.*, **20**, 301– 304, https://doi.org/10.1029/93GL00106.

Gelaro, R., and Coauthors, 2017: The Modern-Era Retrospective Analysis for Research and Applications, Version 2 (MERRA-2). *J. Climate*, **30**, 5419–5454, https://doi.org/10.1175/JCLI-D-16-0758.1.

Gettelman, A., 2004: Radiation balance of the tropical tropopause layer. *J. Geophys. Res.*, **109**, D07103, https://doi.org/10. 1029/2003JD004190.

Gettelman, A., and P. d. F. Forster, 2002: A Climatology of the Tropical Tropopause Layer. *J. Meteor. Soc. Japan*, **80**, 911–924, https://doi.org/10.2151/jmsj.80.911.

Gettelman, A., and Coauthors, 2010: Multimodel assessment of the up- per troposphere and lower stratosphere: Tropics and global trends. *J. Geophys. Res. Atmos.*, **115**, 1–22, https://doi.org/ 10.1029/2009JD013638.

Gill, A. E., 1980: Some simple solutions for heat induced tropical circulation. *Quart. J. Roy. Meteor. Soc.*, **106**, 447–462, https://doi.org/10.1002/qj.49710644905.

Goff, J. A., and S. Gratch, 1946: Low-pressure properties of water from -160 to 212 F. *Trans. Am. Heat. Vent. Eng.,* **52***,* 95–122.

Hagos, S., and Coauthors, 2010: Estimates of Tropical Diabatic Heating Profiles: Commonalities and Uncertainties. *J. Climate*, **23**, 542–558, https://doi.org/10.1175/2009JCLI3025.1.

Hale, G. M., and M. R. Querry, 1973: Optical Constants of Water in the 200-nm to 200-microm Wavelength Region. *Applied optics*, **12**, 555–563, https://doi.org/10.1364/AO.12.000555.

Hansen, J. E., and L. D. Travis, 1974: Light scattering in planetary atmospheres. *Space Sci. Rev.*, **16**, 527–610, https://doi.org/10.1007/ BF00168069.

Healy, S. B., 2001: Radio occultation bending angle and impact parameter errors caused by horizontal refractive index gradients in the troposphere: A simulation study. *J. Geophys. Res. Atmos*, **106**, 11 875–11 889, https://doi.org/10.1029/2001JD900050.

Henderson, D. S., T. L'Ecuyer, G. Stephens, P. Partain, and M. Sekiguchi, 2013: A Multisensor Perspective on the Radiative Impacts of Clouds and Aerosols. *J. Appl. Meteor.*, **52** , 853–871, https://doi.org/10.1175/JAMC-D-12-025.1.

Heymsfield, A. J., D. Winker, and G. J. van Zadelhoff, 2005: Extinction- ice water content-effective radius algorithms for CALIPSO. *Geophys. Res. Lett.*, **32**, 1–4, https://doi.org/10.1029/ 2005GL022742.

Highwood, E. J., and B. J. Hoskins, 1998: The tropical tropopause. *Quart. J. Roy. Meteor. Soc.*, **124**, 1579–1604, https://doi.org/10.1002/qj.49712454911.

Hitchman, M. H., and C. B. Leovy, 1986: Evolution of the Zonal Mean State in the Equatorial Middle Atmosphere during October 1978- May 1979. *J. Atmos. Sci.*, **43**, 3159– 3176, https://doi.org/10.1175/1520- 0469(1986)043<3159:EOTZMS>2.0.CO;2.

Hogan, R. J., M. E. Brooks, A. J. Illingworth, D. P. Donovan, C. Tinel, D. Bouniol, and J. P. V. P. Baptista, 2006: Independent Evaluation of the Ability of Spaceborne Radar and Lidar to Retrieve the Microphysical and Radiative Properties of Ice Clouds. *J. Atmos. Oceanic. Technol.*, **23**, 211–227, https://doi.org/10.1175/JTECH1837.1.

Hollander, M., D. A. Wolfe, and E. Chicken, 2015: *Nonparametric Statistical Methods*. Third edit ed., Wiley Series in Probability and Statistics, Wiley, 848 pp., https://doi.org/10.1002/9781119196037.

Holton, J. R., P. H. Haynes, M. E. McIntyre, A. R. Douglass, R. B. Rood, and L. Pfister, 1995: Stratosphere-troposphere exchange. *Rev. Geophys.*, **33**, 403, https://doi.org/10.1029/95RG02097.

Houze Jr, R. a., 2004: Mesoscale Convective Systems. *Rev. Geophys.*, **42**, 1–43, https://doi.org/10.1029/2004RG000150.1.INTRODUCTION.

Hsu, N. C., R. Gautam, A. M. Sayer, C. Bettenhausen, C. Li, M. J. Jeong, S. C. Tsay, and B. N. Holben, 2012: Global and regional trends of aerosol optical depth over land and ocean using SeaWiFS measurements from 1997 to 2010. *Atmos. Chem. Phys.*, 12 (17), 8037–8053, https://doi.org/10.5194/acp-12-8037-2012.

Huang, H., P. Yang, H. Wei, B. A. Baum, Y. Hu, P. Antonelli, and S. Ackerman, 2004: Inference of ice cloud properties from high spectral resolution infrared observations. *IEEE Trans. Geosci.*, **42**, 842–853, https://doi.org/10.1109/TGRS.2003.822752.

Huang, Y., M. Zhang, Y. Xia, Y. Hu, and S. W. Son, 2016: Is there a stratospheric radiative feedback in global warming simulations? *Clim. Dyn.*, **46**, 177–186, https://doi.org/10.1007/s00382-015-2577-2.

Hurst, D. F., S. J. Oltmans, H. Vomel, K. H. Rosenlof, S. M. Davis, E. A. Ray, E. G. Hall, and A. F. Jordan, 2011: Stratospheric water vapor trends over Boulder, Colorado: Analysis of the 30 year Boulder record. *J. Geophys. Res.*, **116**, D02306, https://doi.org/10.1029/2010JD015065.

Iguchi, T., R. Meneghini, J. Awaka, T. Kozu, and K. Okamoto, 2000: Rain profiling algorithm for TRMM Precipitation Radar data. *Adv. Space. Res.*, **25**, 973–976, https://doi.org/10.1016/S0273-1177(99)00933-3.

Immler, F., K. Kruger, S. Tegtmeier, M. Fujiwara, P. Fortuin, G. Verver, and O. Schrems, 2007: Cirrus clouds, humidity, and dehydration in the tropical tropopause layer observed at Paramaribo, Suri- name (5.8N, 55.2W). *J. Geophys. Res. Amos.*, **112**, 1–14, https://doi.org/10.1029/2006JD007440.

Inness, A., and Coauthors, 2013: The MACC reanalysis: An 8 yr data set of atmospheric composition. *Atmos. Chem. Phys.*, **13**, 4073–4109, https://doi.org/10.5194/acp-13-4073-2013.

Inoue, T., 1985: On the Temperature Measurements and Effective Cirrus Emissivity Clouds by Window Determination Region of Semi- Transparent in the. *J. Meteor. Soc. Japan*, **63**, 88–99.

Jensen, E. J., O. B. Toon, L. Pfister, and H. B. Selkirk, 1996: Dehydration of the upper troposphere and lower stratosphere by sub-visible cirrus clouds near the tropical tropopause. *Geophys. Res. Lett.*, **23**, 825–828, https://doi.org/10.1029/96GL00722.

Jensen, E. J., and Coauthors, 2013: Ice nucleation and dehydration in the Tropical Tropopause Layer. *Proc. Natl. Acad. Sci.*, **110**, 2041–2046, https://doi.org/10.1073/pnas.1217104110.

Jin, F., and B. J. Hoskins, 1995: The Direct Response to Tropical Heating in a Baroclinic Atmosphere. *J. Atmos. Sci.*, **52**, 307–319, https://doi.org/10.1175/1520-0469(1995)052<0307: TDRTTH>2.0.CO;2.

Jin, H., and S. L. Nasiri, 2014: Evaluation of AIRS Cloud-Thermodynamic-Phase Determination with CALIPSO. *J. Appl. Meteor.*, **53**, 1012–1027, https://doi.org/ 10.1175/JAMC-D-13-0137.1.

Kahn, B. H., A. Eldering, M. Ghil, S. Bordoni, and S. a. Clough, 2004: Sensitivity Analysis of Cirrus Cloud Properties from High-Resolution Infrared Spectra. Part I: Methodology and Synthetic Cirrus. *J. Climate*, **17**, 4856–4870, https://doi.org/10.1175/JCLI- 3220.1.

Kahn, B. H., and Coauthors, 2014: The Atmospheric Infrared Sounder version 6 cloud products. *Atmos. Chem. Phys.*, **14**, 399–426, https://doi.org/10.5194/acp-14-399-2014.

Kahn, B. H., and Coauthors, 2015: Pixel-scale assessment and un- certainty analysis of AIRS and MODIS ice cloud optical thickness and effective radius. *J. Geophys. Res. Atmos.*, **120**, 11669–11689, https://doi.org/10.1002/2015JD023950.

Kawatani, Y., J. N. Lee, and K. Hamilton, 2014: Interannual variations of stratospheric water vapor in MLS observations and climate model simulations. *J. Atmos. Sci.*, **71**, 4072–4085, https://doi.org/10.1175/JAS-D-14-0164.1.

Kim, J., W. J. Randel, and T. Birner, 2018a: Convectively Driven Tropopause-Level Cooling and Its Influences on Stratospheric Moisture. *J. Geophys. Res. Atmos.*, **123**, 590–606, https://doi.org/10.1002/2017JD027080.

Kim, J., W. J. Randel, T. Birner, and M. Abalos, 2016a: Spectrum of Wave Forcing Associated with the Annual Cycle of Up-welling at the Tropical Tropopause. *J. Atmos. Sci.*, **73**, 855–868, https://doi.org/10.1175/JAS-D-15-0096.1.

Kim, J.-E., C. Zhang, G. N. Kiladis, and P. Bechtold, 2018b: Heating and Moistening of the MJO during DYNAMO in ECMWF Reforecasts. *J. Atmos. Sci.*, **75**, 1429–1452, https://doi.org/10.1175/JAS-D-17-0170.1.

Kim, J.-E., and Coauthors, 2016b: Ubiquitous influence of waves on tropical high cirrus clouds. *Geophys. Res. Lett.*, **43**, 5895–5901, https://doi.org/10.1002/2016GL069293.

Kummerow, C., W. Barnes, T. Kozu, J. Shiue, and J. Simpson, 1998: The Tropical Rainfall Measuring Mission (TRMM) sensor package. *J. Atmos. Oceanic Technol.*, **15**, 809– 817, https://doi.org/10.1175/1520-0426(1998)015<0809:TTRMMT>2.0.CO;2.

Kursinski, E. R., G. A. Hajj, J. T. Schofield, R. P. Linfield, and K. R. Hardy, 1997: Observing Earth's atmosphere with radio occultation measurements using the Global Positioning System. *J. Geophys. Res. Atmos.*, **102**, 23429–23465, https://doi.org/10. 1029/97JD01569.

Lambert, A., and Coauthors, 2007: Validation of the Aura Microwave Limb Sounder middle atmosphere water vapor and nitrous oxide measurements. *J. Geophys. Res*, **112**, D24S36, https://doi.org/10.1029/2007JD008724.

L'Ecuyer, T. S., P. Gabriel, K. Leesman, S. J. Cooper, and G. L. Stephens, 2006: Objective Assessment of the Information Content of Visible and Infrared Radiance Measurements for Cloud Microphysical Property Retrievals over the Global Oceans. Part I: Liquid Clouds. *J. Appl. Meteor.*, **45**, 20–41, https://doi.org/10.1175/JAM2326.1.

L'Ecuyer, T. S., and G. Mcgarragh, 2010: A 10-year climatology of tropical radiative heating and its vertical structure from TRMM observations. *J. Climate*, 23 (3), 519–541, https://doi.org/10.1175/ 2009JCLI3018.1.

Lensky, I. M., and D. Rosenfeld, 2008: Clouds-Aerosols-Precipitation Satellite Analysis Tool (CAPSAT). *Atmos. Chem. Phys.*, **8**, 6739–6753, https://doi.org/10.5194/acp-8-6739-2008.

Li, F., D. W. Waugh, A. R. Douglass, P. A. Newman, S. E. Strahan, J. Ma, J. E. Nielsen, and Q. Liang, 2012: Long-term changes in stratospheric age spectra in the 21st century in the Goddard Earth Observing System Chemistry-Climate Model (GEOSCCM). *J. Geophys. Res. Atmos.*, **117**, 1– 15, https://doi.org/10.1029/2012JD017905.

Li, Y., D. W. Thompson, S. Bony, and T. M. Merl, 2019: Thermodynamic control on the poleward shift of the extratropical jet in climate change simulations: The role of rising high clouds and their radiative effects. *J. Climate*, **32**, 917–934, https://doi.org/10.1175/JCLI-D-18-0417.1.

Li, Y., D. W. Thompson, G. L. Stephens, and S. Bony, 2014: A global survey of the instantaneous linkages between cloud vertical structure and large-scale climate. *J. Geophys. Res.*, **119**, 3770–3792, https://doi.org/10.1002/2013JD020669.

Li, Y., D. W. J. Thompson, and Y. Huang, 2017: The Influence of Atmospheric Cloud Radiative Effects on the Large-Scale Atmospheric Circulation. *J. Climate*, **30**, 5621–5635, https://doi.org/ 10.1175/JCLI-D-16-0643.1.

Lin, J., B. Mapes, M. Zhang, and M. Newman, 2004: Stratiform Precipitation, Vertical Heating Profiles, and the Madden Julian Oscillation. *J. Atmos. Sci*, **61**, 296–309, https://doi.org/10.1175/1520- 0469(2004)061<0296:SPVHPA>2.0.CO;2,

Liou, K., 1986: Influence of Cirrus Clouds on Weather and Climate processes: a global perspective. *Mon. Wea. Rev.*,

Livesey, N. J., and Coauthors, 2017: Version 4.2 x Level 2 data quality and description document, JPL D-33509 Rev. C. *Jet Propulsion Laboratory*, https://mls.jpl.nasa.gov/data/v4-2_data_quality_document.pdf.

Luo, B. P., and Coauthors, 2003: Dehydration potential of ultrathin clouds at the tropical tropopause. *Geophys. Res. Lett.*, **30**, 1557–1560, https://doi.org/10.1029/2002GL016737.

Maloney, C., and Coauthors, 2019: An Evaluation of the Representation of Tropical Tropopause Cirrus in the CESM/CARMA Model Using Satellite and Aircraft Observations. *J. Geophys. Res. Atmos.* **124**, 8659–8687, https://doi.org/10.1029/ 2018jd029720.

Masunaga, H., 2012: A Satellite Study of the Atmospheric Forcing and Response to Moist Convection over Tropical and Subtropical Oceans. *J. Atmos. Sci.*, **69**, 150–167, https://doi.org/ 10.1175/JAS-D-11-016.1.

Masunaga, H., and T. S. L'Ecuyer, 2014: A Mechanism of Tropical Convection Inferred from Observed Variability in the Moist Static Energy Budget. *J. Atmos. Sci.*, **71**, 3747–3766, https://doi.org/10.1175/JAS-D-14-0015.1.

Matsuno, T., 1966: Quasi-Geostrophic Motions in the Equatorial Area. *J. Meteor. Soc. Japan Ser. II*, **44**, 25–43, https://doi.org/10.2151/jmsj1965.44.1 25.

Moran, K. P., B. E. Martner, M. J. Post, R. A. Kropfli, D. C. Welsh, and K. B. Widener, 1998: An Unattended Cloud- Profiling Radar for Use in Climate Research. *Bull. Amer. Meteor. Soc.*, **79**, 443–455, https://doi.org/10.1175/15200477(1998)079<0443:AUCPRF>2.0.CO;2.

Mote, P. W., H. L. Clark, T. J. Dunkerton, R. S. Harwood, and H. C. Pumphrey, 2000: Intraseasonal variations of water vapor in the tropical upper troposphere and tropopause region. *J. Geophys. Res. Atmos*, **105**, 17457–17470, https://doi.org/10.1029/ 2000JD900158.

Mote, P. W., and Coauthors, 1996: An atmospheric tape recorder: The imprint of tropical tropopause temperatures on stratospheric water vapor. *J. Geophys. Res.*, **101**, 3989, https://doi.org/10.1029/95JD03422.

Murgatroyd, R. J., and F. Singleton, 1961: Possible meridional circulations in the stratosphere and mesosphere. *Quart. J. Roy. Meteor. Soc.*, **87**, 125–135, https://doi.org/10.1002/qj.49708737202.

Nakajima, T., and M. D. King, 1990: Determination of the Optical Thickness and Effective Particle Radius of Clouds from Reflected Solar Radiation Measurements. Part I: Theory. *J. Atmos. Sci.*, **47**, 1878–1893, https://doi.org/ 10.1175/1520-0469(1990)047<1878:DOTOTA>2.0.CO;2.

Nedoluha, G. E., R. Michael Gomez, D. R. Allen, A. Lambert, C. Boone, and G. Stiller, 2013: Variations in middle atmospheric water vapor from 2004 to 2013. *J. Geophys. Res. Atmos.*, **118**, 11285–11293, https://doi.org/10.1002/jgrd.50834.

Nesbitt, S. W., R. Cifelli, and S. A. Rutledge, 2006: Storm Morphology and Rainfall Characteristics of TRMM Precipitation Features. *Mon. Wea. Rev.*, **134**, 2702–2721, https://doi.org/10.1175/MWR3200.1.

Nishimoto, E., and M. Shiotani, 2012: Seasonal and interannual variability in the temperature structure around the tropical tropopause and its relationship with convective activities. *J. Geophys. Res. Atmos.*, **117**, 1–11, https://doi.org/10.1029/2011JD016936.

Nowack, P. J., N. Luke Abraham, A. C. Maycock, P. Braesicke, J. M. Gregory, M. M. Joshi, A. Osprey, and J. A. Pyle, 2015: A large ozone-circulation feedback and its implications for global warming assessments. *Nature Climate Change*, **5**, 41–45, https://doi.org/10.1038/nclimate2451.

Park, M., W. J. Randel, A. Gettelman, S. T. Massie, and J. H. Jiang, 2007: Transport above the Asian summer monsoon anticyclone inferred from Aura Microwave Limb Sounder tracers. *J. Geophys. Res.*, **112**, D16309, https://doi.org/10.1029/2006JD008294.

Paulik, L. C., and T. Birner, 2012: Quantifying the deep convective temperature signal within the tropical tropopause layer (TTL). *Atmos. Chem. Phys.*, **12**, 12183–12195, https://doi.org/10.5194/acp-12-12183-2012.

Petty, G. W.: On some shortcomings of Shannon entropy as a measure of information content in indirect measurements. *J. Atmos. Ocean. Tech*, **35**, 1011–1021, doi:10.1175/JTECH-D-17-0056.1, 2018

Pirscher, B., U. Foelsche, M. Borsche, G. Kirchengast, and Y.-H. Kuo, 2010: Analysis of migrating diurnal tides detected in FORMOSAT- 3/COSMIC temperature data. *J. Geophys. Res.*, **115**, D14108, https://doi.org/10.1029/2009JD013008.

Podglajen, A., R. Plougonven, A. Hertzog, and E. Jensen, 2018: Impact of gravity waves on the motion and distribution of atmospheric ice particles. *Atmos. Chem. Phys.*, **18**, 10799–10823, https://doi.org/10.5194/acp-18-10799-2018.

Poole, L. R., and M. C. Pitts, 1994: Polar stratospheric cloud climatology based on Stratospheric Aerosol Measurement II observations from 1978 to 1989. *J. Geophys. Res.*, **99**, 13083, https://doi.org/10.1029/94JD00411.

Ramage, C. S., 1968: Role of a tropical Maritime Continent in the atmospheric circulation. *Mon. Wea. Rev.*, **96**, 365–370, https://doi.org/10.1175/1520-0493(1968)096<0365:ROATMC>2.0.CO;2.

Randel, W., and M. Park, 2019: Diagnosing Observed Stratospheric Water Vapor Relationships to the Cold Point Tropical Tropopause. *J. Geophys. Res. Atmos.*, **124**, 7018-7033, https://doi.org/10.1029/2019JD030648.

Randel, W. J., and E. J. Jensen, 2013: Physical processes in the tropical tropopause layer and their roles in a changing climate. *Nat. Geosci.*, **6**, 169–176, https://doi.org/10.1038/ngeo1733..

Randel, W. J., and F. Wu, 2005: Kelvin wave variability near the equatorial tropopause observed in GPS radio occultation measurements. *J. Geophys. Res. Atmos.*, **110**, 1–13, https://doi.org/10.1029/2004JD005006.

Read, W. G., and Coauthors, 2007: Aura Microwave Limb Sounder upper tropospheric and lower stratospheric H_2O and relative humidity with respect to ice validation. *J. Geophsy. Res.*, **112**, D24S35, https://doi.org/10.1029/2007JD008752.

Rind, D., and P. Lonergan, 1995: Modeled impacts of stratospheric ozone and water vapor perturbations with implications for high- speed civil transport aircraft. *J. Geophys. Res.,* **100**, 7381–7396, https://doi.org/10.1029/95JD00196.

Rocken, C., and Coauthors, 1997: Analysis and validation of GPS/MET data in the neutral atmosphere. *J. Geophys. Res. Atmos.*, **102**, 29849–29866, https://doi.org/10.1029/97JD02400.

Rodgers, C. D., 1976: Retrieval of Atmospheric Temperature and Composition From Remote Measurements of Thermal Radiation. *Rev. Geophys. Space Phys.*, **14**, 609–624, https://doi.org/ 10.1029/RG014i004p00609.

Rodgers, C. D., 1996: Information content and optimization of high spectral resolution measurements. *SPIE, Optical Spectroscopic techniques and Instrumentation for Atmospheric and Space Research II*, **2830**, 136–147.

Rodgers, C. D., 2000: *Inverse Methods for Atmospheric Sounding: Theory and Practice*. Series on atmospheric, oceanic and planetary physics, World Scientific.

Rothman, L. S., and Coauthors, 2009: The HITRAN 2008 molecular spectroscopic database. *J. Quant. Spectrosc. Radiat. Transfer*, **110**, 533–572, https://doi.org/10.1016/j.jqsrt.2009.02.013.

Ryu, J.-H., S. Lee, and S.-W. Son, 2008: Vertically Propagating Kelvin Waves and Tropical Tropopause Variability. *J. Atmos. Sci.*, **65**, 1817–1837, https://doi.org/10.1175/2007JAS2466.1.

Sassen, K., Z. Wang, and D. Liu, 2008: Global distribution of cirrus clouds from CloudSat/Cloud-Aerosol Lidar and Infrared Pathfinder Satellite Observations (CALIPSO) measurements. *J. Geophys. Res.*, **113**, D00A12, https://doi.org/10.1029/2008JD009972.

Sassen, K., Z. Wang, and D. Liu, 2009: Cirrus clouds and deep convection in the tropics: Insights from CALIPSO and CloudSat. *J. Geophys. Res. Atmos.*, **114**, 1–11, https://doi.org/10.1029/2009JD011916.

Scherllin-Pirscher, B., W. J. Randel, and J. Kim, 2017: Tropical temperature variability and Kelvin-wave activity in the UTLS from GPS RO measurements. *Atmos. Chem. Phys.*, **17**, 793– 806, https://doi.org/10.5194/acp-17-793-2017.

Schiller, C., J.-U. Grooß, P. Konopka, F. Ploger, F. H. Silva dos Santos, and N. Spelten, 2009: Hydration and de- hydration at the tropical tropopause. *Atmos. Chem. Phys.*, **9**, 9647–9660, https://doi.org/10.5194/acp-9-9647-2009.

Schoeberl, M. R., E. J. Jensen, and S. Woods, 2015: Gravity waves amplify upper tropospheric dehydration by clouds. *Earth Space Sci.*, **2**, 485–500, https://doi.org/10.1002/2015EA000127.

Schumacher, C., and R. A. Houze, 2003: The TRMM Precipitation Radar's View of Shallow, Isolated Rain. *J. Appl. Meteor.*, **42**, 1519–1524, https://doi.org/10.1175/1520-0450(2003)042<1519:TTPRVO>2.0.CO;2.

Seviour, W. J. M., N. Butchart, and S. C. Hardiman, 2012: The Brewer- Dobson circulation inferred from ERA-Interim. *Quart. J. Roy. Meteor. Soc.*, **138**, 878–888, https://doi.org/10.1002/qj.966.

Shige, S., Y. N. Takayabu, S. Kida, W.-K. Tao, X. Zeng, C. Yokoyama, and T. L'Ecuyer, 2009: Spectral Retrieval of Latent Heating Pro- files from TRMM PR Data. Part IV: Comparisons of Lookup Tables from Two- and Three-Dimensional Cloud-Resolving Model Simulations. *J. Climate*, **22**, 5577–5594, https://doi.org/10.1175/ 2009JCLI2919.1.

Shige, S., Y. N. Takayabu, and W. K. Tao, 2008: Spectral retrieval of latent heating profiles from TRMM PR data. Part III: Estimating apparent moisture sink profiles over tropical oceans. *J. Appl. Meteor.*, **47**, 620–640, https://doi.org/ 10.1175/2007JAMC1738.1.

Shige, S., Y. N. Takayabu, W.-K. Tao, and D. E. Johnson, 2004: Spectral Retrieval of Latent Heating Profiles from TRMM PR Data. Part I: Development of a Model-Based Algorithm. *J. Appl. Meteor. Clim.*, **43**, 1095–1113, https://doi.org/ 10.1175/1520-0450(2004)043<1095:SROLHP>2.0.CO;2.

Shige, S., Y. N. Takayabu, W.-K. Tao, and C.-L. Shie, 2007: Spectral Retrieval of Latent Heating Profiles from TRMM PR Data. Part II: Algorithm Improvement and Heating Estimates over Tropical Ocean Regions. *J. Appl. Meteor. Clim.*, **46**, 1098–1124, https://doi.org/10.1175/JAM2510.1.

Shine, K., 1989: Sources and sinks of zonal momentum in the middle atmosphere diagnosed using the diabatic circulation. *Quart. J. Roy. Meteor. Soc*, **115**, 265–292, https://doi.org/10.1002/qj.49711548604.

Sidran, M., 1981: Broadband reflectance and emissivity of specular and rough water surfaces. *Applied Optics*, **20**, 3176, https://doi.org/10.1364/AO.20.003176.

Simpson, J., R. F. Adler, and G. R. North, 1988: A Proposed Tropical Rainfall Measuring Mission (TRMM) Satellite. *Bull. Amer. Meteor. Soc.*, **69**, 278–295, https://doi.org/10.1175/1520- 0477(1988)069<0278:APTRMM>2.0.CO;2,

Smith, W. L., and C. M. R. Platt, 1978: Comparison of Satellite-Deduced Cloud Heights with Indications from Radiosonde and Ground-Based Laser Measurements. *J. Appl. Meteor. Clim.,* **17**, 1796-1802, https://doi.org/ 10.1175/1520-0450%281978%29017<1796%3ACOSDCH>2.0.CO%3B2.

Sofieva, V. F., 2003: Information approach to optimal selection of spectral channels. *J. Geophys. Res*, **108**, 1–9, https://doi.org/ 10.1029/2002JD002980.

Solomon, S., J. T. Kiehl, R. R. Garcia, and W. Grose, 1986: Tracer Transport by the Diabatic Circulation Deduced from Satellite Observations. *J. Atmos. Sci.,* **43**, 1603-1617, https://doi.org/ 10.1175/1520-0469%281986%29043<1603%3ATTBTDC>2.0.CO%3B2.

Solomon, S., K. H. Rosenlof, R. W. Portmann, J. S. Daniel, S. M. Davis, T. J. Sanford, and G.-K. Plattner, 2010: Contributions of Stratospheric Water Vapor to Decadal Changes in the Rate of Global Warming. *Science*, **327**, 1219–1223, https://doi.org/10.1126/science.

Sourdeval, O., L. C.-Labonnote, A. J. Baran, and G. Brogniez, 2015: A methodology for simultaneous retrieval of ice and liquid water cloud properties. Part I: Information content and case study. *Quart. J. Roy. Meteor. Soc.*, **141**, 870–882, https://doi.org/10.1002/qj.2405.

Spinhirne, J. D., 1993: Micro Pulse Lidar. *IEEE Trans. Geosci.*, **31**, 48–55, https://doi.org/10.1109/36.210443.

Spurr, R. J. D., 2006: VLIDORT: A linearized pseudo-spherical vector discrete ordinate radiative transfer code for forward model and retrieval studies in multilayer multiple scattering media. *J. Quant. Spectrosc. Radiat. Transfer,* **102**, 316– 342, https://doi.org/10.1016/j.jqsrt.2006.05.005.

Stephens, G. L., P. M. Gabriel, and P. T. Partain, 2001: Parameterization of Atmospheric Radiative Transfer. Part I: Validity of Simple Models. *J. Atmos. Sci.*, **58**, 3391– 3409, https://doi.org/10.1175/1520-0469(2001)058<3391:POARTP>2.0.CO;2.

Stephens, G. L., and Coauthors, 2008: CloudSat mission: Performance and early science after the first year of operation. *J. Geophys. Res.*, **113**, D00A18, https://doi.org/10.1029/2008JD009982.

Strow, L. L., S. E. Hannon, S. De-Souza Machado, H. E. Motteler, and D. C. Tobin, 2006: Validation of the Atmospheric Infrared Sounder radiative transfer algorithm. *J. Geophys. Res.*, **111**, D09S06, https://doi.org/10.1029/2005JD006146.

Susskind, J., J. M. Blaisdell, and L. Iredell, 2014: Improved method- ology for surface and atmospheric soundings, error estimates, and quality control procedures: the atmospheric infrared sounder science team version-6 retrieval algorithm. *J. Appl. Remote Sens.*, **8**, 84 994, https://doi.org/10.1117/1.JRS.8.084994.

Suzuki, J., M. Fujiwara, T. Nishizawa, R. Shirooka, K. Yoneyama, M. Katsumata, I. Matsui, and N. Sugimoto, 2013: The occur- rence of cirrus clouds associated with eastward propagating equatorial n = 0 inertio-gravity and Kelvin waves in November 2011 during the CINDY2011/DYNAMO campaign. *J. Geophys. Res. Atmos.*, **118**, 12941–12947, https://doi.org/10.1002/2013JD019960.

Tao, W. K., S. Lang, X. Zeng, S. Shige, and Y. Takayabu, 2010: Relating convective and stratiform rain to latent heating. *J. Climate*, **23**, 1874–1893, https://doi.org/10.1175/2009JCLI3278.1.

Tao, W.-K., and J. Simpson, 1993: Goddard Cumulus Ensemble Model. Part I: Model Description. *Terr. Atmos. Ocean Sci.*, **4**, 035, https://doi.org/10.3319/TAO.1993.4.1.35(A.

Tao, W.-K., and Coauthors, 2016: TRMM Latent Heating Retrieval: Applications and Comparisons with Field Campaigns and Large-Scale Analyses. *Meteorological Monographs*, **56** (Code 612), 2.1–2.34, https://doi.org/ 10.1175/AMSMONOGRAPHS-D-15-0013.1.

Troyan, D., 2012: Merged sounding value-added product. Tech. rep., US Department of Energy, Washington, D. C. https://www. arm.gov/publications/tech_reports/doe-sc-arm-tr-087.pdf.

Virts, K. S., and J. M. Wallace, 2014: Observations of Temperature, Wind, Cirrus, and Trace Gases in the Tropical Tropopause Transition Layer during the MJO*. *J. Atmos. Sci.*, **71**, 1143–1157, https://doi.org/10.1175/JAS-D-13-0178.1.

Von Engeln, A., S. Healy, C. Marquardt, Y. Andres, and F. Sancho, 2009: Validation of operational GRAS radio occultation data. *Geophys. Res. Lett.*, **36**, 5–8, https://doi.org/10.1029/ 2009GL039968.

Wang, C., S. Platnick, Z. Zhang, K. Meyer, G. Wind, and P. Yang, 2016a: Retrieval of ice cloud properties using an optimal estimation algorithm and MODIS infrared observations: 2. Retrieval evaluation. *J. Geophys. Res. Atmos.*, **121**, 5827–5845, https://doi.org/10.1002/2015JD024528.

Wang, C., S. Platnick, Z. Zhang, K. Meyer, and P. Yang, 2016b: Retrieval of ice cloud properties using an optimal estimation algorithm and MODIS infrared observations: 1. Forward model, error analysis, and information content. *J. Geophys. Res. Atmos.*, **121**, 5809– 5826, https://doi.org/10.1002/2015JD024526.

Wang, S., A. H. Sobel, F. Zhang, Y. Q. Sun, Y. Yue, and L. Zhou, 2015: Regional Simulation of the October and November MJO Events Observed during the CINDY/DYNAMO Field Campaign at Gray Zone Resolution. *J. Climate*, **28**, 2097–2119, https://doi.org/ 10.1175/JCLI- D-14-00294.1.

Wang, Z., and K. Sassen, 2002: Cirrus Cloud Microphysical Property Retrieval Using Lidar and Radar Measurements. Part II: Midlatitude Cirrus Microphysical and Radiative Properties. *J. Atmos. Sci.*, **59**, 2291–2302, https://doi.org/ 10.1175/1520-0469(2002)059<2291:CCMPRU>2.0.CO;2.

Waters, J., and Coauthors, 2006: The Earth observing system microwave limb sounder (EOS MLS) on the aura Satellite. *IEEE Trans. Geosci.*, **44**, 1075– 1092, https://doi.org/10.1109/TGRS.2006.873771.

Welch, P. D., 1967: The Use of Fast Fourier Transform for the Estimation of Power Spectra: A Method Based on Time Averaging Over Short, Modified Periodograms. *IEEE Trans. Audio Electroacoust.*, **15**, 70-73,https://doi.org/10.1109/TAU.1967.1161901.

Wickert, J., and Coauthors, 2001: Atmosphere sounding by GPS radio occultation: First results from CHAMP. *Geopys. Res. Lett.,* **28**, 3263–3266, https://doi.org/10.1029/2001GL013117.

Wilks, D. S., 2011: Statistical Methods in the Atmospheric Sciences. Academic Press, Academic Press, https://doi.org/ 10.1016/B978-0-12-385022-5.00020-8.

Winker, D. M., and C. R. Trepte, 1998: Laminar cirrus observed near the tropical tropopause by LITE. *Geophys. Res. Lett.*, **25**, 3351–3354, https://doi.org/10.1029/98GL01292.

Winker, D. M., and Coauthors, 2010: The CALIPSO Mission. *Bull. Amer. Meteor. Soc.*, **91**, 1211–1230, https://doi.org/10.1175/2010BAMS3009.1.

Xiong, X., J. Sun, J. A. Esposito, B. Guenther, and W. L. Barnes, 2003a: MODIS Reflective Solar Bands Calibration Algorithm and On-orbit Performance. *Optical Remote Sensing of the Atmosphere and Clouds III*, **4891**, 95–104, https://doi.org/10.1117/12.466096.

Xiong, X., J.-Q. Sun, J. A. Esposito, B. Guenther, and W. L. Barnes, 2003b: MODIS reflective solar bands calibration algorithm and on-orbit performance. *Proc. SPIE*, **4891**, 392–401, https://doi.org/10.1117/12.466083.

Yanai, M., S. Esbensen, and J.-H. Chu, 1973: Determination of Bulk Properties of Tropical Cloud Clusters from Large- Scale Heat and Moisture Budgets. *J. Atmos. Sci.*, **30**, 611-627, https://doi.org/10.1175/1520-0469%281973%29030<0611%3ADOBPOT>2.0.CO%3B2.

Yang, P., L. Bi, B. a. Baum, K.-N. Liou, G. W. Kattawar, M. I. Mishchenko, and B. Cole, 2013: Spectrally Consistent Scattering, Absorption, and Polarization Properties of Atmospheric Ice Crystals at Wavelengths from 0.2 to 100 μm. *J. Atmos. Sci.*, **70**, 330–347, https://doi.org/10.1175/JAS-D-12-039.1.

Zeng, Z., W. Randel, S. Sokolovskiy, C. Deser, Y.-H. Kuo, M. Hagan, J. Du, and W. Ward, 2008: Detection of migrating diurnal tide in the tropical upper troposphere and lower stratosphere using the Challenging Minisatellite Payload radio occultation data. *J. Geophys. Res.*, **113**, D03102, https://doi.org/10.1029/2007JD008725.

Zeng, Z., S. Sokolovskiy, W. S. Schreiner, and D. Hunt, 2019: Representation of vertical atmospheric structures by radio occultation observations in the upper troposphere and lower stratosphere: Comparison to high-resolution radiosonde profiles. *J. Atmos. Oceanic Technol.*, **36**, 655–670, https://doi.org/10.1175/JTECH-D-18-0105.1.

Zhang, C., and J. Ling, 2011: Potential Vorticity of the Madden Julian Oscillation. *J. Atmos. Sci.*, **69**, 65–78, https://doi.org/ 10.1175/jas-d-11-081.1.

Zhou, X., and J. R. Holton, 2002: Intraseasonal Variations of Tropical Cold-Point Tropopause Temperatures. *J. Climate*, **15**,1460–1473, https://doi.org/10.1175/1520-0442(2002)015<1460:IVOTCP>2.0.CO;2.